Gas and Dust Chemistry in Planet-Forming Disks

Thesis by

Jacqueline Kessler-Silacci

In Partial Fulfillment of the Requirements

for the Degree of

Doctor of Philosophy

California Institute of Technology

Pasadena, California

2003

(Defended August 13, 2003)

For my parents, Jay and Gail, and my husband, Lucas.

Acknowledgements

This thesis was written the help and support of several people. First, a special thanks to my advisor Geoff Blake. Before I met you I didn't know what an "Astrochemist" was; your example has helped me find my place in the science community and your enthusiasm for the field is truly inspiring. Without your superior knowledge of chemistry, astronomy and, most of all, grammar, this thesis could not be written.

To my committee members, Mitchio Okumura, Harry Gray and Rudy Marcus, thank you for encouraging me to pursue a subject which is so interdisciplinary. Your questions and guidance bound me to chemical principles and kept me from being swallowed up by the astronomers' view of chemistry (which regards all elements heavier than helium as metals!).

I would like to thank Anneila Sargent, Lynne Hillenbrand, Nick Scoville and Geoff Blake for demonstrating that it is possible to value family life and still have a lasting impact on the world of science. Including also Michiel Hogerheijde, Karen Willacy, Bill Langer and Ewine van Dishoeck, thank you for your collaboration and guidance. I have learned a lot from all of you.

My thanks to the OVRO group(s) of 1999–2003 (Adwin Boogert, John Carpenter, Carmen Sanchez Contreras, Dave Frayer, Shardha Jogee, Sheng-Yuan Liu, Jenny Patience, Charlie Qi, Fabian Walter and Eva Schinerer) for schooling me in the art of radio astronomy and answering my many questions along the way, even when it meant directing me to someone else. In particular, thank you Charlie Qi, Adwin Boogert and Sheng-Yuan Liu for allowing me to pester you with a multitude of questions ranging from reaction mechanisms to spectroscopic constants to temperature conversions.

Members of the Blake group, I will never forget your show of support during my props exam and thesis defense; thank you so much! Also, thank you Susanna Widicus, Rebecca Washenfelder, Dawn Erb, Dave Kaplan, George Becker and Edo Berger for many lunchtime (and tea time) conversations about science, politics and life. And thanks to Jenny Patience, Carmen Sanchez Contreras, Armando Gil de Paz, Kartik Sheth and Tony Gianetti for the most entertaining racquetball games that I have ever played. Micol Christopher, Naveen Reddy, Pat Udomprasert and Rob Simcoe thank you for keeping me company during the late nights and weekends while I wrote this thesis, and for making me feel like I was one of the most sane people there. And thanks to many friends outside of Caltech for reminding me that there is a world outside of Caltech.

Last, but not least, I would like to thank my parents, Jay and Gail, for supporting everything I do and my brothers for making fun of it. And to my husband Lucas for his loving support and distraction and for planning most of our wedding so that I could finish writing this thesis.

Abstract

As analogs to the solar nebula, circumstellar disks offer a unique opportunity to study the conditions during the star and planet formation process. Interpretation of molecular line observations is dependent on the development of extensive models of the chemistry and radiative transfer in accretion disks. In this study, several millimeter-wave molecular lines were observed toward a sample of disks encircling T Tauri and Herbig Ae stars with the Owens Valley Millimeter Array. The intent of these studies is the quantitative examination of the chemistry of the biogenic elements (C, N, O, S) in accretion disks. Toward this goal, radiative transfer models were modified for direct comparison with the observations to aid in the interpretation of molecular line emission and comparison with the predictions of chemical models. A survey of CN, HCN, CO and HCO^+ in 7 Herbig Ae and T Tauri star disks was performed in order to probe the effects of UV fields on disk chemistry; CN and HCO^+ are found to be sensitive to the strength of the local UV field. The first interferometric studies of deuterium in disks were performed and HDO and DCN were detected toward the T Tauri disk LkCa 15 and the Herbig Ae disk HD 163296. The deuterium enrichments are similar to that of molecular clouds, hot cores, and comets, consistent with comet formation in the outer regions of disks. The distribution of HDO in LkCa 15 was found to be similar to predictions from chemical models, which suggest a steep gradient as a function of disk radius. Finally, Keck LWS observations of the 8-13 μm silicate emission feature toward several T Tauri and Herbig Ae stars at various stages of the star formation process indicate an evolutionary trend similar to that previously seen with ISO for disks around intermediate mass stars. However, emission from crystalline silicates was only detected toward one low mass star, Hen 3-600A, possibly indicating that crystallization processes occur less frequently, or are more difficult to observe at mid-infrared wavelengths, in these disks.

Contents

List of Figures

List of Tables

Chapter 1

Introduction

Abstract

The ongoing radial velocity searches for extrasolar planets have resulted in the detection of >120 planets around other main sequence stars, and also around pulsars and white dwarfs (Dorminey, 2002[1]). The vast majority of exoplanetary systems appear to be very different from our own solar system, possessing large gaseous planets, similar to Jupiter, which orbit with high eccentricities, close to the star (most at < 3 AU). If these systems are representative of extrasolar planets (and not largely due to selection effects of the detection mechanisms)[2], then the diversity of planetary systems most likely arises from differences in conditions during the planet-forming phase. Specifically, the composition of gas, dust and ices in each stage of star formation plays a major role in determining what kind of planetary system, if any, can be formed. Observations tracing the evolution of material in young stellar objects (YSOs) are thus essential for addressing these issues. Such observations can additionally shed light on the formation of comets and the development of prebiotic molecules and planets that can sustain life. For example, similarities between comets and older "debris" disks, in particular the dust composition, indicate that comets are assembled in the later stages of star formation; observations of saturated molecules in hot cores and production of organic molecules by laboratory photolysis of "astronomical" ices indicate that the development of prebiotic molecules may be highly dependent on the energetic processing of grain mantles.

1.1 Star formation, chemistry and SEDs

Within the interstellar medium there exist clouds with sufficiently high densities (n = 10^2–10^6 molecules/cm^3) that the gas phase is dominated by H_2 and CO, which, once synthesized, are self-shielding from photodissociation by UV. Stars are formed from the gravitational collapse of cores within such clouds. The radiation of the star+dust system ranges from the UV (dominated by

[1] http://exoplanets.org/science.html
[2] Jupiter sized planets located at 5 AU are just now becoming detectable using standard radial velocity methods.

stellar blackbody emission) to the infrared and millimeter (dominated by dust emission) regions. The spectral energy distribution (SED) of the emergent radiation changes with the morphology of the YSO and is often used to classify the stages of stellar evolution (as shown in Figure 1.1).

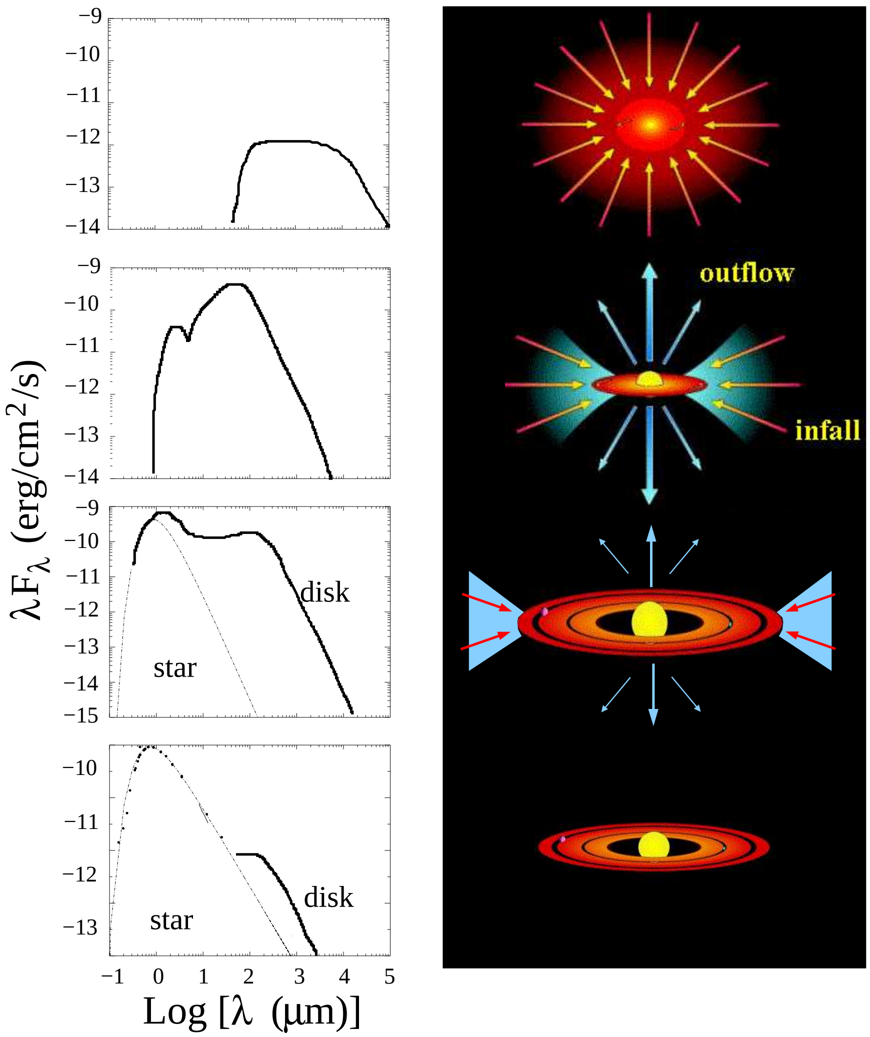

Figure 1.1 Evolution of YSOs and their SEDs, adapted from a figure by McCaughrean (private communication). The right panel shows a cartoon of the evolution of YSOs from a Class 0 embedded protostar to a Class III optically thin disk. The left panel shows the corresponding changes in the SED.

The initial collapse phase (the so-called Class 0 phase) is identified by radiation at millimeter and far-IR wavelengths that is typical of cool dust (T = 10–40 K). At these low temperatures, gaseous species (atoms and molecules) rapidly accrete onto the dust grain surfaces at roughly the collision rate (at densities of $\gtrsim 10^4$ cm^{-3}, this is $\gtrsim$ one H_2 molecule per day; Tielens & Allamandola, 1987) forming ice mantles with thicknesses of $\sim$1 μm. Class 0 objects are therefore associated with ice absorption bands from several species including CO, CO_2, H_2O, and X-CN, indicating a rich grain mantle chemistry. As the core collapses, the forming star illuminates the surrounding dust and gas, evaporating the ices and increasing the chemical complexity in the gas phase. Angular momentum is largely conserved during collapse, and so the infalling matter forms a disk around the star, and a fraction of this material is funneled along magnetic field lines into an outflow perpendicular to the plane of the disk. The outflow clears a cavity in the core and reveals warm dust close to the forming star, leading to emission at shorter wavelengths. Objects in this phase form Class I. The high densities and velocities within the outflow in this phase lead to increased collisions between grains resulting in the evaporation of ices from grain mantles and the sputtering of metals from grain cores. For this reason, the outflows of Class I objects are characterized by gas-phase emission from species such as H_2CO, CH_3OH and SiO, which are thought to be formed on grain surfaces or require atoms located in grain cores. As material from the disk slowly moves toward the star on the path to accretion, what is left of the original cloud core either falls onto the disk, accretes onto the star, or is removed from the system by the outflow. As the outer envelope begins to clear ($\sim 10^6$ yr), the star becomes visible. The SED at this stage is characterized by emission from the star in the optical and UV and radiation from circumstellar dust at $\lambda > 1$ μm (Class II). The chemistry in the circumstellar disk is a complex function of the temperature and density variations with distance from the star, and the surface chemistry within the disk is the main focus of this thesis. Over time, this outer envelope is eventually cleared away, leaving only the disk, and because there is no material left to fuel it, the outflow ceases. As the gas is cleared, increased grain collisions in the Keplerian velocity field lead to grain growth and the disk becomes optically thin (Class III). It is these circumstellar disks that are the site of planetary formation (c.f. Pollack et al., 1996).

1.2 Planet formation, the solar system and the solar nebula

What is known about the process of planet formation within such disks is based primarily on knowledge of our own solar system and in particular the chemical and physical properties of the planets, Kuiper Belt Objects (KBOs), comets and meteorites. The terrestrial planets (Mercury, Venus, Earth, and Mars) are located less than two astronomical units from the Sun (1 AU = 1.5×10^{13} cm). They have dense (3.9–5.5 g/cm^3) cores composed of primarily iron- and magnesium-bearing silicates and iron-nickel alloys along with thin atmospheres composed primarily of CO_2 and N_2, which are thought to have originated from partial outgassing of the planets' interiors. These rocky planets also have small numbers of satellites, typically only one or two. In contrast, the giant planets (Jupiter, Saturn, Uranus, and Neptune), located greater than 5 AU from the Sun, are lower in bulk density (0.7–1.7 g/cm^3) and possess thick atmospheres (8–21 g/cm^3), which constitute a up to 95% of the planetary mass. These atmospheres differ from those of the terrestrial planets in that they are composed of predominantly H_2 and He (at $\sim$solar proportions) and reduced species,

Table 1.1. Properties of the planets. From Encrenaz (2001).

Planet	Helioc.Distance (AU)	Radius (R_E)	ρ (g/cm^3)	Number of satellites	Atmosph. Composition
Terrestrial planets					
Mercury	0.39	0.38	5.44	0	...
Venus	0.72	0.95	5.25	0	CO_2(96%),N_2(4%)
Earth	1.0	1.0	5.52	1	N_2(77%),O_2(21%)
Mars	1.52	0.53	3.91	2	CO_2(95%),N_2(3%)
Giant Planets					
Jupiter	5.20	11.19	1.31	16	H_2(91%),He(9%)
Saturn	9.55	9.41	0.69	21	H_2(96%),He(4%)
Uranus	19.22	3.98	1.21	15	H_2($\sim$90%),He($\sim$10%)
Neptune	30.11	3.81	1.67	8	H_2($\sim$90%),He($\sim$10%)
Pluto	39.44	0.18	2	1	CH_4,N_2?

CH_4 and NH_3 (Table 1.1). Unlike the rocky planets, large numbers (8–21) of satellites have been found around the gas giant planets. The orbits of all planets (except Pluto) are quasi-circular in the ecliptic plane and rotate in the same direction, with the planet often in direct rotation around its axis (except Venus) in a manner similar to the rotation of planets around the sun. Gas giants also possess rings of ice and rock, similar in composition to their satellites.

The orbits of the planets and satellites can be explained by formation from a flattened primordial disk, which revolved around the protosun. A lower bound to the mass of the protoplanetary nebula (10^{-2} $M_\odot$) is often obtained from the current masses of the planets, adding enough hydrogen and helium to establish solar elemental abundances (the so called Minimum Mass Solar Nebula model, or MMSN). The accepted model of formation of the solar system is that planets form from accretion of planetesimals and nebular gas (Encrenaz, 2001). In this model, grains evaporate near the protostar during the gravitational collapse of a high-density region of an interstellar cloud. As the nebula cooled, material was condensed and the composition of this material varied as a function of distance from the star, with metals and silicates condensing close to the star and ices forming in the outer regions of the nebula.

This theory is supported by studies of ^{26}Mg (t_λ = 7$\times$10^5 yr) which suggest that most (but not all) grains were formed very early in the solar system. These initial grains were micron-sized and thoroughly mixed with the gas, and grain growth proceeded through the freezout of ices onto grain surfaces, increasing the sticking probability of grain-grain collisions and resulting in the formation of fluffy grain aggregates. As these particles grew (in size), they settled to the disk midplane, where accretion was accelerated by high gas and particle densities. In the outer nebula (R > 5 AU) colder temperatures and increased abundances of ices led to the formation of large cores (M = 15 M_E). These cores then attracted large amounts of gas from the nebula, forming precursors to the gas giants.

Table 1.2. Properties of the giant planets

	Sun	Jupiter	Saturn	Uranus	Neptune
Total mass[a](M_E)	...	318.1	95.1	14.6	17.2
Envelope mass (M_E)	...	288.1–303.1	72.1–79.1	1.3–3.6	0.7–3.2
Core mass (M_E)	...	15–30	16–23	11–13.3	14–16.5
Atmospheric composition[b]					
C/H	4.7×10^{-4}	2.9±0.5	2–6	25	25
N/H	9.8×10^{-3}	3.2±1.4	2–4	$\ll$1	$\ll$1
O/H	8.3×10^{-4}	0.033±0.015	...	...	...
D/H	2×10^{-5}	0.35-6.5	3.0	3.0	...

[a]In units of the Earth's mass = 5.98×10^{27}g

[b]Planetary elemental ratios $\times$solar

The inner nebula consisted of primarily metals and silicates and ices were less abundant, therefore only small, dense cores were formed in $\gtrsim 10^7$ years and atmospheres were generated by secondary processes. Due to accretion of gas onto the giant planets and other forms of gas loss, the nebula is expected to have dissipated in $\sim 10^6$–10^7 yr. Thus, the relative amounts of atmospheric material present in the gas giants, namely, Jupiter $\geq$ Saturn > Uranus > Neptune, are often explained by early formation of Jupiter and Saturn (t $\sim 10^6$ yr) followed by formation of Uranus and Neptune (t = 10^7 yr) at a point where little gas was left in the nebula.

Trends in the composition of the giant planets also provide important information about their formation mechanism and the nature of the protoplanetary nebula. The MMSN model discussed above indicates that carbon should be in the form of CO or CH_4, nitrogen as N_2 or NH_3 and additional oxygen in the form of H_2O. Table 1.2 (compiled by Gautier, 1988) shows the elemental ratios of the giant planets, which are all enriched in C, N and O compared to the Sun. The enhancement in C, N, O is indicative of the formation mechanism for these planets. There is a marked increase in the C/H and D/H ratios from Jupiter to Neptune, which can be explained by a temperature gradient in the disk. (Additional support for a temperature gradient is that the core size of the planets is approximately constant with varying atmospheric masses that are approximately solar.) The D/H increase as a function of heliocentric distance occurs because deuterium fractionation is increased at low temperatures, and thus in the core ices, with the larger atmospheres of the inner gas giants diluting the overall D/H ratio. The increase of C/H with heliocentric distance can be explained in a similar manner, but requires that the initial cores were composed primarily of CH_4 as opposed to CO, decreasing the gas-phase C/H ratio. The C/H ratio is then smaller in Jupiter because the gas:ice ratio is larger than that of Neptune.

Table 1.3. Observed exoplanet properties, August 2003

Property	value
R_{sep}	0.38–3 AU
$M_P \sin i$	0.16–17 M_J
period	3–2300 days
ϵ	0.0–1.0

1.3 Extrasolar planet formation and protoplanetary disks

Observations of extrasolar planets indicate that the process of planet formation have not been as straightforward for other planetary systems as it was for the Solar System. Among the >120 planets found orbiting other stars, many are in extrasolar planetary systems which appear to be quite different from our own (see Table 1.3). Large numbers of very close-in Jupiter mass planets have been detected and the radius of one such planet, HD 209458, indicates a very low density, corresponding to a temperature 10 times warmer than Jupiter, T = 1300–1400 K. The presence of these "hot Jupiters" can be explained by the formation of these planets farther out (R≈5 AU), followed by migration inward at later times, which is stopped by dissipation of nebular gas. However, current models of gas accretion result in migration faster than the timescale for nebular dissipation and the planets are accreted into the star. Additionally, the orbital eccentricities (ϵ; see Table 1.3) observed for extrasolar planets are much larger than those of Solar System planets, and those produced by early accretion disk models ($\epsilon \approx 0$). Recent models of planet-disk interactions (Goldreich & Sari, 2003) indicate, however, that eccentricities may be enhanced as the planet clears a gap in the disk. Another anomaly in the observations of extra solar planets is the paucity of large planets with $M_P \sin i > 20\ M_J$. This mass cutoff is likely related to the relative timescales for planetary formation and dissipation of molecular gas from the protoplanetary disk, but its exact nature is not yet understood.

Circumstellar disks similar to models of the solar nebula have now been detected around several stars with masses comparable to our sun (0.2–10 $M_\odot$) and are a good environment in which to address the question of planet formation (see Beckwith & Sargent 1996 for review). The distribution of dust with radius affects the frequency of planet formation; the final mass of planets depend on properties of the gas and the occurrence of multiple systems may be dependent on the disk size and mass. Observations of disks indicate that they often extend beyond the size of the current Solar System, with R_{disk} = 10–1000 AU. The timescales for dust agglomeration and gas dissipation in disks provide perhaps the most important observational constraint on the method of planet formation. Near-IR observations indicate that by ∼3 Myr half of the disks have lost most of their warm dust (within a radius of 0.1 AU), while ISO 25–60 μm observations indicate that cooler dust is lost, or accreted, by 10 Myr (R = 0.3–3 AU). Timescales for loss of gas from disks are also observed to be on the order of 10^7 yr (Thi et al., 2001). From observation of UV excesses associated with accretion, rates of $\dot{M} = 10^{-8}\ M_\odot$/yr are derived for disks of age t $\approx 10^6$ yr (Calvet et al., 2002).

1.4 The chemistry of protoplanetary disks

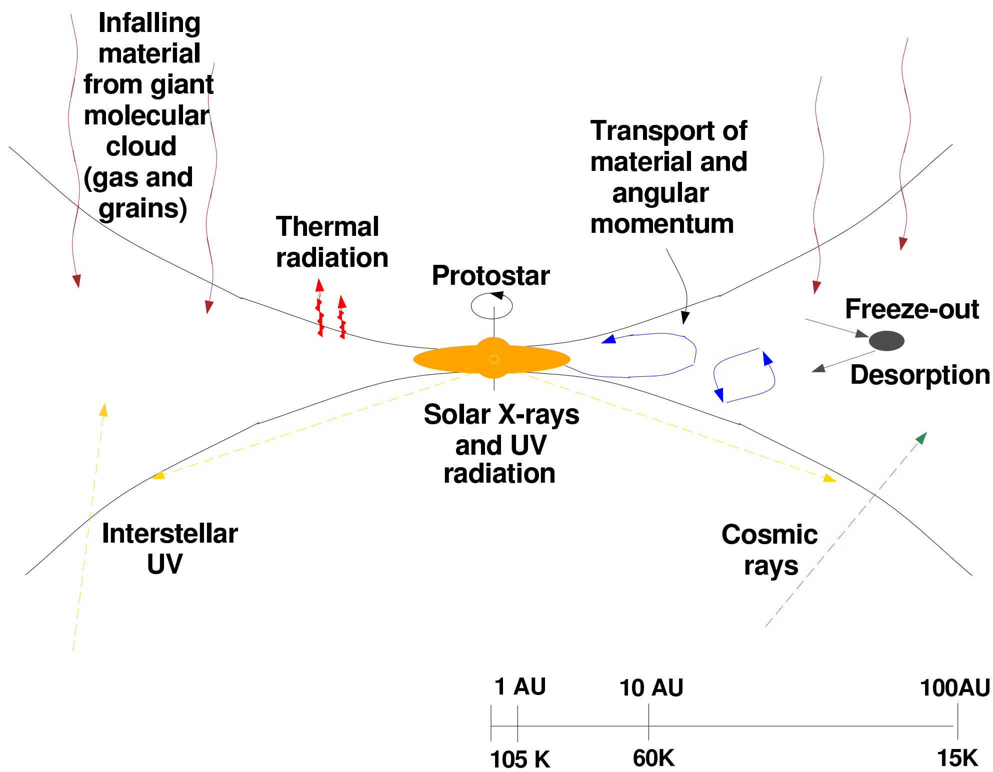

Figure 1.2 The circumstellar environment, modeled after a figure from van Zadelhoff (2002). The solid lines indicate dynamical processes. Infalling material from the molecular cloud likely affects the chemical properties of gas and dust in the outer disk. The transport of material and angular momentum refers to the radial and vertical mixing suggested by disk models. Although the diagram is truncated at a disk radius of 100 AU, observations indicate that disk sizes can be much larger (R∼500 AU) in systems of age t $\geq 10^6$ yr.

As discussed above, the chemical composition of planets are directly related to how and where they formed. The assessment of the chemical composition at each radius of the disk would therefore provide valuable information (i.e., the density, thermal history and composition versus distance) about the initial conditions in the planet-forming zones of the solar nebula and help determine the origin of primitive bodies such as comets. In particular, molecular emission studies of accretion disks can facilitate the quantification of gas-to-dust ratios and the timescales over which they are dissipated (which is important for the process of planet formation) as well as the description of the distribution of volatile species in its outer regions (necessary in the derivation of the evolution of comets and Kuiper Belt Objects).

By means that are not yet fully understood, circumstellar accretion disks radially transport material inward and angular momentum outward. Due to radiation from the central star and the liberation of gravitational energy there are strong density and temperature gradients in the disk. In the outer, colder regions much of the (C,N,O,S)-bearing gas should be frozen out onto an icy mantle on the surfaces of dust grains in the dense mid-plane of the disk (c.f. Figure 1.2). As matter accretes toward the warmer innermost regions, the ice mantle evaporates (R $<$ 10 AU), while at radii smaller than $\sim$0.3 AU dust destruction begins (Willacy et al., 1998). This results in complex chemical reactions releasing large, less volatile molecules, into the gas phase in the inner part of the disk (Bauer et al., 1997; Duschl et al., 1996; Willacy et al., 1998). At radii less than 0.05 AU, there exists complete molecular dissociation, leaving only free atoms. The extent to which radial mixing occurs is very important to the overall chemical balance, but is very difficult to predict theoretically, and occurs over such small spatial scales that observational studies are beyond current capabilities.

Current models of the chemistry in the outer regions of circumstellar disks (Aikawa et al., 2002; Willacy & Langer, 2000; Finocchi et al., 1997; Bauer et al., 1997) suggest that at large radii the chemistry is controlled kinetically by two-body gas-phase processes and by adsorption onto and desorption from grains. In the early versions of these models, it was assumed that only thermal desorption occurs. Several models (Aikawa et al., 2002; Willacy & Langer, 2000) are now beginning to apply recently developed self-consistent treatments of the optical/infrared radiative transfer in the disk (Chiang & Goldreich, 1997; Chiang et al., 2001; D'Alessio et al., 1998), instead of using cold mid-plane temperatures. These models include the effects of the processing of radiation by grains near the photosphere, or disk surface, which lead to enhanced disk surface temperatures and a flared geometry. The chemical effects of radiation from the young star and interstellar medium are are thus very important in these surface layers and the likelihood of depletion onto grain mantles is lessened, leading to increased abundances of gas-phase species with respect to early models that had artificially high dust-to-gas ratios. Some models (Glassgold et al., 1997; Finocchi et al., 1997) also take into account the effects of X-rays, short-lived radionuclides, cosmic ray ionization, and photochemistry; but, there are several important processes, such as dust versus gas settling and size sorting, that continue to be neglected.

Advances in molecular modeling of the chemistry of accretion disks are codependent upon the observational study of the disks through molecular line emission. The study of this emission has heretofore been greatly limited by the sensitivity of astronomical instrumentation, however. This has resulted in the primary use of the emission lines of isotopomers of CO and the continuum emission of circumstellar dust for imaging, which allow only the mass and size of disks around young stars to be modeled (Koerner & Sargent, 1995; Koerner et al., 1998; Mannings & Sargent, 1997). The reliance on CO emission, in addition to limiting the scope of the modeling effort, is otherwise problematic in several ways. One main example is that CO emission data sometimes indicate that the masses of gas are much (up to two orders of magnitude) lower than those inferred from the continuum emission (Zuckerman et al., 1995; Dutrey et al., 1996, 1997). There are several proposed explanations for this discrepancy, including loss of gas through freezout of molecules onto grains, inadequate spatial resolution, poor radiative transfer models, and the possibility that the time scale of gas dissipation is shorter than that of dust agglomeration. A more complete assessment of the chemical distribution within the disk could be made with the acquisition of the emission spectra of a greater variety of molecules, specifically species in each chemical family (C-, N-, S-, O-bearing).

Recently, emission from molecules such as CN, HCN, HNC, CS, HCO^+, C_2H and H_2CO, with intensity comparable to ^{13}CO and $C^{18}O$, has been detected through single dish studies of the disks surrounding TW Hya (Kastner et al., 1997), LkCa 15 (van Zadelhoff et al., 2001), DM Tau and GG Tau (Dutrey et al., 1997). From these pioneering studies, some important conclusions can be made. It is known that the transition optical depths for species such as HCN and HCO^+ are sufficiently large that their emission should be comparable to that of ^{12}CO if the gas is well mixed and interstellar abundances are maintained (M.R. Hogerheijde, private communication). However, it was found in the above studies that they are lower, implying either substantial molecular depletion, or a strong species dependence on the sizes of the emitting regions. In addition, ratios such as CN/HCN and HNC/HCN are too high to be accounted for by quiescent chemical models alone. This suggests that both ion-molecule and photon-dominated chemistry must contribute to the observed abundances (Spaans, 1996; Dutrey et al., 1997; Kastner et al., 1997).

These first detections, in beams large compared to the sizes of the disks, indicate that an initial study of the nature and variation of the chemical composition of disks is now feasible. To this end, the research described here includes the imaging of several molecular emission lines from the circumstellar disks of T Tauri and Herbig Ae stars with the Owens Valley Radio Observatory (OVRO) Millimeter Array. In particular, the distributions of several species around the T Tauri star LkCa 15 have successfully imaged, including HCN, DCN, CN, ^{13}CO, SO, H_2S, CS, SO_2, CH_3OH and HCO^+. The $1''$–$3''$ resolution available at OVRO means that such observations of low excitation transitions are sensitive primarily to the outer (R $>$ 30–100 AU) region of the circumstellar disk.

Thus, other tracers must presently be used to examine the warmer, inner regions of the disk. Such tracers would also assist in efforts to constrain the radial and vertical thermal distribution within circumstellar disks. Early models assessed the temperature structure through the use of spectral energy distributions assuming either a flat (Adams et al., 1987) or flaring (Kenyon & Hartmann, 1987) disk geometry. However, the calculations of the mid-plane and surface temperature structure by various groups (Bell et al., 1997; Men'shchikov & Henning, 1997; etc.) differ considerably. Further, in the flared-disk geometry, the surface layer is thought to be heated by the star to temperatures as high as 100 K at radii as large as 100 AU (Chiang & Goldreich, 1997). Accordingly, high spatial resolution observations with 10-meter class telescopes should be able to resolve the silicate dust emission features in the outer layers of disks, and in this way support or discount the existence of a flared geometry. I therefore also describe here the use of Keck Long Wavelength Spectrometer 10 μm long-slit silicate imaging spectroscopy.

The fundamental aim of the research program described here is the quantitative examination of the chemistry of the biogenic elements (C, N, O, S) in circumstellar accretion disks. This was achieved by combining state-of-the-art observational tools at millimeter through infrared wavelengths using various Caltech observatories with state-of-the-art chemical and dynamical codes. As described below, both the observational and theoretical capabilities have only now advanced to the point where such studies are possible, and the results from this research are of interest not only in their own right, but may help pave the way for future ground-based efforts and space-borne missions in the NASA Origins program. An outline of the thesis is as follows. Chapter 2 describes radiative transfer models and the interpretation of molecular line emission from disks. In Chapter 3, a survey of CN, HCN, CO and HCO^+ is presented and the implications for nitrogen chemistry are discussed. Chapter 4 contains a discussion of deuterium fractionation in YSOs and in the solar system, centering on a search for HDO and DCN in three protoplanetary disks. Spectroscopic observations of the 8–13 μm silicate emission feature toward several T Tauri and Herbig Ae stars at various stages of the star formation process are presented in Chapter 5 and an evolutionary trend is suggested. Finally, a summary of the current understanding of disk chemistry (including the results presented in this thesis) and directions for future research are presented in Chapter 6.

Chapter 2

Models of molecular line emission from circumstellar disks

Abstract

High-resolution observations of molecular line emission allow the determination of the chemical composition at each radius of protoplanetary disks, providing valuable information (i.e., density, thermal history and composition) about the initial condition of the solar nebula. However, it is impossible to interpret this molecular line emission without knowledge of the transfer of radiation within the object of study. Therefore, we have combined an existing two-dimensional radiative transfer code, *RATRAN* (Hogerheijde & van der Tak, 2000) with a physical disk model based on D'Alessio et al. (2001) and constrained by observations of several CO transitions. In this chapter I will describe this model. In §1, I will provide a discussion of the basic concepts of radiative transfer, including the difficulties in solving the radiative transfer equation and the assumptions that are generally made in order to do so. Non-LTE radiative transfer solutions will be discussed in §2, concentrating on the Monte Carlo method used by *RATRAN*. §3 will describe the physical parameters of our disk model constructed by D'Alessio (private communication) for the T Tauri star LkCa 15, the molecular lines of which have now been studied extensively. The model is used to reproduce the observed CO 2-1 spectrum and the line shape and peak strength of the CO 2-1 transition (Qi et al., 2003) are used to constrain the inner R_{in} and outer R_{out} radius, inclination i, turbulent velocity width Δv, and the scaling factor for the modeled temperature profile. The detailed vertical temperature distribution is also examined through additional fits to observations of the CO 3-2 and CO 6-5 transitions (van Zadelhoff et al., 2001). In §4, these non-LTE models are used to fit the spectra of the 1-0 transitions of ^{13}CO, C^{18}O, HCO^{+}, H^{13}CO^{+} and N$_2$H^{+}, by scaling the column densities, which are approximated with radial and vertical distributions similar to that of hydrogen. Finally, in §5, the channel maps produced from the resulting models, before and after being sampled at the observed (u, v) coverage, are presented.

2.1 Radiative transfer: Basic concepts

The equation for radiative transfer states that the intensity I of emission at frequency ν integrated along a particular line of sight ds is simply the difference between the flux emitted and absorbed by the dust and gas along the same line of sight, or

$$\frac{dI_\nu}{ds} = j_\nu - I_\nu \alpha_\nu = S_\nu - I_\nu, \tag{2.1}$$

where $\tau_\nu = \alpha_\nu ds$ is the optical depth along the line of sight, α_ν is the absorption coefficent and j_ν is the emission coefficient of the gas and dust combined. (Note: j_ν is the emission coefficient along the line of sight and is related to ϵ_ν the (volume) emission coefficient.) The (line) source function is the ratio of the absorption and emission coefficients, $S_\nu = \frac{j_\nu}{\alpha_\nu}$. For the case when a background source of intensity $I_\nu(0)$ is included, the solution of the radiative transfer equation (Equation 2.1 above) is

$$I_\nu = I_\nu(0)e^{-\tau_\nu} + \int_0^{\tau_\nu} e^{\tau_\nu - \tau_\nu'} S_\nu d\tau_\nu = I_\nu(0)e^{-\tau_c}[e^{-\tau_\nu} - 1] + S_\nu e^{-\tau_c}[1 - e^{-\tau_\nu}], \tag{2.2}$$

where τ_c is the optical depth in the continuum.

In the absence of collisional excitation, emission and absorption in the gas phase are determined by the rates of spontaneous emission, stimulated emission, and absorption of photons between energy states u and l, with $\Delta E = E_u - E_l = h\nu_o$. These processes are described by the Einstein coefficients A_{ul}, B_{ul} and B_{lu}, respectively. The emission and absorption coefficients can be written in terms of the Einstein coefficients as

$$j_\nu^{ul} = \frac{h\nu_o}{4\pi} n_u A_{ul} \phi(\nu) \tag{2.3}$$

$$\alpha_\nu^{ul} = n_i \sigma_\nu = \frac{h\nu_o}{4\pi}(n_l B_{lu} - n_u B_{ul})\phi(\nu), \tag{2.4}$$

where the 4π comes from an assumption of isotropic emission, σ_ν is the absorption cross section and $\phi(\nu)$ is the normalized line shape, defined such that $\int \phi(\nu) d\nu = 1$. In the case of Doppler broadening, $\phi(\nu)$ is Gaussian in nature and is given by

$$\phi(\nu) = \frac{c}{b\nu_o\sqrt{\pi}} exp[-\frac{c^2(\nu - \nu_o)^2)}{\nu_o^2 b^2}]. \tag{2.5}$$

It follows that the source function can be defined in terms of the Einstein coefficients:

$$S_\nu = \frac{j_\nu^{ul}}{\alpha_\nu^{ul}} = \frac{n_u A_{ul} \phi(\nu)}{n_l B_{lu} - n_u B_{ul}}. \tag{2.6}$$

Thus, the solution of the equation for radiative transport depends on the level populations through the calculation of the source function. In a two-level system, the level populations are easily calculated from detailed balance, i.e., assuming that the total population of both levels is constant, so that the number of transitions from u to l is the same as from l to u, or

$$n_l(B_{lk}J_\nu + C_{lk}) = n_u A_{kl} + n_u(B_{kl}J_\nu + C_{kl}), \tag{2.7}$$

where the level populations are determined by radiative and collisional processes and C is the collision rate (per second per molecule) of the species of interest. The collision rate depends on the density of the collision partner n_{col} as $C_{ij} = q_{ij}\ n_{col}$ and on the relative velocity of the collision partners (through q_{ij}), with the collision rates for absorption and emission related by

$$C_{lu} = \frac{g_u}{g_l} C_{ul} e^{-\Delta E/kT}. \tag{2.8}$$

Extending this calculation to a multilevel system, the population of one level l depends on the emission and absorption from all other levels $k{\neq}l$ as,

$$n_l[\sum_{k<l} A_{lk} + \sum_{k\neq l}(B_{lk}J_\nu + C_{lk})] = \sum_{k>l} n_k A_{kl} + \sum_{k\neq l}(B_{kl}J_\nu + C_{kl}), \tag{2.9}$$

where the radiation field J_ν is the intensity integrated over all solid angles, $J_\nu = \frac{1}{4\pi}\int I_\nu d\Omega$. The level populations are thus dependent on the radiation field and the source function is in turn dependent on the level populations; the level populations and the intensity I_ν are degenerate. There are several approximations that simplify the problem by decoupling the radiative transfer calculations from the calculation of the level populations. The most common methods involve approximations about the opacity of the gas (in optically thin or optically thick limits), the probability of escape of scattered radiation from the system and the dominance of collisional versus radiative processes, and are summarized briefly next.

2.1.1 Escape probability

If we can replace the source function with a factor that does not depend directly on the level populations or the radiation field, then we can break the degeneracy and solve for J_ν. One such factor is the probability that a photon located at some position in the cloud can escape from the system. For a completely opaque source, the intensity is equal to the source function S. So in terms of the escape probability β, J $= \int \mathrm{F}_\nu d\nu = S(1-\beta)$. Thus, the level populations become

$$\frac{dn_u}{dt} = n_l C_{lu} - n_u C_{ul} - \beta n_l A_{ul}, \tag{2.10}$$

and are now independent of the radiation field. The escape probability must depend on source geometry and optical depth and therefore has several forms. The most common example is the escape probability for a one-dimensional radially expanding sphere, for which

$$\beta = \frac{1 - e^{-\tau}}{\tau}. \tag{2.11}$$

This is called the Sobolov or large velocity gradient (LVG) approximation. One can define similar escape probabilities for homogeneous slabs, uniform spheres or turbulent media.

2.1.2 LTE and opacity approximations

As shown above, the source function can be written in terms of the Einstein coefficients and level populations as

$$S_\nu = \frac{j_\nu^{ul}}{\alpha_\nu^{ul}} = \frac{A_{ul}}{B_{ul}} \frac{1}{\frac{n_l g_l}{n_u g_u} - 1}. \tag{2.12}$$

The excitation temperature T_{ex} is defined such that

$$\frac{n_u}{n_l} = \frac{g_u}{g_l} exp[\frac{h\nu}{kT_{ex}}]. \tag{2.13}$$

By substituting the definition of the excitation temperature into the equation above we find that the source function is equal to a blackbody radiation field at the excitation temperature T_{ex},

$$S_\nu = \frac{2h\nu^3}{c^2} \frac{1}{e^{h\nu/kT_{ex}} - 1} = B_\nu(T_{ex}). \tag{2.14}$$

In the case of Local Thermal Equilibrium, or LTE, the density becomes sufficiently high ($n > n_{crit} = \frac{A_{ul}}{q_{ul}}$) such that the level populations are controlled by collisional processes, because the timescale for collisions is much less than that of spontaneous emission ($C_{ul} \gg A_{ul}$). The level populations are then solely dependent on the mean free path in the gas, the excitation temperature is equal to the kinetic temperature and the source function (and absorption ceofficient) is now independent of the radiation field, or $S_\nu = B_\nu$ (T_{kin}). In this limit, the solution of the equation for radiation transport becomes trivial:

$$I_\nu = B_\nu + e^{-\tau_\nu}(I_\nu(0) - B_\nu). \tag{2.15}$$

If, in addition to LTE, the medium is optically thick, $\tau_\nu \gg 1$, then the intensity approaches that of blackbody radiation ($I_\nu \approx B_\nu$). Similarly, if the medium is optically thin, $\tau_\nu \ll 1$, then the intensity of the emission in a cell is approximately the intensity before passing through the cell, or $I_\nu \approx I_\nu(0)$. This makes the calculation of column densities N_T from observed antenna temperatures (T_A) particularly easy by removing the optical depth dependence. For example, for emission in the Rayleigh-Jean limit, the column density of a species is related to the beam-filling factor ($\frac{\Delta\Omega_A}{\Delta\Omega_S}$), where $\Delta\Omega_A$ and $\Delta\Omega_S$ are the solid angles subtended by the antenna (FWHM of the main beam)

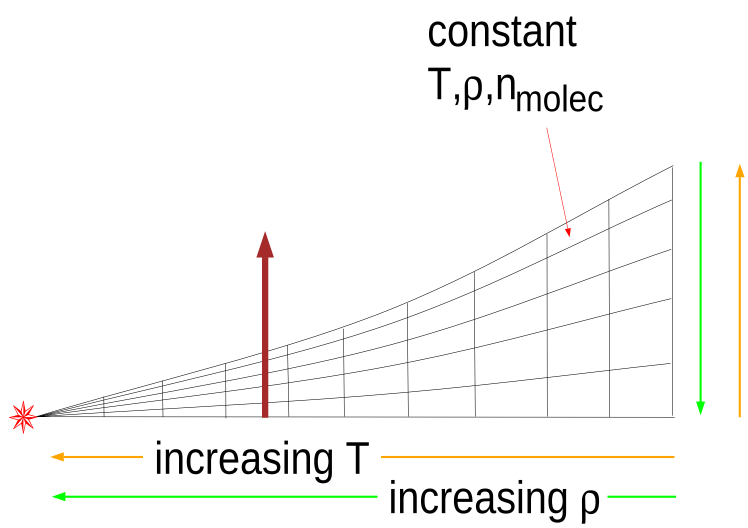

Figure 2.1 This cartoon depicts the grid used for our 2-D Monte Carlo radiative transfer model. Each cell is of constant temperature, total density and density of the molecule in question. Temperature and density variations with radius and height are as indicated. The path of the calculation is indicated by the heavy arrow.

and source, respectively, and the optical depth τ as

$$N_T = \frac{8\pi k\nu^2}{hc^3 A_{ul}} \frac{\Delta\Omega_A}{\Delta\Omega_S} \frac{\tau}{1-e^{-\tau}} T_A \Delta\nu \frac{\sum g_i e^{-E_i/kT}}{g_l e^{-E_l/kT}}, \tag{2.16}$$

where g_x is the degeneracy of level x, $\sum g_i e^{-E_i/kT}$ is the partition function, and $T_A\Delta\nu$ is the equivalent width of the observed line. If we assume that the source fills the beam ($\frac{\Delta\Omega_A}{\Delta\Omega_S} \approx 1$) and if the medium is optically thin ($\frac{\tau}{1-e^{-\tau}} \approx 1$), then

$$N_T = \frac{8\pi k\nu^2}{hc^3 A_{ul}} T_A \Delta\nu \frac{\sum g_i e^{-E_i/kT}}{g_l e^{-E_l/kT}}, \tag{2.17}$$

and the column density can be calculated directly from the observed antenna temperature. In the optically thick limit ($\frac{\tau}{1-e^{-\tau}} \approx \tau$), the column density is easily calculated provided the antenna temperature and the optical depth are known,

$$N_T = \frac{8\pi k\nu^2}{hc^3 A_{ul}} T_A \Delta\nu \frac{\sum g_i e^{-E_i/kT}}{g_l e^{-E_l/kT}} \tau. \tag{2.18}$$

2.2 The non-LTE model

Temperatures indicated by ratios of (sub)millimeter CO emission lines observed toward several protoplanetary disks (van Zadelhoff et al., 2001) indicate that the emission comes from disk surfaces. In these surface layers, the densities are considerably lower than at the disk midplane (see Figures 2.1 and 2.2) and fall short of thermalizing the level populations. Because the conditions are far from LTE the radiation transfer must be calculated explicitly. Additionally, 2-D approaches are necessary to quantitatively treat inclined disks, thanks to the Keplerian velocity fields involved. For this reason we have used an accelerated Monte Carlo model (Hogerheijde & van der Tak, 2000) to solve the two-dimensional radiative transfer and molecular excitation in the LkCa 15 disk, taking both collisional and radiative processes into account. This model produces a simulated observation of each transition as observed by a telescope with resolution equivalent to the model grid for a disk of a given size, inclination and temperature distribution.

The source model is divided into discrete grid cells of constant density, temperature, molecular abundance, turbulent line width, etc. (c.f. Figure 2.1). Thus, the average radiation field (J_ν) is the sum of the emission received in cell i from each of the other cells j after propagation through the intervening cells and weighted by the solid angle subtended by each of these cells j as seen from cell i. The cell size is chosen to be small enough that the molecular excitation is constant throughout the cell. The velocity field is constructed assuming a Keplerian velocity gradient, as expected for circumstellar disks (i.e., Beckwith & Sargent, 1993). The velocity variations within each cell are continuous and integration along a ray is divided into subunits within a cell to track the variation of the velocity projected along the ray.

The radiative transfer code operates by calculating the radiation field J_ν using the equation

$$J_\nu = \Lambda[S_{ul}(J_\nu)], \tag{2.19}$$

where the operator Λ is a matrix that describes how the radiation field of each cell depends on the excitation in all other cells. The source function S_{ul}, which includes the effects of both gas and dust absorption and emission, remains dependent on the level populations; but the model is simplified through iterative solution of equation 2.1 by using the previous level populations and previous S_{ul}. Therefore, J_ν can be evaluated using simple matrix multiplication and the same set of rays can be used throughout the calculation. This method is often referred to as Λ-iteration.

As discussed above, the radiation field of each cell is described by the equation

$$J_\nu = \frac{1}{4\pi}\int I_\nu d\Omega, \tag{2.20}$$

where I_ν is the intensity contribution from all other cells to the radiation field in each of the individual

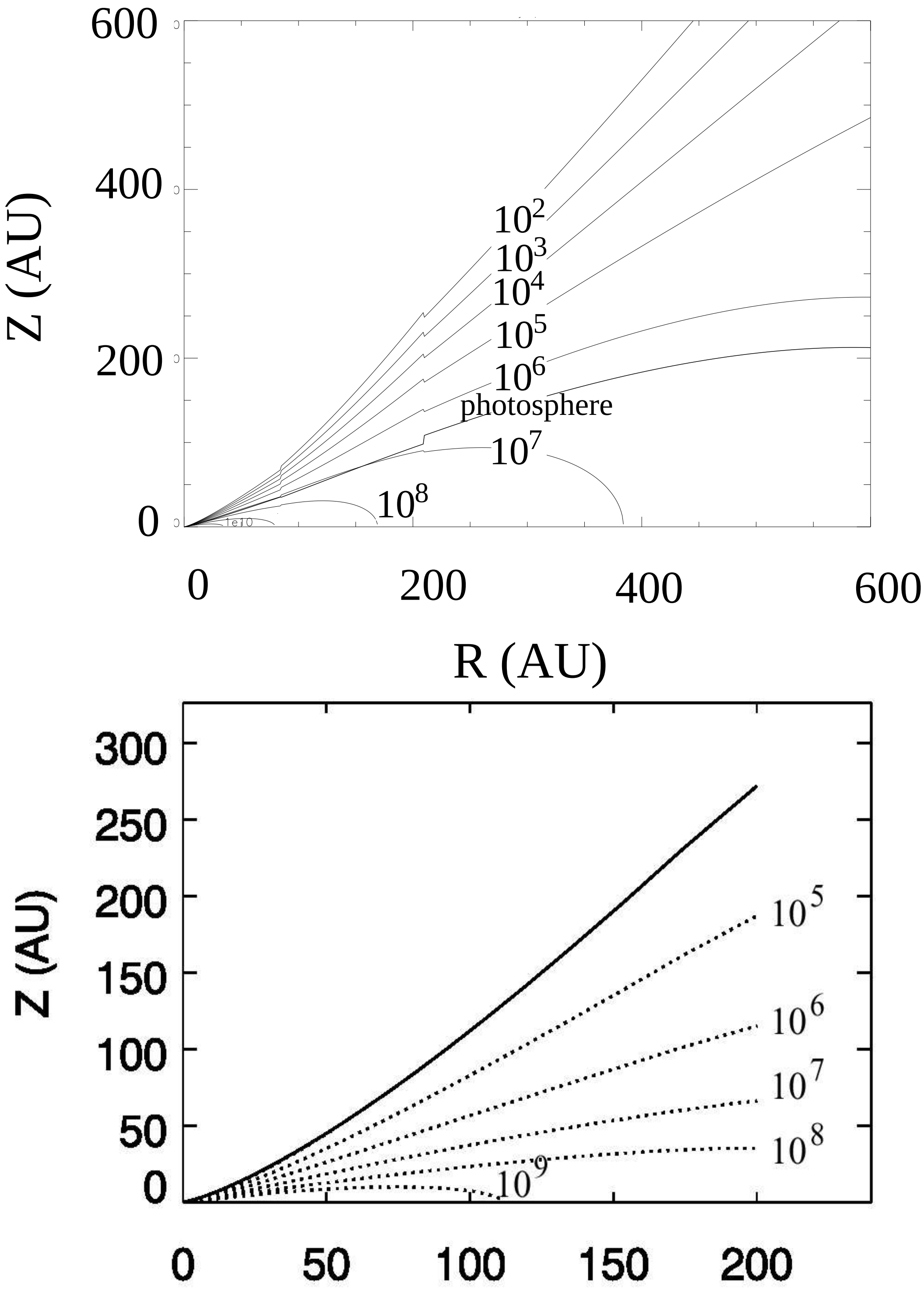

Figure 2.2 Plots of a radial cut of the density distribution for a circumstellar disk as described by the models of (a) Chiang & Goldreich (1997) and (b) D'Alessio et al. (2001).

cells received from the solid angle $d\Omega$. The Hogerheijde & van der Tak model adopts a Monte Carlo approach, approximating this integral by the summation of rays which enter the cell from infinity from a random set of directions and contribute to the radiation field at a random point in the cell's volume. Using this method, the incident radiation is easily separated into local and external radiation fields

$$J_\nu = J_\nu^{external} + J_\nu^{local} = \frac{1}{N}\sum_i I_{0,i}e^{-\tau_i} + \frac{1}{N}\sum_i S_{ul}[1 - e^{-\tau_i}], \tag{2.21}$$

where N is the number of rays i which result in an incident radiation $I_{0,i}$ from a distance to the boundary of the cell ds_i. The level populations are used to calculate the source function S_{ul} and the path length ds_i is converted into an opacity $d\tau_i$. In this case the form of the equation used to solve for the radiation field is

$$J_\nu = (\Lambda - \Lambda^*)[S_{ul}^\dagger(J_\nu)] + \Lambda^*[S_{ul}(J_\nu)], \tag{2.22}$$

where Λ^* is the local radiation field and operates on the current source function $S_{ul}^\dagger$. This improves convergence of the calculation for optically thick cells for which the radiation field is close to the local source function.

The approximation of J_ν from a randomly chosen set of directions is valid only if enough directions are included to fully sample the space in sufficient detail. Because the variance σ is dependent on the number of rays N making up J_ν in a particular cell, as $1/\sqrt{N}$, the method arrives at an appropriate sampling by increasing (doubling) N in that cell until the variance drops below a specified value. In this way, each cell has the appropriate sampling; cells close to LTE are not over sampled.

The calculation of J_ν is broken down into two stages. In the first stage, the same set of rays with initially random directions is used to iteratively evaluate J_ν. This iteration is considered complete when the difference between subsequent solutions is a factor of ten smaller than the user-specified level. In the second stage, a different set of rays with random directions is used to calculate J_ν for each iteration. The number of rays is now increased in each iteration (as described above) until the variance drops below a specified value.

The code consists of two parts. The main portion calculates the excitation through the source model, solving the radiative transfer and molecular excitation. The second part of the program integrates the equation of radiative transport,

$$\frac{dI_\nu}{ds} = -\alpha_\nu I_\nu + j_\nu, \tag{2.23}$$

along several lines of sight for a source at a specified inclination angle and distance, calculating the emission that would be observed from this source above the atmosphere and with complete spatial and velocity resolution.

2.3 The physical disk model

The physical disk model, and its effect on the radiative transfer, and in particular the density and temperature gradients, turbulent velocity structure and disk size and inclination, has a large effect on the observed emission. One quadrant of our model is shown schematically in Figure 2.1. With current computers, the three-dimensional codes and sampling needed to examine forming planets are *extremely* slow. Therefore, for simplicity, the disk is approximated as axisymmetric and also symmetric about the disk midplane. Each cell displayed in Figure 2.1 is thus actually a cylinder with its central axis normal to the disk. Stellar radiation is absorbed by dust in disk surface layers and re-emitted in the infrared, warming the disk surface layer and resulting in a flared disk geometry, in which the height of the disk increases with radius from the central star (Chiang & Goldreich, 1997; D'Alessio et al., 2001). As is shown in Figure 2.1, the density increases toward the midplane and toward inner radii. Temperature increases toward the disk surface and, of course, toward radii closer to the star.

As mentioned above, stellar radiation and its absorption, scattering and reradiation by dust has a large effect on the temperature gradient through heating of disk surface layers, which in turn affects the degree of flaring of the disk and thus the portion of the disk in the direct line of sight of stellar radiation. There are several models that simulate the effect of the reprocessing of stellar radiation. In this work, we model the radiation transfer for disks using the temperature and pressure gradients calculated by D'Alessio et al. (2001), who calculate disk structure self-consistently assuming complete mixing and thermal balance of the gas and dust. The pressure as a function of height is determined by calculations of vertical hydrostatic equilibrium. The temperature gradients and variation of the pressure as a function of radius are controlled by energy produced via viscous dissipation, radioactive decay (primarily of ^{26}Al), cosmic rays and stellar irradiation and transport of this energy by turbulent flux (radially and vertically), radiation and convection.

In the D'Alessio model, the solid phase is composed of silicates (olivine and orthopyroxene, see Chapter 5), water ice, troilite and organics in mass fractional abundances of 4.4:1:7.3:5.4. The grains have a powerlaw size distribution $n(a) = n_o\, a^{-p}$, where a is the grain radius, n_o is a normalization constant and the exponent p is a free parameter. The input parameters for the LkCa 15 model were taken from the literature, with a uniform disk mass accretion rate of $\dot{M} = 1.0{\times}10^{-8}$ M$_\odot$/yr, stellar mass M$_* = 1$ M$_\odot$, stellar radius R$_* = 1.64$ R$_\odot$, and stellar temperature T$_* = 4395$ K. The turbulent viscosity is described by the parameter $\alpha = 0.01$–0.001, which was fit to the disk mass (0.01 is consistent with the Balbus-Hawley magnetohydrodynamical instability; Hawley & Balbus, 1991). The maximum grain size was found to be a$_{max} = 1$ mm with the powerlaw exponent of the size distribution $p = 3.5$. This maximum grain size indicates that silicates dominate the SED at $\lambda = 1$ mm, troilite dominates in the cm range, and in the mid- and far-IR, water ice and organics

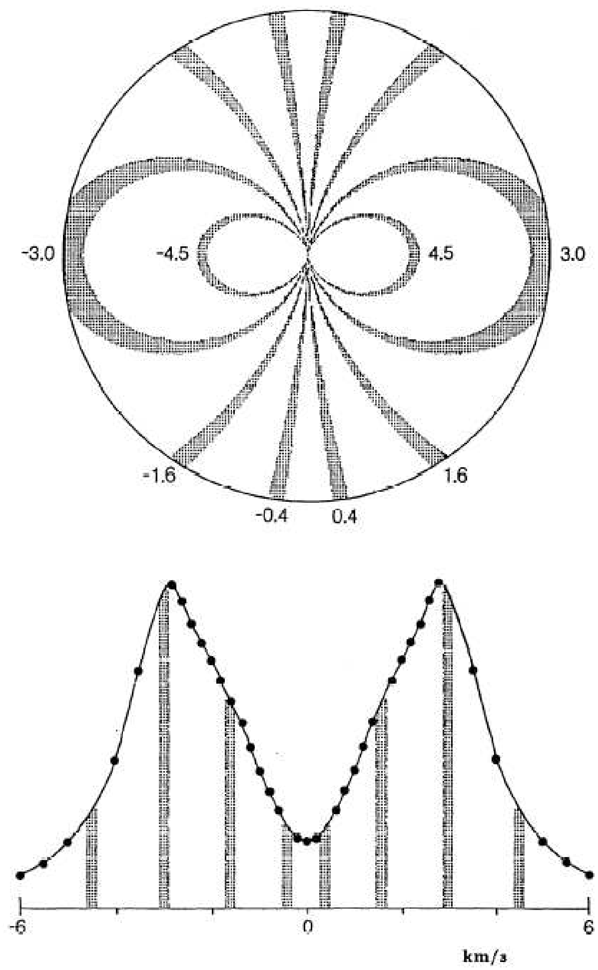

Figure 2.3 Translation of disk position and velocity for an inclined disk, taken from Beckwith & Sargent (1993). The shaded regions in the diagram of the disk (top) correspond to the velocities in the spectrum (bottom) via the equation $r(\phi) = \frac{GM}{v_{obs}^2} \sin^2\theta \cos^2\theta$.

dominate the SED. This is consistent with the SED for LkCa 15 (Chiang et al., 2001). Mie scattering (Wiscombe & Joseph, 1977) is used to calculate the absorption efficiency (Q_{abs}), treating the grains as spheres for simplicity.

A disk of material rotating in Keplerian motion ($v_{Kep} = (\frac{GM}{R})^{1/2}$) about a central star which is inclined with respect to the observer exhibits a double peaked spectrum as the line of sight encounters material moving with different orbital velocities. The emission line profile can be thought of as a sum of the independent emission from each position in the disk, modified by the appropriate Doppler shift due its radial motion ($v_D = v_{Kep}$ sin$i$ sinθ), characterized by the azimuthal angle θ and the inclination angle i between a vector normal to the disk plane and the observer's line of sight. For the case of an inclined disk, the translation between disk position $r(\phi)$ and projected velocity v_{obs}

(Figure 2.3; Beckwith & Sargent, 1993) is

$$r(\theta) = \frac{GM}{v_{obs}^2}\ \sin^2 i\ \cos^2\theta. \tag{2.24}$$

The line shape, in particular the separation and sharpness of the peaks, is indicative of the disk inclination, size, temperature and turbulent velocity width as well as the column density of the emitting material (c.f. Horne & Marsh, 1986; Beckwith & Sargent, 1993), for

$$F_\nu(v_{obs}) = \frac{4}{4-q}\ \frac{2kT_d\nu^2}{c^2}\ \frac{R_{out}^2}{D^2}\ \frac{\Delta v_d}{v_d}\ (\frac{v_{obs}}{v_d})^m, \tag{2.25}$$

where $v_d = (GM/R_{out})^{1/2}$ is the velocity at the outer edge of the disk R_{out}, q is the powerlaw index of the temperature distribution ($T(r) = T_d(\frac{r}{R_d})^{-q}$), D is the distance to the disk from the observer, and $\Delta v_d = (2kT_d/m_0)^{1/2}$ is the local velocity dispersion. The value of m varies from $m = 3q - 5$ in the high-velocity limit to $m = 1$ in the low velocity limit, indicating a double peaked profile, with peak values occurring at $v_{obs} = \pm v_d$ and a decreasing flux toward low velocities.

We can use the observed CO emission and the relationships described above to constrain the physical structure of disks. Figure 2.4 shows how the modeled CO 2-1 emission spectrum for LkCa 15 changes as the disk parameters are varied. The scale factor for the disk temperature and the inclination, turbulent velocity width ($\delta v^2 = \frac{2kT}{m_0} + v_{turb}^2$) and disk limits R_{in} and R_{out} were selected to best match the observed CO 2-1 emission. As the disk temperature T_d is increased (keeping the distribution of temperature with radius constant), the total flux of the emission line and the strength of the peaks relative to the flux at the line center also increase. Because the CO 2-1 emission line is optically thick, the disk temperature is very similar to the gas brightness temperature. Increasing the outer radius of the disk [1]results in an increase in the flux of the line emission, but little change in the line shape. The line center flux depends is proportional to R_{out}^2 and increasing R_{out} fills in the region between the two peaks. We find that an outer radius of R_{out}=426 AU is necessary to fit the CO 2-1 emission, which is consistent with that required from fits to the integrated intensity maps with a 2-D Gaussian (Qi et al., 2003). An inner radius cutoff of $R_{in} \leq 5$ AU is required to fully sample the inner disk radii and replicate the image of CO 2-1 in LkCa 15. The double peaked nature of the line shape arises from material rotating at an angle inclined to the line of sight and thus is strongly affected by the disk inclination (as $\sin^2 i$), with emission from a face on orientation being single peaked. The double peak widens with increased inclination from face on (see Horne & Marsh, 1986) and an inclination of 60° with the disk surface facing toward the observer best matches the spectrum and gives minimal residuals when compared to the integrated intensity map of CO 2-1 toward LkCa 15. This is consistent with the intensity obtained via fitting the integrated intensity

[1]The D'Alessio model has a maximum outer radius of R_{out} = 500 AU. In order to explore the extension of the outer radius beyond 500 AU, we expand the model to farther radii by keeping the disk parameters (i.e., hydrogen density, temperature, pressure) constant at the same values as the outermost cell of the D'Alessio model.

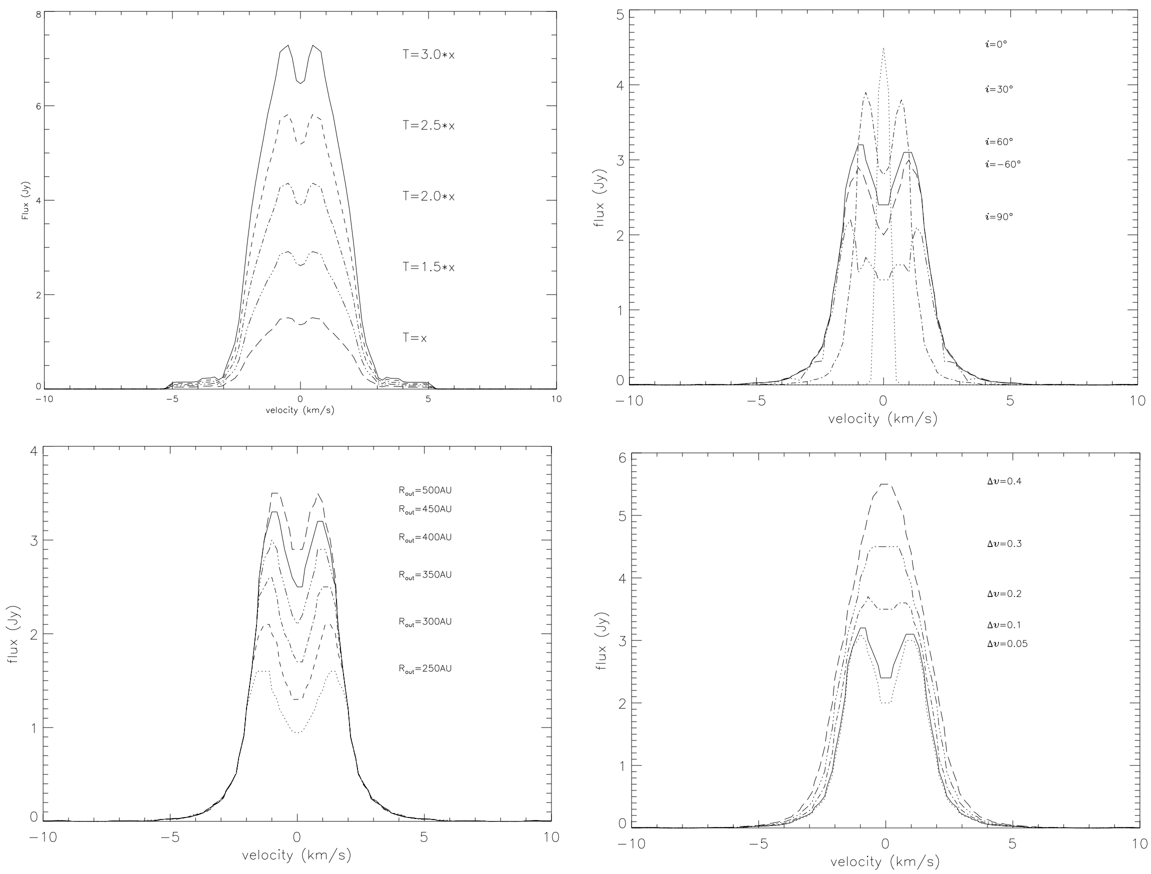

Figure 2.4 This figure indicates the response of the model for the CO 2-1 transition to variations in the physical parameters of the disk. (a) The emission line strengthens and sharpens as the temperature is increased through scaling of the profile from D'Alessio et al. (2001), denoted by x. (b) The peak shape changes drastically from a narrow single peak when the disk is oriented face on ($i = 0°$) to a broad double peak when the disk is edge on ($i = 90°$). (c) Increasing the outer radius R_{out} results in increased line strength and a decrease in the separation between the peaks, because the emission near the line center arises from the outer disk. (d) Increasing the turbulent velocity width (Δv) essentially increases the interaction between material in different radii, thus smearing the emission line; with $\Delta v = 0.05$ km/s the line shape is virtually unchanged and for $\Delta v = 0.4$ the double peak completely disappears.

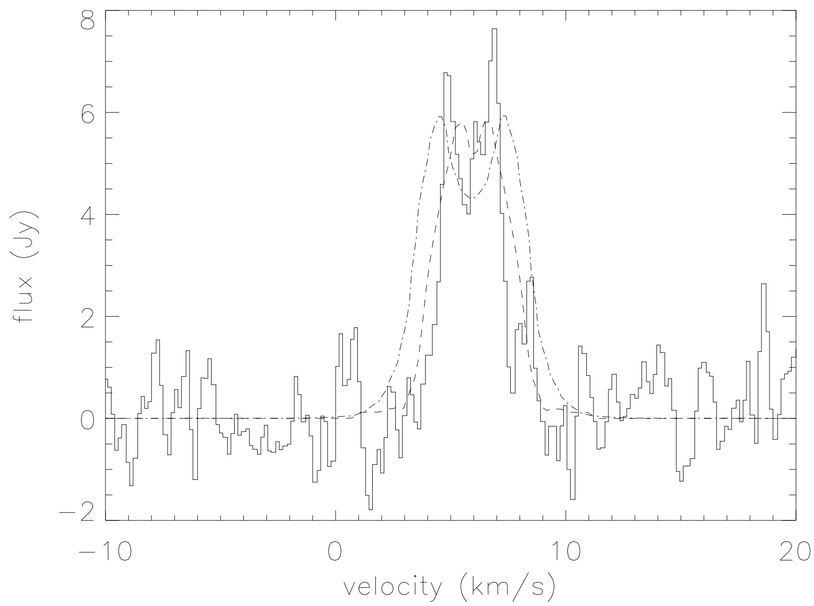

Figure 2.5 CO is a good tracer of disk structure and kinematics. Here we use our model to show that CO emission from the LkCa 15 disk (solid line) is well matched to model CO emission (dotted/dashed lines) from a disk with an inclination of 58 degrees, a turbulent velocity of 0.1 km/s and an outer radius of 430 AU. This model assumes that the CO abundance can be simply scaled from the hydrogen abundance, which appears to be sufficient for this optically thick emission. The dotted and dashed lines are models using temperature distributions as calculated by Chiang & Goldreich (1997) and D'Alessio et al. (2001). The simple two-layer model of Chiang & Goldreich (1997) produces temperatures that are too high to fit our data.

maps assuming that the disk is circular. Variation in the turbulent broadening width also has a large effect on the line shape. A turbulent velocity width of less than 0.2 km/s is necessary for the spectrum to be double peaked and a turbulent velocity width of $\Delta v = 0.1$ km/s best fits the splitting of the observed double peaked spectrum (see Figures 2.4 and 2.5). In summary, the best agreement with the observed spectrum and map of CO 2-1 emission toward LkCa 15 is a disk with an inner radius and outer radius cutoffs $R_{in} = 5$ AU and $R_{out} = 426$ AU inclined toward the observer with $i = 60°$ and a turbulent velocity width $\Delta v = 0.1$ km/s. In these simulations, the column density of CO is scaled from the D'Alessio et al. (2001) hydrogen density as 10^{-5} N_H.

Observations of high-J transitions can provide additional information about the temperature structure in the disk. For this reason, observations of CO 3-2 and CO 6-5 emission from LkCa 15 were obtained at the Caltech Submillimeter Observatory (van Zadelhoff et al., 2001). Using the model described above, with all other parameters held constant, the temperature scale factor was varied until the CO 3-2 and 6-5 spectra were fit. The resulting temperatures as a function of radius are shown in Figure 2.6. The temperature increases with increase in J, indicating that the high-J levels probe material closer to the disk surface. In essence what we have obtained is the temperature

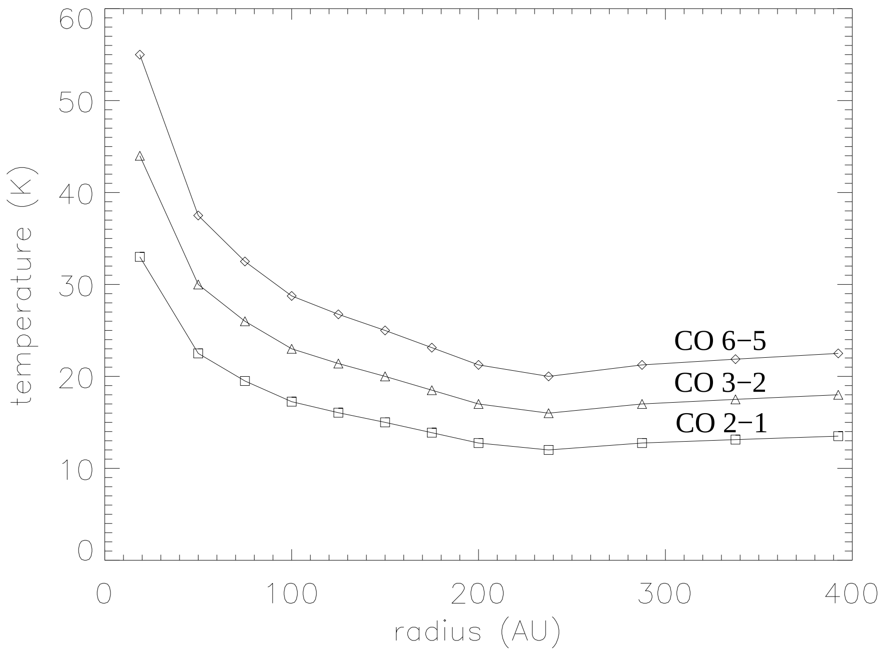

Figure 2.6 Temperature distributions required to fit the observed CO 2-1, 3-2, and 6-5 transitions toward LkCa 15. The temperature increases for transitions with increasing J, indicating that these high-J transitions probe warmer gas, at higher vertical heights within the disk.

as a function of height in the disk; the temperature ranges from 30–60 K on the disk surface near the star, but temperatures are much cooler 15–30 K in the outer regions of disks ($R > 75$ AU) to which we are sensitive with OVRO. This temperature structure is very similar to that predicted with the D'Alessio et al. (2001) and Chiang & Goldreich (1997) models.

2.4 Comparing models with observations: Constant column density calculations

We have used the non-LTE accelerated Monte Carlo model described above (Hogerheijde & van der Tak, 2000), with the disk parameters now fixed, to solve the two-dimensional radiative transfer and molecular excitation for several other molecular transitions observed with OVRO toward the LkCa 15 disk. This model produces a simulated image of each transition as observed by a telescope with a resolution equivalent to the model for a disk of a given size, inclination and temperature distribution. The MIRIAD function UVMODEL and the observed visibility data set were used to sample this model at the observed (u, v) spacings and the model data set was processed in a manner identical to that of the OVRO data, thus allowing a direct comparison of the two. For each transition observed, the integrated line intensity was calculated from the resulting model and compared to the

Table 2.1. Observed molecular intensities and column densities toward LkCa 15

Transition	Beam (arcsec)	$\int T_A dv$(LTE) (K km/s)	N(30K,LTE) (cm^{-2})	N(Model) (cm^{-2})	Model Ratios N(Model)/N(30K,LTE)
CO 2-1	1.81×1.49	12.5	7.28(15)	1.68(18)	230
^{13}CO 1-0	2.74×2.41	6.39	1.11(16)	3.04(16)	2.74
C^{18}O 1-0	5.05×3.59	1.90	3.31(15)	1.40(15)	0.42
HCO^+ 1-0	7.74×5.64	3.30	9.25(12)	2.31(13)	1.79
$H^{13}CO^+$ 1-0	6.30×4.41	<0.88	<2.60(12)	<1.12(12)	0.43
N_2H^+ 1-0	3.51×3.17	3.83	1.71(13)	3.07(13)	1.80

observed integrated line intensity. Iteration of the model over a range of column densities for each observed transition was performed to provide a fit to the observed integrated line intensity. The column density was assumed to be constant as a function of radius. This is consistent with the results of various chemical models (Willacy & Langer, 2000; Aikawa & Herbst, 1999) at the large radii (> 50 AU) to which we are sensitive with the current OVRO Millimeter Array. For these model calculations, the temperature and hydrogen density as a function of radius and height were acquired from the model of D'Alessio et al. (2001), calculated specifically for the stellar parameters of LkCa 15.

The resulting column densities are shown in Table 2.1. The column densities calculated using this non-LTE radiative transfer model are 1–2 orders of magnitude larger than those calculated in the Willacy & Langer (2000) models of disk chemistry, but consistent with those calculated by Aikawa & Herbst (2001). As indicated in the last column of Table 2.1, for CO 2-1, ^{13}CO 1-0, HCO^+ 1-0 and N_2H^+ 1-0 emission the column densities are smaller when calculated using the LTE assumption. This is due to the fact that the emission from these transitions is optically thick. The LTE calculations assume that the gas is optically thin and that the entire disk is being probed by the line emission and thus result in an underestimation of the total amount of CO, HCO^+ and N_2H^+ present. Comparison of the CO isotopologues and HCO^+ and $H^{13}CO^+$ agree with the assessment that the CO 2-1, ^{13}CO 1-0 and HCO^+ 1-0 transitions are optically thick (see above discussion). In the case of the C^{18}O 1-0 and $H^{13}CO^+$ 1-0 emission, which are believed to be optically thin, the column densities are overestimated when thermal equilibrium is assumed. This supports the conclusion that conditions in the emitting region are not at LTE, and that both radiative and collisional processes play a part in the excitation. The population of higher energy rotational states is thus much lower than would be the case if collisions were dominant; and the assumption of thermal equilibrium therefore results in an overestimation of the population of the upper states and thus in the total column density, which at LTE is directly proportional to the density of the upper state.

A curve of growth, or plot of the equivalent width (W_λ) of the line (or line flux) and the number

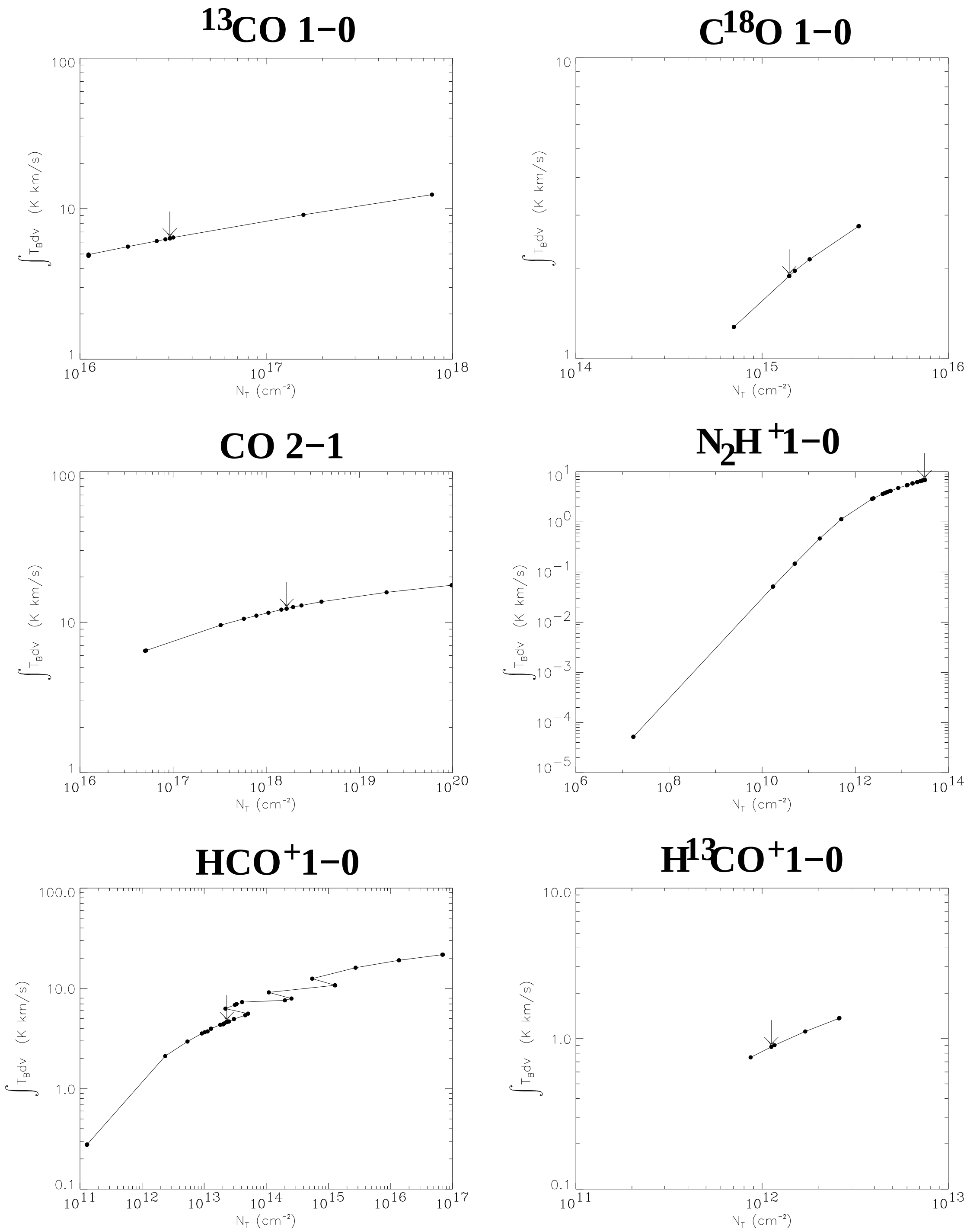

Figure 2.7 Curve of growth analysis for the constant column density model. The arrows depict the points where a successful fit to the observed spectrum was obtained. For the optically thick transitions, ^{13}CO 1-0, CO 2-1, HCO$^+$ 1-0 and N$_2$H$^+$ 1-0, the column densities are approaching the flat part of the curve of growth and therefore the integrated intensity is not extremely sensitive to column density. C^{18}O 1-0 and H^{13}CO$^+$ 1-0 appear to be optically thin, with the integrated intensity linearly related to the column density.

of absorbers ($N_j f_{jk}$, where N_j is the column density and f_{jk} is the oscillator strength), is often used to describe the sensitivity of an observation to changes in the (column) density of a molecule. In order to evaluate how sensitive our models are to changes in the column density of the observed species, we performed a slight variation on the standard curve-of-growth analysis. In this analysis, we plot the integrated intensity ($\int T_B dv$) of the modeled line is versus the column density N_T as shown in Figure 2.7 for the transitions discussed above. We find that for ^{13}CO 1-0, CO 2-1, HCO^+ 1-0 and N_2H^+ 1-0 the column densities are approaching the flat part of the curve of growth and therefore the integrated intensity is not extremely sensitive to column density. However, for $C^{18}O$ 1-0 and $H^{13}CO^+$ 1-0 the relationship appears to be closer to the linear part of the curve of growth. The curve of growth is linear when the total rate of energy emission varies linearly with the number of molecules, meaning that emission from essentially each molecule reaches the observer. Thus, the curve of growth is directly related to the optical depth, and $C^{18}O$ 1-0 and $H^{13}CO^+$ 1-0 are in the linear region of the curve of growth because these transitions are optically thin. In this manner, our model is also sensitive to optical depth, with the most accurate estimates of the column densities coming from the analysis of optically thin transitions.

2.5 Comparing models with observations: Imaging

Molecular distributions are essential to understanding the chemistry taking place in disks. However, proper interpretation of interferometric observations require an understanding of the effects of telescope resolution and incomplete sampling of the (u, v) plane. For this reason, we use our model to simulate images of the observed CO 2-1 emission toward LkCa 15, in two scenarios: 1) the observations were made using an array with complete UV coverage that matches the model resolution, and 2) the observations were made under the same conditions as the OVRO observations. Comparison of these two will help us understand what information is lost due to the imperfections of real observations. In both cases, the models are produced with the parameters (R_{out}, i, Δv, etc.) derived above for the CO 2-1 emission toward LkCa 15. The first scenario is the default output from the *RATRAN* radiative transfer code (Hogerheijde & van der Tak, 2000). To simulate the observations, the models are resampled at the observed (u, v) coverage and resolution by replacing the amplitudes of the observed visibilities with the model amplitudes at the same positions.

It is easiest to see the differences between these two scenarios in channel maps displaying the integrated intensity in 0.6 km/s channels, which demonstrate how the material of different velocities is distributed (Figure 2.8). These channel maps are equivalent to taking the shaded regions of Figure 2.3 and plotting each on its own map. The top panels show the perfect telescope scenario. These channel maps are very similar to what we would expect from Figure 2.3. The "butterfly" shape of the observed emission in each channel arises from the distribution of material with the same

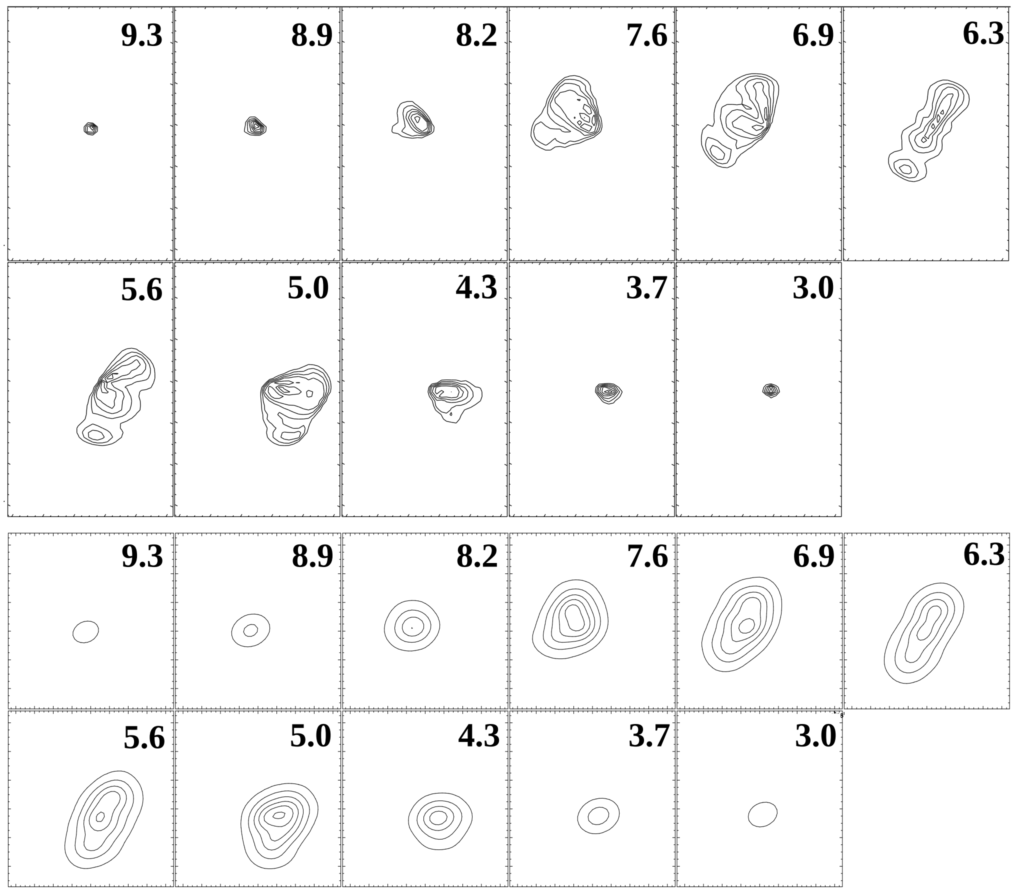

Figure 2.8 Channel maps produced using the model described above to simulate observations of CO 2-1 emission from LkCa 15. The unconvolved channel maps (top) are equivalent to observations using an array with complete sampling of the (u, v) plane to a resolution that matches that of the model. These maps depict a migration from left to right as the velocity shifts from red to blue around the systemic (average) velocity (~6.3 km/s). The channel maps on the bottom result from sampling the original model at the observed (u, v) coverage (θ_{beam} ~$2''$). This has the effect of smoothing out the structure seen in the previous maps, and making the shift in position with velocity less evident. The difference between these models indicate the importance of (u, v) coverage to the interpretation of such observations.

velocity in the disk. In the case of our simulation, emission from material with velocities to the red (blue) of the line center, shows up to the west (east) of the stellar position. From the spectrum of CO 2-1 toward LkCa 15 (Figure 2.5), the line center is at ∼6.3 km/s with a velocity range of about ±3 km/s, consistent with these channel maps. The small peak toward the south is due to the fact that the disk has a finite radius and is flared; when inclined at 58°, a corner of the underside of the disk is visible and this is the peak that we see. The bottom panels show the resulting channel maps when the model is sampled at the observed (u, v) coverage and resolution (∼2″). This has the effect of smoothing out the structure seen in the previous maps, and making the shift in position with velocity less evident. It is quite astonishing how big the change is between these scenarios. The difference between these models indicates the importance of (u, v) coverage to the interpretation of such observations. This is particularly important when analyzing more complicated molecular distributions as discussed in Chapters 3 and 4.

2.6 Summary

A non-LTE Monte Carlo radiative transfer model (Hogerheijde & van der Tak, 2000) was used to simulate molecular line emission from the T Tauri star LkCa 15 disk. Temperature distributions and hydrogen densities from D'Alessio (private communication) calculated for a star with $M_* = 1\ M_\odot$, $R_* = 1.64\ R_\odot$, $M_* = 4395$ K, $\dot{M} = 1.0\times10^{-8}\ M_\odot$/yr were used. Fits to the CO 2-1 emission establish the physical parameters of the model; the best agreement with the observed spectrum and map is a disk with inner radius and outer radius cutoffs $R_{in} = 5$ AU and $R_{out} = 426$ AU inclined toward the observer with $\imath = 60°$ and a turbulent velocity width of $\Delta v = 0.1$ km/s. These models were used to solve the radiative transfer and molecular excitation for the observed 1-0 transitions of ^{13}CO, $C^{18}O$, HCO^+, $H^{13}CO^+$ and N_2H^+ using the physical model described above and varying the fractional abundance of each molecule to match the integrated intensity. The resulting column densities are larger by a factor of ∼2 than those predicted from a standard LTE, $\tau\ll1$ analyses for ^{13}CO, HCO^+, and N_2H^+, which are believed to be optically thick, and smaller than those predicted from a standard LTE, $\tau\ll1$ analyses for $C^{18}O$ and $H^{13}CO^+$, which are optically thin. This indicates that the emitting regions are not at LTE and that optical depth effects play a large role in the relationship between column densities and observed integrated intensities in the regions probed by low-J transitions of molecular gas in circumstellar disks. The models were also used to simulate integrated intensity and channel maps of the emission for a telescope with essentially infinite resolution and complete (u, v) coverage and for the observed (u, v) spacings for CO 2-1. Even with 2″ resolution it was found that detailed disk structure is largely undersampled by current observations and image deconvolution techniques.

Chapter 3

A survey of CN, HCN, CO and HCO^+ emission from TTs and HAe disks

Abstract

Models indicate that molecular line emission from CN, HCN and HNC should serve as good tracers of the temperature, UV and X-ray radiation fields in the surface layers of circumstellar disks. This is consistent with previous OVRO observations of T Tauri (LkCa 15 and GM Aur) and Herbig Ae disks (HD 163296 and MWC 480), which indicate that CN/HCN and HCO^+/CO ratios increase with increasing UV field, where the UV field can be enhanced either via dust settling or due to a higher luminosity of the central star. In this work, we expand the previous study, choosing disks which have been previously mapped in CO and demonstrate Keplerian rotation, along with large disk masses and sizes, so that CN and HCN should be confined to the disks and observable. We have also chosen systems with a range of X-ray and optical luminosities and dust properties, as described by L_{FIR}/L_{bol} and stellar A_V, in order to examine whether the properties of the disk (dust settling) or the central star (radiation field) exert a stronger influence on the chemistry.

3.1 Introduction: Tracing temperature and radiation fields in circumstellar disks

A thorough understanding of the physical and chemical structure of disks around older T Tauri and Herbig Ae stars is important for constraining models of dust processing, settling, and agglomeration. It is also necessary for estimating the dispersal timescales for nebular gas and dust, the critical building blocks from which planets are assembled. Indeed, the amount of gas (and dust) available within an accretion disk and the timescale over which it is dissipated play major roles in determining what kind of planetary system, if any, can be formed. Furthermore, an understanding of how various volatile species (H_2O, CO, CH_4, NH_3, N_2, etc.) are distributed in the outer regions of circumstellar disks is particularly important to examining the connection between interstellar and nebular processes in the formation of icy planetesimals such as comets and Kuiper Belt Objects.

The question of planet formation is intimately related to the formation and evolution of disks around protostars. Molecular line emission can be used to probe this special stage in the development of planetary systems. Until recently, most of the imaging of classical T Tauri and Herbig Ae stars outlined above was carried out in various isotopomers of CO for reasons of sensitivity. Through single dish surveys of several T Tauri stars, namely, DM Tau, GG Tau (Dutrey et al., 1997), TW Hya (Kastner et al., 1997), and LkCa 15 (van Zadelhoff et al., 2001), a number of species (HCN, CN, HNC, H_2CO, HCO^+, CS, ...) have been detected in several transitions, with emission intensities similar to that of ^{13}CO or $C^{18}O$. High-resolution molecular line surveys of 4 disks (LkCa 15, MWC 480, GM Aur and HD 163296) with the OVRO interferometer have met with similar success (Qi, 2001; Qi et al., 2003). These important data suggest that, at least in appropriate disks, chemical studies regarding the nature and variation of the disk composition with radius can now be profitably pursued. They further reveal that both ion-molecule chemistry and photon-dominated chemistry must contribute to the observed abundances at large disk radii, since the ratios of species such as CN/HCN and HNC/HCN are too high to be accounted for by quiescent chemical models alone (Spaans, 1996, Dutrey et al., 1997, Kastner et al., 1997).

As van Zadelhoff (2002) shows, the high optical depth of many millimeter-wave transitions and the temperature gradients set up by the interaction of the disk with radiation from the central stars ensures that it is the upper regions of disk that are traced. At disk surfaces molecules can be dissociated by UV radiation, or ionized by UV photons, X-rays and cosmic rays. Recent surveys conducted with the Roentgen satellite (ROSAT) of T Tauri (Feigelson & Montmerle, 1999, Casanova et al., 1995, Neuhaeuser et al., 1995) and Herbig Ae/Be (Zinnecker & Preibisch, 1994) stars indicate that most are X-ray sources. The X-ray luminosity of T Tauri stars lies in the range 10^{29}-10^{30} erg s^{-1} (Glassgold et al., 1997), which can drive ionization rates of $\sim 5\times10^{-14}$ s^{-1} at 1 AU. The standard ionization rate by cosmic rays is 1.3×10^{-17} s^{-1}. Additionally, the protoplanetary disk is irradiated by UV photons from both the interstellar field and the central star. The UV flux from the central star and nearby stars may drive the total UV flux impinging on the disk to values as high as $G_0=10^4$–10^6 Habing, (Herbig & Goodrich, 1986; Johnstone & Penston, 1986; Imhoff & Appenzeller, 1987; Montmerle, 1992), where 1 Habing $= 1.6 \times 10^{-3}$ ergs cm^{-2} s^{-1} is the estimated average flux in the local interstellar medium (Tielens & Hollenbach, 1985). Chemistry in the outermost near-surface regions of disks therefore shows similarities to both ion-molecule chemistry (Millar et al., 1991) and that in photon-dominated regions, or PDRs (Fuente et al., 1993; Jansen et al., 1995; Sternberg & Dalgarno, 1995).

Molecular line emission from CN, HCN and HNC should serve as good tracers of the disk environment in these surface regions. Fuente et al. (1993) show that although the abundance of

Table 3.1. Effects of luminosity and dust settling on the CN/HCN ratio in disks

Source	Luminosity ($L_\odot$)	CN/^{13}CO	$HCO^+/^{13}CO$	CN/HCN	H/h[a]
LkCa 15	0.72	~ 0.01	~ 0.001	~ 10	1.0
GM Aur	0.8	~ 0.003[b]	$\ll 0.00025$	$\ll 1$	4.0
MWC 480	32.4	~ 0.007	~ 0.001	~ 4	1.7
HD 163296	30.2	~ 0.01	~ 0.0005	$\gg 20$	2.0

[a]The ratio of the height of the disk photosphere and the vertical gas scale height from SED fits

[b]HCN/^{13}CO is used instead of CN/^{13}CO

most molecular species decreases with increasing UV radiation, some species increase at moderate UV fields (CH, CH^+, CH_2, $CH_2{}^+$, $CH_3{}^+$, C_2, C_2H and CN). Because of this behavior, CN and C_2H are very sensitive to the presence of UV radiation and thus the luminosity of the central or nearby star(s). At high A_V, CN and HCN both can be formed from the dissociative recombination of the $HCNH^+$ ion. However, HCN can also be ionized by the fast reaction $HCN + H^+ \rightarrow HCN^+ + H$, and results in a decrease in the HCN abundance and an increase the CN/HCN ratio in these regions. This trend has been observed in PDRs; the CN/HCN ratio increases by a factor 15 (Fuente et al., 1993) from A_V=10 mag (CN/HCN $\sim$ 1) to A_V=6 mag (CN/HCN $\sim$ 15). The CN/HCN ratio has therefore been suggested as a tracer of enhanced UV fields. Since UV radiation is attenuated mainly by grains, UV photons will penetrate more deeply into the disk as grain sedimentation and growth proceed, and photochemistry will become more important. Additionally, models (Fuente et al., 1993) predict that the HNC/HCN ratio decreases by a factor of 5 from A_V=10$\rightarrow$6 mag for a constant kinetic temperature of 30 K, and decreases by the same factor if the visual extinction is held constant but the kinetic temperature increases from 15 to 50 K. HNC/HCN will thus decrease with higher temperatures and stronger UV fields.

Initial OVRO observations of four disks indicate similar trends in the ratios of CN, HCN, and HCO^+ abundances (Qi, 2001; Table 3.1). The more luminous Herbig Ae stars MWC 480 and HD 163296 possess high CN/HCN and HCO^+/CO ratios, likely due to increased photodissociation due to the higher UV flux of these stars. Among the two T Tauri stars, LkCa 15 and GM Aur, which have similar luminosity and spectral type, LkCa 15 has higher CN/HCN and HCO^+ ratios by factors of 10. This may be due to dust settling occurring in the LkCa 15 disk, indicated by a decrease in the ratio of the height of the dust photosphere to the gas pressure scale height (H/h). This ratio is calculated from fits to the SED for these disks (Chiang et al., 2001; discussed more below).

In this study, we expand the previous sample to include the sources in Table 3.2, chosen from previous CO surveys (Koerner & Sargent, 1995; Dutrey et al., 1996; Mannings & Sargent,

Table 3.2. Source parameters

Source	Sp.Typ.	Age (Myr)	A_V	d (pc)	M_D ($M_\odot$)	M_G ($M_\odot$)	R_{out} (AU)	L_* ($L_\odot$)	$\log(L_X)$ (erg/s)	L_{FIR}/L_{bol}	Ref
AA Tau	M0Ve	0.45	0.84	140	0.018	...	150	1.5	29.53	0.15	6,8
AB Aur	B9/A0	3–5	0.65	160	0.01	1.3(-3)	450	53.6	29.52	<0.19	1,7,8
CQ Tau	A8Ve	10	0.96	100	0.015	2.62(-5)	<85	8.0	no obs.	0.50	2,9
DL Tau	K7	2	1.28	140	0.087	1.3(-6)	250	0.68	<30.04	0.33	3,6,8
DM Tau	M0.5	5	0.0	140	0.034	4(-3)	800	0.25	<29.66	0.16	4,5,6
Haro 6-5B	...	8.0	>0.02	140	0.021	0.45(-3)	150	...	no obs.	<0.02	5,8
MWC 758	A3e	6	0.22	200	0.005	3.97(-5)	185	20.6	no obs.	0.75	2,9
RY Tau	F8V:e	0.21	0.55	133	0.039	9.6(-6)	107	16.7	29.71	0.25	3,6,8

Note. — References: 1-Mannings & Sargent (1997), 2-Mannings & Sargent (2000b), 3-Koerner & Sargent (1995), 4-Duvert et al. (2000), 5-Dutrey et al. (1996), 6-Damiani et al. (1995), 7-Zinnecker & Preibisch (1994), 8-Kenyon & Hartmann (1995), 9-Chiang et al. (2001).

1997; Mannings & Sargent, 2000b; Duvert et al., 2000), thanks to strong CO emission (0.4–3.2 Jy) whose emission patterns are consistent with models for isolated disks in Keplerian rotation. The sources selected are the largest (R_{out}=100–800 AU) and most massive ($M_{gas}=10^{-5}$–10^{-3} $M_\odot$, $M_{dust+gas}$=0.005–0.04 $M_\odot$) of the disks observed in CO to date. They have been chosen to sample a range of luminosity (see L_* and L_X in Table 3.2) and dust properties, with the degree of dust settling in the disks being represented by L_{IR}/L_{bol}. In the case of DM Tau, single dish observations of CN, HCN and HNC indicate that this source is quite similar to LkCa 15. Due to its large extent (R_{out}=800 AU), DM Tau will provide an excellent opportunity to examine whether the unusual CN and HCN distributions seen in LkCa 15 (c.f. Figure 4.5) are representative of large disks.

3.2 Observations

The observations were made using the Owens Valley Radio Observatory (OVRO) Millimeter Array at Big Pine, California between September 2002 and January 2003. The ^{12}CO 1-0, ^{13}CO 1-0 and CN 1_{023}-0_{012} transitions were observed simultaneously, with a channel width of 0.33 km/s. The HCO^+ 1-0, HCN 1_2-0_1 and HNC 1-0 transitions were also acquired simultaneously at a slightly lower velocity resolution, Δv=0.42 km/s. The sources were observed in combinations of the C and L configurations resulting in the beam sizes shown in Table 3.4. Two sources were observed in each 8 hour track (CQ Tau/MWC 758, DL Tau/DM Tau, AB Aur/RY Tau, and AA Tau/Haro 6-5 B), resulting in approximately 3 hours on source for each disk.

The bandpass was calibrated using a boxcar fit to an internal noise source modified by a second order polynomial fit to observations of an astronomical source; either 3C84, 3C454.3, 3C345, 3C279 or 3C273 were used subject to availability at the time of observation. Integrations on a phase and amplitude calibrator were interleaved with source observations approximately every half hour. The flux density scale was established from observations of the quasars noted above, with fluxes found

Table 3.3. Observed transitions

Molecule	Transition	ν (GHz)	Δv (km/s)
CO	1-0	115.2712018	0.325
HCO^+	1-0	89.1885230	0.420
CN	1_{023}-0_{012}	113.4909850	0.330
HCN	1_2-0_1	88.6318470	0.423
HNC	1-0	90.6635930	0.413

by bootstrapping from ~concurrent observations of Neptune and Uranus. Bandpass, phase and flux calibrations were applied to the data with the MMA software package (Scoville et al., 1993). Subsequent imaging and spectral analysis were performed using the MIRIAD data reduction software package (Sault et al., 1995).

3.3 Column densities

It is convenient to describe the observed intensities, given in Jy (= 10^{-26} Wm^{-2}Hz^{-1}), in terms of the brightness temperature T_B of a blackbody exhibiting the observed specific intensity B_ν at frequency ν,

$$B_\nu = \frac{2\nu^3/c^2}{exp(h\nu/kT_B) - 1}, \tag{3.1}$$

where c is the speed of light in units of m/s and k is the Boltzmann constant in units of J/K. In the Raleigh-Jeans limit, $h\nu \ll kT$, which is appropriate for millimeter observations, the exponential term can be approximated by $[exp(h\nu/kT_B) - 1] \approx h\nu/kT_B$ and the blackbody intensity becomes

$$B_\nu = \frac{2\nu^2}{c^2} kT_B. \tag{3.2}$$

By summing the intensity $B_\nu[Jy/beam = 10^{-26}$ Wm^{-2}Hz^{-1}sr$^{-1}]$ over the source and normalizing by the shape of the synthesized beam, we then obtain a spectrum, which is the total flux over the chosen aperture for each channel in units of spectral flux density $[Jy = 10^{-26}$Wm^{-2}Hz$^{-1}]$,

$$S_\nu[Jy] \quad = \quad \frac{\int B_\nu[Jy/bm] d\Omega_{bm}}{\int d\Omega_{bm}}. \tag{3.3}$$

To obtain the average brightness temperature over the source, one must divide by the solid angle $\Delta\Omega_A$[sr^{-1}] over which the summation was performed,

$$\Delta\Omega_A \quad = \quad \frac{(\theta_a \times \theta_b)}{(2\sqrt{2ln2})^2 (206265)^2}, \tag{3.4}$$

where θ_a and θ_b are the FWHM of the aperture in arcseconds and 206265 is the conversion factor for arcseconds to radians. The Raleigh-Jeans brightness temperature in Kelvin averaged over the source can thus be calculated via the equation,

$$\begin{aligned} T_B &= \frac{S_\nu}{k}\frac{1}{\Delta\Omega_A}\frac{c^2}{2\nu^2} && (3.5)\\ &= \frac{S_\nu[Jy]10^{-26}}{1.38\times10^{-23}J/K}\frac{(2\sqrt{2ln2})^2(206265)^2}{(\theta_a\times\theta_b)}\frac{(2.99\times10^8 m/s)^2}{2(\nu[GHz]10^9)^2} && (3.6)\\ &= 7.68\times10^6\frac{S_\nu[Jy]}{(\theta_a\times\theta_b)\nu[GHz]^2}. && (3.7)\end{aligned}$$

The observed intensity is more accurately represented by the antenna temperature T_A^*, which takes the instrumental efficiency η into account, $T_A^* = \eta T_B$, and is defined as the temperature required by a resistor to generate the observed power density at frequency ν.

Gaussian fits to the observed emission lines were used to obtain the integrated intensities ($\int T_A^* dv$) in units of K km/s, shown in Table 3.4.

$$\int A_0 e^{-(z^2/2\sigma^2)}dz = A_0\sqrt{2\pi\sigma^2} = 1.064 A_0 FWHM \tag{3.8}$$

where A_0 is the peak of the Gaussian, $z = v - v_0$ and $dz = dv$. If emission was not detected, the rms noise level obtained in the observation (Table 3.4) was used to calculate an upper limit for the integrated intensity by integrating over a Gaussian with a peak flux of 3σ and a base width (at 1σ) equal to that of the CO 1-0 transition toward the same source. In all cases, the total column densities were then calculated from the integrated intensities using the following relation, assuming that the emission is optically thin,

$$\int T_A^* dv = \frac{8\pi^3}{3k}\nu\mu^2 S\frac{N_T}{Q(T_{ex})}e^{-E_u/kT_{ex}}. \tag{3.9}$$

Here S is the line strength and is obtained from integrated intensities (I_{cat}) of the emission lines in laboratory spectra obtained at a temperature (T_0 = 300K) as reported in the JPL Molecular Spectroscopy on-line catalog (Pickett et al., 1998) via the relationship,

$$I_{cat} = \frac{8\pi}{3k}\mu^2 S Q(T_0)\left\langle e^{-E_l/kT_0} - e^{-E_u/kT_0}\right\rangle. \tag{3.10}$$

In the two equations above, N_T is the column density in cm^{-2}, $Q(T)$ is the rotational partition function at temperature T, E_u and E_l are the energies (in ergs) of the upper and lower states, ν is the transition frequency (Hz), μ is the permanent dipole moment and k is the Boltzmann constant.

In addition, it was assumed that the emitting region is in Local Thermal Equilibrium (LTE) and is roughly isothermal with a temperature of T$_K$ = T$_{ex}$ = 30 K. The use of LTE may not be the

Table 3.4. Molecular line observations: Intensities and column densities

Source	Transition	θ_{syn} (arcsec)	v_{LSR} (km/s)	Δv (km/s)	Int. Inten (K km/s)	N (30 K) (cm^{-2})	SNR
AA Tau	CO 1-0	5.64×4.21	6.3	5.1	13.0	$2.09\pm0.58\times10^{16}$	3.6
	CN 1_{023}-0_{012}	5.28×5.05	...	...	13.6	$<3.89\times10^{14}$	...
	HCN 1_2-0_1	8.62×7.58	...	...	4.36	$<2.74\times10^{13}$	...
	HCO^+ 1-0	8.82×7.05	6.5	3.8	4.75	$1.40\pm0.50\times10^{13}$	2.8
	HNC 1-0	8.29×7.78	6.4	5.1	3.52	$1.14\pm0.29\times10^{13}$	3.9
AB Aur	CO 1-0	5.57×4.36	5.7	2.6	248	$3.99\pm0.11\times10^{17}$	37
	CN 1_{023}-0_{012}	6.18×4.95	6.5	8.0	38.5	$5.29\pm0.40\times10^{14}$	17
	HCN 1_2-0_1	7.18×5.77	...	...	...	$<6.27\times10^{12}$	...
	HCO^+ 1-0	7.28×5.57	5.0	3.6	5.64	$1.67\pm0.39\times10^{13}$	4.3
	HNC 1-0	7.30×5.91	...	...	...	$<1.39\times10^{13}$	...
CQ Tau	CO 1-0	6.37×4.76	6.1	5.7	8.05	$1.29\pm0.36\times10^{16}$	3.6
	CN 1_{023}-0_{012}	6.80×5.98	...	...	...	$<6.26\times10^{14}$	...
	HCN 1_2-0_1	6.51×4.75	4.0	7.0	7.41	$4.65\pm1.6\times10^{13}$	2.8
	HCO^+ 1-0	6.71×4.55	5.5	7.0	7.66	$2.27\pm0.28\times10^{13}$	8.2
	HNC 1-0	6.78×4.79	...	...	...	$<7.37\times10^{13}$	...
DM Tau	CO 1-0	6.59×6.07	6.1	1.4	10.9	$1.76\pm0.11\times10^{16}$	16
	CN 1_{023}-0_{012}	7.19×6.03	...	...	...	$<1.30\times10^{14}$	...
	HCN 1_2-0_1	5.94×4.23	...	...	...	$<4.58\times10^{13}$	...
	HCO^+ 1-0	6.08×4.13	5.6	3.9	14.0	$4.14\pm0.82\times10^{13}$	5.0
	HNC 1-0	6.31×4.20	...	...	...	$<2.36\times10^{13}$	...
FS Tau	CO 1-0	5.44×4.17	8.6	1.3	26.0	$4.19\pm0.22\times10^{16}$	19
	HCO^+ 1-0	8.68×7.02	7.5	3.8	4.81	$1.42\pm0.31\times10^{13}$	4.6
Haro 6-5B	CO 1-0	5.44×4.17	8.1	0.64	13.3	$2.13\pm0.08\times10^{16}$	24
	CN 1_{023}-0_{012}	5.15×4.92	...	...	...	$<2.29\times10^{14}$	...
	HCN 1_2-0_1	8.56×7.55	7.8	1.2	1.07	$6.71\pm1.8\times10^{12}$	3.8
	HCO^+ 1-0	8.68×7.02	8.6	1.4	3.08	$9.12\pm2.3\times10^{12}$	4.0
	HNC 1-0	8.22×7.66	...	...	...	$<3.83\times10^{12}$	...
MWC 758	CO 1-0	6.59×5.28	5.5	2.6	7.10	$1.14\pm0.11\times10^{16}$	10
	CN 1_{023}-0_{012}	6.73×5.97	...	...	...	$<2.46\times10^{14}$	...
	HCN 1_2-0_1	6.49×4.74	...	...	...	$<7.05\times10^{13}$	...
	HCO^+ 1-0	6.59×4.56	...	...	...	$<2.62\times10^{13}$	...
	HNC 1-0	6.66×4.77	...	...	...	$<3.57\times10^{13}$	...
RY Tau	CO 1-0	5.47×4.31	8.8	7.5	5.71	$9.18\pm1.2\times10^{15}$	7.5
	CN 1_{023}-0_{012}	6.22×4.91	10.7724	0.73386	2.44	$6.99\pm2.3\times10^{13}$	3.0
	HCN 1_2-0_1	7.08×5.88	8.0	8.0	5.94	$3.73\pm1.4\times10^{13}$	2.7
	HCO^+ 1-0	7.16×5.68	...	...	...	$<4.78\times10^{13}$	...
	HNC 1-0	7.26×6.01	...	...	...	$<4.12\times10^{13}$	...

Table 3.5. Summary of the 2.7 mm continuum results

Source	α (hms)	δ (dms)	R_{FWHM} (AU)	F_ν (mJy)	M_D ($M_\odot$)	M_{D+G} ($M_\odot$)
AA Tau	4:34:55.426	24:28:53.105	$<993\pm9$	5.35 ± 0.12	5.89e-4	0.0589
AB Aur	4:55:45.841	30:33:04.693	$<653\pm5$	7.63 ± 0.29	1.10e-3	0.110
CQ Tau	5:35:58.498	24:44:54.318	$<692\pm2$	19.6 ± 0.18	1.10e-3	0.110
DM Tau	4:33:48.767	18:10:09.774	$<522\pm3$	14.4 ± 0.37	1.59e-3	0.159
Haro 6-5B	4:22:00.703	26:57:32.665	$<273.3\pm0.6$	11.0 ± 0.30	1.21e-3	0.121
MWC 758	5:30:27.507	25:19:57.133	$<1680\pm30$	6.33 ± 0.27	1.42e-3	0.142
RY Tau	4:21:57.415	28:26:35.657	$<876.9\pm0.8$	26.3 ± 0.40	2.62e-3	0.262

best assumption as most of the emission is thought to arise near the superheated disk surface (van Zadelhoff et al., 2001), and a more detailed, non-LTE analysis is being pursued in a separate study. An isothermal disk with temperature 30 K is appropriate for the outer radii (> 70 AU) of the disks to which we are sensitive at millimeter wavelengths (D'Alessio et al., 1999). The resulting column densities and 3σ upper limits are presented in Table 3.4. Future work will involve more detailed models of the molecular emission using the computational tools outlined in Chapter 2.

3.4 Continuum and ^{12}CO observations

Maps of the continuum and ^{12}CO 1-0 emission are shown in Figure 3.1. In the left column, the continuum is shown in color scale and the integrated intensity of the ^{12}CO 1-0 is overplotted with contours. The velocity structure of the ^{12}CO 1-0 emission is shown in color scale in the right column. It is evident from these images that the 2.7 mm continuum traces a much smaller portion of the disk than does emission from the CO gas. Similarly, we find that the continuum emission is unresolved toward most of the sources in our sample and constrain the size of the 2.7 mm continuum as shown in Table 3.5. This can be attributed to the rapid decrease in dust emissivity as a function of wavelength, and is not likely due to an absence of small grains at large radii (Sargent & Beckwith, 1987; Lay, 1997; Qi et al., 2003). The CO 1-0 emission is resolved and the FWHM sizes of the disks in our sample are listed in Table 3.6.

The total disk masses $M_{gas+dust}$ are calculated from the continuum flux densities using the approach of Beckwith et al. (1990). The flux density is defined as

$$F_\nu = \int I_\nu d\Omega = \int S_v \tau_v d\Omega, \tag{3.11}$$

where τ is the dust optical depth. We have assumed that the dust is optically thin, which is a fair assumption for wavelengths longer than 300 μm. Typical dust temperatures, T_D, are high enough

Table 3.6. ^{12}CO 1-0 observations

Source	θ_{bm} (arcsec)	PA$_{bm}$ (deg)	v_{LSR} (km/s)	R$_{FWHM}$ [a] (AU)	PA^a (deg)	i [b] (deg)	M$_{H_2}$ (M$_\odot$)
AA Tau	5.64×4.21	-85.4	6.3	1130±60 × 860±30	-88.7±0.7	40	1.07×10^{-4}
AB Aur	5.57×4.36	-54.4	5.7	1549±4 × 1088±2	54.40±0.08	45	3.81×10^{-3}
CQ Tau	6.37×4.76	-86.1	6.1	560±20 × 380±10	86.4±0.5	47	1.61×10^{-5}
DM Tau	6.59×6.07	-29.5	6.1	1076±8 × 683±4	-8.6±0.1	51	8.12×10^{-5}
Haro 6-5B	5.44×4.17	-86.2	8.1	910±10 × 564±6	-77.4±0.1	52	7.03×10^{-5}
MWC 758	6.59×5.28	-72.9	5.5	<1800±10	...	...	1.47×10^{-4}
RY Tau	5.47×4.31	-53.1	8.8	650±50 × 300±20	74±2	62	1.54×10^{-5}

[a]This is the deconvolved source size and position angle.

[b]The inclinations calculated here largely follow the beam ellipticity. Calculations of i via comparison with models (i.e., using the method described in Chapter 2) are more reliable and will be performed in the near future.

(T$_D > 50K$) to make the Rayleigh-Jeans assumption valid;

$$S_\nu \approx B_\nu = 2kT\frac{\nu^2}{c^2}. \tag{3.12}$$

Using the definitions of optical depth ($\tau = \kappa_\nu \Sigma$) and solid angle ($\Omega = \frac{\sigma}{D^2}$), the flux density F_ν can then be related to the dust mass ($M_D = \int \Sigma d\sigma$) via the equation,

$$F_\nu \approx \int 2kT\frac{\nu^2}{c^2}\kappa_\nu \, \Sigma \, d\frac{\sigma}{D^2} = \frac{2k < T >}{D^2}\frac{\nu^2}{c^2}\kappa_\nu M, \tag{3.13}$$

where κ_ν is the mass opacity, Σ is the surface density, σ is the surface area of the disk and D is the distance to the disk. The total emission is proportional to a product of the total mass and the average temperature $< T >$, weighted appropriately by its radial distribution. The major uncertainty in the mass estimates arises from κ_ν. Theoretically, κ_ν is expected to vary as a power of the frequency ν: $\kappa_\nu = \kappa_0 \left(\frac{\nu}{\nu_0}\right)^\beta$. Following Beckwith et al. (1990), we adopt a fiducial value of 0.02 $\left(\frac{\nu}{230GHz}\right)$ cm^{2}g^{-1} and calculate the total gas mass assuming $M_{gas}/M_{dust} = 100$.

The disk gas mass M_G can also be calculated from the CO 1-0 observations, using the column density calculated above, following Scoville et al. (1986),

$$M_{H_2} = N_{CO}\, \mu_G\, m_{H_2}\frac{\pi\theta^2}{4}D^2. \tag{3.14}$$

In this equation, $\mu_G = 1.36$ is the mean atomic weight of the gas, m_{H_2}=3.345×10^{-24} g is the mass of one H$_2$ molecule, and θ is the angular diameter (FWHM) of the uniform disk source. For the standard CO fractional abundance, N$_{H_2}$/N$_{CO} \approx 10^4$, we obtain a lower limit to the gas masses

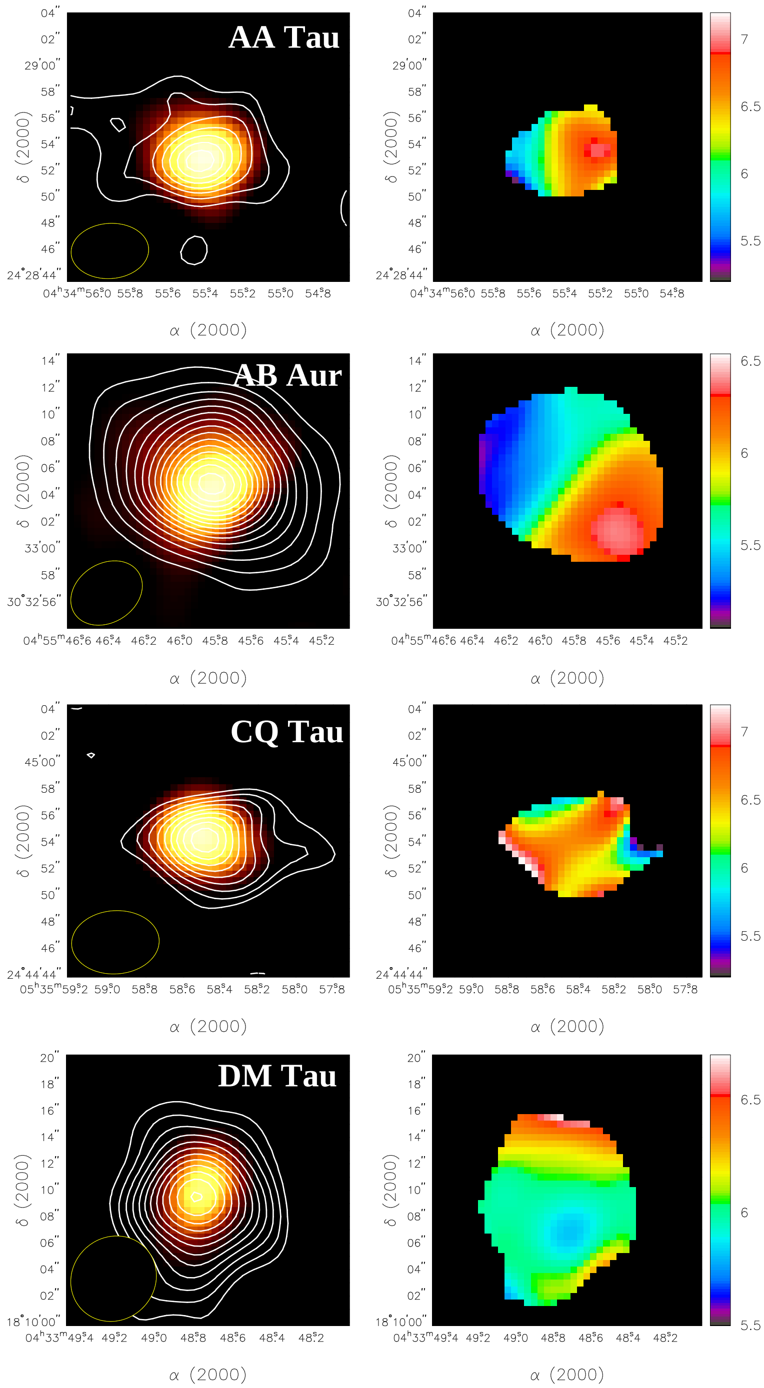

Figure 3.1 Maps of the continuum and CO 1-0 emission toward the sample. The left panel shows the continuum (color scale) and CO 1-0 integrated intensity maps (contours). Contours start at 2σ for AA Tau, AB Aur and DM Tau and at 1σ for CQ Tau, Haro 6-5B, MWC 758 and RY Tau. The right panel shows the CO 1-0 velocity maps, starting at 3σ for all sources.

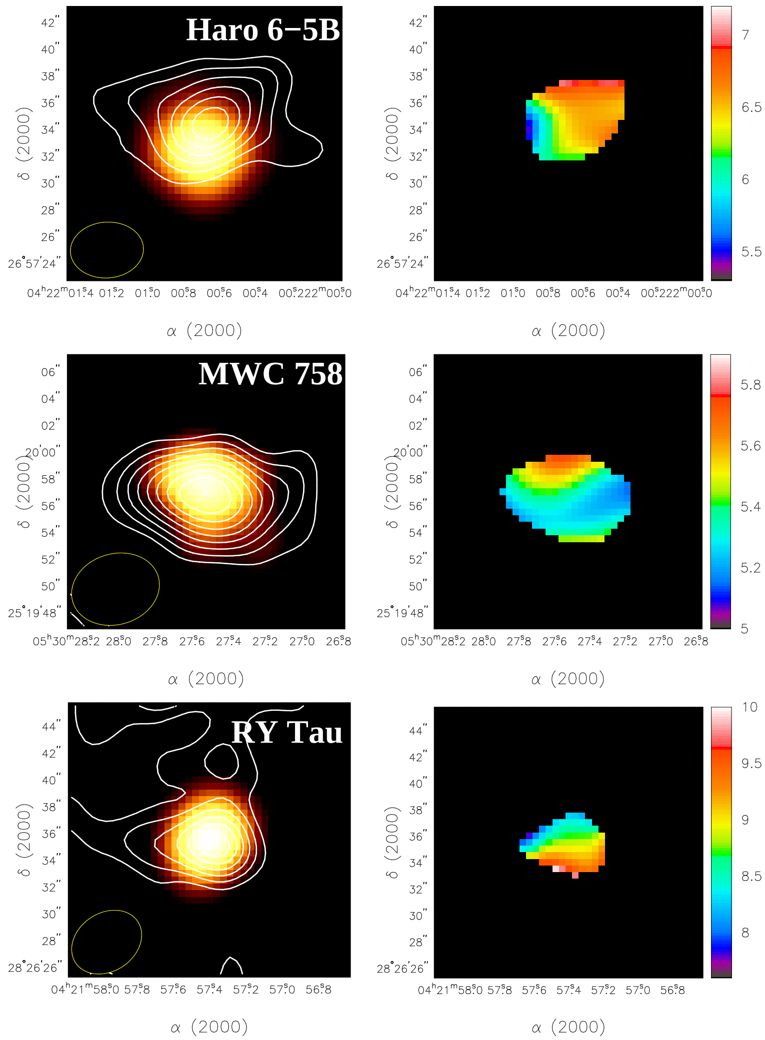

Figure 3.1 -continued.

presented in Table 3.6. Although the gas masses calculated in this way are reasonably consistent with previous observations, the dust masses are consistently too small, perhaps due to low interferometer sensitivity at large radii as discussed above, especially for the short integration times used.

3.5 HCO^+/CO and ionization

The degree of ionization is important because it affects both the physical and chemical structure of disks. Stellar accretion and molecular outflows occur along magnetic field lines and the slowing of disk and stellar rotation are therefore believed to be strongly influenced by magneto-hydrodynamic processes. Radiative and vertical transport in the outer disk also likely depend on the degree of ionization, with coupling between the neutral and magnetic fields occurring at fractional ionizations of $\geq 10^{-8}$ (Feigelson & Montmerle, 1999). The chemical complexity within disks is also stimulated by ionization. Ion-molecule reactions proceed much more quickly than neutral-neutral reactions, as ions induce dipoles in their collision partners, thus increasing collision rates; $k_c \sim 10^{-11}$ cm^3/s for neutral-neutral reactions while $k_c \sim 10^{-9}$ cm^3/s for ion-molecule reactions. Because H_2 is very abundant in disks, the formation rate of H_2^+ is equal to the ionization rate of the disk. For the same reason, H_2^+ once formed reacts quickly with additional H_2 to form H_3^+. Due to the efficiency of charge transfer reactions, the charge and degree of protonation spreads quickly to other molecules (and atoms) and the protonation of C and O by H_3^+ is a vital step in the production of carbon chains and prebiotic molecules.

In the dense and cold disk midplane, extensive molecular depletion ensures that H_3^+ is the dominant gas-phase cation. H_3^+ is unobservable at millimeter wavelengths, but fortunately near the disk surface CO is the most abundant molecule after H_2 and carries much of the charge as HCO^+. HCO^+ is produced and destroyed via the mechanism

$$\begin{aligned}
H_2 + ion.flux &\rightarrow H_2^+ + e^- && (3.15)\\
H_2^+ + H_2 &\rightarrow H_3^+ + H && (3.16)\\
H_3^+ + CO &\rightarrow HCO^+ + H_2 && (3.17)\\
H_3^+ + e^- &\rightarrow H_2 + H && (3.18)\\
HCO^+ + e^- &\rightarrow H + CO. && (3.19)
\end{aligned}$$

The charge transfer reactions producing H_2^+, H_3^+ and HCO^+ proceed at the Langevin rate ($\sim 10^{-9}$ cm^3 s^{-1}), but the dissociative recombination reactions are also efficient ($\sim 10^{-7}$ cm^3 s^{-1}) and it can be assumed that the system is in steady state and the abundances of H_2^+, H_3^+ and HCO^+ remain fairly constant with time. Therefore,

$$\begin{aligned}
\frac{d[H_2^+]}{dt} &= 0 = \zeta[H_2] - k_{3.16}[H_2^+][H] && (3.20)\\
\frac{d[H_3^+]}{dt} &= 0 = k_{3.16}[H_2^+][H_2] - k_{3.18}[H_3^+][e] - k_{3.17}[CO][H_3^+] && (3.21)\\
\frac{d[HCO^+]}{dt} &= 0 = k_{3.17}[CO][H_3^+] - k_{3.19}[HCO^+][e]. && (3.22)
\end{aligned}$$

In the equations above, the bracket [ ] represents the fractional abundance of the species and ζ is the ionization rate due to cosmic rays, x-rays and UV radiation. Rate constants for the reactions above $k_{3.16} - k_{3.19}$ are taken from the UMIST database for astrochemistry and are presented in Table 3.7. As discussed above, H_3^+ is very abundant in disks so that $[H_3^+]/[HCO^+] > 1$ and solution of equation 3.22 gives an upper bound to the electron abundance [e];

$$\frac{[e]}{[CO]} < \frac{k_{3.17}}{k_{3.19}}. \quad (3.23)$$

Table 3.7. Relevant reactions and rate coefficients, $k_r = \alpha\ (T/300)^{-\beta}$. Rate coefficients are from the UMIST database (Millar et al., 1997).

R1	R2	P1	P2	α	β
H_2^+	H_2	H_3^+	H	2.08×10^{-9}	0.0
H_3^+	CO	HCO^+	H_2	6.56×10^{-10}	0.5
H_3^+	e^-	H	H_2	1.15×10^{-7}	0.65
HCO^+	e^-	CO	H	2.00×10^{-7}	0.75

This results in an upper limit for the fractional ionization ([e]/[H_2]) of $\sim10^{-8}$, with an assumed H_2 column density of $N_{H_2} = 10^5\ N_{CO}$ (Qi et al., 2003).

Although we cannot use the observed HCO^+ abundances alone to establish the electron abundance, we can estimate the fractional ionization from our understanding of the ionization rates due to cosmic rays, X-rays and radioactive decay. The degree of ionization depends largely on the effectiveness of cosmic ray ionization of He and H_2 through the following reactions (Duley & Williams, 1984):

$$\begin{aligned} & He + CR && \rightarrow && He^+ && (3.24)\\ 2\% \quad & H_2 + CR && \rightarrow && H + H^+ + e^- && (3.25)\\ 10\% \quad & H_2 + CR && \rightarrow && 2H && (3.26)\\ 88\% \quad & H_2 + CR && \rightarrow && H_2^+ + e^- && (3.27)\end{aligned}$$

Nakano & Tademaru (1972) perform detailed calculations of cosmic ray ionization rates and find that the rate of ionization is $\zeta_{CR} = 6.1\times10^{-18}$ exp(-x/r) s^{-1},where r = 66 g/cm^2, and x is a measure of the surface density at depth h into the disk, defined by $x = \rho h$. Using this method they find that cosmic rays are quenched when the surface density approaches x=96 g/cm^3. This is much higher than the surface density of the outer disk, and thus cosmic rays are believed to be largely unattenuated in disks and a standard value of $\zeta_{CR} = 1.3 \times 10^{-17}$ s^{-1} per H atom is often used for the cosmic ray ionization rate beyond ~30 AU (Umebayashi & Nakano, 1981; Aikawa et al., 2002).

Nakano & Tademaru (1972) also calculate the ionization rate due to hard (E>1 keV) X-rays, via the relation,

$$\zeta_x = 1.9 \times 10^{-23} x^{-1.23} s^{-1}, \tag{3.28}$$

and find that ζ_x in disks is negligible compared to cosmic rays at depths beyond the very surface of disks, x < 0.03 g cm^{-3}. However, they do not consider the effects of secondary electrons in their calculation of the ionization rate. Upon inclusion of secondary electrons, Igea & Glassgold (1999) find that even at low stellar X-ray luminosities, 10^{29} erg s^{-1}, hard X-rays are important in the ionization

Table 3.8. HCO^+ Observations and estimated ionization rates and fractional ionization

Source	HCO^+/CO	R	ζ_X	$n_i/n_H(0)$	$n_i/n_H(IG)$
AA Tau	$6.7\pm3.1\times10^{-4}$	100	1×10^{-15}	7.63×10^{-9}	1×10^{-6}
AB Aur	$4.2\pm0.97\times10^{-5}$	250	2×10^{-16}	6.69×10^{-9}	2×10^{-7}
CQ Tau	$1.7\pm0.53\times10^{-3}$	67	7×10^{-16}[a]	4.47×10^{-9}	5×10^{-7}
DM Tau	$2.3\pm0.5\times10^{-3}$	425	8×10^{-17}	1.86×10^{-8}	4×10^{-7}
Haro 6-5B	$4.3\pm1.1\times10^{-4}$	100	3×10^{-16}[a]	2.12×10^{-8}	1×10^{-6}
MWC 758	$<2.3\times10^{-3}$	117	2×10^{-16}[a]	4.88×10^{-9}	2×10^{-7}
RY Tau	$<5.2\times10^{-3}$	78	2×10^{-15}	4.54×10^{-9}	1×10^{-6}

[a] L_X has not been measured for these sources, so $\log(L_X) = 29$ was assumed.

of disk material, penetrating deeper than Galactic cosmic rays and producing large ionization rates (ζ up to 10^{-12} s^{-1} at R=1 AU). The vertical penetration depth of the X-rays ($\sim10^{25}$ cm^{-2}) is comparable with the thickness of the disk at moderate radial distances (R$\sim$1-10 AU, depending on disk mass). Igea & Glassgold (1999) perform a full 3D calculation of X-ray transport and ionization in axially symmetric disks using a Monte Carlo method and find that the X-ray ionization rate is largely independent of disk surface density and mass and proportional to X-ray luminosity ($\zeta_x \propto L_X$) and to the inverse square of the disk radius ($\zeta_x \propto R^{-2}$) for any particular vertical column density. Since these models are calculated for $L_X = 10^{29}$ erg s^{-1} and $R = 1$ AU, the ionization rate for any X-ray luminosity and radius can be can be represented by

$$\zeta_x = \zeta_{IG}(N_T)\left(\frac{L_X}{10^{29}}\,\mathrm{ergs}^{-1}\right)\left(\frac{R}{1\;AU}\right)^{-2}, \tag{3.29}$$

where $\zeta_{IG}(N_T)$ is the ionization rate from Igea & Glassgold (1999), at the appropriate vertical column density (N_T). The X-ray ionization rates for the disks in our sample have been calculated in this manner and are shown in Table 3.8. Because molecular line emission from low-lying J states has been proven to arise from a warm layer near disk surfaces (van Zadelhoff et al., 2001; Qi et al., 2003), we assume that our observations probe such a layer and use $\zeta_{IG}(N_T) \approx 3\times10^{-12}$, the value at the disk surface at $R = 1$ AU. This is then scaled via the equation above to an appropriate radius depending on the disk size. The resulting X-ray ionization rates are much higher than the canonical value of $\sim10^{-20}$ s^{-1}, obtained via equation 3.28 using $x = 0.003$ g cm^{-2} for a depth of 50 AU, which corresponds to a density of $n_H = 10^6$ cm^{-3} in a typical disk. In fact, the X-ray ionization rates calculated here are larger than the Galactic cosmic ray ionization rate ($\zeta_{CR} = 2\times10^{-17}$ s^{-1}). Thus, hard X-ray emission from the central star is an important contributor to the ionization rate near the disk surface. This may additionally be enhanced by soft X-rays from the central star, although such low energy X-rays would likely be absorbed by any outflow activity near the stellar surface (Igea & Glassgold, 1999).

The effect of the increase in the X-ray ionization on the total fractional ionization can be calculated by evaluating the mechanisms for production and destruction of ions within the disk (see Nakano & Tademaru, 1972). We will consider the production of ions via cosmic ray ionization, using the methods of Nakano & Tademaru (1972) to calculate the cosmic ray ionization rates (ζ_{CR} = 6.1×10^{-18} exp(-x/66) s^{-1}) near the disk surface ($x = 0.007$ as above), and the production of ions via X-ray ionization using the rates calculated above by scaling the results of Igea & Glassgold (1999). Radioactive decay (of ^{26}Al, for example, $\zeta_R = 6\times10^{-18}$ s^{-1}, Umebayashi & Nakano, 1981) may also play an important role in ionization in disks, particularly near the disk midplane and so is also included. Ions can be destroyed through recombination on grain surfaces or radiative recombination (rate = σ_g v_s (n_g/n_H)) in the gas phase (2.08×10^{-11} $T^{-1/2}$ 0.5 n_e). Assuming equilibrium between ionization and recombination, the number of ions can be calculated using the equation,

$$n_i = \frac{\zeta_{CR}(x) + \zeta_R + \zeta_x(x)}{\sigma_g c_s \frac{n_g}{n_H} + 2.08 \times 10^{-11} T^{-1/2} \phi n_e}. \tag{3.30}$$

The grain cross-sectional area and the fractional abundance of grains are fixed at σ_g = 7x10^{-10} cm^2 and $n_g/n_H = 10^{-12}$. The product $\sigma_g n_g \approx 7\times10^{-22}$ can be assumed to be constant as grains coagulate and grow. The sound speed, c_s = (H/R)$\times\sqrt{GM_{cent}/R}$, is approximately the relative velocity of ions and grains, and is calculated using an aspect ratio (H/R) $\sim$0.12, typical of circumstellar disks (i.e., D'Alessio et al., 2001) at the radii probed by our observations, as indicated in Table 3.8. Radiative recombination is proportional to n_i^2, so as n_i decreases, this process becomes less important relative to recombination on grain surfaces, and can be ignored for $n_i/n_H < 10^{-5}$ (Nakano & Tademaru, 1972). Therefore, we consider only the effects of grain surface recombination.

Using the method described above, we calculate the ionization fraction at the appropriate radii in each disk, both with the standard X-ray ionization rate calculated by Nakano & Tademaru (1972) and the increased X-ray ionization rates from Igea & Glassgold (1999). The resulting ionization fractions, shown in Table 3.8, are larger by a factor of 10^{2-3} when $\zeta_x(IG)$ is used. From these calculations it can be seen that the inclusion of ionization by the secondary electrons produced from X-rays can have a large impact on the ionization rate in the outer regions of disks.

3.6 Nitrogen chemistry: CN, HCN and HNC

As discussed above, protonation of atomic carbon and oxygen by H_3^+ initiates the production of most C- and O-bearing molecules, when starting with largely atomic gas. However, because the protonation of N by H_3^+ is endothermic and the reaction

$$H_3^+ + N \rightarrow NH_2^+ + H \tag{3.31}$$

possesses a significant activation energy (Herbst et al., 1987), nitrogen atoms are expected to be more abundant than ionized nitrogen, resulting in a very different chemistry than that of O and C (as described by Pineau des Forets et al. (1990) and shown in Figure 3.2). The production of N_2 occurs via the following radical-radical reactions:

$$\begin{aligned} N + OH &\rightarrow NO + H & (3.32) \\ N + NO &\rightarrow N_2 + O, & (3.33) \end{aligned}$$

with reaction 3.33 proceeding at a temperature-dependent rate of 8.2×10^{-11} exp(-410/T) cm^3/s (Prasad & Huntress, 1980) or a rate of 3.4×10^{-11} cm^3/s at $200 \leq T \leq 400$ K (Langer & Graedel, 1989). Subsequent ionization or protonation of NO and N_2 leads to the production of NH_3 and N_2H^+, which are frequently observed in molecular clouds. Alternately, atomic nitrogen may react with CH and CH_2 to form CN and HCN,

$$\begin{aligned} N + CH &\rightarrow CN + H & (3.34) \\ N + CH_2 &\rightarrow HCN + H. & (3.35) \end{aligned}$$

Rates of $k_{3.34} = 2.1\times10^{-11}$ cm^3/s (at T = 298 K; Smith 1988) and $k_{3.35} = 2.0\times10^{-11}$ $(T/300K)^{1/2}$ cm^3/s (Prasad & Huntress, 1980) have been measured in the laboratory for these reactions, although abundances of NH_3, CN and HCN in molecular clouds are best reproduced by introducing a small barrier to these rate coefficients (Pineau des Forets et al., 1990). The abundances of carbon-bearing nitrogenated molecules are thus partially dependent on the C/O ratio in the gas. Ion-atom reactions also play a role in the nitrogen chemistry. The inclusion of reactions of atomic nitrogen with the methyl cation ($k = 6.70 \times10^{-11}$ cm^3/s),

$$\begin{aligned} N + CH_3^+ &\rightarrow HCN^+ + H_2 & (3.36) \\ N + CH_3^+ &\rightarrow HCNH^+ + H, & (3.37) \end{aligned}$$

rapidly leads to the production of CN and HCN through electron recombination reactions (at rates of 1.50×10^{-7} cm^3/s and 1.75×10^{-7} cm^3/s for CN and HCN, respectively; Figure 3.2). The primary production mechanism for HNC is believed to be dissociative recombination of $HCNH^+$, competing with the production of HCN at a similar rate ($k_{3.38} = 1.75\times10^{-7}$ cm^3/s),

$$HCNH^+ + e^- \quad \rightarrow \quad HNC + H_2. \tag{3.38}$$

The abundance of HNC is thus a good tracer of the importance of the CH_3^+ pathway for formation of CN and HCN, and the detection of significant amounts of HNC in circumstellar disks (HNC/HCN $\sim$0.4 for DM Tau (Dutrey et al., 1996) and $\sim$0.6 for TWHya (Kastner et al., 1997), indicates that formation of CN and HCN through ion-molecule chemistry cannot be neglected.

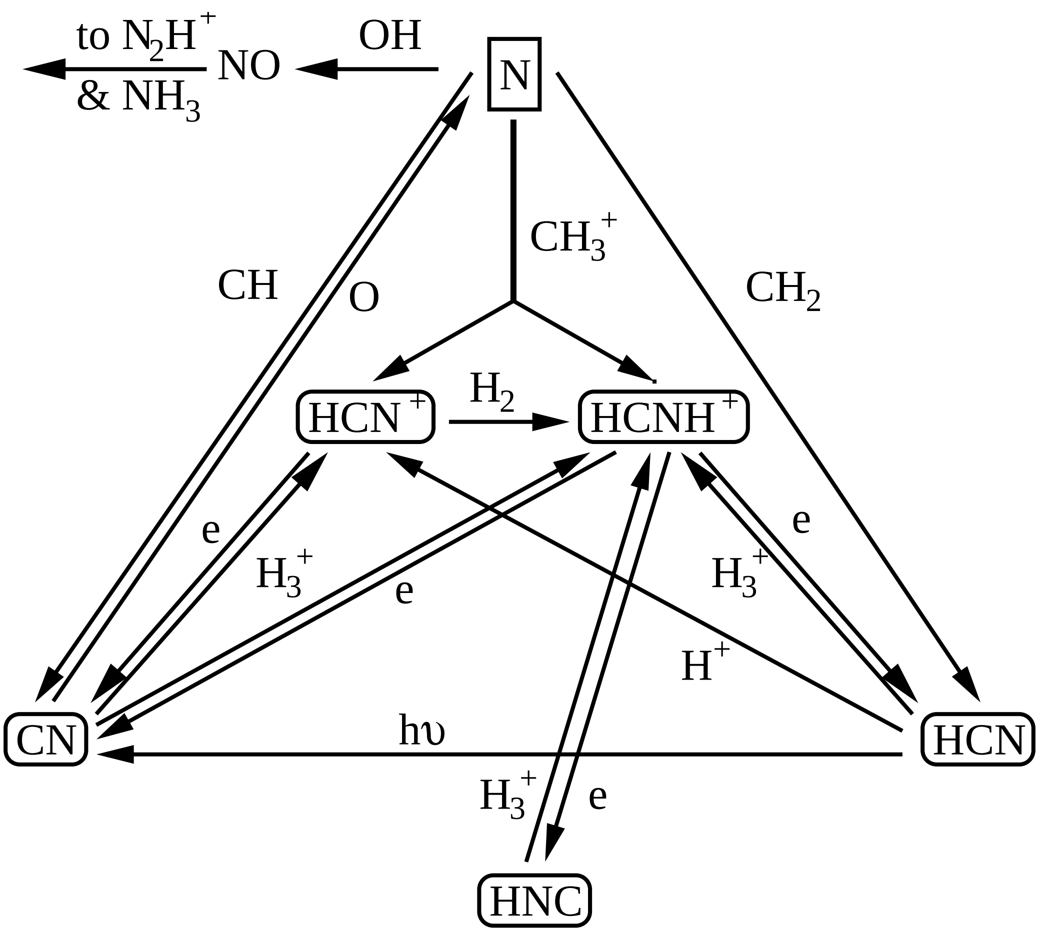

Figure 3.2 A graphical summary of the nitrogen chemistry in protoplanetary disks, adapted from Pineau des Forets et al. (1990) and Willacy & Langer (2000).

CN, HCN and HCN have been observed in several molecular clouds (Turner et al., 1997), planetary nebulae (Bachiller et al., 1997), AGB stars (Johansson et al., 1984) and photodissociation regions (PDRs; Fuente et al., 1993) as well as two protoplanetary disks, TW Hya (Kastner et al., 1997) and DM Tau (Dutrey et al., 1997). In all cases, the abundances of these molecules appear to be sensitive to variations in temperature and UV flux. From these observations, and chemical models developed to interpret them, the following trends have been noted. The HNC/HCN ratio appears to be fairly stable from source to source. In studies of 27 translucent molecular clouds, Turner et al. (1997) find a typical HNC/HCN ratio of ∼0.17–0.4, which is similar to that found for the pNe CRL 618 (HCN/HNC∼1.0; Bujarrabal 1988) and for protoplanetary disks. Observations of the PDR NGC 7023 by Fuente et al., 1993, show that HNC/HCN ranges from 0.2 nearest to the star to ∼1 farthest from the stellar position. Models suggest even stronger variations with temperature and UV flux; HNC/HCN decreases by 5 orders of magnitude from $A_V = 10$ to 6 mag at constant temperature, T = 30 K, or from 15 to 50 K at constant A_v (of 10 mag). Models of PDRs suggest that HCN and HNC should both decrease with increasing kinetic temperature, because rates of reactions producing N_2 and NH_3 increase, reducing the supply of atomic N. In regions with larger UV fields, production of both HNC and HCN should increase due to increased production of hydrocarbons. The destruction of both HNC and HCN should also *increase* with increasing UV fields, via the reactions

$$HCN + H^+ \rightarrow HCN^+ + H \tag{3.39}$$

$$HNC + H \rightarrow HCN + H. \tag{3.40}$$

Because the destruction of HNC results in the production of HCN, the HNC/HCN ratio is expected to decrease in regions with enhanced UV fields, as is indicated by the observations discussed above. However, observations of comet Hale Bopp indicate that HNC increased near perihelion (Charnley et al., 2002), which the authors explain by the reverse of reaction 3.40 driven by suprathermal H atoms produced via the UV photodissociation of water.

Fuente et al. (1993) show that the CN/HCN ratio is strongly enhanced in regions of moderate UV fields, increasing by a factor of 15 from $A_V = 10$ mag to $A_V = 6$ mag in PDRs, but is relatively insensitive to temperature, remaining constant from T = 15–50 K for $A_V = 10$ mag. This is because increases in temperature affect the abundances of CN and HCN in the same manner, whereas HCN is much more sensitive than CN to changing UV fields. Higher temperatures lead to increases in the abundance of oxygenated molecules (HCO^+, CO, CO_2) relative to CH, CH^+ and C_2H. Thus, N atom reactions with OH lead more efficiently to N_2 and NH_3 than CN, HCN and HNC, proceeding off to the left in Figure 3.2, and the production of CN, HCN and HNC decreases. CN increases with increasing UV field, but decreases with increasing temperature. At low UV fields, the situation is similar, due to low abundances of C and C^+. At moderate UV fields ($A_V = 6$–8 mag with $G_0 = 2{\times}10^3$), C and C^+ abundances increase, stimulating hydrocarbon chemistry, and N reacts with C bearing molecules instead of OH to produce substantial amounts of CN, HCN and HNC. However, HCN and HNC are also destroyed by reaction with H^+ and C^+ (CN is destroyed by reaction with O and N), thus their abundances are not as high as CN in these regions. The observed enhancement in the CN/HCN ratio can therefore be explained by the decrease in the HCN abundance in regions exposed to moderate UV fields. Additionally, the relative abundance of CN versus HCN is affected by the relative photodestruction rate of HCN (producing CN) and the photodestruction of CN itself in the presence of UV radiation. The dissociation energy of CN is higher than that of HCN, requiring photons of shorter wavelengths for dissociation, <1150 Å for CN (Nee & Lee, 1985) and near 1216 Å for HCN (Nuth & Glicker, 1982). Photons of shorter wavelengths are more efficiently absorbed or scattered by dust, an effect that has also been used to explain the dominance of CN over HCN (CN/HCN $\approx$ 10) in planetary nebulae (Cox et al., 1992), with models of such nebulae estimating that the effective photodissociation rate of CN is smaller than that of HCN by a factor of 2–3.

It is evident from the discussion above that both the CN/HCN and HNC/HCN ratios are greatly affected by UV radiation. Due to the flared geometry of protoplanetary disks, the overall UV field of the outer disk is a combination of stellar and interstellar radiation fields (ISRF). Typical disk models assume a stellar FUV flux of 10^4 times higher than the ISRF at 100 AU (Willacy & Langer, 2000; Aikawa & Herbst, 2001). Radiative transfer calculations of the relative contributions of the interstellar and stellar radiation fields have been performed (van Zadelhoff et al., 2001, Aikawa et al., 2002) and find that the stellar radiation field, in particular continuum FUV radiation, is most important in disk surfaces. Using a protoplanetary disk model with a typical T Tauri star SED and stellar parameters ($M_* = 0.5\ M_\odot$, $R_* = 2\ M_\odot$, $T_* = 4000$ K, $\dot{M} = 3\times10^{-8}\ M_\odot$/yr), Bergin et al. (2003) follow the transport of FUV radiation through the disk using an analytical approximation which includes both scattering and pure absorption by dust grains of sizes 0.005 μm – 1 mm. They find that the stellar radiation dominates over interstellar radiation in the upper 30 AU of the disk and decreases with decreasing height, becoming equally or less important than the interstellar radiation in the disk midplane largely due to the contribution of strong Lyman α emission lines to the stellar FUV radiation field. These lines, however, are difficult to observe due to severe extinction by the large quantities of dust and atomic gas present in the molecular clouds in which T Tauri stars form. The impact of variations in Ly α flux versus CN/HCN is therefore difficult to verify observationally.

The effective UV field in disk surface layers is also largely dependent on the attenuation by dust grains in the surface layers of the circumstellar disk. As dust grains grow, they decouple from the gas and sink to the disk midplane. Both grain growth and sedimentation enhance the effective radiation field by decreasing the total grain cross section. This then leads to increases in the photodissociation and photoionization as discussed above, likely resulting in enhanced CN to HCN abundances. Aikawa & Herbst (1999) model this decrease in dust shielding at R = 700 AU and t = 3×10^5 yr by increasing the hydrogen column density corresponding to $A_V = 1$ mag to 1.8×10^{22} cm^2, an order of magnitude larger than in the standard ISM. This effectively increased the UV field and resulted in decreases in the CO, CN, HCN and HNC column densities by factors of 4.4, 2.1, 2.4 and 2.3, respectively. In contrast to the reasoning above, the CN/HCN ratio did not change significantly, although the HCO^+ column density was found to increase by a factor of 2.2,

Table 3.9. Column densities of observed molecules, assuming optically thin emission in LTE.

Source	$N_T(CO)^a$	$N_T(HCO^+)$	$N_T(CN)$	$N_T(HCN)$	$N_T(HNC)$
AA Tau	$2.09\pm0.58\times10^{16}$	$1.40\pm0.50\times10^{13}$	$<3.89\times10^{14}$	$<2.74\times10^{13}$	$1.14\pm0.29\times10^{13}$
AB Aur	$3.99\pm0.11\times10^{17}$	$1.67\pm0.39\times10^{13}$	$5.29\pm0.40\times10^{14}$	$<6.27\times10^{12}$	$<1.39\times10^{13}$
CQ Tau	$1.29\pm0.36\times10^{16}$	$2.27\pm0.28\times10^{13}$	$<6.26\times10^{14}$	$4.65\pm1.6\times10^{13}$	$<7.37\times10^{13}$
DM Tau	$1.76\pm0.11\times10^{16}$	$4.14\pm0.82\times10^{13}$	$<1.30\times10^{14}$	$<4.58\times10^{13}$	$<2.36\times10^{13}$
Haro 6-5B	$2.13\pm0.08\times10^{16}$	$9.12\pm2.3\times10^{12}$	$<2.29\times10^{14}$	$6.71\pm1.8\times10^{12}$	$<3.83\times10^{12}$
MWC 758	$1.14\pm0.11\times10^{16}$	$<2.62\times10^{13}$	$<2.46\times10^{14}$	$<7.05\times10^{13}$	$<3.57\times10^{13}$
RY Tau	$9.18\pm1.2\times10^{15}$	$<4.78\times10^{13}$	$6.99\pm2.3\times10^{13}$	$3.73\pm1.4\times10^{13}$	$<4.12\times10^{13}$

[a] $N_T(CO)$ are lower limits, as it is likely that $\tau(CO) \not\ll 1$ (van Zadelhoff et al., 2001); CO column densities calculated from ^{12}CO and ^{13}CO have been observed to differ by up to 2 orders of magnitude (Qi et al., 2003).

supporting the above scenario.

Based on the discussion above, we expect the observed CN, HCN and HNC abundances to be related to the effective stellar and interstellar radiation fields near the disk surface. In order to investigate this relationship, we search for correlations of the observed CN and HCN abundances with tracers of disk and stellar structure, including stellar luminosity (temperature), fractional IR luminosity (L_{IR}/L_{bol}; disk flaring and optical depth), the height of the dust photosphere versus the gas scale height (dust settling) and X-ray luminosity (L_X; ionization fraction). The results of these studies are presented in Table 3.10 and described below.

3.6.1 Gas temperature, stellar UV and L_*

The stellar luminosity L_* has an impact on disk chemistry through its effect on the temperature of the gas and through the its relationship with the stellar UV field. L_* is defined as the flux F summed over the solid angle (Ω) subtended by the star,

$$L = \int F d\Omega = 4\pi r^2 F \tag{3.41}$$

$$F(T) = \frac{2h\nu^3/c^3}{exp(h\nu/kT) - 1}, \tag{3.42}$$

where $F(T)$ is the stellar blackbody flux at temperature T, h is the Planck constant, k is the Boltzmann constant, c is the speed of light and ν is the frequency of the radiation. At the frequencies observed here, $\nu \sim 100$ GHz, $h\nu/kT$ is small ($\ll$1), the Raleigh-Jeans approximation holds and the flux is directly related to the stellar temperature $[F(T)\approx\frac{2\nu^2}{c^2}\, kT]$. Most models indicate temperature distributions which decrease as a function of distance from the star as T $\propto \frac{1}{\sqrt{R}}$. For a star of T = 1000 – 10000 K, the Wein law is applicable in the UV ($h\nu\gg kT$), such that the stellar UV flux

Table 3.10. Abundance ratios and physical parameters.

Source	CN/CO	CN/HCN	HNC/HCN	L_{star}	L_{IR}/L_{bol}	H/h
AA Tau	$<1.9\times10^{-2}$	...	>0.41	1.5	0.15	3.8
AB Aur	$2.8\pm0.2\times10^{-3}$	>84	...	53.6	0.37	...
CQ Tau	$<4.8\times10^{-2}$	<13	<0.44	8.0	0.50	5.0
DM Tau	$<7.4\times10^{-3}$	...	...	0.25	0.16	...
Haro 6-5B	$<1.1\times10^{-2}$	< 34	<0.57	...	0.02	...
MWC 758	$<2.1\times10^{-2}$	...	...	20.6	0.75	1.5
RY Tau	$7.6\pm2.7\times10^{-3}$	1.9±0.9	<1.1	16.7	0.65	...
LkCa 15	2.55×10^{-4}	10.2	<0.22	0.724	0.11	1.0
GM Aur	7.73×10^{-5}	1.89	...	0.741	0.11	2.0
HD 163296	1.74×10^{-4}	>17.17	...	35.2	0.16	1.7
MWC 480	1.12×10^{-3}	4.07	...	32.4	...	4.0
TW Hya	7×10^{-4}	8	<0.6	0.25	0.3	5.6
DM Tau	2.3×10^{-4}	5.8	0.44	0.16	0.25	3.4

Note. — Observations presented in the first half of the table are from this survey and those in the second half of the table come from the literature (with CO abundances calculated from ^{13}CO and $C^{18}O$ column densities, when available). Values for LkCa 15, GM Aur, HD 163296, MWC 480 were obtained at OVRO by Qi (2001). Observations of TW Hya were taken at the JCMT 15m telescope (Kastner et al., 1997). The DM Tau ratios presented in the second half of the table are from Dutrey et al. (1997) obtained with the IRAM 30m telescope.

increases exponentially with the stellar temperature ($F(T) = \frac{2h\nu^3}{c^2}exp(\frac{-h\nu}{kT})$). Thus, the stellar luminosity should have a large impact on both the temperature of and the stellar UV field at the disk surface.

The CN/CO, HCN/CO and HCO^+/CO abundances as a function of stellar luminosity (L_*) for the sources in this sample are shown in Figure 3.3. For comparison, values for other disks for which CN, HCN and HCO^+ have been observed are also included; these include two T Tauri and two Herbig Ae disks from Qi (2001), LkCa 15, GM Aur, HD 163296 and MWC 480, the nearby T Tauri star TW Hya (Kastner et al., 1997). DM Tau, which is a T Tauri star in our sample, has also been observed with the IRAM 30 m telescope (Dutrey et al., 1997) and the observed abundance ratios are also included here. The abundances are shown relative to CO to remove dependence on the gas mass in the emission region. Although CO is not an effective tracer of the total disk mass, it is a reasonable measure of the mass in disk surface layers to which we are sensitive (see Chapter 2). The observed ratios show no correlation with the stellar luminosity, although they all have similar distributions. This indicates that at the large radii probed by millimeter observations ($R > 70$ AU), the stellar UV radiation field may not penetrate sufficiently to have a large impact on disk chemistry. This indicates that the interstellar radiation field is very important in photochemical processes in the outer disk, as concluded by Willacy & Langer (2000) in chemical models of disks including the effects of photoprocessing in disk surface layers.

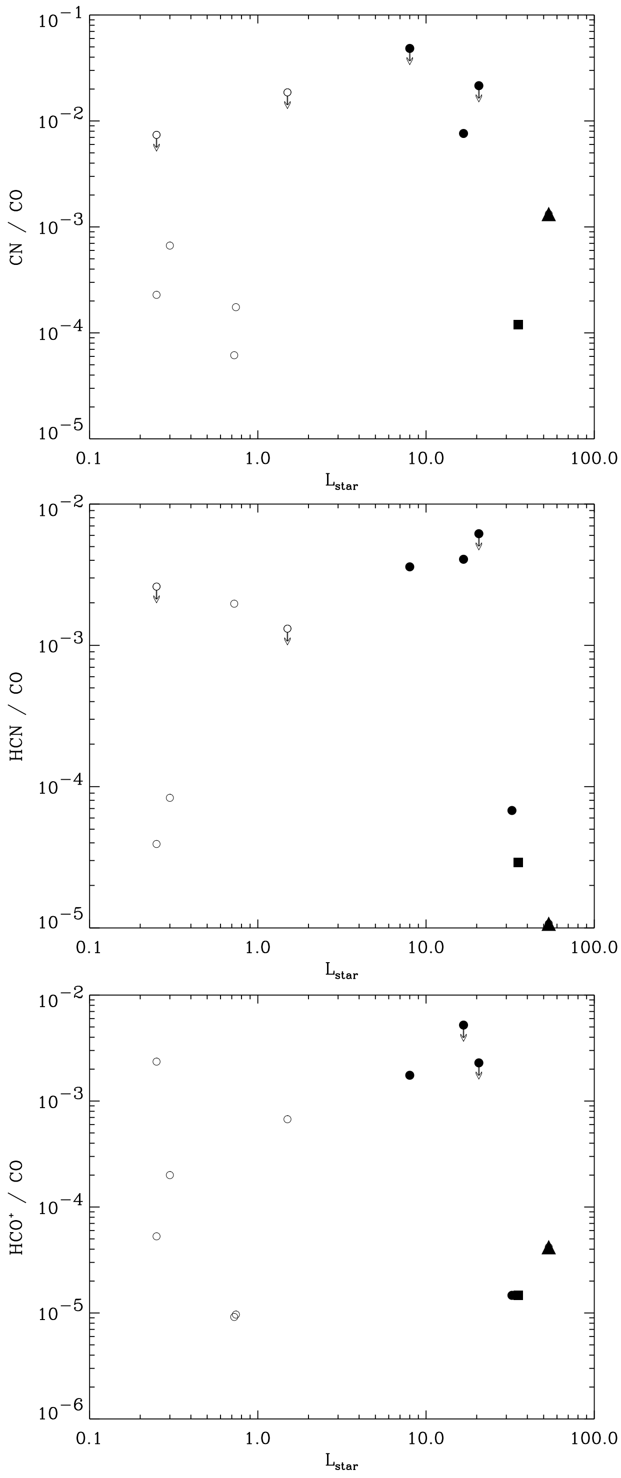

Figure 3.3 CN/CO, HCN/CO and HCO^+/CO abundances shown as a function of stellar luminosity (L_*) for all sources observed in this survey (open circles). For comparison, values for other disks are included; LkCa 15, HD 163296, GM Aur, MWC 480 (Qi, 2001) are plotted as filled circles, TW Hya (Kastner et al., 1997) is plotted as a filled triangle and the single dish observation for DM Tau (Dutrey et al., 1997) is plotted as a filled square.

3.6.2 Disk flaring and L_{IR}/L_{bol}

Dust in the circumstellar disk absorbs stellar radiation and re-radiates it in the IR, such that the luminosity integrated over all wavelengths, or the bolometric luminosity, is a sum of the stellar and reprocessed radiation:

$$L_{bol} = 4\pi d^2(F_{star} + F_{IR}) \tag{3.43}$$

The fractional IR luminosity L_{IR}/L_{bol} is thus proportional to the solid angle intercepted by the disk as seen from the star and can be used as a measure of disk flaring (Kenyon & Hartmann, 1995). For YSOs inclined with respect to the observer, the "shadowing" of the star by the disk and foreshortening of the disk must be taken into account. Radiation from the disk decreases as cos i (where i = 0 if edge-on). For any disk around a star, the ratio of disk to total flux (disk + star) must be larger than 0.3 (around 0.45) for i = 0, $f_* = 0$ and 0.37 for i = 60, $f_* = 0.29$. At all inclinations $L_{tot} > L_{star}$. While an infinite flat and "passive" disk absorbs and reradiates ∼25% of the stellar flux, "thick" or "flaring" disks with finite scale heights reprocess ∼30%–40% of the stellar flux. In a large photometric survey of T Tauri stars, Kenyon & Hartmann (1987) find that weak line T Tauri stars, with optically thin disks, have L_{IR}/L_{bol} <0.1, while most class II sources possess $L_{IR}/L_{bol} \approx$ 0.0–0.3. This is a bit higher than that of a random collection of flat reprocessing disks for which $L_{IR}/L_{bol} = 0.05$ and is suggestive of flared disks (L_{IR}/L_{bol}=0.13). Stars embedded in a spherical envelope of dust, possess much larger fractional IR luminosities $L_{IR}/L_{bol} > 0.8$ (most > 0.9).

Plots of the correlation of L_{FIR}/L_{bol} with CN, HCN and HCO^+ abundances relative to CO are shown in Figure 3.4. A weak correlation between the CN/CO and HCO^+/CO ratios and the fractional IR luminosity is visible, with the abundances increasing as a function of the IR luminosity. However, there appears to be no correlation between the HCN/CO ratio and L_{FIR}/L_{bol}. If it is assumed that increased flaring corresponds to increasing the exposure to UV radiation, then this can be explained by the PDR model presented by Fuente et al. (1993) and discussed above in which increased UV fields lead to increased formation of C^+ and C (and thus HCO^+). This in turn leads to an increase in the production of CH and CH_2, and thereby CN and HCN. The increase in HCN production, however, is restricted by an increase in the destruction of HCN through reaction with C^+ and H^+.

3.6.3 Dust settling and H/h

Hydrostatic, radiative equilibrium models (Chiang & Goldreich, 1997) indicate that "passive," flared disks can account for the magnitude of the far-infrared luminosity and the flat shape of SEDs of typical T Tauri stars. In these models, the dust in the disk surface absorbs stellar radiation and re-radiates at IR wavelengths, as discussed above. Approximately half of this reprocessed radiation is directed into space and half radiates into the disk, heating the gas and dust in the surface, and

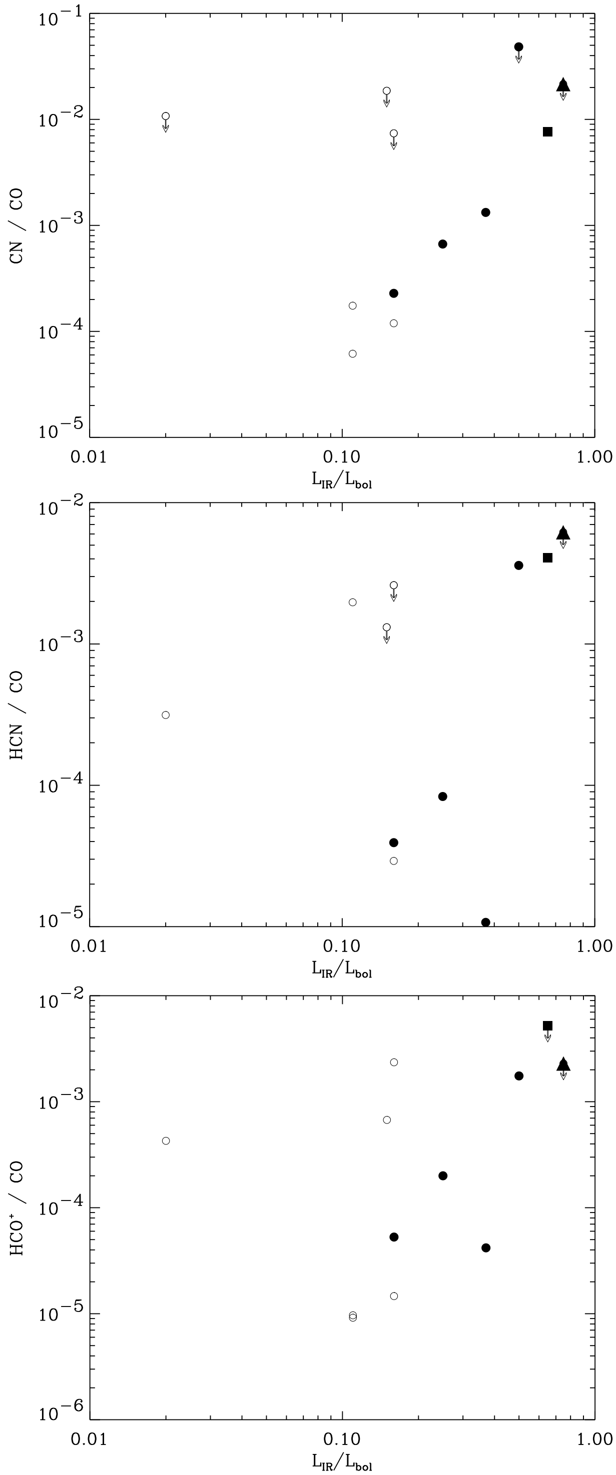

Figure 3.4 CN/CO, HCN/CO and HCO^+/CO abundances shown as a function of the fractional luminosity L_{IR}/L_{bol} Points are labeled as in Figure 3.3.

causing the disk to flare. Due to the flared geometry, the surface material is exposed to more stellar radiation and the SED remains flat at longer wavelengths. This can be expressed mathematically as

$$\begin{aligned} 4\pi d^2 \nu F_\nu &\approx \alpha L_* && (3.44)\\ &\approx \left[\left(\frac{d\,ln\,H}{d\,ln\,a} - 1\right)\frac{H}{a} + \frac{R_*}{a}\right]\frac{L_*}{2}, && (3.45) \end{aligned}$$

where α is the angle at which the stellar radiation strikes the surface of the disk, H is the vertical height of the visible disk photosphere (superheated surface region) above the disk midplane and a is the radial distance to the disk rotation axis. If we assume that the dust-to-gas ratio is uniform throughout the disk, then the height of the disk photosphere (H) and the scale height of the gas (h; defined by the condition of hydrostatic equilibrium) can be related through the equation

$$\frac{H}{h} = \left[2ln\left(\frac{n_0}{n_{ph}}\right)\right]^{1/2}, \tag{3.46}$$

which represents the number of gas scale heights that the visible photosphere sits above the disk midplane. Chiang et al. (2001) systematically explore the dependence of SEDs on grain size distributions, disk geometries and surface densities, and stellar photospheric temperatures and find that this is the most robust parameter in their model.

H/h can be directly related to dust settling. For a disk in which gas and dust are well mixed in interstellar proportions, $H/h \approx 4$–5 (Chiang & Goldreich, 1997). As dust settles, the height of the photosphere H decreases faster than the gas scale height and H/h also decreases. For a dust grain of size r and mass density $\rho_p = 2$ g/cm^3, the timescale for sedimentation from height $z = 4h$ to height $z = 1h$ is (Creech-Eakman et al., 2002)

$$\begin{aligned} t_{settle} &\approx 0.1 \quad \frac{\Sigma}{\rho_p r \Omega} && (3.47)\\ &\approx 10^5 \quad \left(\frac{0.1\mu m}{r}\right)\left(\frac{\Sigma_0}{300gcm^{-2}}\right)\left(\frac{2M_\odot}{M_*}\right)^{1/2} yr, && (3.48) \end{aligned}$$

where Σ_0 is the surface density and Ω is the local orbital angular frequency of disk material. Thus, for the outer radii of disks ($\Sigma_0 \sim$ 1–10 g cm^{-2} for R = 100 AU; D'Alessio et al., 2001) surrounding stars in the 1–3 $M_\odot$ range, the timescale for grains to spiral into the midplane of a disk is 10^5 yr for 1 μm particles and $\sim$ 100 yr for 1 cm particles. The stars in the sample studied here have ages of $\sim$1–10 Myr and thus we can expect that some growth and sedimentation have occurred.

SEDs for seven of the stars in this sample have been modeled using the Chiang & Goldreich method (Chiang et al., 2001; Chiang & Goldreich, 1997; and private communication), the resulting H/h values are shown in Table 3.10. There is a large range in H/h for our sample, with LkCa 15 ($H/h = 1.0$) and CQ Tau ($H/h = 5.0$) representing the two extremes in which the dust has settled

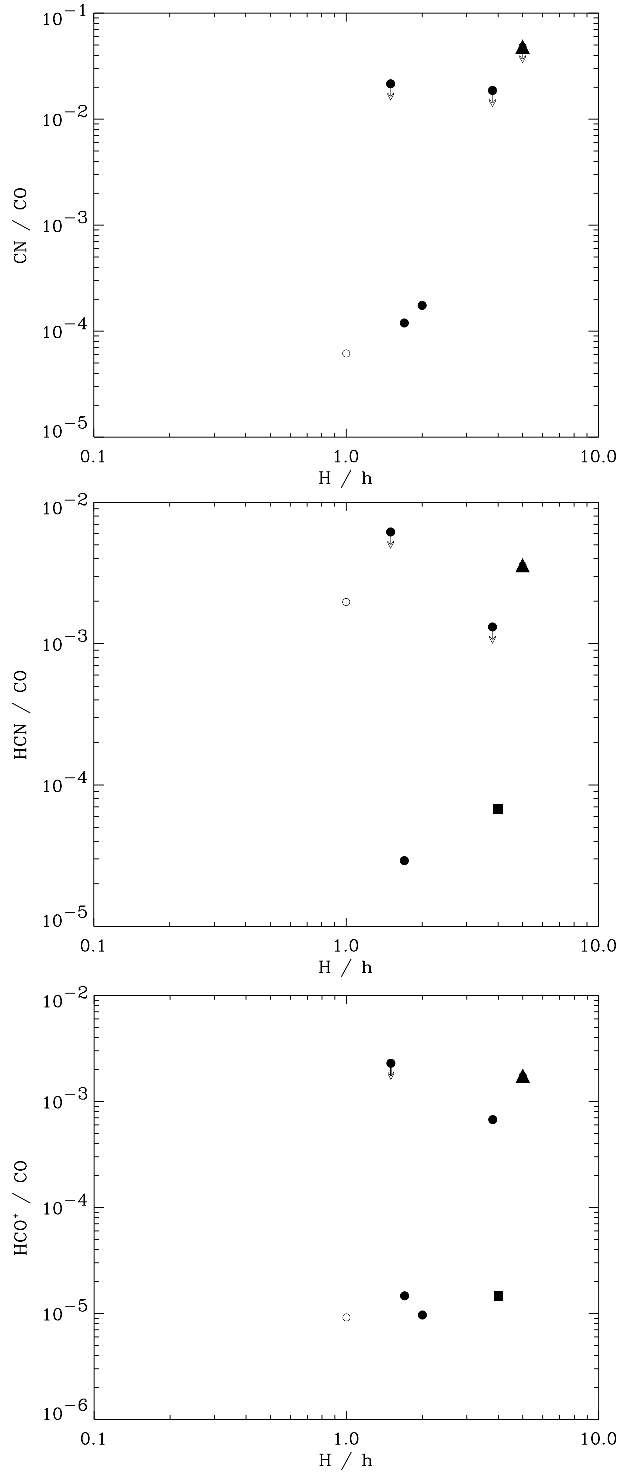

Figure 3.5 CN/CO, HCN/CO and HCO^{+}/CO abundances shown as a function of the number of scale heights that the visible disk photosphere sits above the disk midplane (H/h). Points are labeled as in Figure 3.3.

to the midplane ($z = 1$) and where the gas and dust are uniformly mixed, respectively. As discussed above, the production of CN, HCN and HCO^+ should be tied to the effective UV field. As dust settles to the disk midplane, the effective UV field is enhanced due to reduced shielding by the dust. To explore this relationship, the fractional abundances of CN, HCN and HCO^+ (relative to CO) are plotted versus the modeled H/h dust settling parameter in Figure 3.5. Due to the small sample of sources for which the observed molecules were detected and H/h values have been calculated, a trend is difficult to establish. However, the distribution of the fractional CN and HCO^+ abundances with H/h appear to be quite similar, and quite different than that of HCN. This is similar to what was noted for the fractional IR luminosity L_{IR}/L_{bol} relations and suggests that both quantities are in fact tracing enhanced effective UV fields in the disk.

3.7 Summary

In this study, the J = 1-0 transitions of CO, CN, HCN, HCO^+ and HNC were observed toward protoplanetary disks surrounding several T Tauri and Herbig Ae stars. The CO and continuum measurements were used to constrain the inclination and radial extent of the disks, but because of the low spatial resolution of the observations (4–5″), there are large errors associated with these estimates. It can be stated firmly, however, that the emission from the gas extends to larger radii then that of the dust, as the dust emission was consistently found to be unresolved for all disks in contrast to the CO 1-0 emission. This is likely due to a more rapid fall-off in dust emissivity, and not an absence of dust, at large radii (Sargent & Beckwith, 1987, Qi et al., 2003). The abundances of CO in these disks were found to be consistent with previous observations. The CO and continuum observations were used to calculate the disk gas and dust masses, respectively. Although the gas masses were reasonably consistent with previous observations, the dust masses are consistently too small. This could be due to an observational effect, such as beam dilution, or to variations in the dust opacity, which will have a large effect at the long wavelengths ($\kappa \propto \nu^\beta$; we assumed $\beta \approx 1$). Calculations of the electron fraction for these disks indicated that inclusion of X-ray ionization rates which account for ionization by secondary electrons increases the fractional ionization by 10^{2-3}. Upper limits calculated from the observed HCO^+ emission do not put significant constraints on the ionization fraction, indicating the importance of other ions, such as H_3^+ and N_2H^+ in disk surfaces.

The effects of UV fields were measured in the disks from observations of CN, HCN and HCO^+. Although CN and HCN are produced in a similar manner, through reactions of N with neutral and ionic hydrocarbons, CN is destroyed through neutral-neutral reactions, while HCN is destroyed by ion-molecule chemistry and UV photolysis. An increase in the effective UV field results in increased photoionization, and photodissociation, which in turn leads to increased production of HCO^+, CN and HCN. The increase in HCN production, however, is moderated by a coincident increase in

HCN destruction, while the destruction rate of CN remains constant (or decreases). Observations of the CN/HCN ratio should therefore trace the strength of the effective UV field at disk surfaces, with increased CN/HCN corresponding to stronger UV fields. This has been found to be true in molecular clouds and photodissociation regions. In the work presented here, CN, HCN, HNC and HCO^+ were observed toward several circumstellar disks. CN and HCO^+ were found to be (at least weakly) correlated with tracers of the effective UV field; abundances of both molecules increased with increases in the fractional IR luminosity and the dust settling parameter H/h. HCN, on the other hand, did not appear to be correlated with these or other disk parameters, likely due to the complexity of the reaction network for this molecule. Surprisingly, no molecular abundances appeared to be correlated with stellar parameters, such as L_{star}. This may indicate that in the outer regions of disks (R $>$ 70 AU) probed by these observations the interstellar radiation field has a much larger effect on the chemistry than the stellar UV field. HNC is produced and destroyed via ion-molecule reactions and thus is expected to be a very good probe of ion-molecule chemistry in disk surfaces. Unfortunately, HNC was only detected toward one source in our sample and a statistical analysis could not be performed, but observations of HNC with more sensitive instruments may prove to be very valuable to improving the understanding of nitrogen chemistry in disks.

The Owens Valley Radio Observatory is supported by the National Science Foundation, AST 9981546. J.E.K. was sponsored by the NASA Graduate Student Researchers Program, NGT5-50231.

3.8 Appendix: Integrated intensity maps and spectra for the observed molecules.

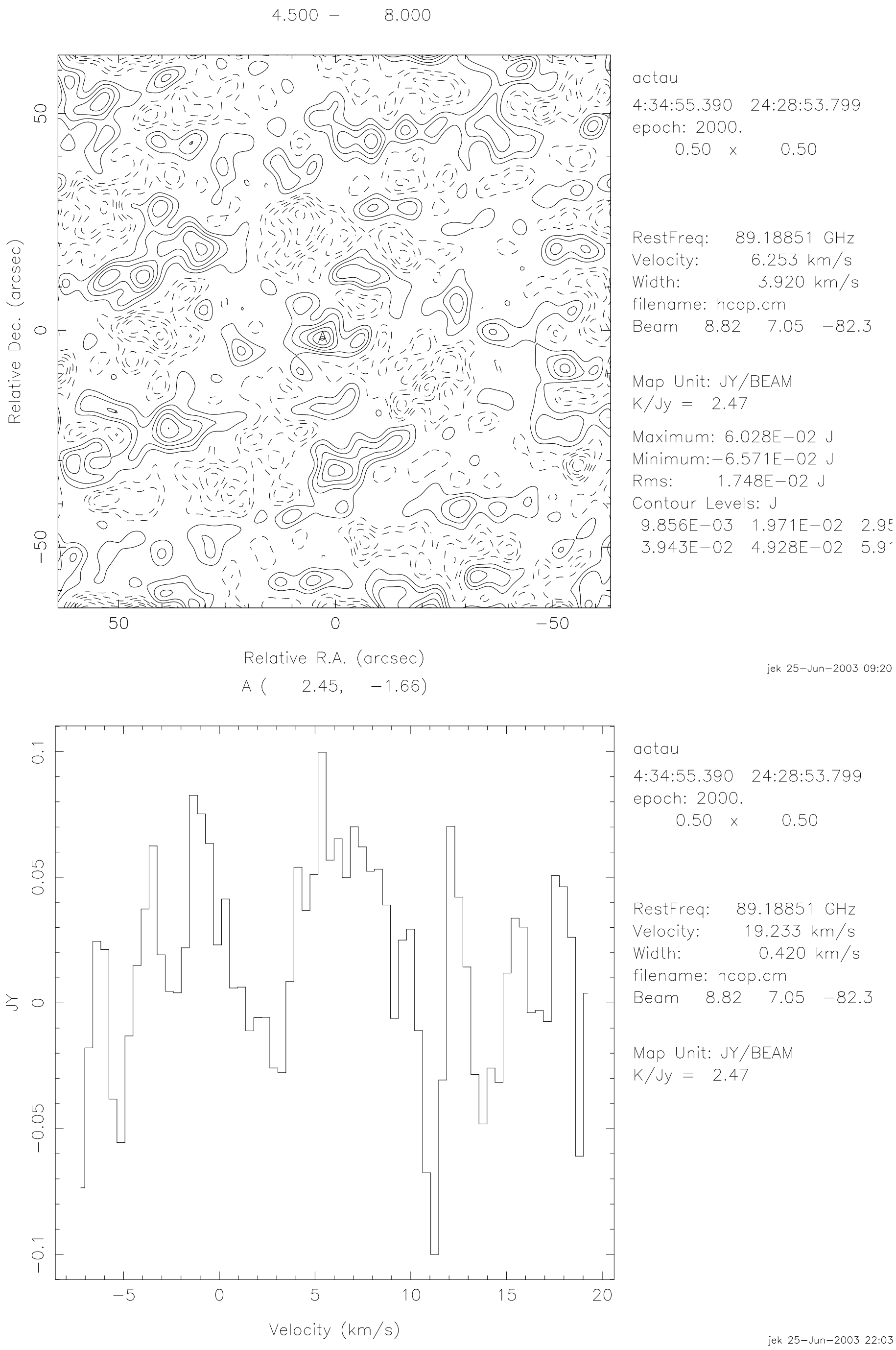

Figure 3.6 HCO^+ 1-0 observations toward AA Tau. Although the spectrum is a bit noisy, the moment 0 map shows strong HCO^+ 1-0 emission peaking at the stellar position.

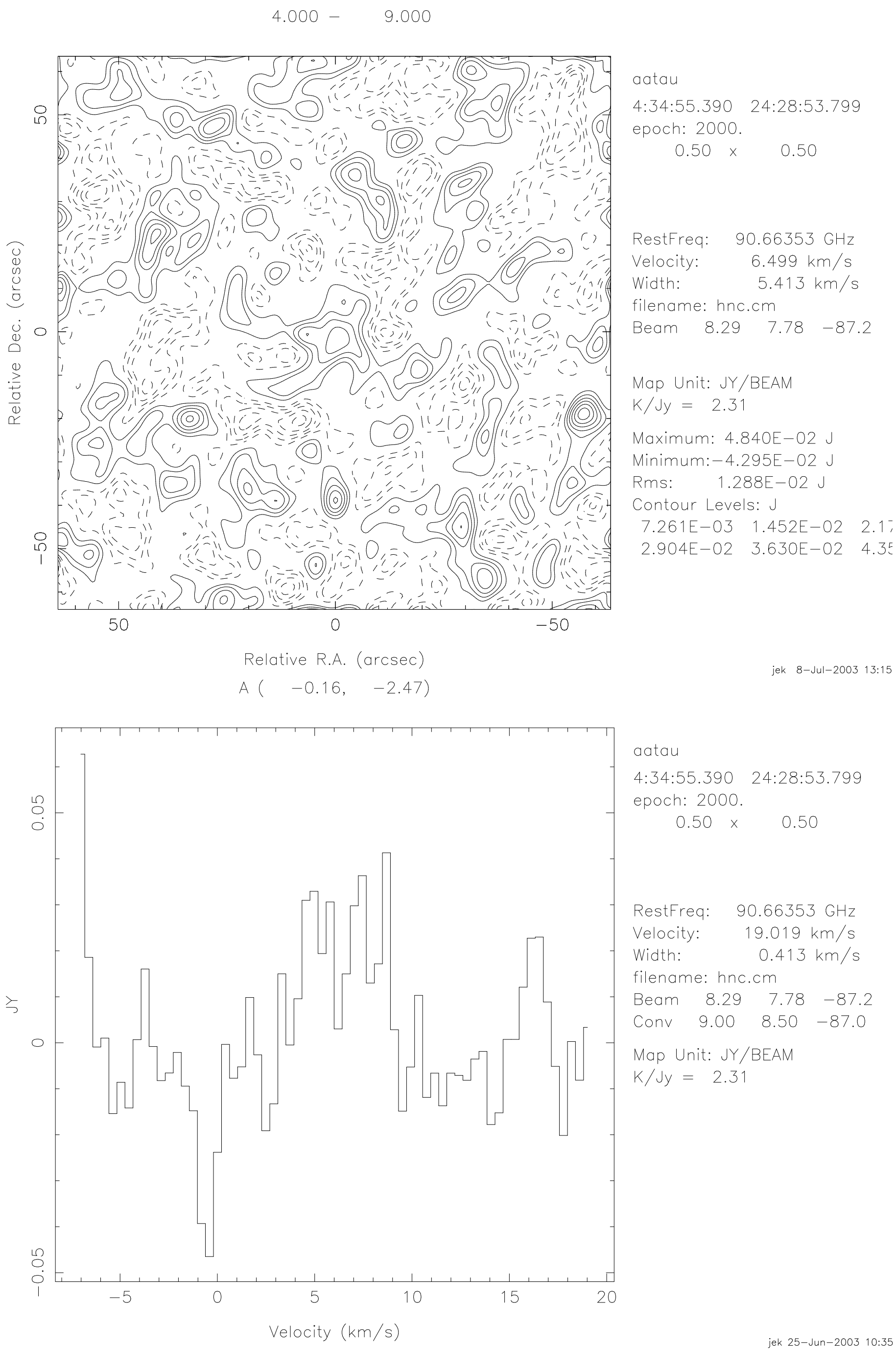

Figure 3.7 HNC 1-0 observations toward AA Tau. HNC emission is strong in the map, although diffuse and clearly visible in the spectrum which is quite similar to that of HCO^+ and CO 1-0.

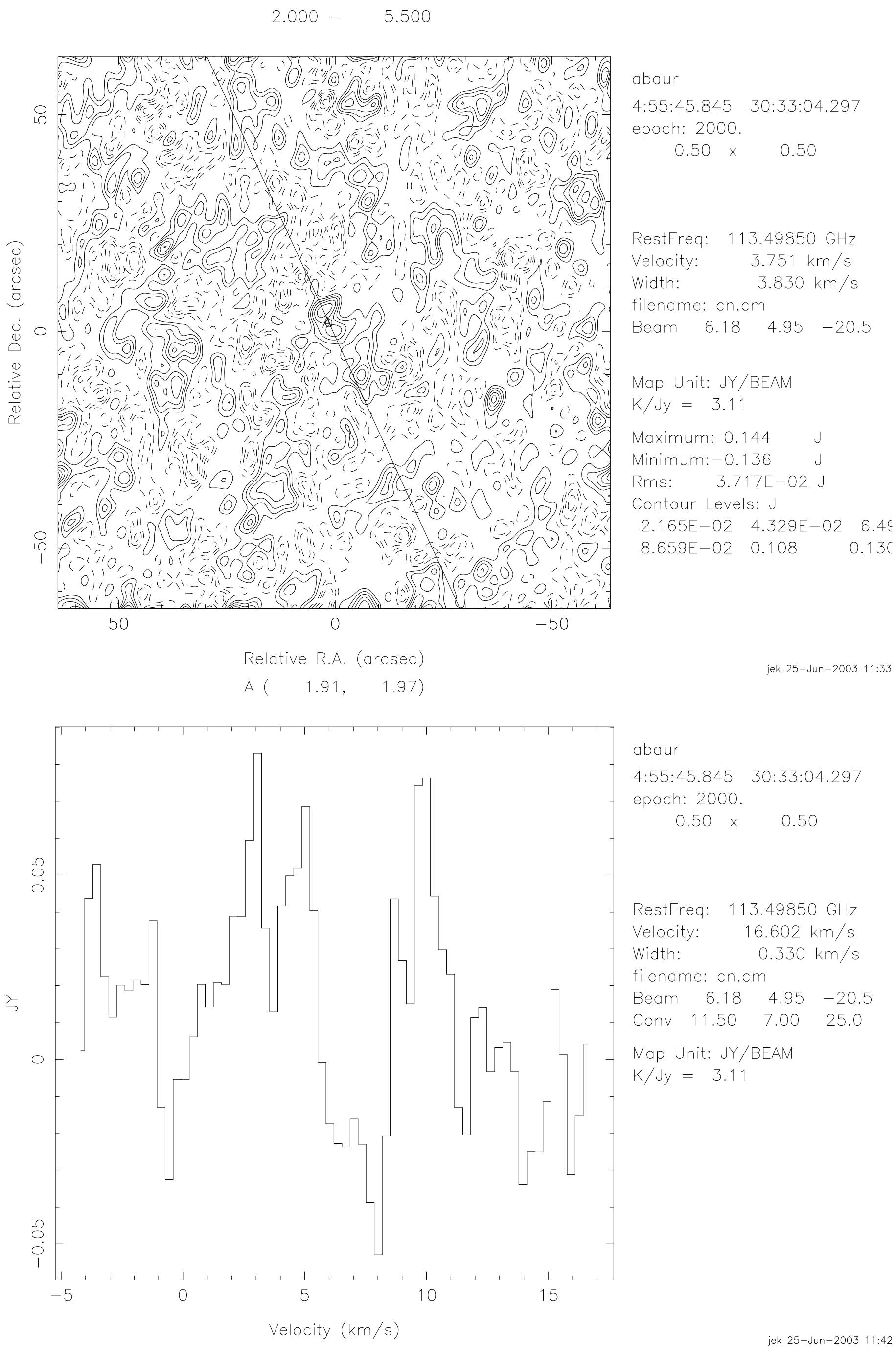

Figure 3.8 CN observations toward AB Aur. CN is strongly detected with a double peak in the map and spectrum.

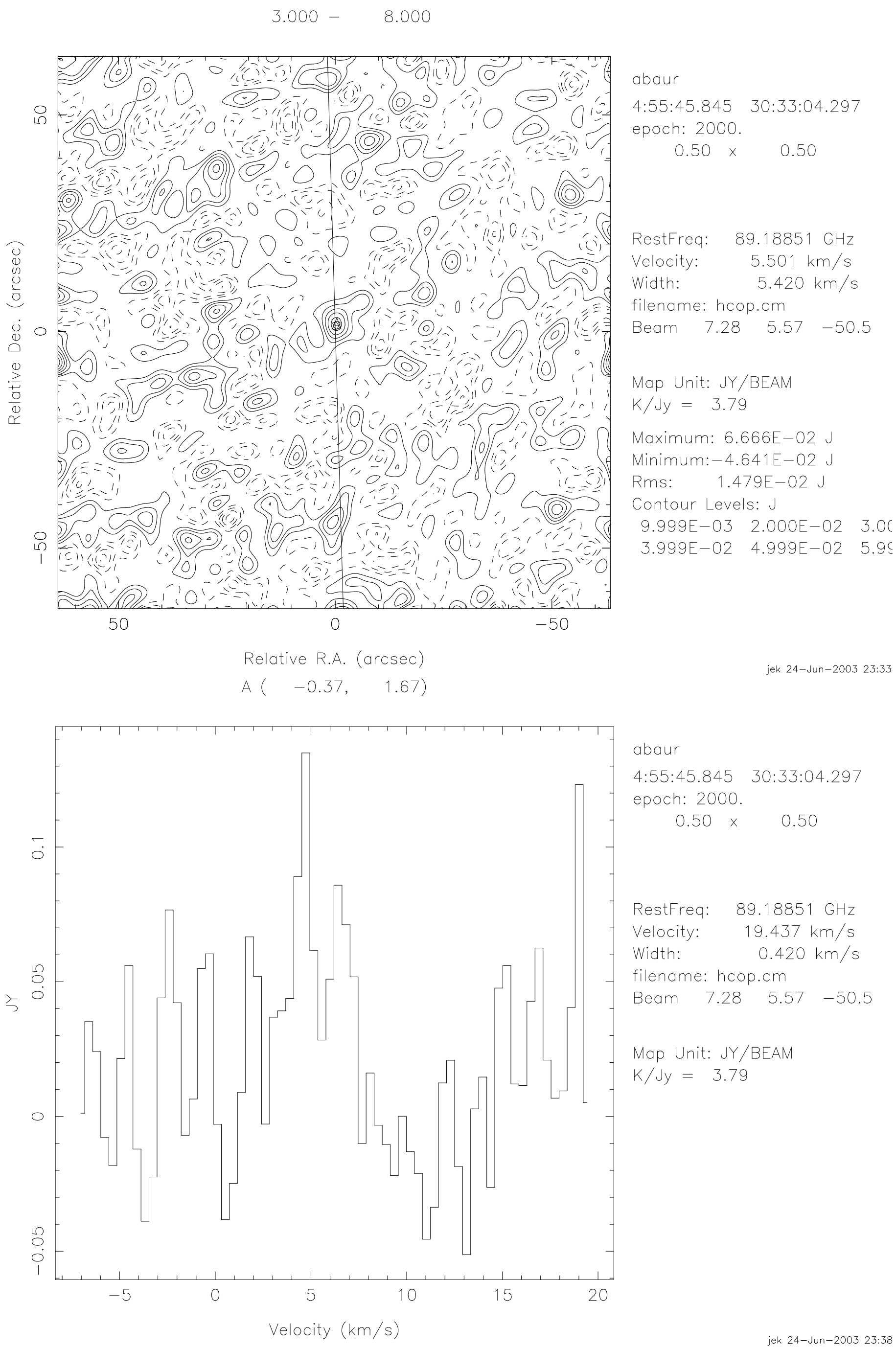

Figure 3.9 HCO^+ observations toward AB Aur.

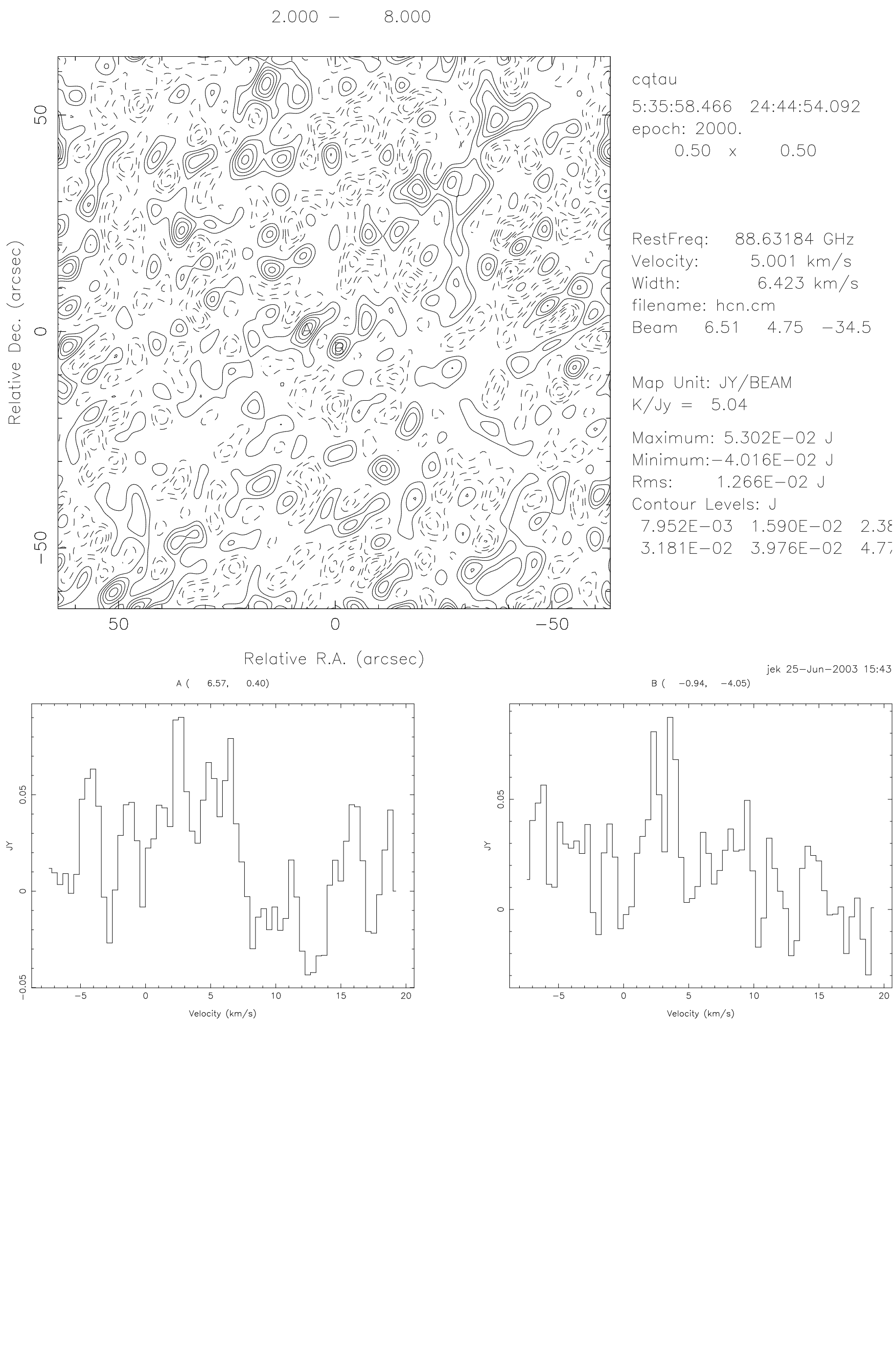

Figure 3.10 HCN observations toward CQ Tau.

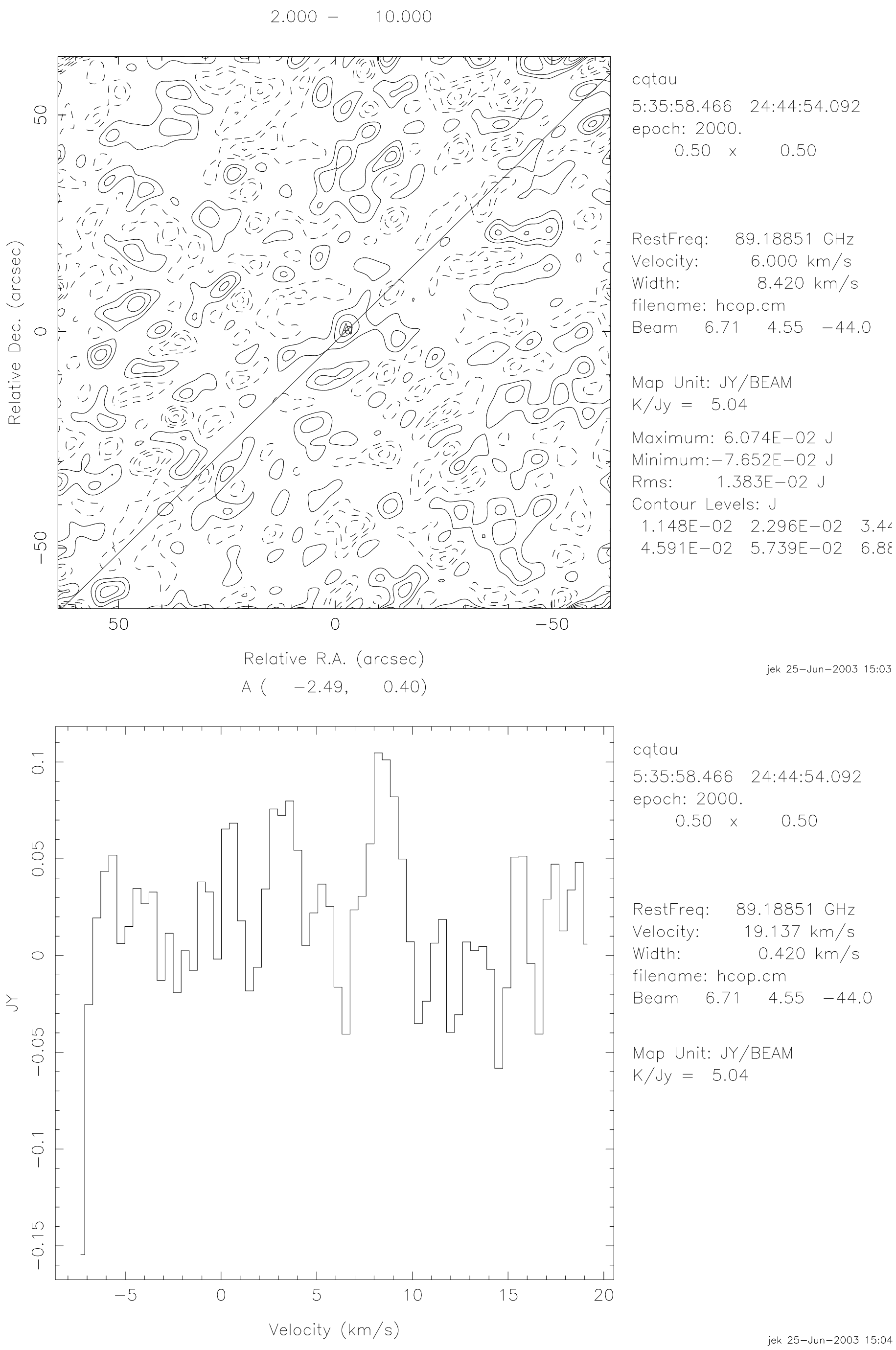

Figure 3.11 HCO^+ observations toward CQ Tau.

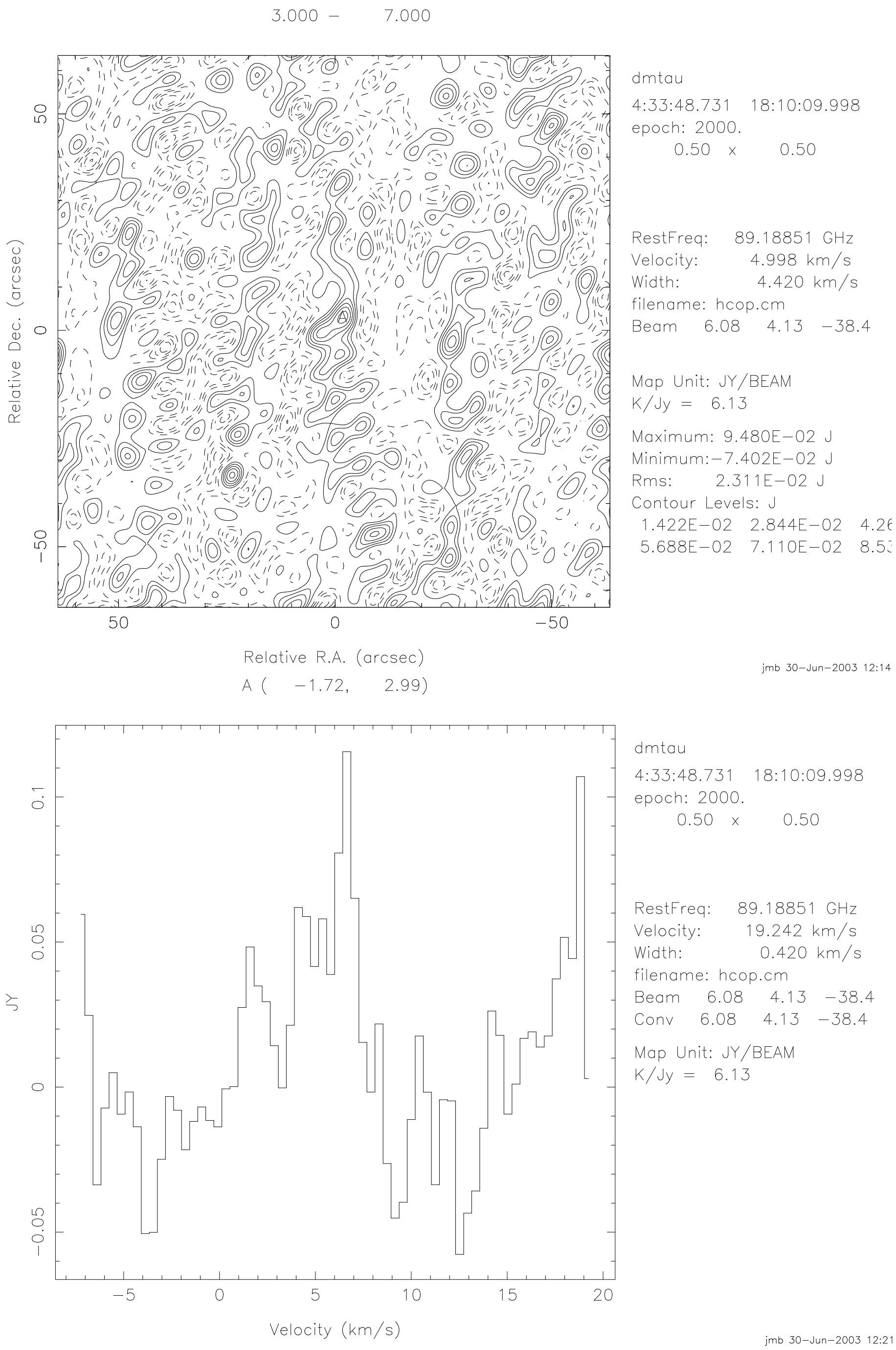

Figure 3.12 HCO^+ observations toward DM Tau.

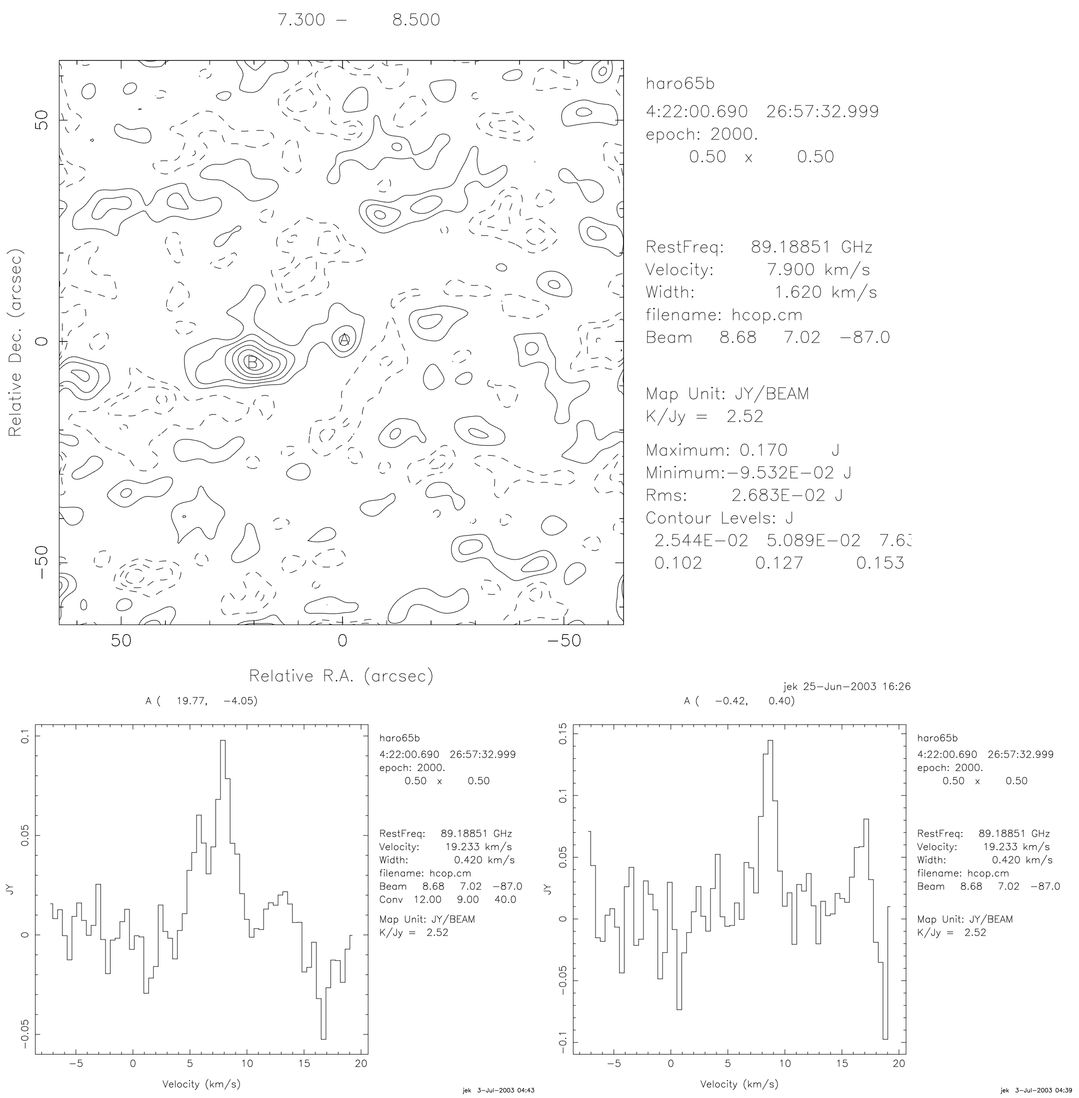

Figure 3.13 HCO^+ observations toward Haro 6-5B (right) and accompanying FS Tau (left).

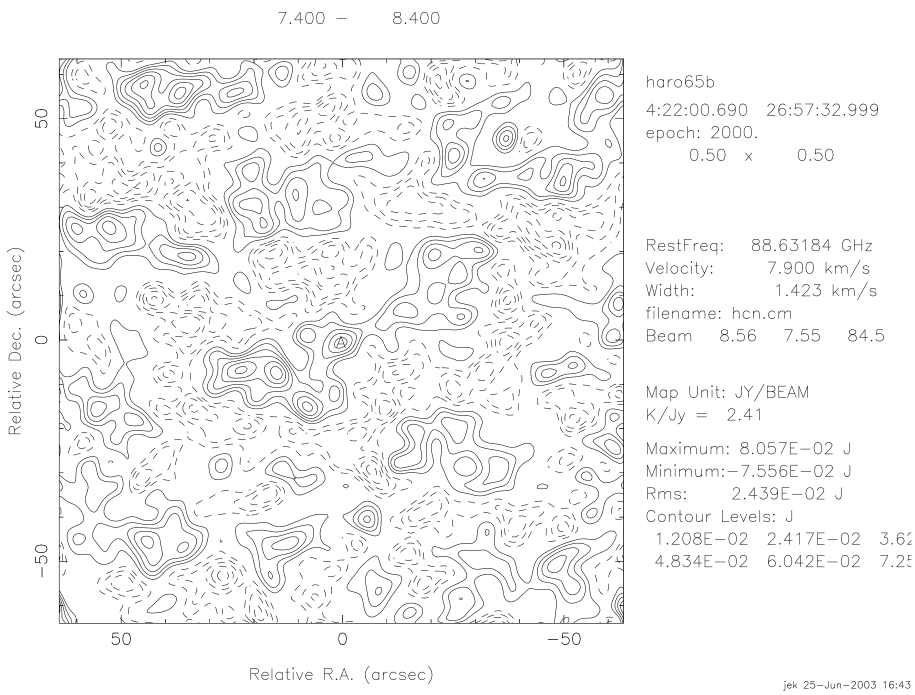

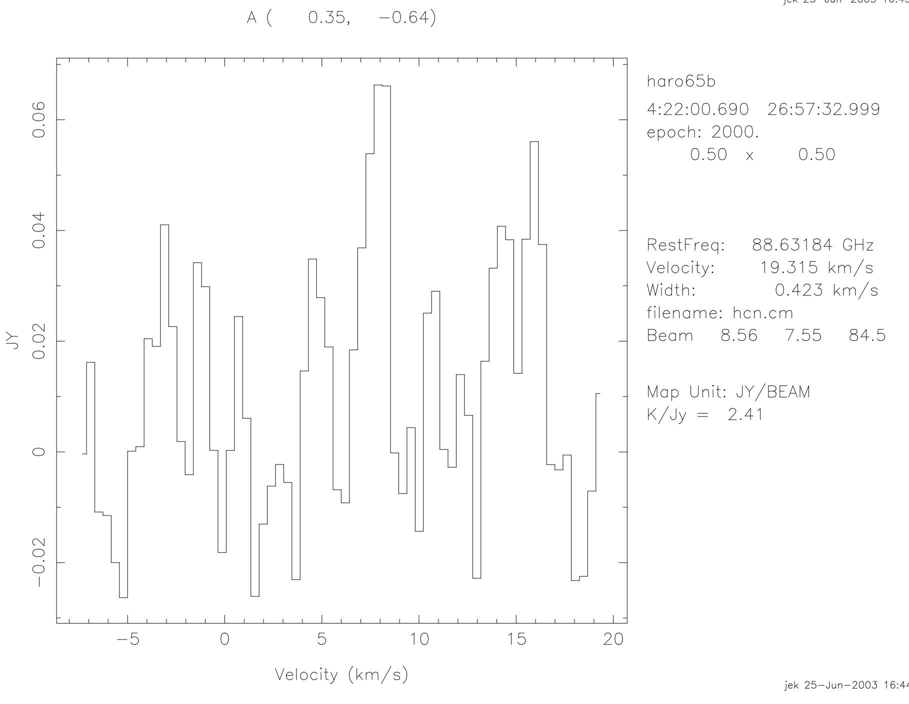

Figure 3.14 HCN observations toward Haro 6-5B.

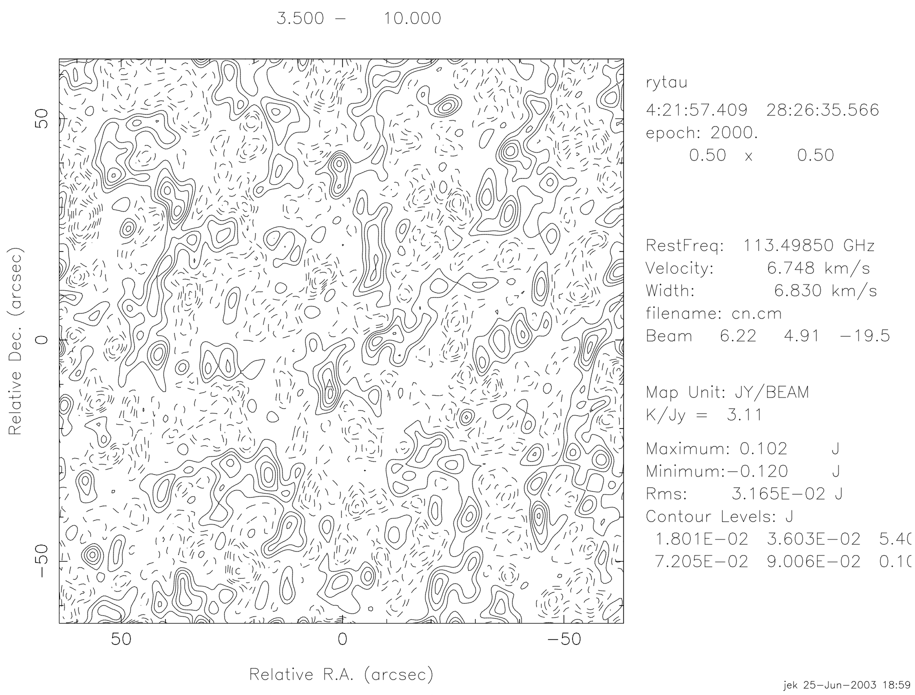

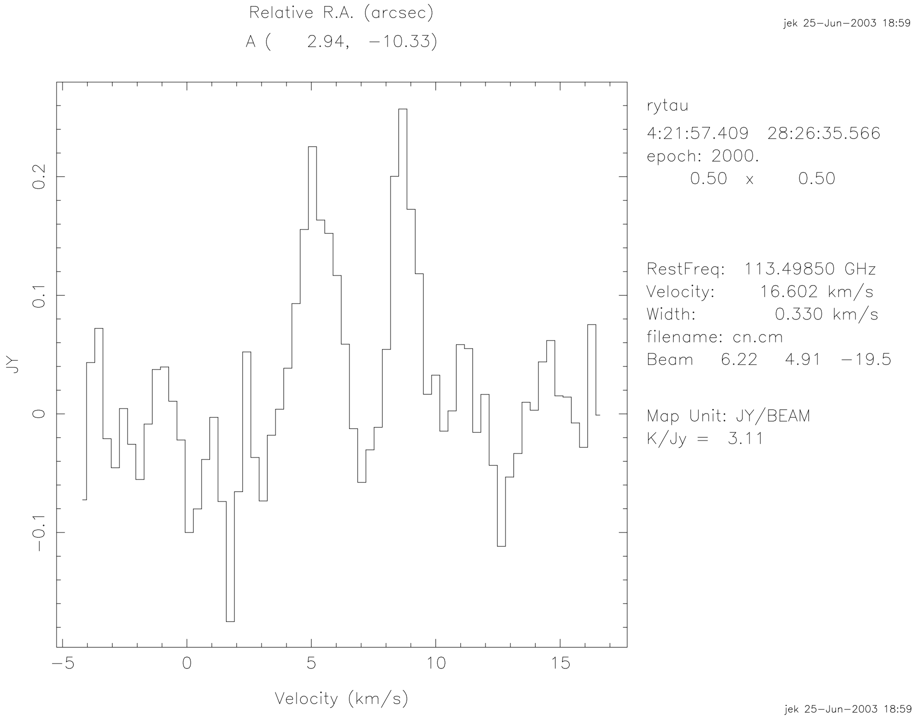

Figure 3.15 CN observations toward RY Tau.

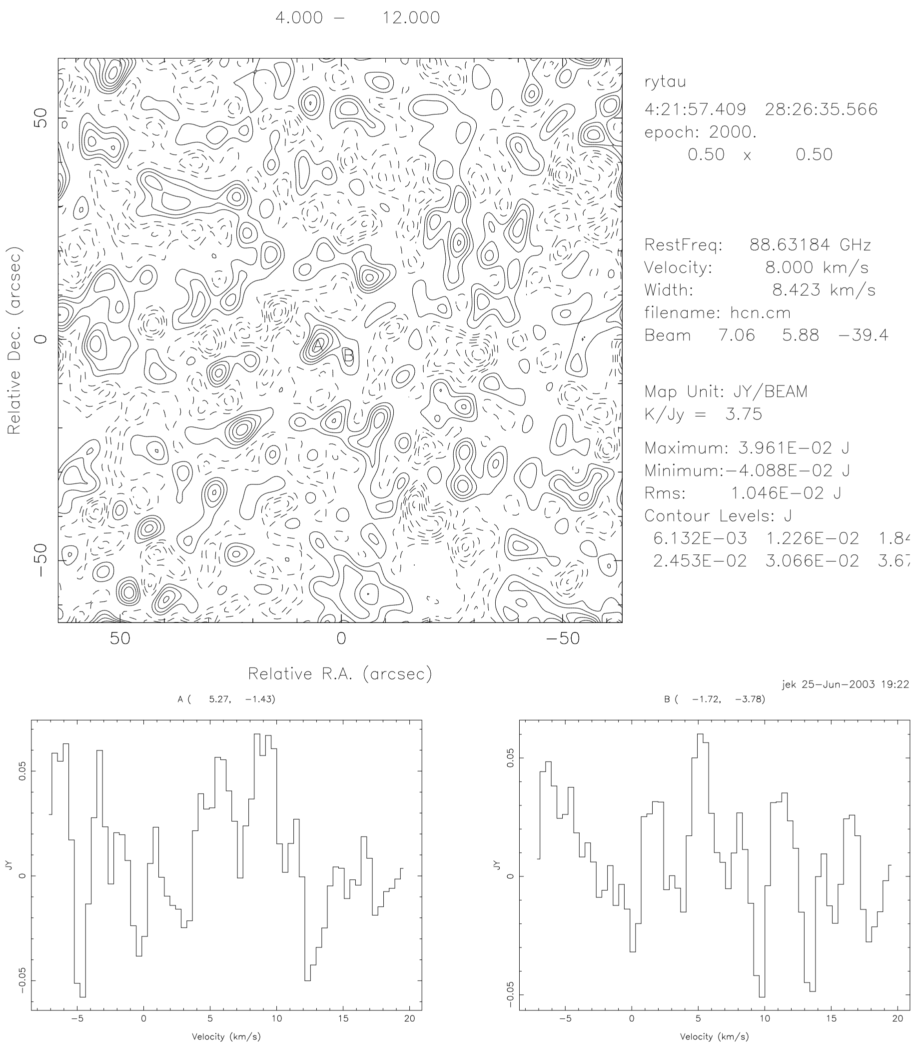

Figure 3.16 HCN observations toward RY Tau. The spectra on the left and right were obtained at points A and B, respectively.

Chapter 4

Tracing temperature and radiation fields in TTs and HAe disks

Excerpts from this chapter were previously published in “Millimeter observations of HDO and DCN in the circumstellar disks of protostars LkCa 15, MWC 480 and HD 163296.” in the conference proceedings, SFChem 2002: Chemistry as a Diagnostic of Star Formation, Waterloo, Ontario, Canada N2L 3G1. To be published by NRC Press, Ottawa, Canada, p. 55.

Abstract

Deuterium-to-hydrogen ratios are sensitive tracers of the conditions throughout the star formation process. In particular, observations of deuterium in disks can be used to constrain the location and timescales of comet formation. In this study, we searched for the deuterated species DCN and HDO toward the T Tauri protostar LkCa 15 and the Herbig Ae stars HD 163296 and MWC 480 using the Owens Valley Radio Observatory Millimeter Array. DCN was detected toward HD 163296 and HDO was detected toward LkCa 15 indicating column densities of 1.30×10^{12} cm^{-2} and 2.88×10^{15} cm^{-2}, respectively, for optically thin emission. Upper limits are given for column densities of DCN in LkCa 15 and HDO in HD 163296 and MWC 480. We also present the detection of $H^{13}CN$ toward LkCa 15, which in combination with the upper limits obtained for DCN indicates $D/H_{DCN} < 1.0{\times}10^{-3}$ for this disk. HCN has been searched for, but not detected, in HD 163296 (Qi, 2001) and the detection of DCN presented here indicates $D/H_{DCN} < 0.094$ in this source. HDO/H_2O was estimated through comparison with predicted H_2O abundances from chemical models, scaled by the HCN(modeled)/HCN(observed) abundances. The resulting deuterium fractionations in LkCa 15 and HD 163296 were found to be similar to those found toward the T Tauri star disk TW Hya and those observed in molecular clouds and hot cores. The structure of the HDO emission toward LkCa 15 was modeled and is discussed in this chapter.

4.1 Introduction

Changes in the composition of ice and gas during the process of planet formation likely lead to the rich diversity of planetary systems discussed in Chapter 1. Observations tracing the evolution of material in young stellar objects (YSOs) are also essential for addressing issues such as the formation of comets and the origin of life. The ratio of deuteron-bearing to hydrogen-bearing forms of a species (D/H) can be indicative of the physical and chemical evolution during the star formation process. D/H ratios have been measured for several objects in our solar system, including planets, comets and meteorites, as well as presolar analogues like hot cores and molecular clouds. As Figure 4.1 shows, these observations indicate that deuterium abundance is a sensitive tracer of the changes in the composition of circumstellar material that occur throughout (pre)stellar evolution; the D/H ratio decreases by orders of magnitude from molecular clouds to hot cores to the presolar nebula. Thus, the comparison of the D/H ratios in these stages of star formation (i.e., the comparison of protoplanetary disks with comets and Kuiper Belt objects) will allow us to take full advantage of YSOs as a laboratory in which to study the chemical and physical properties of our own Solar System in its infancy and to investigate the origin of primitive solar system bodies.

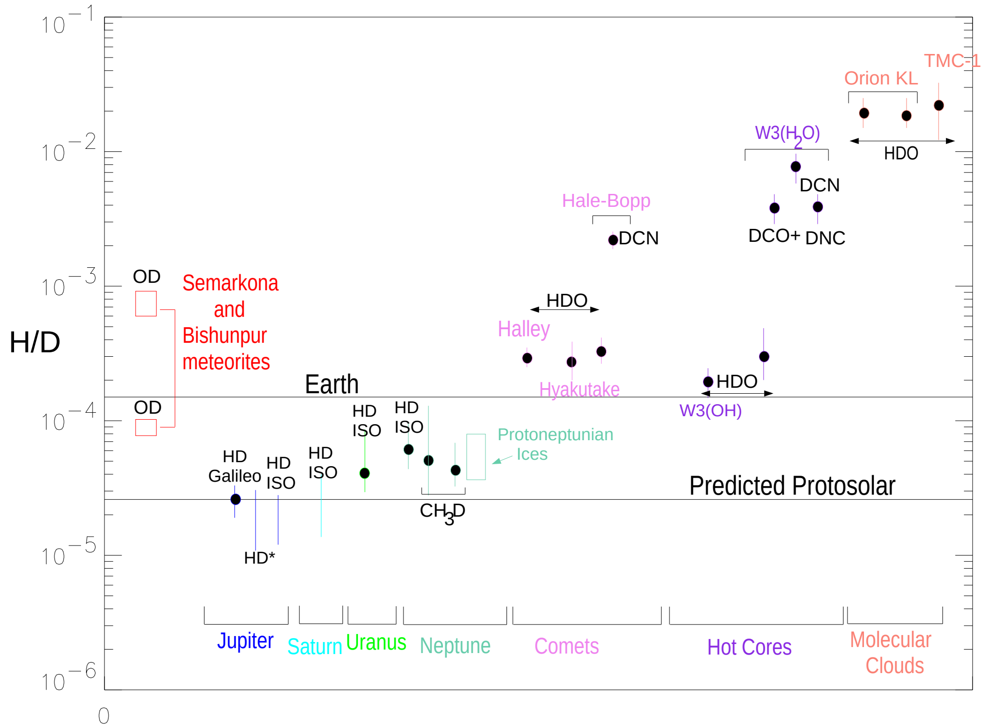

Figure 4.1 This graph is modeled after that presented in Bockelée-Morvan et al. (1998) and Drouart et al. (1999) (see these papers for a review of observations of solar system objects). The deuterium abundances for hot cores (Mangum 1991; Helmich et al., 1996) and molecular clouds (Mangum et al., 1991; Wootten, 1987) were added for comparison with that found for the accretion disks encircling LkCa 15, HD 163296 and MWC 480 studied here.

It is the strong dependence of deuterium enrichment on fractional ionization and temperature that makes the ratio of deuterium-to-hydrogen a particularly sensitive tracer of evolving physical conditions during the star formation process. The D/H ratio in the local ISM has been found to be $(1.4\text{–}2.2)\times10^{-5}$ (Linsky et al., 1995; Linsky & Wood, 1996; Piskunov et al., 1997) and is consistent with the estimated protosolar D/H value of $\sim1.6\times10^{-5}$ (as calculated from the conversion of D to ^{3}He in the solar wind; Gautier & Morel, 1997). Observations of cold molecular clouds indicate deuterium enrichments as high as D/H$\sim$0.01–0.05 (Wootten, 1987), however. Gas-phase chemical models of molecular clouds suggest that deuterium is enriched as a result of rapid ion exchange reactions, the most important of which are

$$H_3^+ + HD \rightleftharpoons H_2D^+ + H_2 \tag{4.1}$$

$$CH_3^+ + HD \rightleftharpoons CH_2D^+ + H_2 \tag{4.2}$$

$$C_2H_2^+ + HD \rightleftharpoons C_2HD^+ + H_2 \tag{4.3}$$

The difference in the zero-point energies of H- and D-bearing species is typically 100–400 K. For the reactions above, this small difference makes the reactions highly temperature dependent under the conditions prevailing in molecular clouds. High temperatures will overcome the modest endothermicities and push these reactions to the left, decreasing production of the deuterated species, but at the low temperatures (T $<$ 20 K) of dense molecular cloud cores, the reactions proceed efficiently to the right. In these cold environments, depletion onto grain surfaces may also enhance the deuterium enrichment. As neutral species are depleted from the gas through accretion onto grain surfaces the primary destruction mechanism for deuterated ions is blocked and the D/H ratios in the gas phase increase (Brown & Millar, 1989). The presence of ionized species, such as H_3^+ and H_2D^+, is highly dependent on the abundance of atoms or molecules such as CO, O and N_2, which have a proton affinity greater than that of H_2. The abundances of these neutral species are largely dependent on the degree of depletion onto grain surfaces. The combination of these two effects is the most likely cause of the observed cloud-to-cloud variations in deuterium enrichment, where decreasing deuterium enrichment can be associated with increasing cloud temperature (Wootten, 1987).

Observations of deuterated species in hot cores (Jacq et al., 1990; Helmich et al., 1996; Gensheimer et al., 1996) find $(D/H)_{H_2O}$ of $(1\text{–}3)\times10^{-4}$ and $(D/H)_{HCN}$ of $(5\text{–}8)\times10^{-3}$, much higher than expected due to their temperature (T $\approx$ 200 K). These results were initially puzzling, but were later explained by models in which the gas-phase abundances in hot cores result directly from evaporation of largely unprocessed interstellar material, which has previously been frozen out onto grain mantles (Walmsley et al., 1987; Brown et al., 1988). Although grain surface reactions occur, the D/H ratio is not expected to change considerably, because the mobility of deuterium atoms on grain surfaces is similar to that of hydrogen (which scans a 0.05 μm grain in $\sim 1\times10^{-7}$ s; Brown & Millar, 1989). The degree of enrichment in hot cores thus reflects that in molecular clouds prior to accretion onto grain surfaces. Only after a significant amount of time, models suggest $\sim 10^5$yr (Brown et al., 1988), are gas-phase reactions believed to significantly affect the deuterium abundances due to the very large initial D/H ratios of grain mantle ejecta.

For some molecules, ion exchange reactions like those discussed above are slow and the main source of deuterium enrichment is ion-molecule and deuteron exchange reactions with heavily deuterated parent molecules (Millar et al., 1989). The efficiency of ion-molecule reactions, and the ionization rate, thus also affects the degree of deuterium enrichment. Observations indicate that D/H ratios in hot cores and molecular clouds are much larger than that of the early solar nebula ($\sim 10^{-5}$), where ion-molecule reactions as well as neutral-neutral reactions are important. Direct measurements of D/H in disks can therefore greatly improve our understanding the chemistry occurring in this nebular stage, particularly if they resolve the disk probing radial variations in the D/H ratio. If neutral-neutral reactions dominate (Geiss & Reeves, 1981), then D/H enrichments higher than a factor of a few are difficult to obtain. However, more recent chemical models (Finocchi et al., 1997; Willacy & Langer, 2000; Aikawa et al., 2002) indicate that ion-molecule reactions play an important role in disk chemistry because cosmic rays and X-rays increase the ionization rate (to $\geq 10^{-17}$ s^{-1}) and thus the importance of ion-molecule reactions. Additionally, the effectiveness of deuteron transfer reactions in altering the deuterium enrichment is dependent on the mixing processes in disks, which are in turn controlled by the ionization of the gas (Aikawa & Herbst, 2001). Evaporation from and recondensation onto grain surfaces will likely occur repeatedly in disks thanks to mixing and processes such as grain-grain collisions. Therefore, measurements of deuterated molecules in disks can constrain the importance of ion-molecule reactions and ionization in disks and possibly explain the apparent decrease in D/H ratio during stellar and planetary evolution.

Comparison of the deuterium enrichment in each stage of star and planet formation with that of comets and meteorites can also be used to gain a more complete understanding of the formation of small bodies in our solar system. As noted above, molecules in cold clouds are enriched in deuterium relative to the ISM. This notable deuterium enrichment in molecular clouds and the moderate enrichment in comets, $\sim 2\times10^{-3}$ for DCN/HCN and $\sim 3\times10^{-4}$ for HDO/H_2O, has been interpreted as a possible indication of interstellar versus nebular cometary origins (Eberhardt et al., 1995; Bockelée-Morvan et al., 1998; Meier et al., 1998a). However, recent models of chemistry in circumstellar accretion disks (Aikawa & Herbst, 1999; Aikawa & Herbst, 2001) suggest that the deuterium fractionation changes significantly during the collapse of the molecular clouds and during the accretion process itself. So, although the D/H ratios of comets are similar to that of molecular clouds, it is not likely that comets are formed of truly "pristine" interstellar material. Their composition should, in fact, be strongly dependent on the structure of the circumstellar disk in which they were assembled.

Temperatures and densities in circumstellar disks are thought to vary strongly as a function of radius and height, and detailed chemical models (Willacy & Langer, 2000; Aikawa et al., 2002) predict that these gradients should be reflected in molecular abundances–as can be seen in the measured D/H ratios of the solar system. Most solar system objects, including planets, protoneptunian ices and the majority of carbonaceous meteorites, appear to have been formed in a reservoir with deuterium content (D/H $< 9 \times 10^{-5}$) similar to the accepted protosolar value. However, the presence of a minor component of the sample of carbonaceous meteorites with a much larger D/H ratio $\approx 7 \times 10^{-4}$ (Deloule et al., 1997) indicates that the solar nebula was most likely heterogeneous and suggests the presence of reservoirs in which there was substantial deuterium enrichment.

The effects of nebular heterogeneity should also be visible in the deuterium content of comets. Although the origin of comets is currently not well understood, measurements of D/H ratios in comets should help clarify the physical and chemical conditions under which they formed. It has been proposed that short-period comets originated in a cold (T$\sim$25 K) region beyond Neptune's orbit (Kuiper, 1951; Duncan et al., 1988; Fernandez & Ip, 1991; Festou et al., 1993) and that long-period comets formed in a warmer outer-planet region (from Jupiter to Neptune) and were then dynamically scattered into the Oort cloud by interactions with Jupiter (Eberhardt et al., 1995). The difference in the physical conditions (particularly temperature) of the formation regions for these two types of comets should be evident in their chemical and isotopic composition, with Kuiper belt comets possessing a more "interstellar" composition and Oort cloud comets more closely resembling the solar nebula (Eberhardt et al., 1995).

The deuterium fractionation in comets Halley, Hayukutake and Hale-Bopp, believed to be Oort cloud comets, has been observed to be intermediate between that of the early solar nebula and that of cold molecular clouds; DCN/HCN in Hale-Bopp is $\sim 2 \times 10^{-3}$ (Meier et al., 1998a) and HDO/H_2O is $\sim 3 \times 10^{-4}$ in Haley, Hayukutake and Hale-Bopp (Eberhardt et al., 1995; Bockelée-Morvan et al., 1998; Meier et al., 1998b). To date, deuterated species have not been observed in short-period comets. However, as discussed by Rodgers & Charnley (2002), the comets Linear S4 (believed to have originated near Jupiter in the protosolar nebula) and Giacobini-Zinner (thought to be a Kuiper belt object) have chemistry which deviates from the "norm", including large (factors as high as $\sim$15) depletions of volatile carbon-chain molecules, (Weaver et al., 1999, Mumma et al., 2001) indicating that chemical composition of comets may indeed be dependent on their place of origin.

It is clear that a better understanding of the role of deuterium fractionation in stellar evolution and comet formation is dependent upon the development of a detailed model of nebular conditions. Observations of circumstellar disks around other protostars provide an opportunity to directly study environments that may be similar to the early stages of our Solar System. Recently, millimeter-wave interferometers have imaged disks of gas and dust surrounding several young T Tauri and Herbig

Table 4.1. Stellar properties of observed sources.

Star colhead	R.A. (1950)	Dec. (1950)	SpT	d (pc)	T_{eff} (K)	R_* ($R_\odot$)	L_* ($L_\odot$)	M_* ($M_\odot$)	Age (Myr)	V_{ref} (km/s)
LkCa 15	04 36 18.40	+22 15 11.6	K7	140	4365	1.64	0.72	0.81	11.7	6.0
HD 163296	17 53 20.61	-21 56 57.3	A3Ve	122	9550	2.2	30.2	2.3	6	6.0
MWC 480	04 55 35.69	+29 46 05.7	A3ep+sh	131	8710	2.1	32.4	2	4.6	5.1

Ae/Be stars (see Beckwith & Sargent, 1996 for a review) resulting in dramatically improved models of disk physical and chemical structure. Among the characteristics now under study, disk geometry, velocity structure, dust and gas masses, fractional ionization, temperature distributions, and the degree of depletion of gas-phase species onto grain surfaces have now been examined in a handful of sources (Dutrey et al., 1997; Qi, 2001; Simon et al., 2001; Dartois et al., 2003; Qi et al., 2003). Observations of deuterated species in circumstellar disks are particularly exciting, in that they should directly constrain the (D/H) fractionation in the outer (low temperature) regions of these disks. The accretion in protoplanetary disks is largely viscous; material spirals inward toward the star at a typical accretion rate of 10^{-8} $M_\odot$/yr and by the end of the accretion phase material which was at radii of hundreds of AU from the star now resides in the comet-forming region. When combined with the previously obtained information about disk structure, the observed deuterium fractionation in the outer disk can be directly compared to that in comets and in the ISM to more fully understand comet formation.

In this study, the deuterated species DCN and HDO were observed toward the disks surrounding LkCa 15, a T Tauri star, and HD 163296 and MWC 480, Herbig Ae stars, using the Owens Valley Radio Observatory (OVRO) Millimeter Array. These sources were previously identified through ^{12}CO observations to possess circumstellar material with Keplerian velocity structure (Beckwith & Sargent, 1996; Mannings & Sargent, 1997), except for HD 163296 for which the velocity field has not yet been modeled in detail. These objects were also found to be strongly emitting in initial molecular line observations of HCN 1-0, HCO^+ 1-0 and CN 1-0 and are part of a larger survey of molecular line observations in circumstellar accretion disks, in which the dominant chemical species in the C,N,O,S-budgets are being observed (Qi, 2001; Qi et al., 2003; this thesis). Stellar and disk parameters for these three sources are presented in Table 4.1.

The observations will be presented in §2. In §3, the deuterium fractionation will be evaluated in each disk through the comparison of the observed DCN abundances with those found for HCN and $H^{13}CN$ and of the observed HDO abundances with H_2O abundances predicted by chemical models, scaled by the CO(predicted)/CO(observed) or HCN(predicted)/HCN(observed) abundances of the disks in our sample. The observed deuterium fractionation in these three disks will be compared to those obtained via chemical models and those observed for molecular clouds, hot cores, comets and

Table 4.2. Observational parameters

Source	Molecule	Transition	ν (GHz)	Θ (arcsec)	configuration(s)	$\int T_A^* dv$ (K km/s)	N_i (cm^{-2})
LkCa15	HDO	1_{11}-2_{12}	225.8967	2.16×2.10	C+L+H	4.94	7.25(15)
-	HDO	3_{12}-2_{11}	241.5615	1.43×1.18	C+L+H	18.1	4.24(15)
-	DCN	3-2	217.2386	3.24×1.78	L+E+C	<3.01	<3.06(12)
-	$H^{13}CN$	3-2	259.0118	0.87×0.72	H	65.1	5.34(13)
-	$H_2{}^{18}O$	3_{13}-2_{20}	203.4075	2.71×1.25	E+C	<3.01	<3.23(16)
HD 163296	HDO	1_{11}-2_{12}	225.8967	1.78×1.23	L+H	<188	<2.76(17)
-	DCN	3-2	217.2386	3.58×2.24	L+E	1.04	1.30(12)
MWC 480	HDO	1_{11}-2_{12}	225.8967	4.60×2.50	C+L	0.285	4.18(14)

solar system objects in §4.

4.2 Observations

The observations were made using the Owens Valley Radio Observatory (OVRO) Millimeter Array[1] at Big Pine, California, between October 1997 and March 2002. The sources were observed in combinations of the C, L, E and H configurations of the array. The beam sizes and receiver tunings for the observed transitions toward each source are shown in Table 4.2. Average single sideband system temperatures ranged from 400–750 K. The bandpass was calibrated using a boxcar fit to an internal noise source modified by a second order polynomial fit to observations of an astronomical source; either 3C84, 3C454.3, 3C345, 3C279 or 3C273 were used subject to availability at the time of observation. Observations of a phase and amplitude calibrator were interleaved with source observations approximately every half hour, using 3C111 and 0528+134 for LkCa 15, NRAO 530 for HD 163296 and 0538+134 for MWC 480. The flux density scale was established from concurrent observations of Neptune and Uranus during their transit or the quasars used for bandpass calibration, whose fluxes were found by "boot-strapping" from ∼concurrent planet observations. Bandpass, phase and flux calibrations were applied to the data with the MMA software package (Scoville et al., 1993). Subsequent imaging and spectral analysis were performed using the MIRIAD data reduction software package (Sault et al., 1995).

4.3 Column densities and D/H ratios

Gaussian fits to the observed emission lines were used to obtain the integrated intensities ($\int T_A^* dv$) shown in Table 4.2. If emission was not detected, the rms noise level obtained in the observations (Table 4.2) was used to calculate an upper limit for the integrated intensity by assuming a line width at the 1σ level that was consistent with observed line widths of the ^{13}CO 1-0 transition toward these sources (Qi, 2001; Duvert et al., 2000; Mannings & Sargent, 1997) and calculating the integrated

[1]OVRO observations were supported by the National Science Foundation, AST 9981546.

intensity at 3σ. In all cases, the column densities were then calculated from the integrated intensities using the following relation, assuming that the emission is optically thin,

$$\int T_A^* dv = \frac{8\pi}{3k}\nu\mu^2 S \frac{N_T}{Q(T_{ex})} e^{-E_u/kT_{ex}}, \tag{4.4}$$

where S is the line strength and was obtained from integrated intensities (I_{cat}) of the emission lines in laboratory spectra at a temperature ($T_0 = 300$ K) as reported in the JPL Molecular Spectroscopy on-line catalog (Pickett et al., 1998) by,

$$I_{cat} = \frac{8\pi}{3h}\mu^2 S \frac{\langle e^{-E_l/kT_0} - e^{-E_u/kT_0}\rangle}{Q(T_0)}. \tag{4.5}$$

In the two equations above, N_T is the total column density in cm^{-2}, Q is the rotational partition function, E_u and E_l are the energies (in ergs) of the upper and lower states, ν is the transition frequency (Hz), μ is the permanent dipole moment, h is the Planck constant and k is the Boltzmann constant.

In addition, it was assumed that the emitting region is in Local Thermal Equilibrium (LTE) and approximately isothermal with $T_K = T_{ex} = 30$ K. The assumption of LTE may not be valid, especially for water, as most of the emission is thought to arise near the superheated disk surface (van Zadelhoff et al., 2001), and a more detailed, non-LTE analysis is being pursued in a separate study (Chapter 2). An isothermal disk with temperature 30 K is appropriate for the outer radii (70 $< R <$ 400 AU) of the disks to which we are sensitive at millimeter wavelengths (D'Alessio et al., 1999). The resulting column densities and upper limits are presented in Table 4.2.

DCN was detected toward the Herbig Ae star HD 163296, with a column density of 1.30×10^{12} cm^{-2} (Figure 4.2). Only one L track was obtained, however, and the poor (u, v) sampling resulted in the triple peaked integrated intensity map shown in Figure 4.2. This is similar to that seen for the continuum radiation toward HD 163296 in the same observations and is not believed to be the true structure of the DCN emission. The left panel of Figure 4.2 shows the continuum emission (in color scale) overlaid with continuum+DCN emission for HD 163296. Although the map is clearly dominated by the strong 1 mm continuum, spectra of the left, middle and right lobes reveal detectable DCN emission. The velocity of the DCN emission (right panel) matches that seen for CO 2-1 (Mannings & Sargent, 2000a). This detection of DCN was unexpected because HCN was not seen toward this source, restricting the column density of HCN to $<1.1\times10^{13}$ cm^{-2}. Assuming the highest DCN/HCN ratio seen in molecular clouds, $\sim2.0\times10^{-2}$, we would expect a column density of DCN of $\leq2.2\times10^{11}$, or an integrated intensity of $\times10^{-4}$ K km/s. HDO was not detected toward HD 163296 and upper limits of 6.96×10^{15} cm^{-2} were obtained.

Toward LkCa 15, both the HDO 1_{11}-2_{12} and 3_{12}-2_{11} transitions were marginally detected and

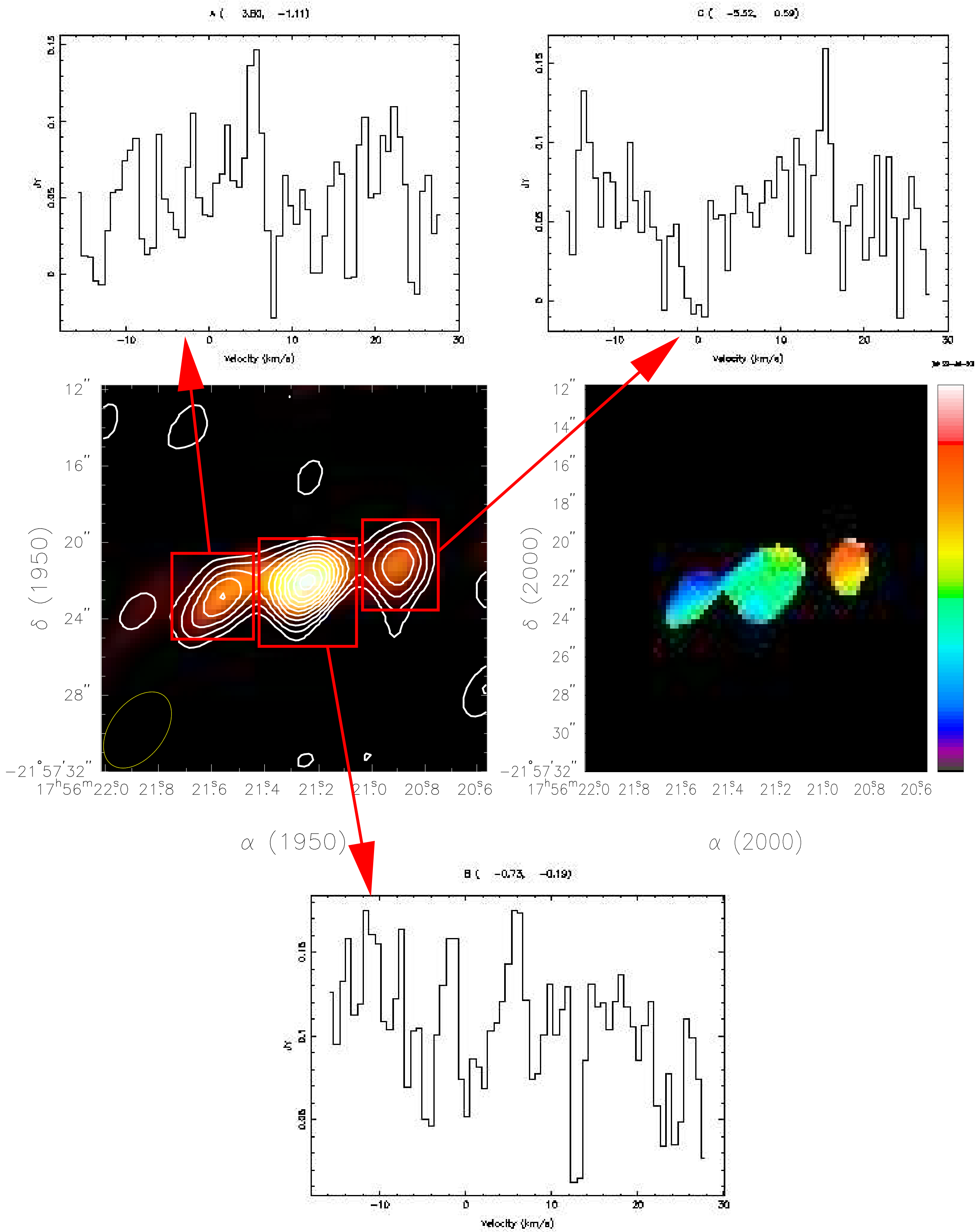

Figure 4.2 DCN 3-2 emission from HD 163296. The left panel shows the continuum emission (in color scale) overlaid with continuum+DCN emission (contours), with contours spaced by 1σ starting at 1σ. The color scale starts at 3σ. Spectra of the left, middle and right lobes are shown as indicated. The right panel shows the moment 1, or velocity map, that matches that seen in CO 2-1 (Mannings & Sargent, 2000a).

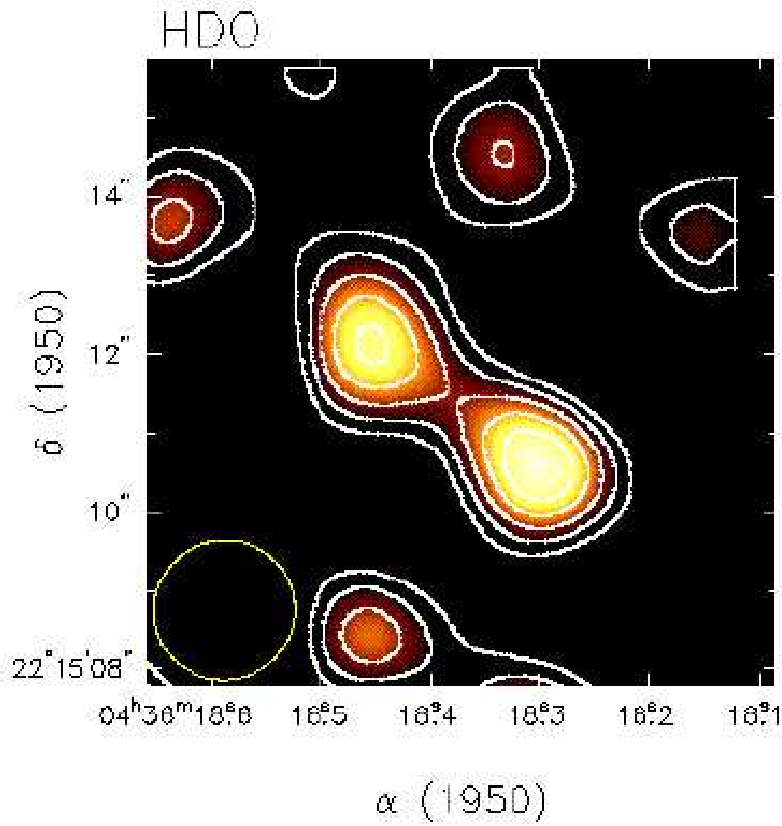

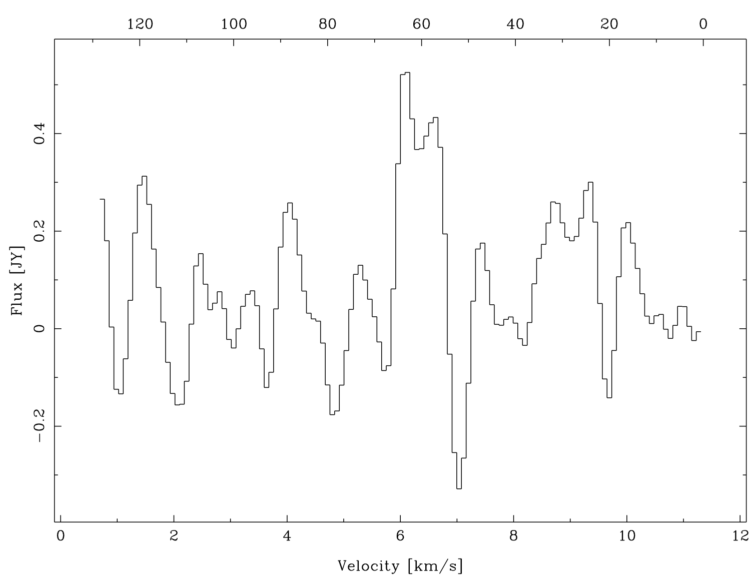

Figure 4.3 HDO 1_{11}-2_{12} emission from LkCa 15. The top panel shows the integrated intensity map, with contours starting at 0.5σ and spaced by 0.5σ to emphasize the spatial distribution of the emission, which is quite similar to that of HCN toward this source. The spectrum in a $4'' \times 4''$ box is shown in the lower panel.

yield column densities of 4-7.25$\times10^{15}$ cm^{-2} (Figure 4.3). The integrated intensity map for the HDO 1_{11}-2_{12} emission depicts two peaks approximately 2" away from the continuum (stellar) position, located along the major axis of the disk. Although the emission is weak, the spectral line shape and the velocity distribution of the HDO emission is similar to that of previously observed for CO 2-1 toward this source (Qi et al., 2003), indicating that it does arise from disk material. The spatial distribution of the HDO emission is quite similar to the morphology of the CN and HCN emission toward this source and can be simulated by emission from an annulus of gas extending from R = 200–400 AU (§6). $H_2{}^{18}O$ was not detected toward LkCa 15 and we use the upper limit to the column density of $H_2{}^{18}O$ (1.25$\times10^{16}$ cm^{-2}) and the typical $^{16}O/^{18}O$ ratio for the local ISM (560$\pm$25; Wilson & Rood, 1994) to find an upper limit to the water column density of 7.0$\times10^{18}$ cm^{-2} in order to derive a D/H ratio. DCN was not detected toward LkCa 15 and upper limits for DCN (of 5.40$\times10^{11}$ cm^{-2}) were obtained. $H^{13}CN$ was detected toward LkCa 15 (Figure 4.4) at a column density of 9.23$\times10^{12}$ cm^{-2} and will be used in combination with the upper limits obtained for DCN to calculate a DCN/HCN ratio in LkCa 15. HDO was not detected toward MWC 480, resulting in an upper limit of 3.66×10^{15} cm^{-2}.

The $(D/H)_{HCN}$ ratio can be calculated directly from the DCN abundances presented here and previous observations of HCN in LkCa 15 and HD 163296 (Qi, 2001). For LkCa 15, HCN 1-0 emission was observed to be optically thick, and therefore the column density of $H^{13}CN$ measured here and the interstellar $^{13}C/^{12}C$ ratio of 60 were used to estimate the HCN abundance of 5.5$\times10^{14}$ cm^{-2}. For HD 163296, HCN was not detected (Qi, 2001) so an upper limit of 1.1$\times10^{13}$ cm^{-2} for HCN was used, as derived from an optically thin, LTE calculation. The resulting $(D/H)_{HCN}$ ratios in the disks around LkCa 15 and HD 163296 are $<2\times10^{-3}$ and > 0.176, respectively. Because water has not been detected toward these three sources, the calculation of the $(D/H)_{H_2O}$ is not as straightforward as that of $(D/H)_{HCN}$. For these reasons, the HDO abundances obtained from our observations are most useful when compared with model predictions.

4.4 Chemical models of circumstellar disks

Extensive chemical modeling of disk chemistry has been pursued by Aikawa et al. (1999) and Willacy & Langer (2000). These models predict molecular abundances as a function of height and radius in disks of ages ranging from 1–10 Myr. Although the physical models used by these two groups differ, both disk models assume that the gas is in hydrostatic equilibrium in the vertical direction and derive temperature and hydrogen density distributions that are similar. Aikawa et al. (1999) adopt the Kyoto model (Hayashi, 1981) for the physical disk structure, extrapolating to a radius of 700 AU and scaling the mass and density by an order of magnitude; whereas Willacy & Langer (2000) use the physical model of Chiang & Goldreich (1997), extrapolated to an outer radius of 1000 AU.

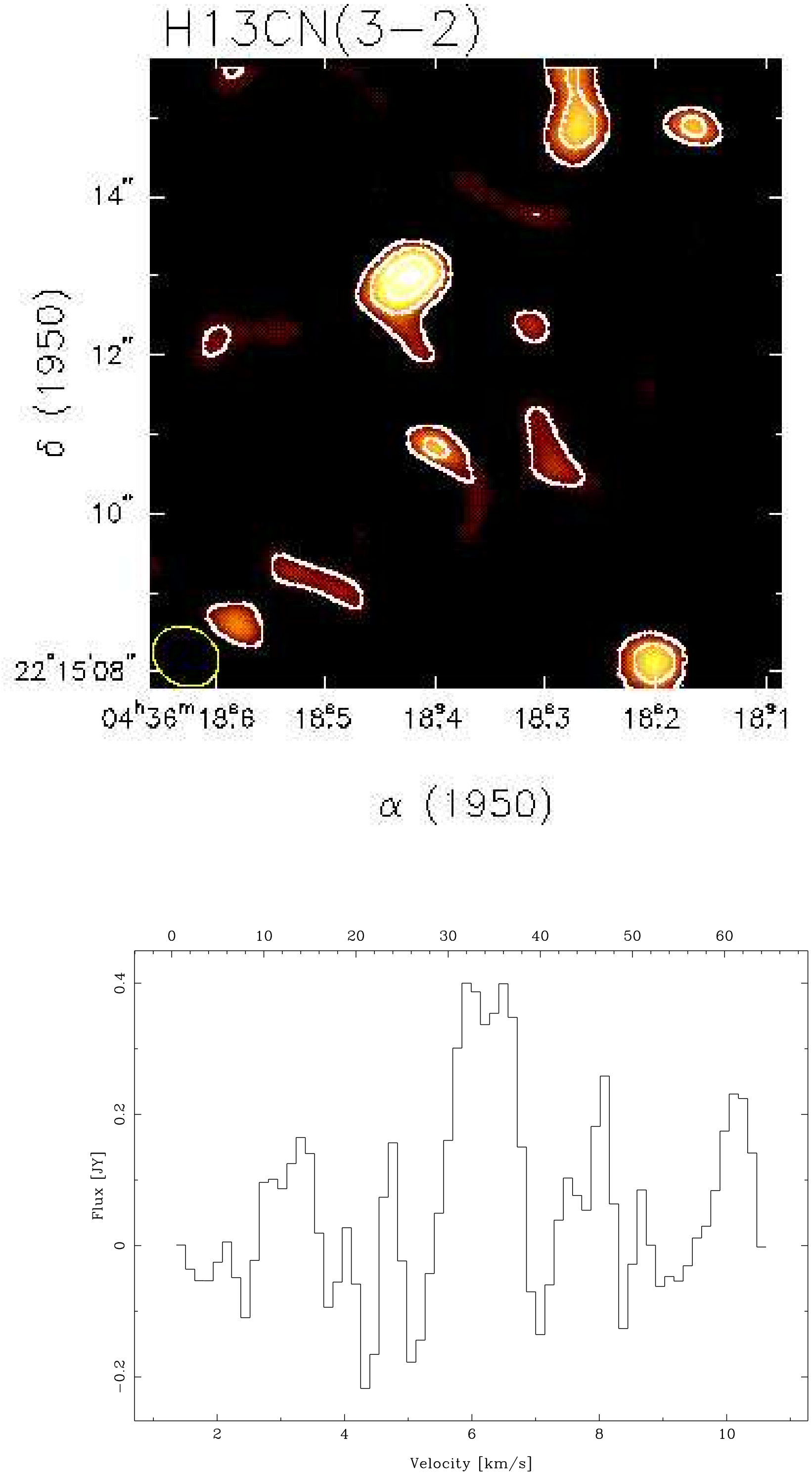

Figure 4.4 $H^{13}CN$ 3-2 emission from LkCa 15. The top panel shows the integrated intensity map of the emission, both contours and color scale, with contours starting at 1σ. The map is over-resolved as the data consists of only one H track, with a resolution of ~1.5" and poor (u, v) coverage near the origin. An emission line can be seen in the spectrum taken at the stellar position over a box of size $1'' \times 1''$, shown in the lower panel.

The two models mainly differ in the treatment of grain surface reactions; Willacy & Langer (2000) include detailed surface chemistry while Aikawa et al. (1999) only include surface formation of H_2 molecules and recombination of ions and electrons and adopt an artificially low sticking probability S = 0.03 instead of the detailed treatment of non-thermal desorption performed by Willacy & Langer (2000). These differences affect the molecular distributions as functions of disk height and radius, but do not greatly effect the average abundances of the major species, including CO, CN, HCN, and HCO^+, which are consistent with the observed abundances of these species in disks (e.g., DM Tau, Guilloteau & Dutrey, 1998; Dutrey et al., 1997; L1157, Goldsmith et al., 1999).

Recently, chemical models of disks have been expanded to include singly deuterated molecules by assuming that the reaction rates are identical to their hydrogen-bearing counterparts (Aikawa & Herbst, 2001; Aikawa et al., 2002). The chemical reactions involving these deuterated molecules include normal exothermic and dissociative recombination reactions (assuming statistical branching ratios) and a subset of deuterium exchange reactions, involving molecular ions and HD, that are predicted to proceed in disks based on theoretical or laboratory studies. Additionally, Aikawa et al. (2002) incorporate a vertical temperature gradient as calculated by D'Alessio et al. (1999). This is the first detailed disk chemical model including deuterated molecules and so will be used for comparison with our observations, although we note that (as discussed above) this model does not include a detailed treatment of grain surface reactions or non-thermal desorption mechanisms.

This model suggests that deuterium fractionation in disks should be similar to that in molecular clouds, beginning with the enrichment through rapid ion exchange reactions and then propagating to other molecules, primarily through ion-molecule chemistry (Millar et al., 1989). Additionally, if the molecular ions which are enriched in deuterium undergo dissociative electron recombination, resulting in a high atomic D/H ratio, then the deuterium enrichment can propagate via neutral-neutral reactions. The distribution of HDO and DCN in disks is determined primarily by the specific formation mechanisms of these species. The Aikawa & Herbst (1999) model predicts that HDO is formed via formation of H_2DO^+ in the following reaction network:

$$CH_4D^+ + O \rightarrow H_2DO^+ + CH_2 \tag{4.6}$$

$$H_2O + H_2D^+ \rightarrow H_2DO^+ + H_2 \tag{4.7}$$

$$H_2D^+ + O \rightarrow OD^+ + H_2 \rightarrow HDO^+ \xrightarrow{\mathrm{H_2}} H_2DO^+ + H \tag{4.8}$$

$$H_2DO^+ + e^- \rightarrow HDO + H. \tag{4.9}$$

Thus, the production of H_2D^+ is pivotal in the formation of HDO. Because the reaction H_3^+ + HD $\rightleftharpoons$ H_2D^+ + H_2 is very sensitive to temperature, the HDO/H_2O ratio will increase dramatically at larger radii and colder temperatures. Near the midplane, depletion of neutral molecules, CO in particular, leads to increased deuterium enrichment as the reactions H_2D^+ + CO → DCO^+ + H_2 and H_2D^+ + CO → HCO^+ + HD are the dominant destruction mechanisms for H_2D^+ at high densities, versus electron recombination or reaction with H_2 at low densities. HDO is therefore predicted to increase as a function of radius in the disk (peaking near R∼200 AU), due to reduced production of HDO near the central star as H_2D^+, the primary precursor to HDO, is destroyed. This scenario naturally explains the double peaked HDO emission observed here (Figure 4.3).

The production of DCN is complicated by the fact that several ion-molecule reactions do not produce a statistical balance of deuterated and H-bearing products:

$$HCN + H_2DO^+ \rightarrow HCND^+ + H_2O \tag{4.10}$$

$$HCN + H_2DO^+ \rightarrow HCNH^+ + HDO \tag{4.11}$$

$$HCN + H_2DO^+ \not\rightarrow DCNH^+ + HDO \tag{4.12}$$

$$HCND^+ + e^- \rightarrow HCN + D \tag{4.13}$$

$$HCND^+ + e^- \not\rightarrow DCN + H. \tag{4.14}$$

Thus, the primary mechanisms for production of DCN involve the grain-surface reactions,

$$(a) \quad H_2CN + D \rightarrow HCN + HD \tag{4.15}$$

$$(b) \quad H_2CN + D \rightarrow DCN + H_2, \tag{4.16}$$

with a branching ratio (a:b) of 5±3 (by experiment; Nesbitt et al., 1990), and the gas-phase reactions

$$CH_2D^+ + N \rightarrow DCN^+ + H_2 \tag{4.17}$$

$$DCN^+ + e^- \rightarrow DCN \tag{4.18}$$

$$DCN^+ + H_2 \rightarrow DCNH^+ + H \tag{4.19}$$

$$DCNH^+ + e^- \rightarrow DCN + H. \tag{4.20}$$

Reactions 4.15, 4.16 and 4.17 are dependent on the grain surface formation of H_2CN and hydrocarbons (CH_4 and CH_3), respectively, and on the subsequent desorption of these molecules into the gas phase. Thus the DCN/HCN ratio is therefore expected to peak at warmer temperatures than the HDO/H_2O ratio, and so Aikawa & Herbst (2001) predict that HDO and DCN will have differing distributions as a function of radius and height (c.f. Figure 2 in Aikawa & Herbst, 2001).

Aikawa et al. (2002) note that D/H ratios should increase with total disk mass, due to increased depletion of molecules onto grain surfaces. For this reason, it is important that the model predictions are scaled by the masses of the three disks in our sample. We simplify this by scaling the deuterated molecule abundances from Aikawa et al. (2002) by the observed abundances. For DCN, we scale by the observed abundance of HCN,

$$N_{DCN}(predicted) = (D/H)_{HCN}(modeled) \times N_{HCN}(observed) \tag{4.21}$$

Because H_2O has not been observed for the disks in our sample, another proxy for the disk mass is required. CO is often used as a proxy for H_2 and the total disk mass. However, disk masses derived from CO isotopomers with standard dense cloud abundances were up to two orders of magnitude less than the minimum mass inferred from dust emission (Beckwith et al., 1990; Qi, 2001). This is likely due to strong depletion of CO onto grain surfaces. Additionally, previous observations of LkCa 15 (Qi et al., 2003) indicate although the predictions of Aikawa & Herbst (2001) for CO and HCO^+ are close to the observed quantities, those for CN and HCN disagree by up to 2 orders of magnitude. In the calculation of N_{HDO}(predicted) we therefore use both the observed CO and HCN abundances as proxies for the disk mass and scale by the ratio of the observed-to-modeled abundances for each.

$$N_{HDO}(predicted) = N_{HDO}(modeled) \times N_{HCN}(observed)/N_{HCN}(modeled) \tag{4.22}$$

$$N_{HDO}(predicted) = N_{HDO}(modeled) \times N_{CO}(observed)/N_{CO}(modeled) \tag{4.23}$$

Using the modeled abundances of DCN, HCN, HDO and CO and previously observed column densities of HCN and CO in the disks in our sample (Qi, 2001), we can predict the column densities of DCN and HDO that are required to be consistent with the Aikawa et al. (2002) model. The modeled column densities are presented in Table 4.3. These are average abundances obtained from Aikawa et al., 2002 for radii from 100 AU to 400 AU, where the outer radius is consistent with CO observations toward LkCa 15, HD 163296 and MWC 480 (Qi, 2001; Table 4.1). As the ^{12}CO and HCN J=1-0 transitions are expected to be optically thick, Qi (2001) obtained ^{12}CO and $H^{12}CN$ abundances from observations of ^{13}CO 1-0, $C^{18}O$ 1-0, HCN 1-0 and $H^{13}CN$ 1-0. In our calculations the rarest isotope detected for each species was used to calculate its molecular abundance, and interstellar $^{12}C/^{13}C$ and $^{12}C/^{18}C$ ratios of 60 and 500 were applied (Table 4.3).

The resulting predictions for the column densities of DCN and HDO for the disks in our sample are close to the observed column densities (Table 4.4) for HDO and DCN where the modeled abundances have been scaled by HCN abundances as calculated from the observed $H^{13}CN$ 1-0 emission. This indicates that HCN 1-0 is optically thick in these disks, and that $H^{13}CN$ 1-0 is a better tracer of the disk mass. This is confirmed by single dish observations of LkCa 15 and a one-dimensional LVG analysis of HCN 1-0 and $H^{13}CN$ 1-0 (van Zadelhoff et al., 2001). The column densities of HDO

Table 4.3. CO and HCN column densities.

Star	N_{HCN}(obs)	N_{CO}(obs)
LkCa 15	5.34×10^{13c}	1.65×10^{18a}
HD 163296	1.38×10^{13}	1.35×10^{18b}
MWC 480	4.07×10^{13c}	1.39×10^{18b}

[a]from $C^{18}O$ 1-0 observations

[b]from ^{13}CO 1-0 observations

[c]from $H^{13}CN$ 1-0 observations

Note. — Observed column densities were obtained from Qi (2001), with the exception of the $H^{13}CN$ 1-0 observations toward LkCa 15 presented in this chapter.

Table 4.4. Observed and predicted column densities.

Star	N_{HDO}(obs)	N_{HDO}(pred)	N_{DCN}(obs)	N_{DCN}(pred)
LkCa 15	5.74×10^{15}	2×10^{13a}-3×10^{15b}	$< 3.06 \times 10^{12}$	2×10^{13}
HD 163296	$< 2.76 \times 10^{17}$	1×10^{13a}-6×10^{13b}	1.30×10^{12}	3×10^{11}
MWC 480	4.18×10^{14}	1×10^{13a}-9×10^{15b}	-	5×10^{13}

[a]Predicted using $N_{CO}(observed)/N_{CO}(modeled)$

[b]Predicted using $N_{HCN}(observed)/N_{HCN}(modeled)$

Note. — Predicted column densities were calculated from modeling done by Aikawa & Herbst (2001) and the observations of Qi (2001)

are underestimated by two orders of magnitude when scaled by the CO column density inferred from $C^{18}O$ 1-0. This difference may be related to the fact that CO is better predicted by Aikawa et al. (2002) for the observed sources than CN and HCN. They suggest that this can be rectified by including the dissociation of CO by interstellar and stellar UV radiation, resulting in increased atomic carbon, and thus CN, in photodissociation regions. This would also result in increased abundances of HDO, since HDO is deuterated through reactions involving H_2D^+, which is destroyed by CO. The treatment of CO photodissociation in the model will have a large effect on the relationship between the predicted CO and HDO (and CO and CN) column densities. Thus, scaling the modeled column densities by HCN more correctly predicts the HDO column densities than does scaling by CO.

4.5 D/H ratios

The ratios of the column densities of deuterated and hydrogenated species are presented in Table 4.5. We have not included $(D/H)_{H_2O}$ for HD 163296 or MWC 480 because we did not detect HDO in these sources and there are no previous observations of water in these disks. The $(D/H)_{H_2O}$ for LkCa 15 is calculated using the predicted column densities for H_2O from the previous section, scaling by the ratio of the observed-to-modeled HCN abundances. The $(D/H)_{DCN}$ ratios are calculated directly from the observed HCN upper limits (for HD 163296) or $H^{13}CN$ abundances (for LkCa 15). We have added the $(D/H)_{HCO^+}$ ratio obtained for the face on disk around the T Tauri star TW Hya (van Dishoeck et al., 2003) to the table for comparison. $(D/H)_{HCO^+}$ in TW Hya is similar to $(D/H)_{H_2O}$ in LkCa 15 and $(D/H)_{HCN}$ in HD 163296, but quite different from $(D/H)_{HCN}$ in LkCa 15. This can be explained by differences in the formation mechanisms of these deuterated species. $(D/H)_{HCO^+}$ and $(D/H)_{H_2O}$ can be expected to be similar in the two T Tauri star disks, because both DCO^+ and HDO are deuterated through H_2D^+ via the highly temperature-dependent reaction,

$$H_3^+ + HD \rightleftharpoons H_2D^+ + H_2 \qquad \Delta E = 230\ K \tag{4.24}$$

At warm temperatures, the reverse reaction becomes more important, and as H_2D^+ is destroyed and $(D/H)_{H_2O}$ and $(D/H)_{HCO^+}$ decrease (Aikawa & Herbst, 2001). $(D/H)_{H_2O}$ and $(D/H)_{HCO^+}$ are also highly dependent on the presence of X-rays and gas-phase CO and H_2, which destroy H_2D^+ (Aikawa & Herbst, 1999). So, for sources with similar conditions (temperature, depletion, etc.) we would expect the $(D/H)_{HCO^+}$ and $(D/H)_{H_2O}$ ratios to be similar. DCN, however, is formed via mechanisms that are very different then the formation of HDO and DCO^+. The major formation pathways of DCN are the reactions of D and H_2CN on grain surfaces and of CH_2D^+ and N in the gas phase, following grain-surface formation of CH_4 or CH_3. The production of DCN is therefore tied to chemistry on, and desorption from, grain surfaces. DCN is also formed by the reaction of N with CHD and HCN via the reaction of N with CH_2. Because the CH_2 is formed more quickly than CHD, $(D/H)_{HCN}$ is also believed to be strongly dependent on the disk age (Aikawa & Herbst, 1999). All of these mechanisms indicate that $(D/H)_{HCN}$ should increase with moderate increases in temperature as $(D/H)_{H_2O}$ and $(D/H)_{HCO^+}$ decrease. The larger $(D/H)_{HCN}$ ratios in the HD 163296 disk (and perhaps also the non-detection of HDO toward this disk) with respect to the K star LkCa 15 may be explained by differing stellar luminosities and hence disk temperatures.

The D/H ratios in the two disks can be compared to those of molecular clouds, hot cores and our solar system. The ratios vary slightly from disk-to-disk and lie within the range of D/H ratios found in molecular clouds and hot cores. All four of these D/H ratios are much larger than that of the early solar nebula (10^{-5}) and consistent with deuterium abundances in comets. Therefore, conclusions from previous observations, which stated that comets were assembled from interstellar material, can

Table 4.5. D/H ratios in disks.

Star	molecule	D/H
LkCa 15	HCN	<0.001
-	H_2O	0.0001–0.064
HD 163296	HCN	>0.094
TW Hya	HCO^+	0.035

Note. — The upper limit for $(D/H)_{H2O}$ was calculated from model abundances of H_2O (Aikawa & Herbst, 2001) scaled by ratios of observed-to-modeled HCN abundances. The lower limit for $(D/H)_{H2O}$ was calculated from nondetections of $H_2{}^{18}O$ using OVRO.

be adapted to state that comets could be formed in or with material that passed through the outer regions of disks where the conditions are more similar to interstellar clouds than nebular regions near proto-Jovian planets.

4.6 Image modeling

Molecular distributions are essential to understanding the chemistry taking place in disks. The HDO emission observed here, as well as previous observations toward LkCa 15 (Qi, 2001), indicates large differences in the morphology of the emission in the integrated intensity maps (Figure 4.5). CO and HCO^+ emission peak at the source position while the HCN, CN and HDO emission peak approximately 2″ away along the major axis of the disk. This is especially interesting because the spectra for CO 2-1, HCO^+, HDO and HCN do not differ significantly. Lack of emission toward the star results in only small changes to the line wings, which are buried in the noise in the HDO spectrum, but may be slightly more visible in the higher signal-to-noise HCN spectrum. Clearly, imaging is necessary to study this type of disk structure and there is a need for detailed models which can be used to reproduce and interpret these images.

For this reason we have created a model to simulate our observed channel maps and images of protoplanetary disks (see Chapter 2). The temperature and hydrogen density distributions are determined using physically self-consistent disk models of D'Alessio et al. (2001), assuming a power law distribution of dust sizes ($n(a) = a^{-3.5}$), an accretion rate of 10^{-8} $M_\odot$/yr and equal dust and gas temperatures. The stellar parameters are specific for LkCa 15 ($M_* = 1.0$ $M_\odot$, $R_* = 1.64$ $R_\odot$, $T_* = 4395$ K). The resulting physical disk model is then combined with the distribution of the

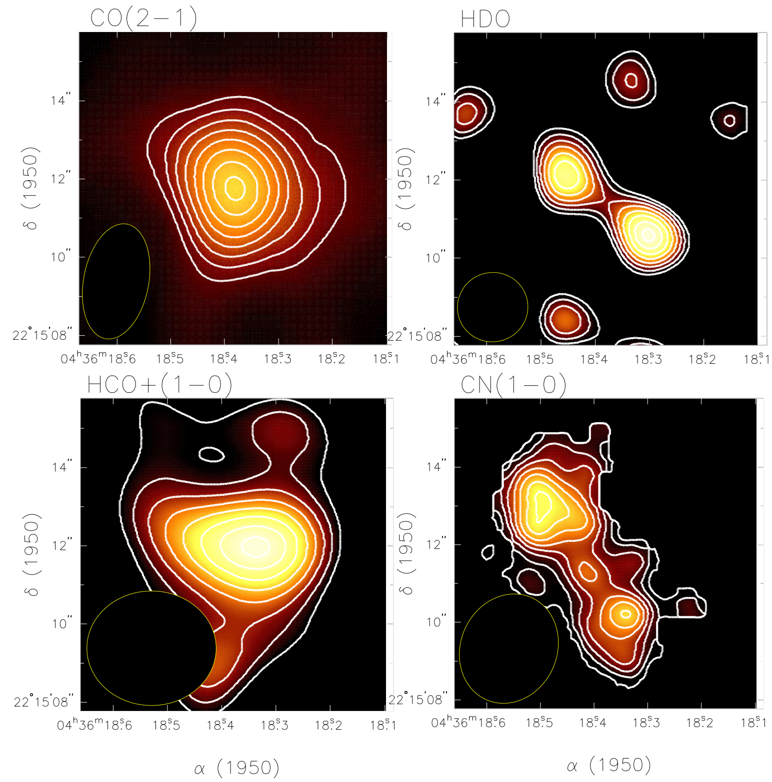

Figure 4.5 OVRO observations of CO (kindly provided by Koerner and Sargent), HDO, HCO^+ and HCN toward the T Tauri star LkCa 15. While CO and HCO^+ are centered at the stellar position, CN, HDO and HCN (not shown) peak $\sim 2''$ away.

molecule of interest and the radiation transfer in the disk is calculated using a non-LTE Monte Carlo code (Hogerheijde & van der Tak 2001). The input parameters for this model are the mass and inclination of the disk, determined from previous observations of the continuum and CO emission toward this source (Beckwith et al., 1990, Duvert et al., 2000). The inner and outer radius of the disk (R_{out} = 430 AU) and turbulent velocity width (0.1 km/s) are parameters which are adjusted to fit our observed CO 2-1 emission spectrum (Qi et al., 2003). The initial results of our model are equivalent to the observations of a telescope with essentially infinite resolution and complete (u, v) coverage. The map is then convolved with the (u, v) sampling obtained, in order to simulate the OVRO observations more explicitly. We will now use these models to interpret our HCN and HDO observations.

The chemical models of Aikawa & Herbst (2001) and Willacy & Langer (2000) suggest that the radial distribution of HCN and CN in disks is determined by the processes of photodissociation by interstellar and stellar UV combined with desorption from grain surfaces. The newest models (Aikawa et al., 2002) suggest that the competition between interstellar and stellar UV in particular determine the variation in the amount of HCN as a function of radius. We simulate the emission morphology discussed above by concentrating the HCN in a ring around the star. We use a simple

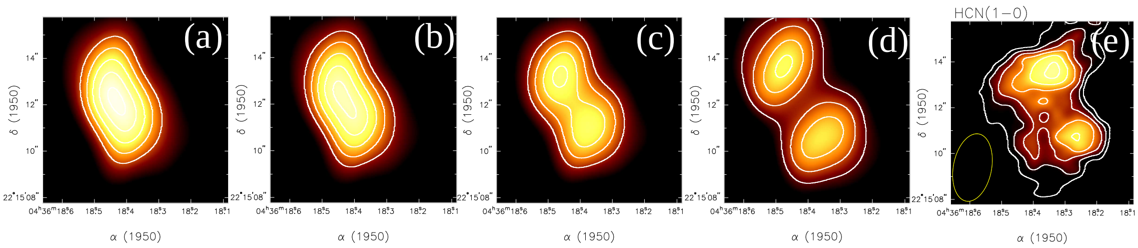

Figure 4.6 Model fits to the HCN J = 1-0 emission from LkCa 15. The observed HCN emission (e) is compared to a model of an annulus of HCN with an outer radius of 400 AU and an inner radius of 50 (a), 100 (b), 200 (c) and 300 AU (d). In each case, the total flux of the model image is set to match the observed HCN map. The observed emission is consistent with an inner radius between 200 AU and 300 AU (i.e., between (c) and (d)).

model, with an outer region in which the column density is constant and the volume density is proportional to that of hydrogen and an inner region in which the column density is zero. We then set the outer radius of the annulus to the disk radius as determined from the CO 2-1 observations (∼430 AU) and vary the inner radius to match the observed integrated intensity maps. In each case the column density of HCN in the ring is set by matching the integrated flux of the modeled map to that observed. As we vary the inner radius we can see that these models can reproduce the structure of the HCN emission only with large depletion zones in the disk center ($R_i \sim$ 200–300 AU). More realistic models that incorporate radial gradients in molecular abundances will be used in the future to simulate the combined effects of desorption from grains and photodissociation of HCN from interstellar and stellar UV.

Although we have not yet modeled the HDO emission, the observed double-peaked emission map may also result from a ring-like distribution (or a steep gradient). Here models suggest that the annulus could be formed due to reduced production of HDO near the star as H_2D^+, the primary precursor to HDO, is created less efficiently due to the increasing temperature gradient in the inner disk. This causes the HDO abundance to peak at R≈250 AU (Aikawa & Herbst, 2001), and as the previous HCN models show, this morphology is consistent with the observed emission.

4.7 Future observations

The observations presented here are severely limited by the sensitivity of current millimeter arrays, especially in the 1 mm window. Although these disks were chosen because of previously observed strong emission from several molecular lines at 3 mm, the observed emission from deuterated species is very weak, on the order of 1.5–3σ for all deuterated molecules, and HDO in HD 163296 and MWC 480 and DCN in LkCa 15 were not detected. From this analysis, it is clear that detailed study of deuteration in disks requires either observations of the same deuterated/hydrogenated molecule in several disks or observations of several deuterated species in a single source. Due to the non-detections of HCN in HD 163296 and DCN in LkCa 15, the D/H ratios obtained represent only lower and upper limits, respectively. Additionally, because water has not been observed toward these three sources, the calculation of the $(D/H)_{H_2O}$ and the interpretation of HDO observations depend largely on model predictions for water abundances. Future millimeter arrays, such as ALMA, will offer vast improvements in sensitivity, and will undoubtedly make studies such as those presented here obsolete. In the near future, the Combined Array for Research in Millimeter Astronomy (CARMA) will make these studies much more efficient. For example, the observations of HDO in LkCa 15 presented here, which represents approximately 40 hours of observing time with OVRO, could be done in 5 hours with CARMA[2].

Although future arrays offer promise for the study of deuterium enrichment in disks, the next step for these studies can be pursued with current instrumentation. Water and HCN (as well as their isotopomers) are frozen out onto grain surfaces in the midplane of disks and therefore the observations of HDO and DCN presented here only serve as an effective probe of D/H ratios in disk surface layers. Observations of molecules that are believed to remain in the gas phase within the disk midplane, specifically ions (DCO^+, N_2D^+ and H_2D^+) can be used to probe planet forming regions. Additionally, D/H ratios are predicted to be much higher in the disk midplane as molecules which typically react to destroy these ions are depleted onto grain surfaces. DCO^+ is a good candidate for millimeter observations because, HCO^+ has been readily observed in large quantities in disks (Qi, 2001; this thesis), and predict column densities of DCO^+ on the order of 10^{12} cm^{-2}. Additionally, as mentioned earlier, DCO^+ has already been observed in the circumstellar disks around TW Hya and, more recently, DM Tau in single dish observations at the JCMT (Thi et al., 2001) and IRAM 30m telescope (Dutrey, 2003). Observations of N_2H^+ with OVRO (Qi et al., 2003) suggest N_2D^+ column densities of $\sim 10^{11}$ cm^{-2}. H_2D^+, which is an isotopomer of H_3^+, the most abundant ion and the cornerstone of ion-molecule chemistry, resides in the ground para state at typical disk midplane temperatures. The strongest transition of H_2D^+ in disks lies at 1370 GHz, and is an excellent project for the CASIMIR instrument on SOFIA. The calculation of HDO/H_2O ratios in our study was limited by the lack of H_2O detections in disks. This will soon be remedied by the HIFI instrument on Herschel, which will be used to perform an extensive survey of strong H_2O lines in many sources, including planet-forming disks.

4.8 Summary

We present the first observations of DCN and HDO toward circumstellar disks. Images of HDO in the T Tauri star LkCa 15 show emission which is consistent with an annulus of inner radius 200 AU and outer radius 400 AU. This is consistent with our current understanding of disk chemistry,

[2] *http://www.mmarray.org*

which suggests that the HDO distribution is actually a gradient as a function of distance from the star and peaks at $\sim$300 AU. The sensitivity of the observed morphology to the steepness of this gradient will be further explored in future work. D/H ratios in disks, including those reported here along with observations of DCO^+ toward the T Tauri star TW Hya, are similar to that of hot cores and molecular clouds and comets, which is consistent with comet formation in the outer regions of disks. Future observations of deuterated ions (H_2D^+ and N_2D^+) should probe much closer to the disk midplane and constrain the deuteration in these regions. With more sensitive, high-resolution arrays such as CARMA and ALMA, we will be able to expand our studies to include more molecules and probe the inner, planet-forming regions of circumstellar disks.

Chapter 5

8–13 μm spectroscopy of YSOs: Evolution of the silicate emission feature

Abstract

In this study, 8–13 μm spectra of $\sim$ 20 stars ranging from YSOs to debris disks and spectral types from A to M were obtained using the Long Wavelength Spectrometer at the W. M. Keck Observatory. The evolution of the silicate feature from absorption in young, embedded sources, to emission in isolated stars and complete absence in older "debris" disks seen in ISO observations of high/intermediate-mass YSOs (Meeus & Waelkens, 1999) is extended here to $\sim$ solar mass stars. In a few objects, the silicate feature is more complex, with absorption near 9.5 μm and emission peaking around 10.3 μm. These sources appear to be at a transitional stage where the star is just becoming visible in the optical. In addition, there appears to be a marked difference between intermediate mass Herbig Ae stars and solar mass T Tauri stars of the same age. For some, but not all, of the Herbig Ae stars in the sample, the emission feature has a bump at $\sim$11 μm, similar to the emission from crystalline silicates seen in comets and the debris disk β Pictoris. All of the T Tauri stars, however, show the classical emission/absorption features which have been attributed to amorphous silicates, although some T Tauri stars show a silicate feature which is much broader than that from the diffuse ISM. It is unclear whether crystalline silicates are truly absent in T Tauri stars, for colder or larger crystalline silicate grains would not emit strongly in the 8–13 μm region, but may be visible through far-infrared lattice modes accessible from space born observations.

5.1 Introduction: Silicates and star formation

Models of dust condensation processes from an initially hot gas (Grossman, 1972, Gail, 1998; Finocchi et al., 1997; Finocchi & Gail, 1997) suggest that grains in the interstellar medium, and thus in the early stages of star formation, are primarily composed of amorphous silicates, particularly olivines ($Mg_{2x}Fe_{(1-x)}SiO_4$, or ortho-silicates), ranging from fayalite ($x = 0$) to forsterite ($x = 1$), and orthopyroxenes ($Mg_xFe_{(1-x)}SiO_3$, or meta-silicates), ranging from ferrosillite ($x = 0$) to enstatite ($x = 1$). Conversions between Fe and Mg dominated silicates are controlled by the reactions,

$$MgSiO_3(s) + (1-x)Fe \quad \leftrightarrow \quad Mg_xFe_{(1-x)}SiO_3(s) + (1-x)Mg \tag{5.1}$$

$$Mg_2SiO_4(s) + 2(1-x)Fe \quad \leftrightarrow \quad Mg_{2x}Fe_{2(1-x)}SiO_4(s) + 2(1-x)Mg, \tag{5.2}$$

such that at high temperatures, the iron component is essentially distilled off from the solution, leaving olivines that are nearly pure forsterite and orthopyroxenes that are nearly pure enstatite–substantial amounts of ($Fe_{1-x}SiO_{3,4}$) remain only at T < 200 K. In a gas of solar composition, transitions between the ortho- and meta-silicates occur via the reaction,

$$Mg_2SiO_4(s) + H_2(g) \quad \leftrightarrow \quad MgSiO_3(s) + Mg + H_2O, \tag{5.3}$$

such that the conversion is controlled by

$$f_o = \frac{\epsilon_{Mg} - \epsilon_{Si} K_c^3 K_p}{(2 + z - (1+z)K_c^3 K_p)\epsilon_{Si}}, \tag{5.4}$$

where f_o is the fraction of ortho-silicates, z is the ratio of meta- to ortho-silicates, ϵ_{Mg} and ϵ_{Si} are the abundances of Mg and Si (relative to H), and K_c and K_p are equilibrium constants for reaction 5.3 at standard concentration and constant pressure. Thus, the fraction of meta- versus ortho-silicates depends on both the temperature and pressure and only for a very narrow region in P-T space does the ortho-silicate (i.e., forsterite) form a significant fraction of the mixture. For a given pressure, the meta-silicate (i.e., enstatite) dominates at low temperatures and decreases with increasing temperature if equilibrium prevails.

Interstellar dust consists of particles from wide range of sources (stellar atmospheres, novae, supernovae). Olivine dominates over orthopyroxene, observationally, and high-energy rays and low temperatures are expected to result in amorphous mixtures of the two. Indeed, strong, smooth features at 9.7 and 18.5 μm, corresponding to the Si-O stretching and bending modes, respectively, are observed to arise from absorption of background light by dust in the diffuse interstellar medium (Bouwman et al., 2001). Molecular clouds also possess a mixture of amorphous olivine and pyroxene, which may be covered with carbonaceous or organic material and ice at sufficiently high extinctions (i.e., densities; Gibb et al., 2000). Silicates are expected to be amorphous in molecular clouds as well, due to cosmic ray impacts, and a broad structureless band centered at 10 μm is observed toward several objects. In contrast, solar system dust (cometary grains, IDPs, CAIs) and dust surrounding main sequence stars contain crystalline silicates, with olivine and enstatite as the dominant components, similar in composition (but not structure) to star-forming regions. The crystallization process is believed to be predominantly thermally controlled.

At high temperatures (T∼1200 K), annealing of anhydrous silicates begins with thermal diffusion of impurities, with mobilities dependent on atomic size. The impurities assemble, leaving local order and microcrystalline lattice structures within the silicates. If the annealing lasts a suffuciently long time, or if the temperatures are hot enough, crystallization begins at critical nuclei. In laboratory experiments, silicate smokes annealed at T = 1200 K develop local order in domains of 1 nm within 1 day (Nuth & Donn, 1982). The evolution of a silicate grain with increasing temperature is expected to proceed as follows (Gail, 1998),

$$amorphous \rightarrow polycrystalline \rightarrow enstatite \rightarrow forsterite. \tag{5.5}$$

The presence of crystalline silicates is thus expected in high-temperature condensates in meteorites, such as CAIs. IDPs are produced by impacts, collisions and/or disintegrations of small bodies and the release, by sublimation, of refractory grains frozen in cometary nuclei, so the presence of crystalline silicates can also be easily explained in these particles. Short- and long-period comet spectra show emission from both crystalline and amorphous silicates, though the crystalline fraction can vary significantly (Hanner et al., 1994; Knacke et al., 1993; Skinner et al., 1992; Fajardo-Acosta et al., 1993; Knacke et al., 1993; review by Wooden, 2002). These results are particularly interesting as they indicate that although some crystalline material may be made when comets pass close to the sun, a substantial fraction must have been crystallized before comets were formed. The abundances of crystalline silicates found in some comets are too high (up to 30%), however, to be accounted for by crystalline silicates in the ISM (<5%), indicating that they were formed around protostars, most likely in circumstellar disks. The presence of crystalline silicates in *both* short- and long-period comets further suggests the presence of long range mixing processes required to bring crystalline grains (annealed at >1000 K) into the colder parts of the disk in which comets form.

Clearly, planet-forming disks are the place to look for the *in situ* crystallization of silicates. In the simplest scenario, amorphous silicates from the interstellar medium enter the accretion disk and are modified depending on their distance from the star, with crystallization of the dust dependent on the exposure to stellar radiation or the age of the disk. The silicates in the outer disk are expected to accrete icy mantles and retain cores that are similar to ISM dust, composed primarily of amorphous olivine and pyroxene. In warmer regions ($T > 1000$ K), annealing leads to crystallization. The diffusion processes start in regions relatively close to the star (the exact distance depends on the stellar luminosity), and result in the conversion of the amorphous lattice structure. At radii corresponding to temperatures above 1000 K, the dust grains should possess regions of localized crystallization that are detectable in the IR; at radii corresponding to $T > 1500$ K, 0.1–1 μm grains should be completely crystallized.

The properties of dust grains in accretion disks therefore must be significantly modified with respect to those of the ISM in order to reproduce silicate observations (D'Alessio et al., 2001). The observed differences in the silicate spectra of interstellar versus solar system dust appears to be an evolutionary sequence, in which the composition of the grains gradually changes from amorphous olivine to crystalline forsterite (as noted above) during the star formation process. Data returned from the Infrared Space Observatory (ISO) enabled the detection of spectra from several intermediate mass (>1 $M_\odot$), Herbig Ae/Be protostars (hereafter referred to as HAEBE) at a range of ages and stellar evolutionary stages, and an evolutionary sequence based on the 2 to 45 μm spectrum has been suggested (Meeus & Waelkens, 1999). The sequence begins with rising featureless spectra indicative of dense cloud cores (i.e., Cep A IRS6); spectra in the second category possess strong absorption by amorphous silicates near 10 μm and are attributed to embedded protostars (Z CMa). Emission from warm silicates near 10 μm and prominent cold dust emission longward of 15 μm (HD 100546) defines the third category, which is likely composed of objects with optically thick protoplanetary disks (known as Class II objects). For several sources (i.e., HD 104237; category 4), warm silicate emission is seen without the cold component and is interpreted as arising from disks undergoing planet formation. Finally in the oldest sources, the spectrum is close to photospheric (i.e., HD 139614) indicating dispersal of most of the circumstellar dust.

ISO and ground based observations have detected crystalline silicate emission bands (11.3, 27.5, 33.5, 35.8 and 70 μm) toward a large sample of class II HAEBE stars (Molster et al., 1999; Meeus et al., 2001) and toward the "debris" disk β Pictoris (Knacke et al., 1993). The emission bands at 27.5, 33.5, 35.8 and 70 μm are highly dependent on the structure of the dust and these studies show large variations in dust crystallinity and composition among YSOs of similar age and stellar properties (Meeus et al., 2001; van den Ancker et al., 2000), indicating the necessity for large samples for the determination of a general theory of disk evolution. However, the differences between the silicate emission features in HAEBE are complex functions of the grain size and composition as well as the disk morphology and optical depth (Meeus et al., 2001; Bouwman et al., 2003; van Boekel et al., 2003). The emission features arising from the dust in HAEBE star disks can be reproduced by models with varying amounts of olivine, forsterite, enstatite and silica and with mixtures of 0.1–2 μm sized grains. Additionally, it was found that grain shape plays a large role in the interpretation of silicate spectra, particularly for strong crystalline bands (Fabian et al., 2001). A combination of spherical and ellipsoidal grains are required to reproduce observed spectra.

Observations from the ISO satellite also indicate the presence of two distinct end member dust populations in the young star HD 142527 (Malfait et al., 1999), including warm (500–1500 K), crystalline silicates with narrow features at 11.3 μm and cold (30–60 K), hydrous semi-crystalline silicates (silicate layers separated by layers of cations and interstitial water), with strong, broad emission that contributes to the far-IR continuum longward of 50 μm. Additionally, large amounts of crystalline water ice are indicated from strong emission features around 44 and 55 μm. Although the amorphous-to-crystalline transition requires high temperatures (T$\sim$1500 K), several other young stars also have been shown to possess cold crystalline silicates (i.e., HD 100546; Bouwman et al., 2003). These observations and those of crystalline silicates in comets indicate that radial mixing may be important as a method of transfer material outward from the warm, inner regions of the disk. Mechanisms for cold crystallization processes have also been suggested. For example, observations indicating copious amounts of water ice and hydrous silicates have been used to suggest aqueous alteration of grains as a crystallization mechanism in circumstellar disks. Collisions might also transiently generate high densities and/or temperatures in the outer disk, which could lead to crystallization in the Class II/III phase.

Observations of silicate emission from older stars have been particularly revealing. As small dust is expected to be cleared from T Tauri and Herbig Ae disks on timescales less than 10^7 years, the material in disks older than 10^7 yr is expected to be "second generation" debris from the collision of planetesimals. β Pictoris is a late type (12^{+8}_{-4} Myr; Zuckerman et al., 2001) A star, whose IR and optical (HST) images have been fit with the model of a warped disk, thought to be indicative of planet formation (Mouillet et al., 1997; Weinberger et al., 2003). The IR spectrum observed (Knacke et al., 1993) exhibits a remarkable resemblance to that of solar system grains and comets, suggesting the presence of a mixture of crystalline and amorphous material and a possible connection between the crystallization of silicates and the formation of planets. Recently, spatially resolved IR spectroscopy of β Pic (Weinberger et al., 2003) revealed that the silicate emission arises only from dust within $0''.8$ of the star. Furthermore, the dust composition (a mixture of amorphous and crystalline dust) appears to remain constant throughout this region. Models of the dust in the disk surrounding the HAE star HD 100546 have been used to demonstrate that collisional destruction of differentiated objects is a possible production mechanism for small crystalline grains. This hypothesis is supported by an absence of thermal contact between the chemical constituents of the dust and an increase in the fraction of crystalline silicates with *increasing* distance from the star. The presence of substantial emission from a small grains (<10 μm) with temperatures of $\sim$200 K suggest a puffed up disk at 10 AU from the star, supporting the idea that the disk has been cleared by planet formation processes.

Although ISO observations have significantly improved our understanding of the composition of circumstellar dust, there are still many questions to be answered. For the most part, due to lack of sensitivity, the ISO observations probed only disks around relatively high-mass, luminous stars. It is unclear whether the dust compositions or disk morphologies will be similar for $\leq$solar mass stars. The large collecting area and therefore increased point source sensitivity of ground based telescopes make them especially valuable tools in the detection of silicate emission from low-mass young stellar objects, which were virtually unprobed by ISO. Additionally, high spectral resolution studies of the warm dust emission (near 10 μm) are vital in understanding the processing of dust necessary to produce the two populations discussed above and observations of mid-infrared dust emission are a useful means of investigating the dust composition in the pivotal planet-forming region (1–10 AU) of circumstellar disks around young stars. Ground based observations are limited to $\lambda \leq 20$ μm, and so such studies also serve a pathfinder role for subsequent space borne observations with the next generation of cooled observatories (i.e., SIRTF and ASTRO-F).

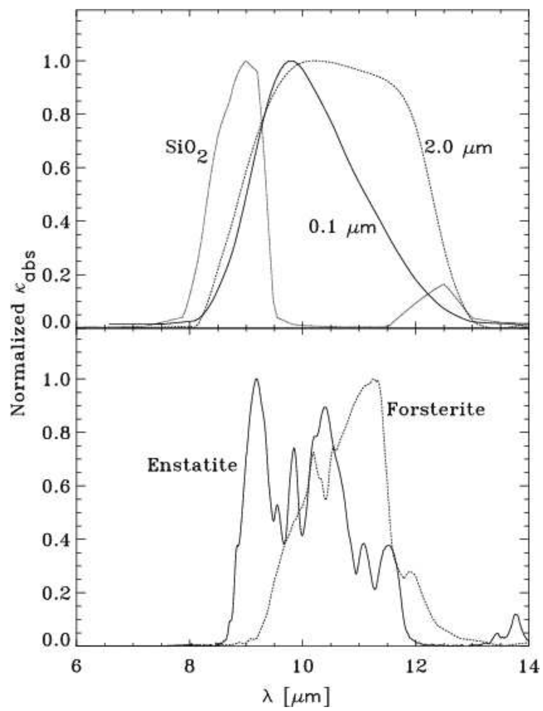

Figure 5.1 The emission properties of silicate dust grains (from Bouwman et al., 2001). Absorption coefficients are normalized and plotted vs. wavelength. The top panel shows emission from quartz and from amorphous olivine grains of two different sizes. The bottom panel shows emission from enstatite and forsterite crystals.

The dominant feature in the 8–13 μm spectrum is emission from amorphous olivine (peaking at 9.5 μm), with smaller emission features arising from silica (SiO_2; 8.6 μm) and crystalline enstatite ($MgSiO_3$; 9.2, 10.4 μm) and forsterite (Mg_2SiO_4; 10.2, 11.3 μm).[1] Thus, the trend from amorphous olivine to crystalline forsterite results in a shift of the 10 μm silicate emission feature from 9.7 to 11.3 μm (see Figure 5.1). Usually, the shift between the emission features of amorphous olivine and the 11.3 μm emission from crystalline forsterite is referred to as the amorphous-to-crystalline transition and used to classify the amount of amorphous-to-crystalline material in the disk. This sort of analysis is complicated by the fact that the strength of the silicate emission features cannot be uniquely correlated with the abundance of silicates in the disk. The presence of organics can increase the opacity at $\lambda < 6$ μm and decrease the contrast between the silicate band at 10 μm and the adjacent continuum (D'Alessio et al., 2001). Also, the width of the amorphous olivine emission feature increases substantially with grain size, with peaks decreasing in strength and spreading from

[1] The peak positions described above are for 0.1 μm grains (Meeus et al., 2001).

9.7 to 12 μm for grain sizes of 2 μm (van Boekel et al., 2003). For large grains ($a_{max} > 1$ mm), the silicate bands at 10 and 20 μm almost disappear entirely (Fabian et al., 2001). Additionally, the interpretation of emission in the 10 μm atmospheric window is complicated by the fact that ground based observations do not have enough spectral coverage to establish a reasonable continuum. The IR flux from the disk varies greatly from source to source, is often not constant across this window, and can have a large effect on the shape of the observed spectrum. There are therefore many methods which have been implemented to calculate and subtract the continuum, but a standard method has not been established.

There have been a number of surveys of ground based 8–13 μm emission from T Tauri star disks. Early surveys of emission from disks around T Tauri stars (Cohen & Witteborn, 1985; Hanner et al., 1998) appeared to indicate that the spectra of young, low-mass stars resembles that of molecular clouds, which show a rather sharp, single peak between 9 and 10 μm, very similar to that seen in the ISM, and may indicate that the dust surrounding these low-mass objects has not undergone significant processing during the collapse of the cloud and evolution of the circumstellar disk. However, 5.9–11.7 μm spectra of 9 low mass sources in Chameleon (Natta et al., 2000) display emission which is significantly broader and stronger than that of the diffuse ISM, especially at the edges of the silicate feature at 8.5 and 11.3 μm, for all stars in the sample. PAHs are not believed to significantly contribute due to the absence of standard PAH emission features at 3.3, 6.2 and 7.6 μm. Approximating the continuum using a powerlaw normalized in the 5.8–8 μm spectral region, Natta et al. (2000) find typical ratios of L_{sil}/L_* of 1–2% (except glass Ia, 10%). They also find that the spectra are consistent in 6 of 9 cases with the luminosities predicted by a simple radiation transfer model of a flared disk in hydrostatic equilibrium similar to that of Chiang & Goldreich (1997). For this model, they adopt the cross section of pyroxene, but the data can also be fit with varying compositions of olivine and pyroxene, for dust sizes of less than 1 μm (or pyroxene alone with larger grains $\sim$1 μm in size).

5.2 Sample selection

In this study, the spectra of the silicate emission feature at 10 μm toward several Herbig Ae and T Tauri objects were acquired at R = 100, using the Long Wavelength Spectrometer at the W. M. Keck observatory. The goal was to use the spectra to characterize the composition of the dust, particularly the dominance of silicates versus PAHs and the degree of crystallinity of the silicate grains present. Objects with varying age and mass were chosen in order to put this information in context with the stellar evolutionary process for both low and high-mass stars. Ten embedded YSOs were observed, including seven low mass stars chosen from Kenyon et al. (1993) and 3 well known high-mass YSOs, the Becklin Neugebauer object (BN), NGC 2024 IRS 2, and MonR2 IRS3 to provide

Table 5.1. Source parameters for Class II and Class III sources

Source	RA(J2000)	DEC(J2000)	d(pc)	M_* ($M_\odot$)	L_* ($L_\odot$)	T_{eff} (K)	Sp.Type	Age (Myr)	R_* ($R_\odot$)	Ref.
49 Cet	01 34 37.78	-15 40 34.9	61	2.4g	23.44	9333	A1V	7.8	2.30	1
HD 17925	02 52 32.129	-12 46 10.972	10.4	0.8g	-	5000	K1V	80	0.82g	3
HD 22049	03 32 55.844	-09 27 29.744	3.3	0.78g	-	5000	K2V	330	0.8g	3,4
AA Tau	04 34 55.2	+24 28 52	140	-	0.71	3981–4000	K7	2.4	0.7g	5
LkCa 15	04 39 17.8	+22 21 03	140	0.97	0.724	4350–95	K5:V	6.6–11.7	0.72	6,7
GM Aur	04 55 10.2	+30 21 58	140	0.84	0.741	4730	K5V:e	1.8	1.78	6,7,8
MWC 480	04 58 46.27	+29 50 37.0	131	2.3	23.7	8890	A2	4.6	2.1	7,9
HD 233517	08 22 46.71	+53 04 49.2	23–40	-	0.20	4170–4500	K2–K7	-	0.7g	-
Hen 3-600A	11 10 27.9	-37 31 52	50.0	0.25	0.23	3388	M3	1.0	0.45g	10,11,12
HD 102647	11 49 03.578	+14 34 19.417	11.1	2.0g	-	8720	A3V–A8	240	2.01	4
HR 4796A	12 36 01.032	-39 52 10.219	76	2.5	35	10000	A0V	-	2.6g	13
IRAS 14050-4109	14 05 05.7	-41 09 40	-	-	-	4406	K5	-	1.39	-
HD 163296	17 56 21.29	-21 57 21.9	120	2.4	35.2	9475	A1V	5.0	2.2	9
HD 179218	19 11 11.254	+15 47 15.630	240^{+70}_{-40}	4.0	221.9	10220	B9/A0/IV/Ve	0.3	4.7	15,16
WW Vul	19 25 58.75	+21 12 31.3	550	2.9	43	8600	A3e/B9V	-	2.4	17
HD 184761	19 34 58.97	+27 13 31.2	65	2.0g	18.3g	7500	A8V	-	1.5g	18
HD 216803	22 56 24.0529	-31 33 56.042	7.70	-	-	4500	K4V	-	-	-

Note. — References: 1-Sylvester et al. (1996), 2-White & Ghez (2001), 3-Habing et al. (2001), 4-Glass (1975), 5-Thi et al. (2001), 6-Qi (2001), 7-Simon et al. (2001), 8-Kenyon & Hartmann (1995), 9-Mannings & Sargent (1997), 10-Geoffray & Monin (2001), 11-Kastner et al. (1997), 12-de La Reza et al. (1989), 13-Jura et al. (1993), 14-Natta et al. (1997), 15-Mannings & Sargent (2000b), 16-van den Ancker et al. (1998), 17-Natta et al. (2001), , 18-Miroshnichenko et al. (1999), 19-Friedemann et al. (1995), 20-Hillenbrand et al. (1992).

"internal calibrants" for this study. The latter observations should also probe the composition of largely unprocessed grains and absorption from amorphous silicates is expected. There are ten class II T Tauri and Herbig Ae stars in the sample, most of which have been studied extensively at other wavelengths and have very well characterized SEDs. ISO observations indicate that at least two Herbig Ae stars in this sample, HD 163296 and WW Vul, possess detectable amounts of crystalline silicates. As discussed above, silicate crystallization is likely occurring at this intermediate stage of stellar evolution and we would expect the most variation of crystalline silicate content with age or luminosity in this part of the sample. Seven debris (Class III) disks were also included, as classified by their optically thin IR continuum and ages older than 6 Myr and are the most likely candidates for detection of crystalline silicates, provided warm dust is present.

5.3 Photometric and spectroscopic observations

8–13 μm spectra and photometry for several intermediate and low mass stars were obtained using Long Wavelength Spectrometer (LWS) at the W. M. Keck Observatory between August 1999 and June 2000 (Table 5.2). LWS provides diffraction-limited imaging (10$''$ field of view, 0.$''$08/pixel) and spectroscopic (R = 100–1400) capabilities in the 3–25 μm wavelength range. Photometry was obtained with the 10.7 μm filter ($\Delta\lambda$ = 10.0–11.4 μm) during the nights of Feb 20–21 and Dec 9, 2000, for which the seeing was poor and variable: 0.$''$3–0.$''$6 at 10 μm (the diffraction limit is 0.$''$22). For the spectroscopic observations, the *Nwide* filter and low resolution grating (LRES) were used to obtain 8.1–13 μm spectra, with R = 100, at a dispersion of 0.037 μm/pixel. Slit widths of 3 and 6 pixels were used, resulting in 0.$''$24 and 0.$''$48 apertures, respectively. Sources were imaged prior to each spectroscopic observation to ensure optimal placement within the slit. For most spectroscopic observations, additional calibration scans were obtained using the Keck routine *LSEC*, in which the data is chopped between an ambient blackbody source (T≈274 K, the temperature of the telescope) and the sky. After normalization, these data were used as a spectral flat field in order to calibrate out grating abnormalities. Dome flats and darks were taken at the end of each night with exposure times equal to those on source. The raw six-dimensional LWS data, consisting of two nod-chop pairs, were coadded into two-dimensional images (Figure 5.2), using the IDL routine LWSCOADD[2] provided by the observatory.

The IRAF/PHOT task was used for the photometric data reduction. Apertures of radius 0.$''$96 (12 pix) were used for the photometry and the sky background was measured in 2.$''$0–3.$''$2-radius (25–40 pix) annuli. Flat-fielding was found to increase the scatter in the photometry and therefore not performed. A curve-of-growth correction of -0.12 $\pm$ 0.01 mag (based on standard star measurements) to a 1$''$.92 (24 pix) aperture was applied to each star, resulting in magnitudes within ~5% of the

[2]LWSCOADD is available at http://www.astro.caltech.edu/mirror/keck/inst/lws/lwscoadd_pro.html, provided by Gregory D. Wirth.

Table 5.2. Observations

Source	Date of Obs.	reference star	aperture	LSEC?
49 Cet	Nov 8, 2000	α Tau	6	n
HD 17925	Feb 21, 2000	HR 1017	6	y
HD 22049	Dec 10, 2000	HR 1017	6	y
IRAS 04295+2251B	Dec 9, 2000	HR 617	6	y
AA Tau	Feb 21, 2000	HR 2990	6	y
LkCa 15	Nov 30, 1999, Nov 8, 2000	α Aur [a]	6,3	n,n
GM Aur	Nov 8, 2000	α Tau [a]	3	n
MWC 480	Nov 30, 1999	α Tau	6	n
HD 233517	Nov 8, 2000	α Aur	3	n
Hen 3-600A	Feb 21, 2000	HR 4786	6	y
HD 102647	Feb 19, 2000	HR 4534	6	y
HR 4796A	Feb 21, 2000	HR 4786	6	y
IRAS 14050-4109	Feb 21, 2000	HR 4786 [a]	6	y
HD 163296	Aug 23, 1999,June 20, 2000	β Oph	6,3	n,y
HD 179218	Feb 21, 2000	HR 5908	6	y
WW Vul	June 20, 2000	ϵ Cyg [a]	3	y *
HD 184761	Nov 8, 2000	α Tau	3	n
HD 216803	Dec 9, 2000	HR 1017	6	y
IRAS 04016+2610	Dec 9, 2000	HR 617	6	y
IRAS 04248+2612	Dec 9, 2000	HR 617	6	y
IRAS 04264+2433	Dec 9, 2000	HR 1017 [a]	6	y
IRAS 04287+1801	Dec 9, 2000	HR 1708	6	y
IRAS 04108+2803B	Dec 10, 2000	HR 1017 [a]	6	y
IRAS 04181+2654A	Dec 10, 2000	HR 531 [a]	6	y
IRAS 04181+2654B	Dec 10, 2000	HR 531 [a]	6	y
IRAS 04381+2540	Dec 10, 2000	HR 531 [a]	6	y
IRAS 04169+2702	Dec 10, 2000	HR 1017	6	y
IRAS 04239+2436	Dec 10, 2000	HR 1017	6	y
BNKL	Dec 10, 2000	HR 2943	6	y
IRS2 NGC2024	Dec 10, 2000	HR 2943	6	y
MonR22 IRS3	Dec 10, 2000	HR 2943	6	y
IRAS 04489+3042	Feb 21, 2000	HR 1708[a]	6	y
Haro 6-10A	Dec 10, 2000	HR 1017	6	y
Haro 6-10B	Dec 10, 2000	HR 1017	6	y

[a]Residuals of incomplete subtraction of the 9.7 μm telluric ozone feature are present in the spectrum.

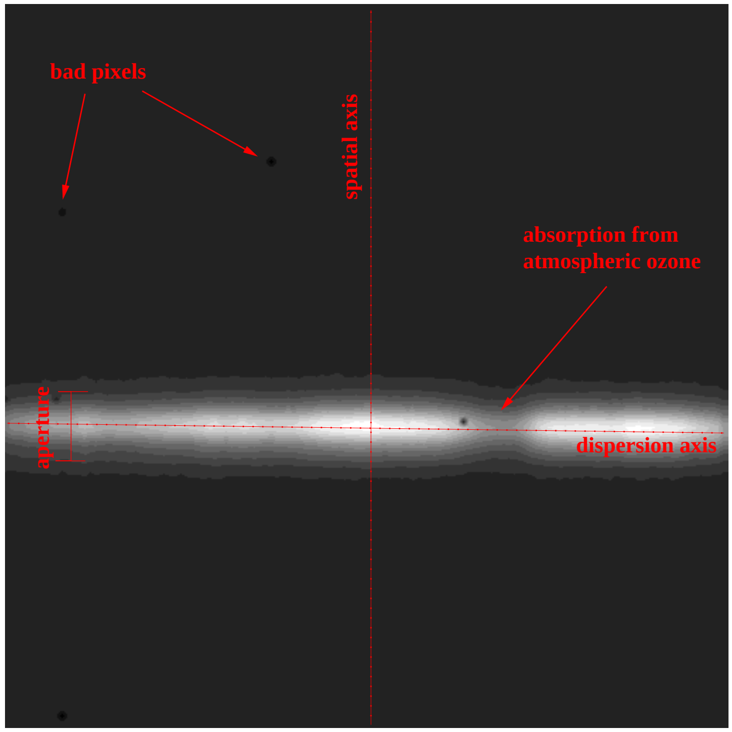

Figure 5.2 Coadded image of standard star HR 1165. Images were corrected for bad pixels, flat fielded and the slope in the dispersion axis is removed. The spectra were then summed along the spatial axis to obtain the final spectrum.

infinite aperture value. Standard star observations were used to obtain extinction curves for each night, resulting in a typical night-to-night variation in the atmospheric zero-points of $\sim$20% and an average atmospheric extinction correction of -0.32 $\pm$ 0.07 mag/airmass. The root-mean-square scatter in the photometry of the standards is 0.06 mag for Feb 20 and 21, and 0.13 mag for Dec 9, 2000.

The spectroscopy data reduction was also performed using the NOAO IRAF/TWODSPEC and ONEDSPEC tasks. Bad pixel masks were composed from the flats and corrected in the source images. The images were flat fielded prior to extraction in order to calibrate for pixel-to-pixel variations across the detector. The images were then divided by those produced from the LSEC calibration scan obtained closest in time to the observation, to correct for variations in the spectral response of the grating. The detector's dark field flux was found to be negligible over the integration times used and therefore not subtracted from the data. Extraction of the spectra was performed using the *IRAF* task *apall*. In this task, a trace function is fit to the dispersion axes and used to correct the center of the apertures at each dispersion point in the image. The spectrum is then extracted from the image by summing over the selected aperture in the spatial direction.

The central wavelength on the detector varies slightly each time the grating and slit are moved, individual wavelength calibration is therefore required. For the purposes of wavelength calibration and removal of the telluric ozone absorption feature at $\sim$9.5 μm, each extracted spectrum was aligned with and divided by a standard star spectrum (see Table 5.2 for details) using the *telluric* task. In order to achieve the best match for each source-calibrator pair (lowest residual rms), the standard star spectrum was scaled and shifted to match the source spectrum before division. However, in some cases (as noted), variations in seeing resulted in small differences in the shape of the ozone feature in the stellar and calibrator spectra and residuals can be seen in the resulting spectra. Although the calibrators are chosen to possess a flat continuum in the 8–13 μm range, the resulting spectra were then multiplied by a blackbody emission spectrum for the calibrator to remove any slope present.

Finally, the spectra were flux calibrated using the photometric observations at similar wavelengths culled from the literature (see Table 5.3). Each spectrum was summed over the bandwidth used for the corresponding photometry and the result was scaled to match the photometric flux. This scaling factor was then applied to obtain the flux calibrated spectra shown in Figures 5.3-5.7. Overplotting the spectra onto the SEDs indicates the success of the flux calibration.

5.4 Spectral energy distributions (SEDs)

Previous observations of continuum fluxes for the sources in our sample were collected from the literature in order to form the Spectral Energy Distributions (SEDs) shown in Figures 5.3-5.7. The data were not de-reddened, but, as the A_V for these sources is small ($A_V < 3$), this should have very little effect on fluxes for wavelengths longer than K band. In order to determine the contribution from stellar radiation, the SEDs were fit with emission arising from a blackbody at the stellar temperature given in the literature for each source (see Table 5.1) by scaling the peak of the blackbody curve to match the SED at that wavelength. The flux from the stellar blackbody F_{bb} $[erg/cm^2/s/\mu m]$ is defined by the equation,

$$F_{bb} = \frac{2hc^2/\lambda^5}{e^{hc/\lambda kT} - 1} \frac{\pi R^2}{D^2}, \tag{5.6}$$

where h, c, and k have the usual definitions, λ is the wavelength in μm, R is the radius of the star and D is the distance to the star so that $\frac{\pi R^2}{D^2}$ is the solid angle subtended by the star. Stellar luminosities were found by integrating this blackbody flux over wavelength,

$$L_* = \int 4\pi D^2 F_{bb} \, d\lambda, \tag{5.7}$$

and are listed in Table 5.4. For comparison, stellar luminosities from the literature are also presented. These are similar to the luminosities derived here, but our estimates are consistently smaller than the luminosities from the literature, which is consistent with errors due to not dereddening the observed SED fluxes.

It is useful to compare the luminosity from circumstellar dust radiated in the millimeter and

Table 5.3. Flux calibration of spectra

Source	$\lambda(\mu m)$	Flux (Jy)	$\Delta\lambda$ (km/s)	Instrument	Ref.
49 Ceti	10.8	0.2 ±0.04	8.0–13.6	KeckII,OSCIR	1
LkCa 15	9.6	0.5 ±0.15	9.5–9.7	ISO,SWS	2
GM Aur	10.1	0.5 ± 0.0	7.55–12.65	IRTF	3
MWC 480	9.6	8.7 ± 2.6	9.5–9.7	ISO,SWS	2
HD 233517	10.1	0.439 ± 0.0	9.595–10.505	UKIRT,Berkcam	4
HD 163296	9.69	18.6 ± 0.5	8.84–10.54	1m,ESO	5
WW Vul	9.6	2.3 ± 0.5	9.5–9.7	ISO,SWS	2
HD 184761	12	2.41 ± 0.0	9.15–14.85	IRAS	6
HD 179218	10.7	17 ± 2	10.15–11.25	O'brien Obs.	7
HD 22049	12	9.5 ± 0.4	9.15–14.85	IRAS	6
BN	10.7	88 ± 0.0	10.0–11.4	Keck,LWS	8
HD 216803	10.7	1.53 ± 0.082	10.0–11.4	Keck,LWS	9
Hen 3-600A	10.7	0.73 ± 0.06	10.0–11.4	Keck,LWS	9
HD 102647	10.7	5.51 ± 0.41	10.0–11.4	Keck,LWS	9
HD 17925	10.7	0.92 ± 0.09	10.0–11.4	Keck,LWS	9
AA Tau	10.7	0.44 ± 0.03	10.0–11.4	Keck,LWS	9
HR 4796A	10.7	0.216 ± 0.02	10.0–11.4	Keck,LWS	9
IRAS 04016+2610	10.7	2.84 ± 0.18	10.0–11.4	Keck,LWS	8
IRAS 04016+2610	10.3	2.5 ± 0.0	9.65–10.95	IRTF	10
IRAS 04108+2803B	10.7	0.68 ± 3.0	10.0–11.4	Keck,LWS	8
IRAS 04108+2803B	10.3	0.57 ± 0.0	9.65–10.95	IRTF	10
IRAS 04248+2612	10.7	0.23 ± 0.009	10.0–11.4	Keck,LWS	8
IRAS 04264+2433	10.7	0.41 ± 0.02	10.0–11.4	Keck,LWS	8
IRAS 04287+1801	10.7	5.02 ± 0.4	10.0–11.4	Keck,LWS	8
IRAS 04295+2251B	10.7	0.69 ± 0.03	10.0–11.4	Keck,LWS	8
IRAS 04489+3042	10.7	0.31 ± 0.02	10.0–11.4	Keck,LWS	8
IRAS 14050-4109	10.7	0.234 ± 0.022	10.0–11.4	Keck,LWS	9
IRAS 04181+2654A	12.0	0.358 ± 0.0	9.15–14.85	IRAS	6
IRAS 04181+2654B	12.0	0.358 ± 0.0	9.15–14.85	IRAS	6
IRAS 04239+2436	12.0	1.712 ± 0.0	9.15–14.85	IRAS	6
IRAS 04381+2540	10.6	0.209 ± 0.0	10.5–10.7	...	...
IRAS 04239+2436	12.0	1.71 ± 0.086	9.15–14.85	IRAS	6

Note. — References: 1-Jayawardhana et al. (2001), 2-Thi et al. (2001), 3-Kenyon & Hartmann (1995), 4-Skinner et al. (1995), 5-Berrilli et al. (1992), 6-Beichman et al. (1988), 7-Lawrence et al. (1990), 8-Hillenbrand, private communication, 9-Metchev et al. (2003), 10-Myers et al. (1987)

Table 5.4. Calculations from SEDs: Class II, III objects

Source	λ_{onset} (μm)	L_*-lit ($L_\odot$)	L_* ($L_\odot$)	L_{IR} ($L_\odot$)	L_{tot} ($L_\odot$)	L_{IR}/L_{tot} ($L_\odot$)	L_{IR}/L_* ($L_\odot$)
LkCa 15	1.65	0.97	0.344	0.452	0.796	0.568	1.31
GM Aur	6.9	0.84	0.697	0.327	1.02	0.319	0.469
MWC 480	2.2	23.7	15.4	3.31	18.7	0.177	0.215
HD 163296	1.4	35.2	25.3	8.41	33.7	0.249	0.332
WW Vul	1.4	43.0	25.6	15.7	41.3	0.380	0.613
HD 184761	2.3	...	9.14	0.641	9.78	6.55e-2	7.01e-2
AA Tau	1.9	0.71	0.221	0.593	0.814	0.729	2.68
HD 179218	0.91	221.9	75.3	35.0	110	0.317	0.465
IRAS 14050-4109	1.5	...	0.440	4.28e-2[a]	0.483	8.86e-2	9.73e-2
Hen 3-600A	5.4	0.23	0.202	-4.52e-2[b]	0.247	<0.183	<0.224
49 Ceti	11.3	23.44	19.5	1.69e-2	19.5	8.66e-4	8.70e-4
HD 233517	6.3	0.20	0.341	1.56e-2	0.356	4.37e-2	4.57e-2
HR 4796A	12.4	35.0	30.7	6.24e-2	30.8	2.03e-3	2.00e-3
HD 22049	100	...	0.364	-2.44e-2[b]	0.340	<6.28e-2	<6.70e-2
HD 216803	20	...	0.209	5.11e-5	0.209	2.44e-4	2.44e-4
HD 102647	60	...	19.0	-3.51e-3[b]	19.0	<1.85e-4	<1.85e-4
HD 17925	60	...	0.368	9.66e-3	0.378	2.56e-2	2.62e-2

[a]This is a lower limit. Had to cut off luminosity estimate at the last observed point (100μm) due to bad fit.

[b]Small IR excesses led to the calculation of negative values for L_{IR}. The absolute values of L_{IR} are used for calculations of upper limits to L_{IR}/L_{tot} and L_{IR}/L_*.

Table 5.5. Calculations from SEDs: Class I objects

Source	RA(J2000))	DEC(J2000)	L_{tot}[c]	Ref.
IRAS 04016+2610	04 04 42.85	+26 18 56.3	3.74	1,3
IRAS 04108+2803B	04 13 52.9	+28 11 23	0.344	1,3
IRAS 04181+2654	04 21 11.42	+27 01 08.9	0.406	1,2,3
IRAS 04239+2436	04 26 57.1	+24 43 36	0.394	1,3
IRAS 04248+2612	04 27 56.7	+26 19 20	22.8	1,3
IRAS 04264+2433	04 29 07.68	+24 43 50.1	0.244	1,3
IRAS 04287+1801	04 31 33.6	+18 08 15	0.292	1,3
IRAS 04295+2251B	04 32 32.07	+22 57 30.3	1.43	1,2,3
IRAS 04325+2402	04 35 33.0	+24 08 14	0.717	1,3
IRAS 04381+2540	04 41 12.48	+25 46 37.1	0.350	1,2
IRAS 04489+3042	04 52 06.9	+30 47 17	0.350	1,3
BN object	05 35 14.17	-05 22 23.1	114	...
NGC 2024 IRS2	05 41 45.8	-01 54 30	...	...
MonR2 IRS3	06 07 47.8	-06 22 55	...	...

[c]Assumed a distance of 140 pc for embedded sources in the Taurus molecular cloud. As the spectral types and A_V's are unknown, no stellar blackbody was fit and SED fits give L_{tot}.

Note. — References: 2-Hartmann,2002ApJ...578..914H - Astrophys. J., 578, 914-924 (2002) - October(III) 2002, 3-IRAS Faint Source Catalogue version 2 (1990)

IR (L_{IR}) with the total luminosity from the source (L_{tot}). In previous studies of T Tauri stars, the fractional luminosity (L_{IR}/L_{tot}) has been measured (using IRAS measurements to calculate L_{IR}) and was found to clearly distinguish between the standard classes (Kenyon & Hartmann, 1987); $L_{IR}/L_{tot} > 0.8$ for class I sources (embedded stars), $L_{IR}/L_{tot} \approx 0.1$–$0.2$ for class II sources (optically thick disks), and $L_{IR}/L_{tot} < 0.1$ for class III sources (optically thin disks). Another important quantity is the ratio of the IR to stellar luminosity (L_{IR}/L_*), which is related to the optical depth of the disk material. For optically thin emission, this luminosity ratio is indicative of the disk geometry as L_{IR}/L_* indicates the optical depth along the midplane for a geometrically thin disk (Backman & Paresce, 1993). The maximum value of L_{IR}/L_* is 1/4 for a flat optically thick disk and L_{IR}/L_* may reach 1/2 for a flared, optically thick disk, in which the thickness increases with distance from the star. Vega-like stars have $L_{IR}/L_* \sim 10^{-5}$–10^{-3} indicating low optical depths at all wavelengths (Sylvester et al., 1996).

The IR luminosity and the ratios L_{IR}/L_* and L_{IR}/L_* were thus estimated from the SEDs collected for our sample in the following manner. First, a polynomial was fitted to the points in the SED and through careful examination the wavelength λ_{onset}, at which this fit and the stellar blackbody diverge, was evaluated. The infrared luminosity of the disk L_{IR} was then calculated by integrating over the fit beyond λ_{onset} ($\lambda = \lambda_{onset} - 1$ cm) and subtracting the integral of the stellar blackbody over the same region. The total luminosities ($L_{tot} = L_{IR} + L_*$) and the resulting fractional IR luminosities L_{IR}/L_{tot} and IR-to-stellar luminosity ratios L_{IR}/L_*, as well as the wavelength of the onset of disk radiation, are presented in Tables 5.4–5.5.

The L_{IR}/L_{tot} classification of Kenyon & Hartmann (1987) appears to be consistent with our sample and applicable to both low and intermediate mass stars; the debris disks possess L_{IR}/L_{tot} < 0.1 and the optically thick protoplanetary disks possess $L_{IR}/L_{tot} > 0.1$–0.7. Additionally, λ_{onset} appears to be in general inversely proportional to the IR excess, and the debris disks are easily identified as those sources with large λ_{onset} and low fractional IR luminosities. For the younger sources, we find very high values of L_{IR}/L_*, always greater than 0.3 with a maximum at 2.68 for AA Tau, similar to the range that was found for a large sample of TTs by Cohen et al. (1989). This cannot be explained by passive thermal reprocessing of radiation by grains and according to the classification of Sylvester et al. (1996) a flared disk geometry combined with energy release due to accretion is a possible explanation of these high IR excesses.

For the class I sources the stellar parameters are unknown and therefore only total luminosities were calculated. In the early stages of star formation, the total, or bolometric, luminosity should be approximately equal to the accretion luminosity (Kenyon & Hartmann, 1995),

$$L_{tot} = L_{acc} = \frac{GM_*\dot{M}}{R_*} \tag{5.8}$$

$$\approx \quad 15\left(\frac{M_*}{0.4M_\odot}\right)\left(\frac{R_*}{2.7R_\odot}\right)^{-1}\left(\frac{\dot{M}}{3\times10^{-6}M_\odot/yr}\right)L_\odot \qquad (5.9)$$

$$\approx \quad 10-50\ L_\odot. \qquad (5.10)$$

Most of the class I objects in our sample, however, possess $L_{tot} < 1\ L_\odot$, similar to what is seen by Kenyon & Hartmann (1995) for a sample of low mass embedded stars. They suggest that this is due to an increased accretion radius or intermittent accretion onto the central star, but these scenarios cannot fully explain the extremely low luminosities observed for a large number of sources.

The SEDs are additionally useful for establishing a continuum around the 8–13 μm silicate emission feature, which is extremely important for analysis of the feature shape and the silicate composition. van Boekel et al. (2003) fit the SED with a blackbody for the star and several blackbodies of different temperatures for the dust emission and interpolate between the two to find the continuum. Natta et al. (2000) fit a powerlaw to the edges of the silicate emission feature to remove the continuum. Upon examination of the overlays of the spectra on the SEDs in Figure 5.4-5.5, we find that the continuum is in most cases adequately represented by connecting the two endpoints of the spectrum (at approximately 8.3 and 12.2 μm). The one exception is the T Tauri star AA Tau for which the SED contains photometry with large flux variations near 10 μm and the continuum is difficult to establish. In this case, a flat continuum with flux equal to the flux at the 8 μm end of the spectrum was used.

In general, we would expect the shape of the feature to be related to the SED and the amount of radiation from the star versus the disk. Specifically, if the changes in the silicate feature are due to processing of the dust, and conversion of the dust composition from primarily amorphous olivines to crystalline enstatite and forsterite, then this should be related to the evolutionary stage of the disk. As described above, the fractional IR luminosity is another indicator of the evolutionary class and thus we would expect that objects with lower L_{IR}/L_{tot} values in any class would be more likely to have flatter 8–13 μm spectra, with more emission from the 11.2 μm crystalline silicate feature.

5.5 10 μm spectra

The flux calibrated spectra and SEDs are shown in Figures 5.3-5.7 and continuum subtracted spectra are shown in Figure 5.8. The sources may be placed into categories based on the shape of the SEDs and 8–13 μm spectra. In general, the debris disks (more evolved than class III primordial disks) were found to have little or no evidence of silicate emission, the class II sources showed strong to moderate silicate emission and the class I sources showed silicate absorption, except for IRAS 04489+3042, IRAS 04108+2803B and IRAS 04264+2433, which show no feature. Possible evolutionary trends are shown in Figures 5.9 and 5.10 for the low mass and intermediate mass stars, respectively. The

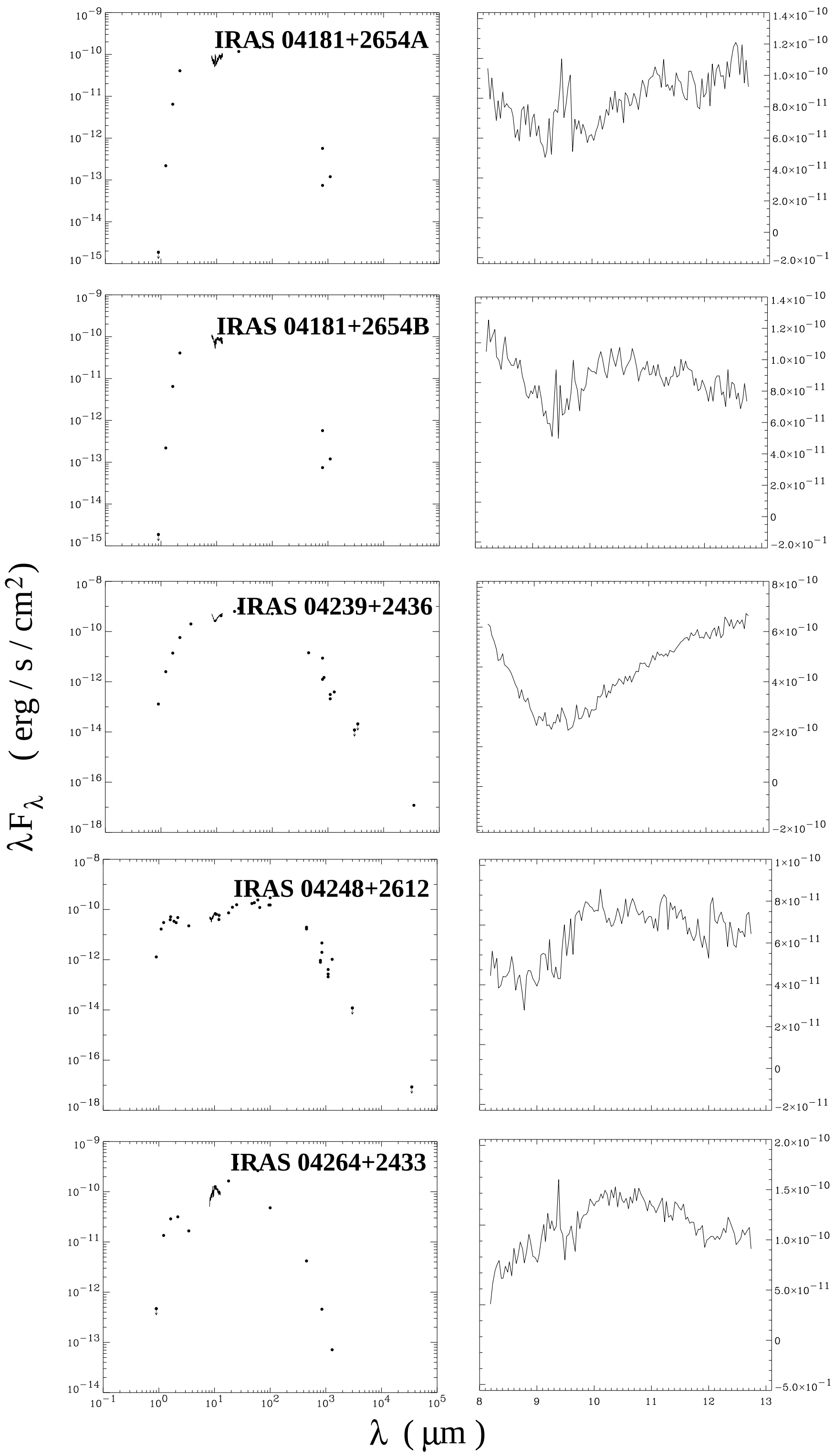

Figure 5.3 SEDs and 10 μm spectra for low mass star disks where silicates are in absorption or not detected. SEDs are plotted on a log scale while the spectra are presented on a linear scale.

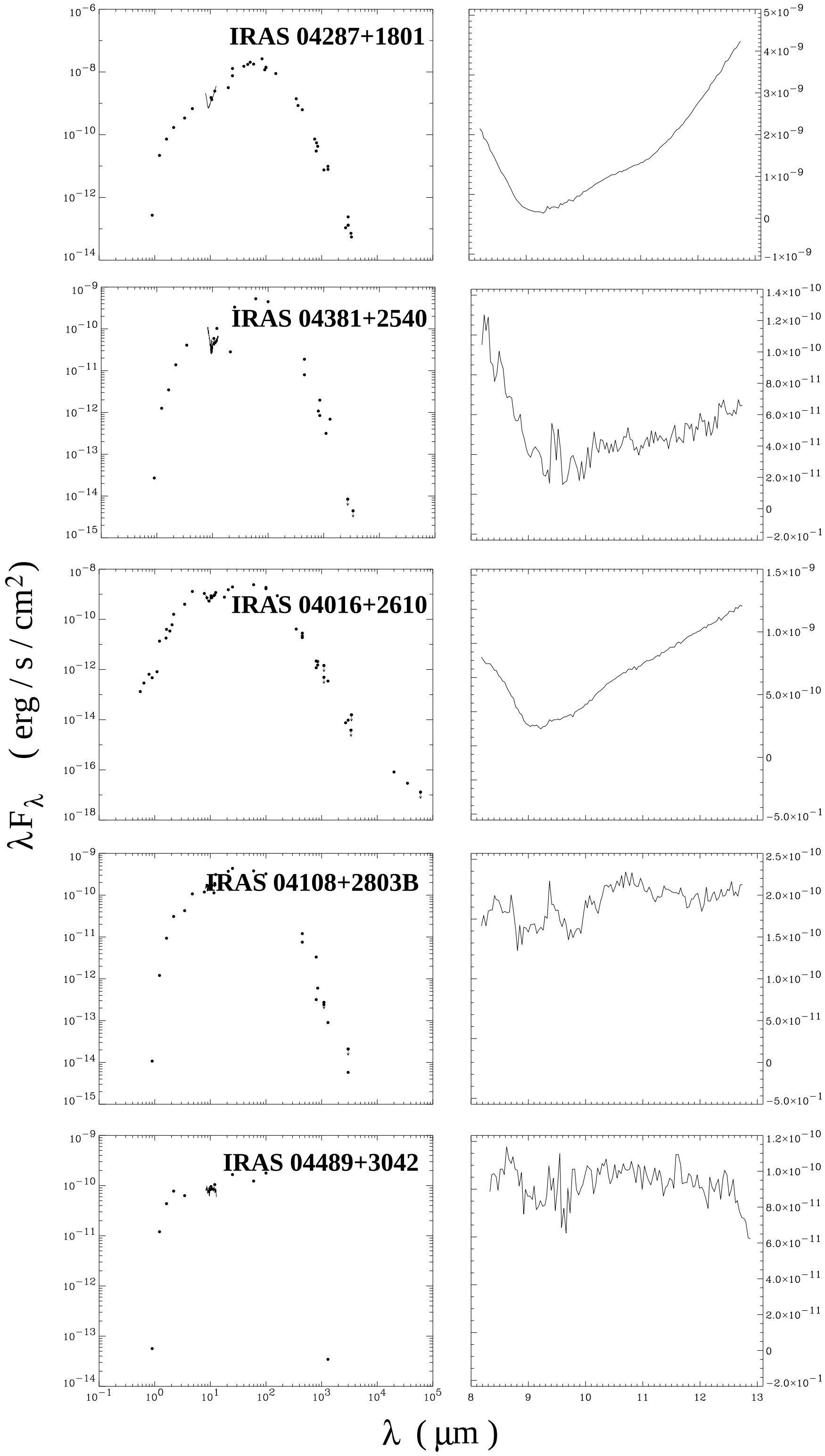

Figure 5.3 -continued

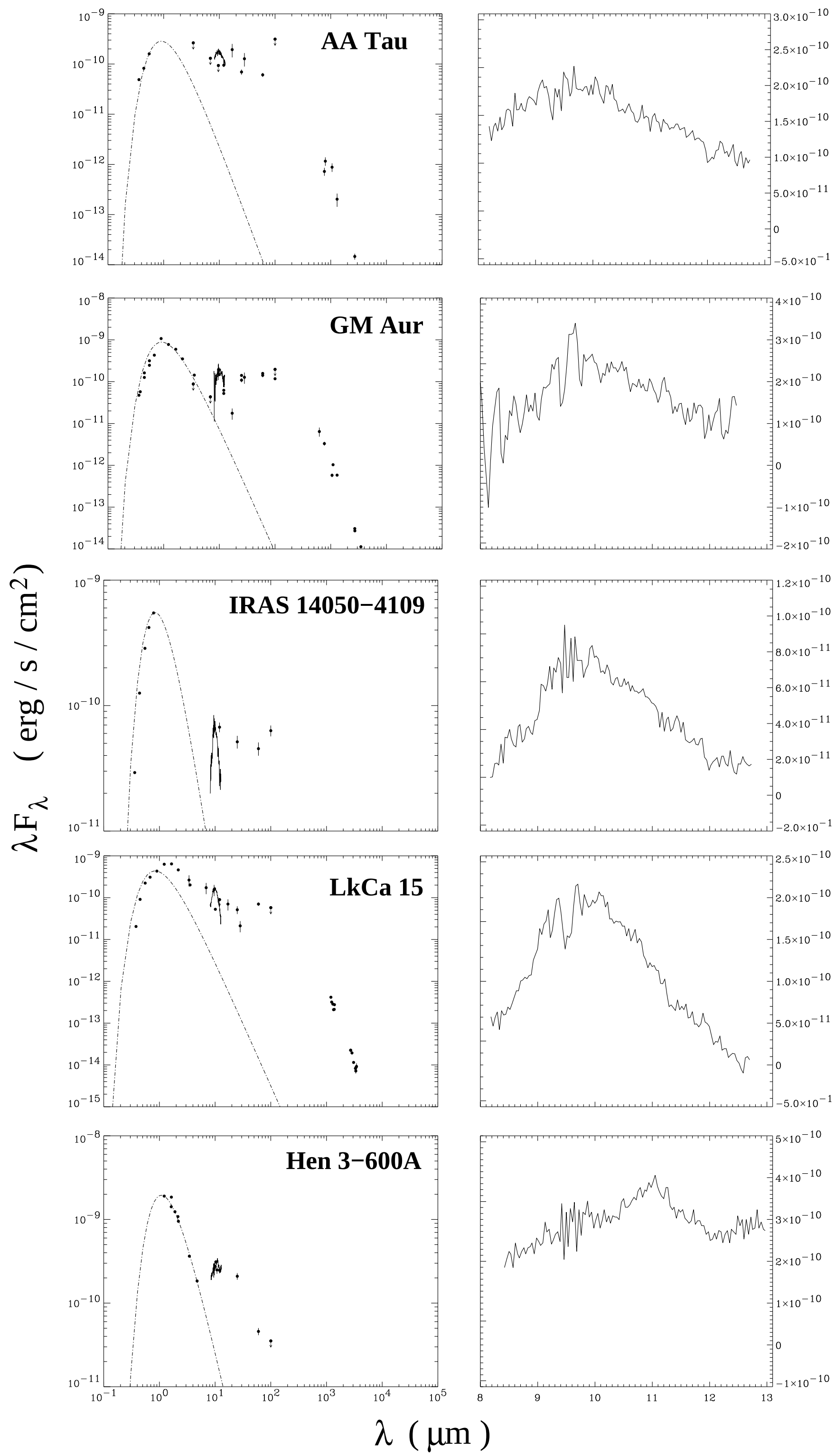

Figure 5.4 SEDs and 10 μm spectra for disks around low mass, T Tauri stars where the silicate 10 μm band is in emission.

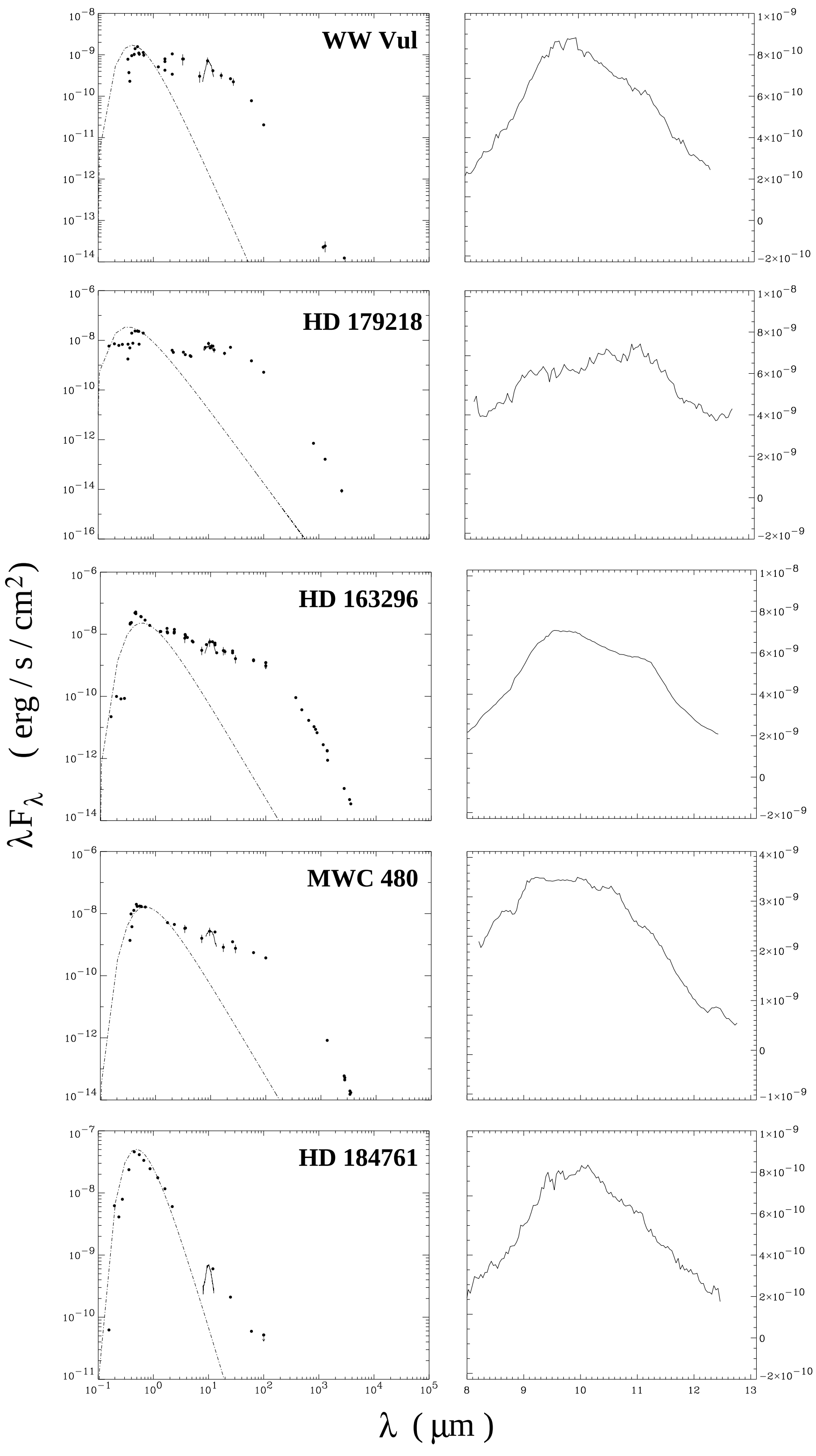

Figure 5.5 SEDs and 10 μm spectra for disks around intermediate mass, HAEBE stars where the silicate 10 μm band is in emission.

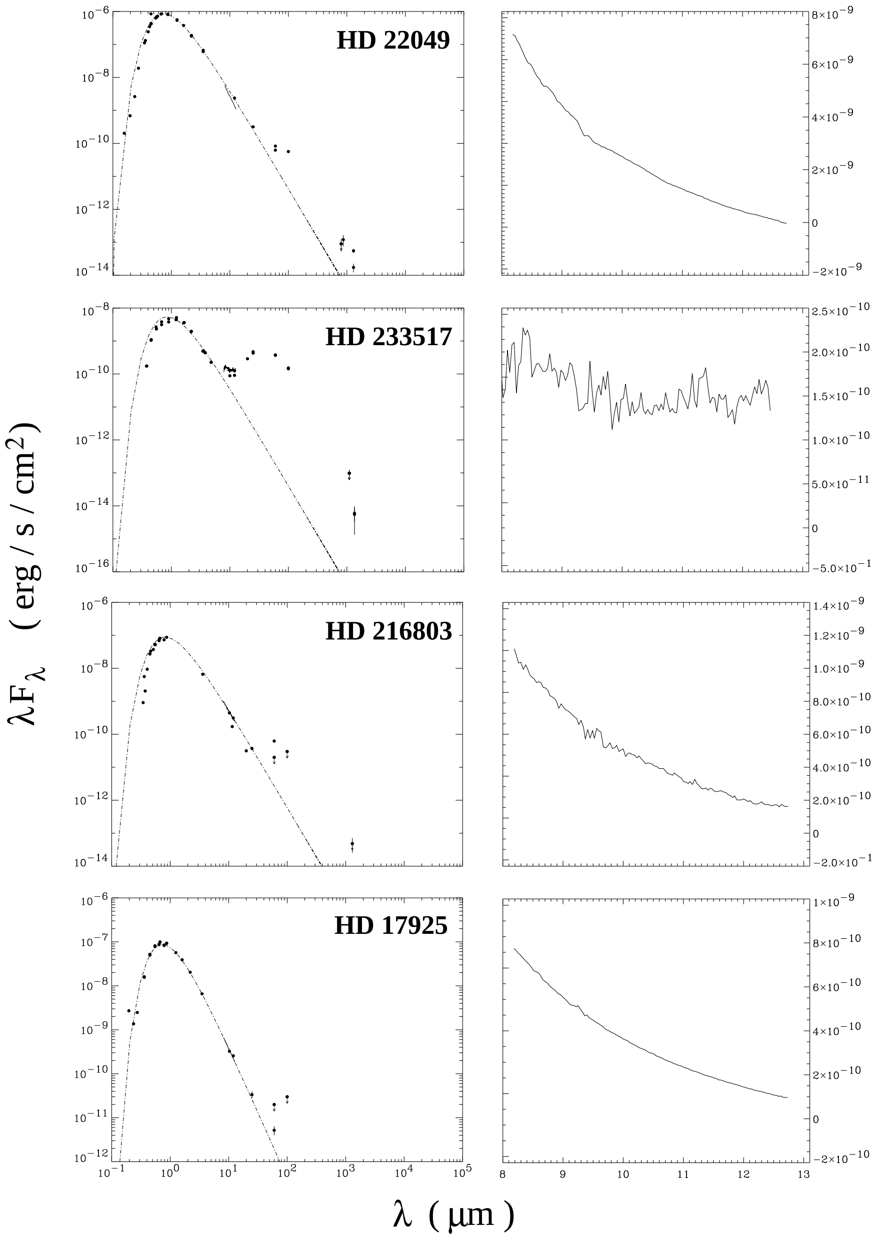

Figure 5.6 SEDs and 10 μm spectra for “debris” disks around low mass stars.

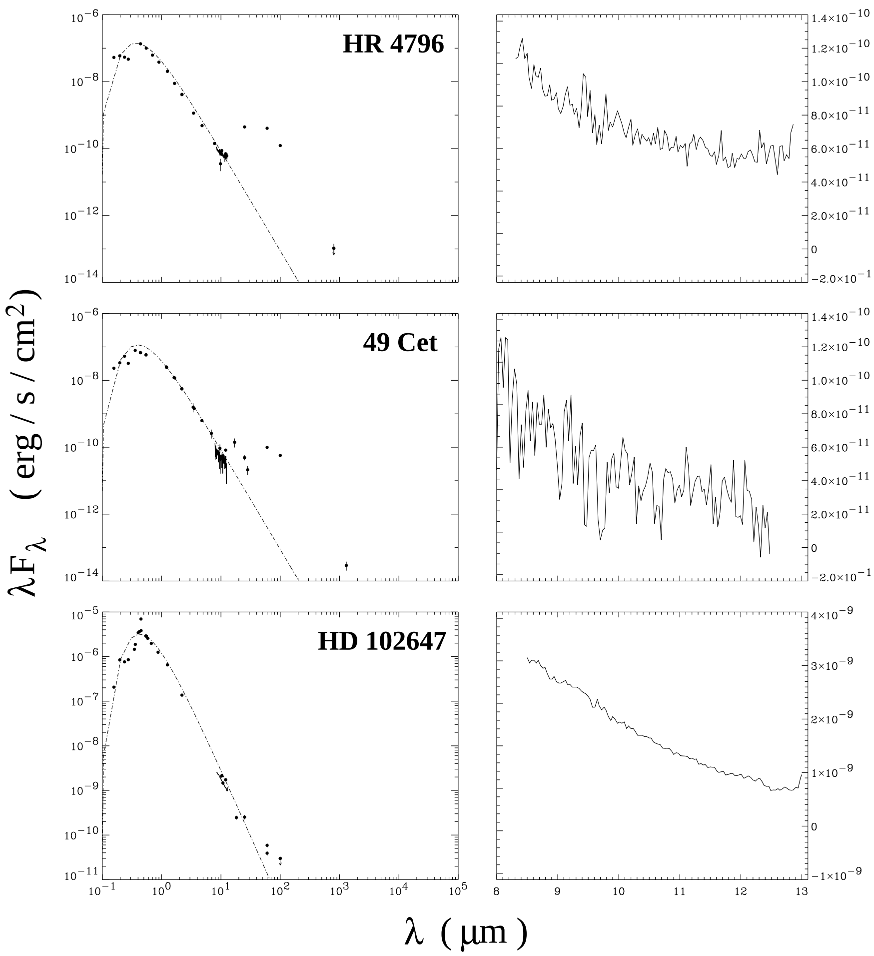

Figure 5.7 SEDs and 10 μm spectra for “debris” disks around intermediate mass stars.

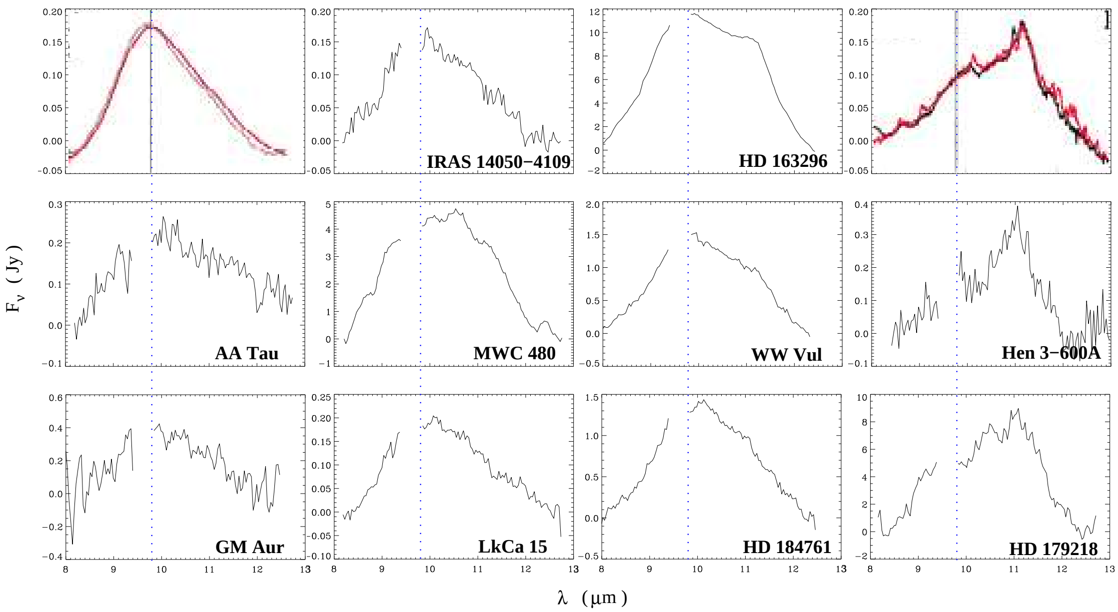

Figure 5.8 Continuum subtracted emission spectra, constructed via the method outlined in the text. Format is similar to Bouwman et al. (2001). The panels in the top left and top right are ISO spectra from Bouwman et al. (2001) of the amorphous olivines in the galactic center and the highly processed, crystalline forsterite-rich spectrum of HD 100546. The vertical dashed line indicates the position of the peak of the amorphous silicate band as observed for the ISM at 9.8 μm.

trend shown in Figure 5.10 is similar to that suggested for HAEBE stars by Meeus et al. (2001). The evolution of low mass star spectra and SEDs does not appear to be that different from intermediate mass stars, with embedded sources showing amorphous olivine in absorption, followed by stages of dust processing (and possibly grain growth) leading to the observation of emission from crystalline forsterite and finally photospheric spectra for debris disks. One significant difference between the low and intermediate mass cases is that for intermediate mass stars, crystalline silicates have been found in sources which possess large FIR excesses, but for low mass stars, the only source in which crystalline silicates have been found is on the verge of being a debris disk.

The spectra observed toward the T Tauri stars GM Aur, AA Tau, IRAS 14050-4109 and LkCa 15 and the Herbig Ae star MWC 480 are similar to that of amorphous olivine. Although no crystalline features are evident, the spectra are wider in comparison to that of the Galactic center, suggesting that some processing has taken place in the disk. The absence of a strong crystalline component in the emission spectra indicates that this processing is more likely related to grain growth (discussed below) than to crystallization.

The spectra that we observed toward the HAeBe stars HD 163296, HD 184761, and WW Vul, each depict an emission feature characteristic of amorphous olivine and a secondary peak at 11.3 μm, perhaps due to a small amount of crystalline forsterite (much less than that seen for β Pictoris or HD 100546 (Meeus et al., 2001). These objects are all intermediate mass stars ($\sim$2 $M_\odot$) of ages $>$

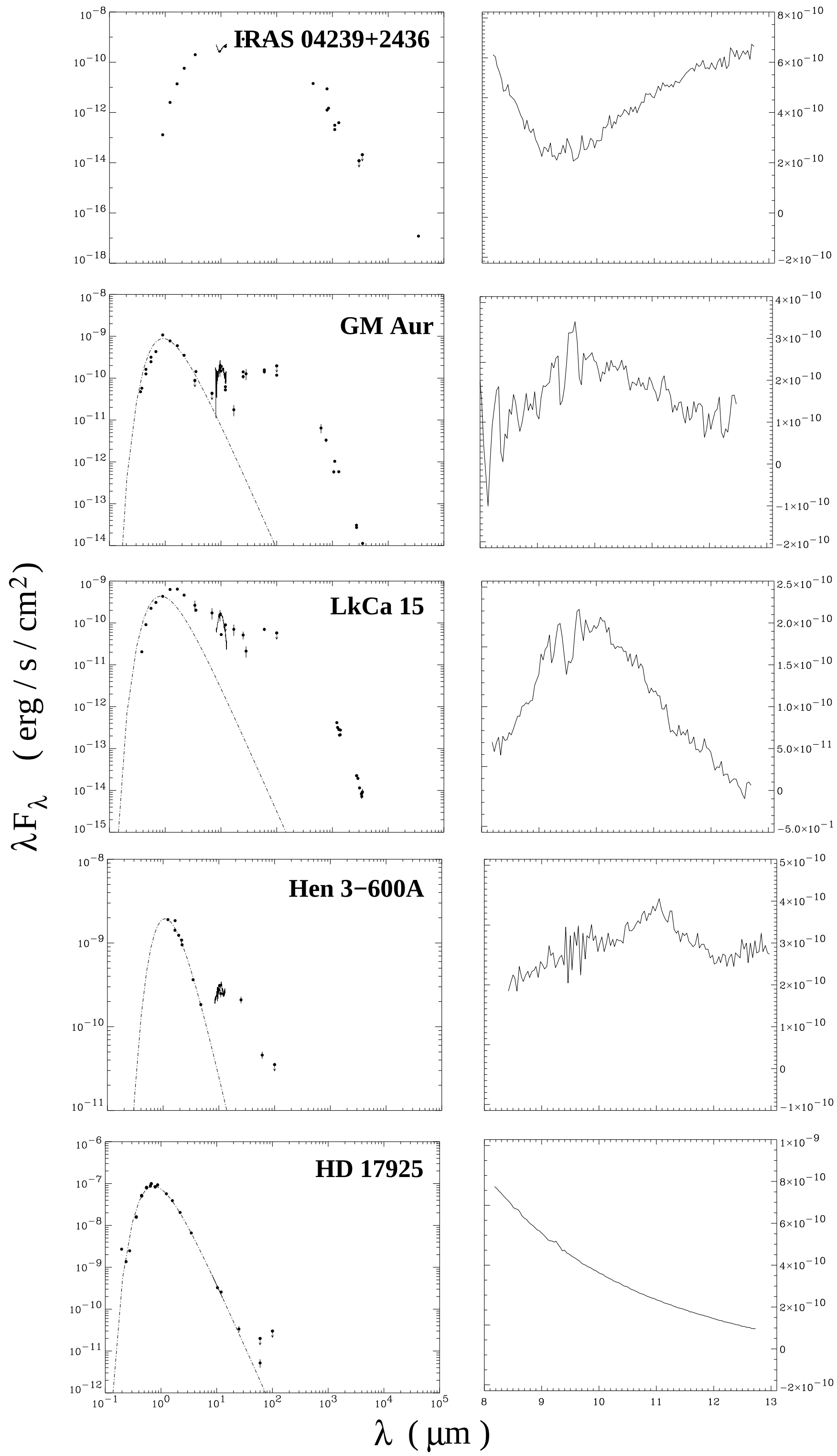

Figure 5.9 Evolution of the silicate spectrum for low mass stars. The evolutionary sequence for low mass stars is quite similar to that for intermediate mass stars (Meeus & Waelkens, 1999).

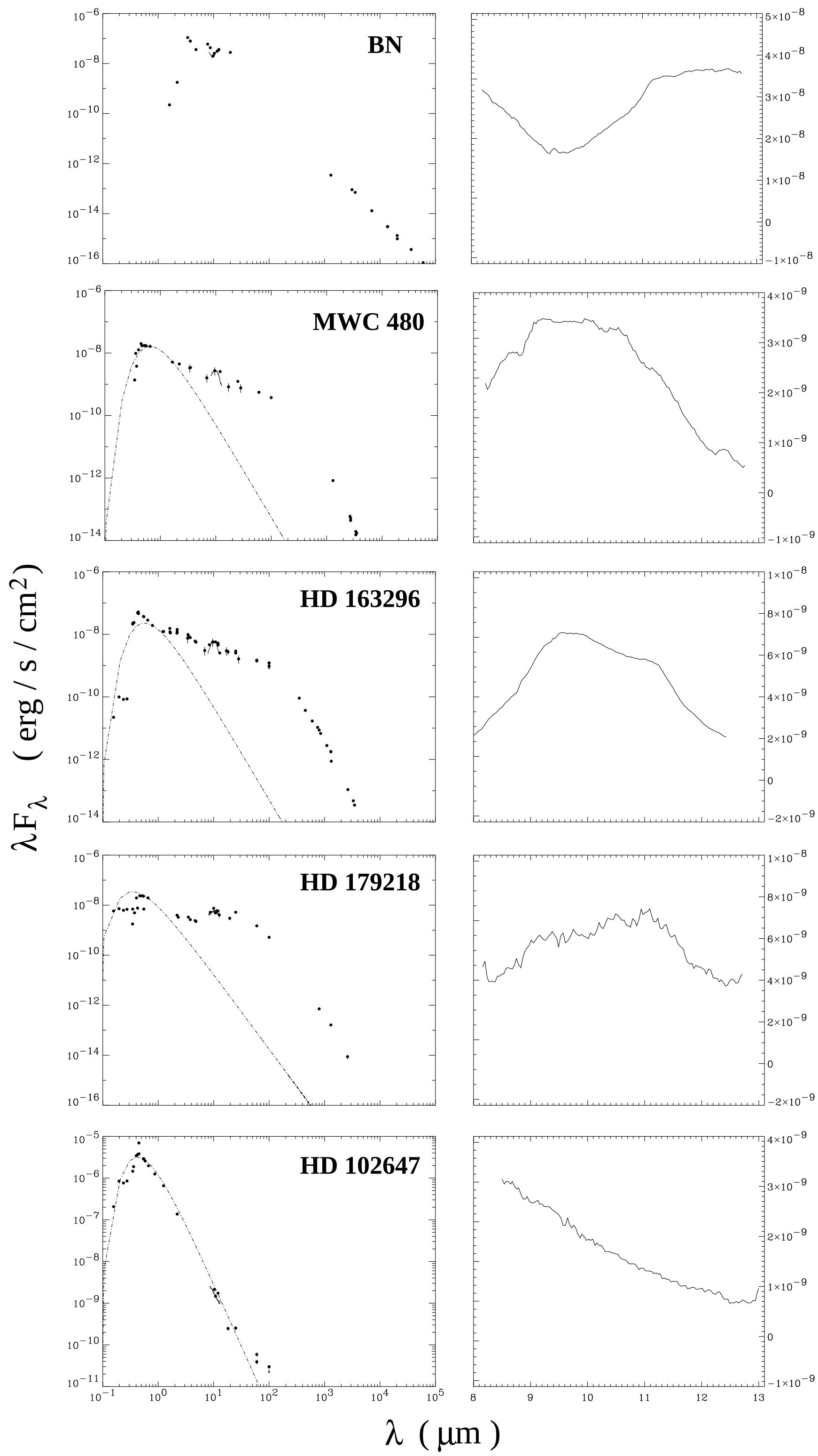

Figure 5.10 Evolution of the silicate spectrum for intermediate mass stars. The evolutionary sequence is similar to that observed for intermediate mass stars in ISO studies (Meeus & Waelkens, 1999).

6 Myr, and all three still possess considerable amounts of silicates, as can be seen by comparison of the silicate flux to that due to the stellar photospheres. This may indicate that dust crystallization is not directly related to the processes involved in dust clearing. The spectra of the latter two objects are similar to that observed toward a few objects by Hanner et al. (1995), which are fit with models that include the emission from both silicates and poly-aromatic hydrocarbons (PAHs).

Perhaps the most interesting result is the similarity between the silicate emission from the low mass star Hen 3-600A and the Herbig Ae star HD 179218 (also similar to the HAEBE star HD 100546; Bouwman et al., 2003). Both show strong peaks at 11.3 μm, which dominate the spectrum. The shape of the emission feature is consistent with that of crystalline enstatite (including the correlating small peak at 10.2 μm). Hen 3-600A is the first low mass object to show emission from crystalline silicates. For these silicates to be detectable, they must be present at radii $<$ 1 AU (T$\approx$200–300 K). In contrast, the warm silicates in the HAEBE star HD 179218 are likely to reside at a much larger distance from the star (R$\sim$10 AU). This observation, along with the presence of crystalline silicates in long period comets and cold crystalline silicates in HAEBE stars, suggests that crystalline silicates must either have a cold formation mechanism or be transferred outward. However, the presence of equivalent fractions of crystalline silicates around an HAEBE star which still possesses strong IR emission, and thus a substantial amount of warm dust as around a T Tauri star with much less IR flux and warm dust, may indicate that the process of crystallization takes longer around low-mass stars, which is consistent with the thermal annealing scenario.

No warm silicate emission was seen toward the debris disks–their spectra are entirely photospheric. A possible exception is HD 233517, which may possess Poly-Aromatic Hydrocarbons (PAHs–with features at 8.3, 9.7 and 11.2 μm) in addition to some silicates, but if so, these features are weak. The lack of silicate emission may indicate either a paucity of small grains (a $<$ 10 μm), possibly due to grain growth, or the absence of a significant amount of optically thin material inside of $\sim$10 AU (T$\geq$200 K). The absence of a substantial continuum at 10 μm is consistent with the SEDs for HD 102647, HD 17925, HD 22049 and HD 216803, which show very low IR and millimeter excesses ($L_{IR}/L_{tot} \sim 0.001$) with $\lambda_{onset} \geq 60$ μm. This suggests that the debris disks have lost most of their (warm, small) circumstellar silicate grains. 49 Ceti, HR 4796A and HD 233517, however, still possess substantial far-IR and millimeter excesses. The presence of dips in the SED around 10 μm and the absence of silicate emission suggest the presence of large gaps in the disk at radii close to the star, similar to that proposed for the T Tauri star GM Aur (Rice et al., 2003).

5.5.1 Variability

Multiple spectra were obtained toward a few sources allowing determinations of the variability of the shape and strength of the silicate emission to be evaluated. Figure 5.11 shows the silicate emission toward HD 163296 and LkCa 15 for two observations, taken approximately one year apart. Spectra from the two observing runs are overlaid, showing that there is no significant variability (above the error) in the shape of the silicate emission feature for these two sources on a yearly timescale. The double peaked structure seen in the spectrum of HD 163296 has been previously observed in spectra obtained by ISO (Bouwman et al., 2001; October, 14 1996) and ground-based observations (Sitko et al., 1999; October, 10 1996) and the shape of the spectra observed does not differ significantly from our observations.

The silicate emission from HD 179218, MWC 480 and Hen 3-600A have also been previously observed by Bouwman et al. (2001) (ISO LWS; Oct 5, 1996), Sitko et al. (1999) (IRTF BAAS; Oct 14, 1996) and Honda et al. (2003) (Subaru COMICS; Dec 27, 2001), respectively. The previous observations of HD 179218 (Bouwman et al., 2001) are virtually identical to our observations (Feb 21, 2000); they depict very similar peak strengths ($\sim$9 Jy, when taking the continuum level at 8.0 μm) and shapes (the slope is approximately the same, the peak lies near 11.3 μm and evidence of small peak at 8.0 μm is seen in both cases). MWC 480, however, exhibits very different emission in the Sitko et al. (1999) study than in our spectrum (Nov 30, 1999); in particular, the 11.3 μm feature (crystalline forsterite) is much less prominent in our observations and there is an additional peak at $\sim$10.5 μm (near the position of crystalline enstatite). However, the (peak-to-continuum) strength of the feature is the same to within $\sim$15%. The observations of Hen 3-600A by Honda et al. (2003) also suggest strong evidence of variability when compared to our data (Figure 5.11; Feb 21, 2000), in this case on shorter timescales ($\sim$ 1 yr). The LWS spectrum taken in 2000 shows much less emission at 9.2 μm and possibly 10.3 μm (both attributed to enstatite), with the peak at 11.3 μm (forsterite) dominating the spectrum. There also appears to be an accompanying decrease in the continuum or in the strength of emission near 12.5 μm from 2000 to 2001.

There is no obvious trend in the variability with respect to spectral type or silicate emission feature shape from these observations. HD 179218 and Hen 3-600A have similar emission features and yet the spectrum of Hen 3-600A is highly variable on 1 yr timescales while the spectrum of HD 179218 appears to have not changed in >3 yr. Although HD 163296 and MWC 480 possessed similar spectra in 1996 (Sitko et al., 1999), the spectra for these sources are quite different from each other in 1999 (our data); HD 163296 appears to be constant, while MWC 480 has undergone changes in the spectrum which appear to indicate conversion between the crystalline forms of forsterite (Mg_2SiO_4) and enstatite ($MgSiO_3$). This is similar to changes in the Hen 3-600A spectrum, which also appear to indicate decreasing emission from forsterite and increasing emission from enstatite, which is the opposite of the expected transition with time during the standard annealing process (see Gail (1998) and above discussion).

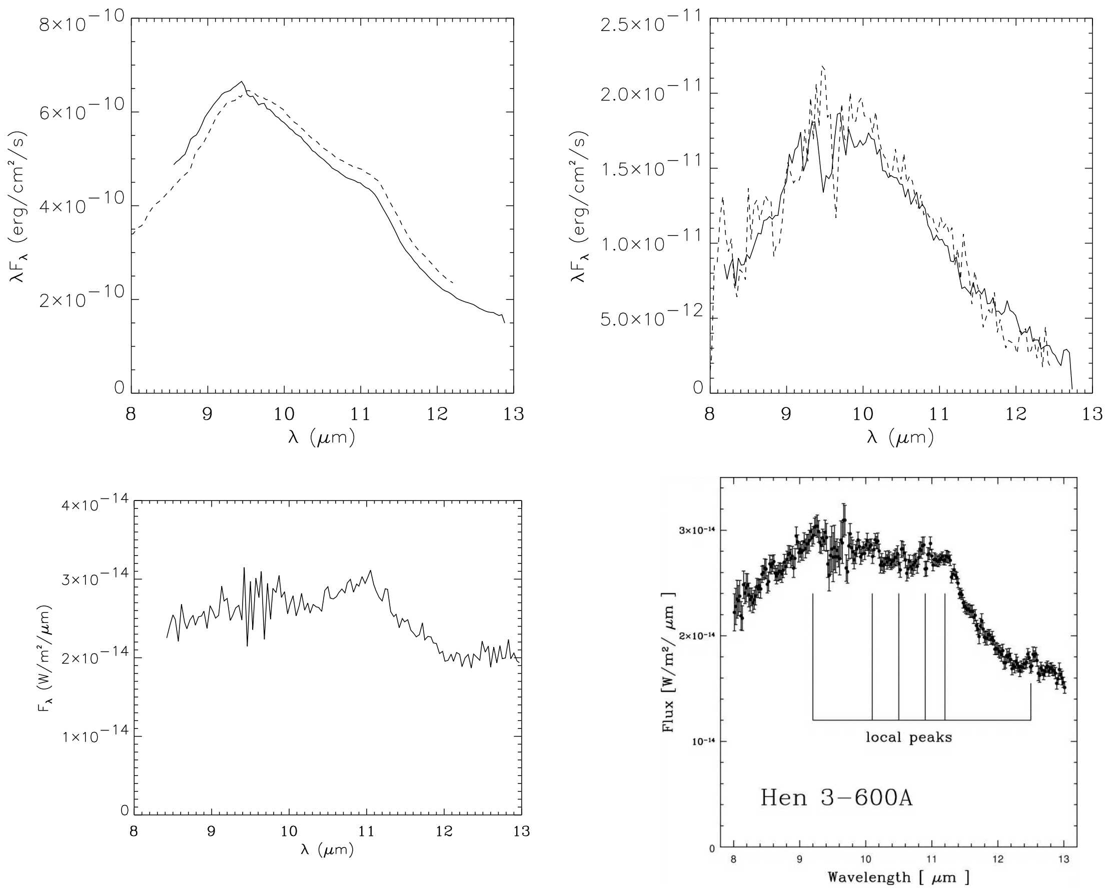

Figure 5.11 Searches for variability. The left panel shows the silicate emission toward HD 163296 observed on Aug 23, 1999 (solid line) and June 20, 2000 (dashed line). The right panel shows the silicate emission observed toward LkCa 15 on Nov 30, 1999 (solid line) and Nov 8, 2000 (dashed line). The spectra from two observing runs are overlaid, showing that there is no significant variability (above the error) in the shape of the silicate emission feature for these two sources on a yearly timescale. The bottom panel shows the Hen 3-600A spectrum in the same units as displayed in Figure 1 of Honda et al. (2003) indicating significant differences in the shape of the spectrum. The continuum was not subtracted for any of these spectra.

5.6 The silicate dust sequence: Dust composition and disk morphology

Having presented our spectra and discussed their overall properties qualitatively, we now embark on a quantitative description of the emission spectra. Sloan & Price (1995, 1998) find that the shape of 10 μm emission from oxygen-rich dust shells around several thousand late type AGB stars (after removal of the stellar continuum with an Engelke function) evolves from sharp emission peaking at 9 μm to broad emission which peaks at $\lambda > 11$ μm. The stars are then classified by the ratios of the flux from the dust shell at 10, 11 and 12 μm and a relationship between the width of the feature, indicated by F_{10}/F_{11}, and the long wavelength shoulder, indicated by F_{10}/F_{12}, was found:

$$F_{10}/F_{12} = 1.32(F_{10}/F_{11})^{1.77}, \tag{5.11}$$

which they called the *silicate dust sequence*. They further define a silicate emission index,

$$n = 10(F_{11}/F_{12}) - 7.5, \tag{5.12}$$

which evolves from SE8 ($n = 8$) for narrow emission centered near 10 μm to broad, structured silicate emission (SE1).

Egan & Sloan (2001) searched for a physical basis for the silicate dust sequence through examination of the dependence of the index on the temperature distribution, optical depth, geometric thickness and chemical composition of the dust shell through radiative transfer models using Mie theory with spherical grains. They find that grain size and shape (fractal versus spherical) only have a slight effect on the shape of the 10 μm silicate emission feature. These models also show that variations in geometric thickness of the dust shell have much smaller effects on the spectral (SE) index than variations in the inner shell radius. However, variations in the geometric thickness do have a large impact on the IR colors (IRAS) and therefore Egan & Sloan (2001) try to match the colors of the observed sequence as well as the SE index. They find that the smooth narrow emission features arise from optically thin shells of amorphous silicate dust and the broad, weak emission arises from optically and geometrically thin shells of alumina dust. For structured spectra in the middle of the silicate dust sequence, they find that more even mixtures of amorphous silicate and alumina *cannot* reproduce the observed spectra and IR colors and the shoulder at 11 μm can only be reproduced by optically thick, but geometrically thin shells of amorphous silicates. Increasing the optical depth of the shell drives the feature into self absorption, decreasing the contribution at 10 μm. The shell must be geometrically thin to match the IRAS colors.

As the composition of dust in protoplanetary disks is expected to be somewhat similar to oxygen

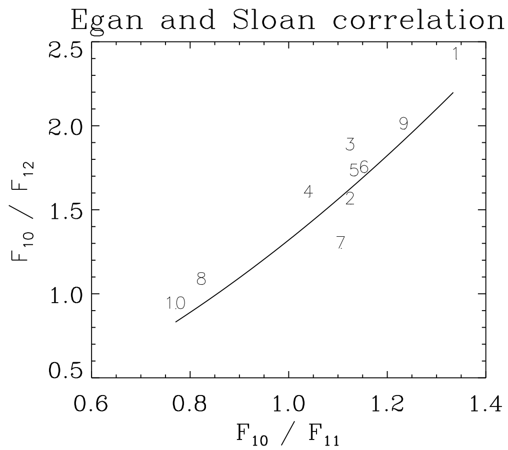

Figure 5.12 Plot of the slope of the feature width (F_{10}/F_{12}) to the slope of the high-wavelength side of the spectrum (F_{10}/F_{11}). The numbers correspond to: 1-LkCa 15, 2-GM Aur, 3-MWC 480, 4-HD 163296, 5-WW Vul, 6-HD 184761, 7-AA Tau, 8-HD 179218, 9-IRAS 14050-4109, 10-Hen 3-600A.

rich dust around AGB stars, although the geometrical distribution of the emitting dust is different, we have examined the applicability of the silicate dust sequence to the circumstellar disks in our sample. As in Egan & Sloan (2001), F_{10}, F_{11}, F_{12} are calculated from regions of ± 0.2 around these central wavelengths. Also following Egan & Sloan (2001), the photospheric flux was divided out, but this has virtually no effect on the shape of our spectra because of the large IR excesses of disks as compared to AGB star continuum. As is shown in Figure 5.12 and Table 5.6, the F_{10}/F_{12} versus F_{10}/F_{11} for our disks are fit nicely by the silicate dust sequence. All of our sources lie at SE > 5, which, based on the interpretation of Egan & Sloan (2001), indicates that they are composed primarily of silicates (>80%), as opposed to alumina, as is expected for dust in circumstellar disks (see discussion above). Additionally SE > 8 for all but two spectra, indicating that most of our sample can be described as optically thin regions of amorphous silicate dust, which supports the model of Chiang & Goldreich (1997), in which the silicate feature arises from emission from an optically thin layer on disk surfaces. Following Egan & Sloan (2001), the other two sources, Hen 3-600A and HD 179218, which have the strongest emission at $\sim$11 μm, would be described as optically thick, but geometrically thin shells/disks of amorphous silicate dust. However, the SED for Hen 3-600A indicates optically thin dust and the spectra for both sources show sharp peaks at 11.2 μm, indicative of the presence of crystalline forsterite, rather than the smoother features expected from self absorption due to increased optical depth.

We also calculate IRAS colors as in Egan & Sloan (2001), using the zero-magnitude fluxes for

Table 5.6. Egan & Sloan calculations for selected sources.

Source	F_{10} Jy	F_{11} Jy	F_{12} Jy	index	[12]-[16]
LkCa 15	0.551	0.411	0.230	4.40	1.79
GM Aur	0.655	0.582	0.427	6.78	0.573
MWC 480	9.01	8.01	4.86	8.06	3.23
HD 163296	20.0	19.2	12.7	6.68	3.70
WW Vul	2.35	2.07	1.38	7.29	4.03
HD 184761	2.28	1.97	1.32	7.31	2.48
AA Tau	0.591	0.534	0.465	5.37	1.23
HD 179218	18.5	22.5	17.5	4.12	1.87
IRAS 14050-4109	0.226	0.183	0.114	8.22	1.95
Hen 3-600A	0.910	1.18	0.998	3.40	2.48

the non-color-corrected 12 and 25 μm IRAS filters (Cohen et al., 1992),

$$[12] - [25] = 2.5 \log \left(\frac{F_{\nu(25)}}{F_{\nu(12)}} \right) + 1.60. \tag{5.13}$$

The colors for our disks are in general much redder ($[12] - [25] > 1$) than those of AGB dust shells of the same spectral index, which contain much less dust. A notable exception is the disk around the T Tauri star GM Aur, which from the SED is expected to have been cleared of material within 4 AU of the central star, possibly due to planet formation (c.f. Rice et al., 2003).

The results of the Egan & Sloan analysis can be understood in terms of protoplanetary disks, through application of a physical model of disks which couples 2-D radiative transfer with the equation of vertical hydrostatics (Dullemond, 2002; Figure 5.13). In this model, the shape of the SED can be related to the radial and vertical optical depth of the disk. In Case A, the vertical and radial optical depth is large, the disk flares (causing increased flux in the SED at FIR wavelengths) and the inner region is shadowed by "puffed up inner wall" near the star (causing the 2 μm bump in the SED). Case B is similar to case A, with the added constraint that the disk remains radially optically thick at large radii and thus is self-shadowed. This does not change the shape of the SED, but may effect the size of the disk measured at millimeter wavelengths. For Case C, the vertical optical depth is small and the disk is not flared, but the radial optical depth is high enough to shadow the entire disk as shown in Figure 5.13 and the radiation in the SED decreases at long wavelengths ($\lambda \approx 50$ μm). Case D is a transparent disk for which both the vertical and radial optical depth is small and the SED falls off rapidly in the IR. Within the framework of this model, it is the hot grains in the inner disk that are being probed by the 10 μm silicate emission. The disks with SE > 8 represent the first scenario in which the flared disk results in a flat SED. This flared geometry is supported by observations of rotational transitions of the molecular gas in these disks (specifically

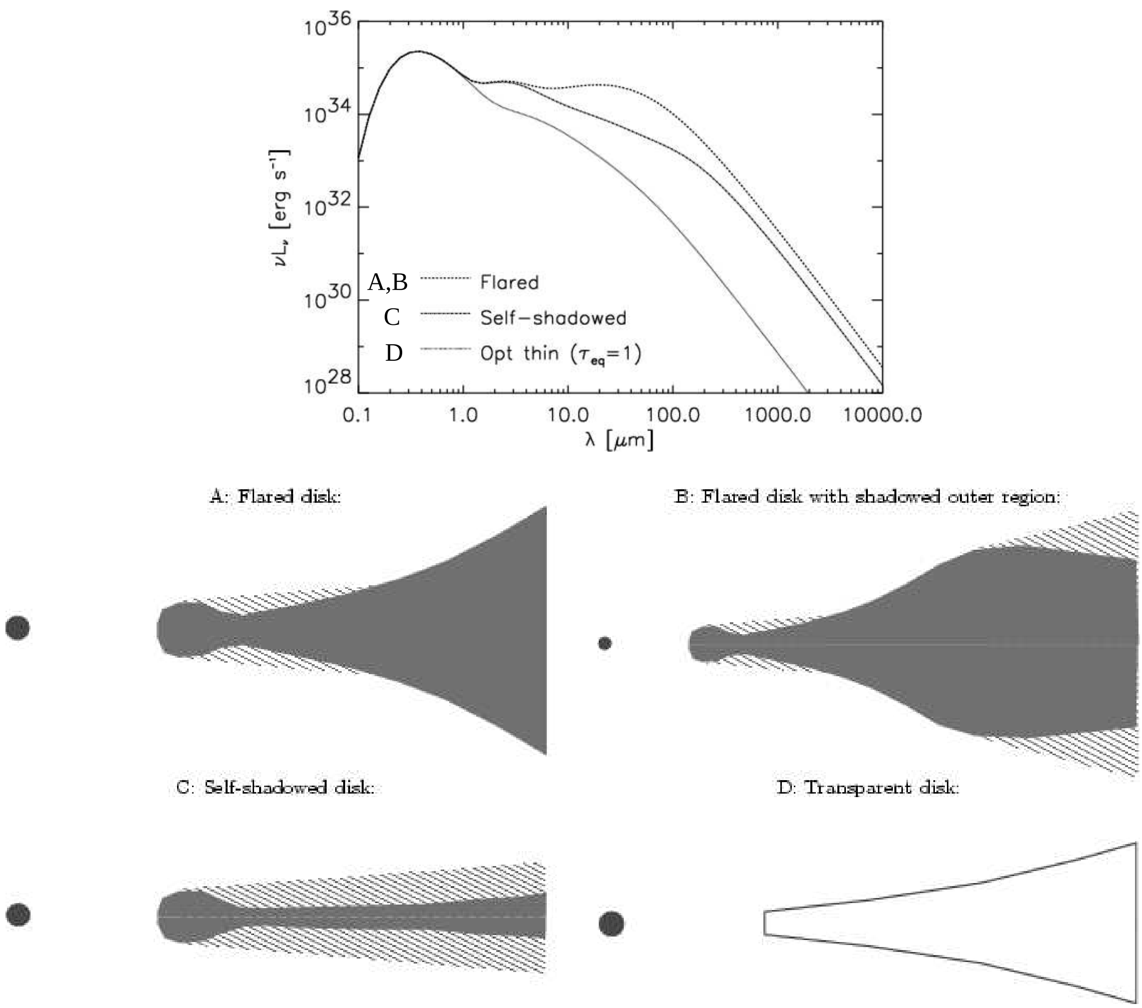

Figure 5.13 Cartoon of radiative transfer and vertical hydrostatic disk models (Dullemond, 2002). In this model, the shape of the SED is related to the radial and vertical optical depth of the disk. In models A and B, the disk is flared leading to shadowing of the inner and outer disk, respectively, and the SED is flat across FIR wavelengths. In model C, the vertical optical depth is small (no flaring), but the radial optical depth is high enough to keep the entire disk in shadow, reducing the radiation at $\sim$50 μm. Model D has low vertical and radial optical depth and thus the emission drops off rapidly in the IR.

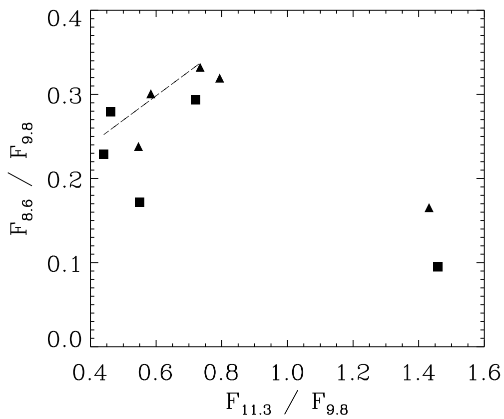

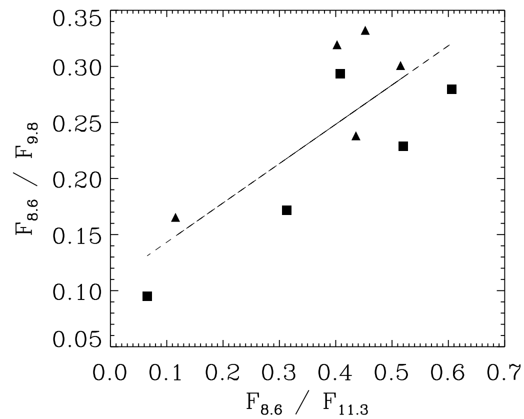

Figure 5.14 IR color-color diagrams. The first plot indicates the relationship between the slopes on the high $F_{11.3}/F_{9.8}$ and low wavelength $F_{8.6}/F_{9.8}$ side of the spectrum. The HD 179218 and Hen 3-600A are outliers, because they show substantial emission at 11.3 μm. The second plot shows the relationship between $F_{9.8}$ and $F_{11.3}$. The strengths of the two features appear to be linearly correlated, indicating that the flux at 11.3 μm does not grow at the expense of that at 9.8 μm, as would be expected if grains were being crystallized.

LkCa 15, GM Aur, MWC 480 and AA Tau; see Chapters 2–3), which indicate warm temperatures expected from additional heating by reprocessing of stellar radiation by dust in disk surface layers of flared disks. Surprisingly, however, the disk with the largest spectral index (SE$\sim$ 14), LkCa 15, is not expected to be the most flared and analysis of the SED indicates that much of the (large) circumstellar grains have settled to the disk midplane (Chiang et al., 2001). For Hen 3-600A and HD 179218, the low spectral indices indicate that the disk is vertically optically thin, but radially optically thick, shielding the outer disk from direct stellar radiation, so that these disks are less likely to be flared and more likely to be self shadowed. This is consistent with the SED for Hen 3-600A, but less so for that of HD 179218, as the flux is still quite high in the FIR.

5.7 Silicate emission feature and grain size

Here we discuss the relationship of the shape of the spectra with the grain size and composition. Van Boekel et al. (2003) examined the spectra from 12 Herbig Ae/Be stars and found that there is a correlation between the feature strength (peak-to-continuum flux) and shape (as indicated by the ratio of the flux at 11.2 to 8.9 μm), with broader emission features being weaker as shown in Figure 5.15 (open triangles). They also showed that the absorption coefficients of 0.1 and 2.0 μm olivine grains match the strong, narrow and broad, weak silicate emission, respectively, indicating that grain size can play a large role in determining the shape/strength of the emission feature.

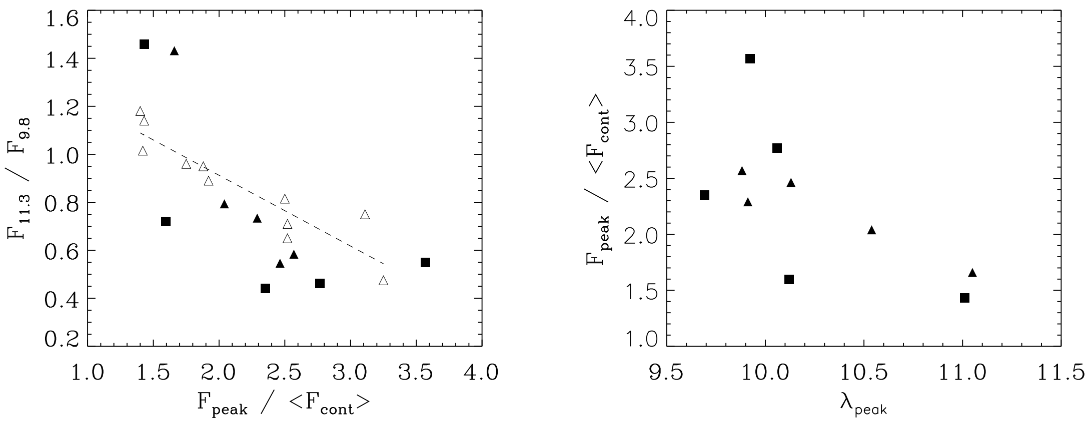

Figure 5.15 Feature characteristics. In both plots, the solid squares and triangles represent the observations of T Tauri and Herbig Ae/Be stars in our sample. The first plot shows the correlation between feature strength and shape, as noted in van Boekel et al. (2003). The dashed line is a linear fit to the van Boekel data set (open triangles). The second plot shows the strength of the silicate feature as a function of the wavelength at which the spectrum peaks. It appears that as the peak shifts to higher wavelengths, indicating larger percentages of crystalline silicates, the strength of the feature decreases.

The solid squares and triangles in Figure 5.15 represent the observations of T Tauri and Herbig Ae/Be stars in our sample. The dashed line is a linear fit to the van Boekel data set. The new data, for the most part, is roughly consistent with the previous trend (including the T Tauri stars). Previous studies of HAEBE stars by Bouwman et al. (2001) indicated that the trend depicted here is a function of both the size and crystallinity of the dust, and thus it is reasonable to think of the strong, narrow and the broad, weak silicate emission features as arising from "unprocessed" and "processed" dust, respectively. However, the two sources with spectra depicting significant emission at 11.3 μm possess stronger silicate features that would be expected to fit the trend found by van Boekel et al. (2003). This can easily be explained if the trend presented by van Boekel et al. (2003) arises primarily from variations in the size of the grains and the additional flux at 11.3 μm for Hen 3-600A and HD 179218 requires the presence of crystalline silicates. The contributions from dust size and composition can then be separated in this manner.

In Figure 5.15 the strength of the silicate feature is plotted with respect to the wavelength of the peak emission. As discussed above, the position of the peak emission likely corresponds to the degree of dust processing as the silicates change from predominantly amorphous olivine (9.7 μm) to enstatite (10.3 μm) to forsterite (11.3 μm). The plot indicates that as the peak position shifts from the classical shape to that of processed dust, the amount of emitting material decreases. 10 μm emission probes the warm, small ($<$ 10 μm) dust grains at the disk surface within 5 AU of the star. The trend observed can thus be explained by a removal of small grains from the disk surface, either through grain growth (supported by the connection between grain growth and the flatness of the spectrum presented above), dust settling, or gap clearing. If the trend were related to removal of dust through gap clearing, then we would expect that GM Aur, which shows evidence of a substantial gap, would peak longward of 9.6 μm. It has also been suggested (Gail, 1998) that progressing crystallization should be accompanied by a drop in opacity of the dust material.

5.8 Spectra and SEDs

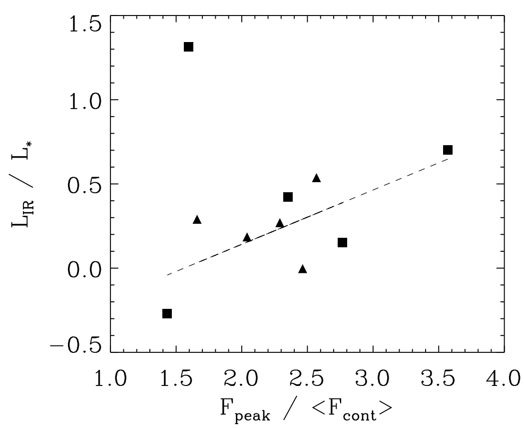

Figure 5.16 Correlations with the SED. This plot shows the correlation between the strength of the silicate feature and the IR-to-stellar luminosity ratio, a measure of the amount of dust in the disk. The outlier is AA Tau, for which the continuum could not be fit and was assumed to be flat at the flux of the 8 μm end of the spectrum.

In order to determine how the amount of warm disk material affects the strength and shape of the silicate emission feature, L_{IR}/L_{tot} and L_{IR}/L_* were calculated from the SEDs as described above. The fractional IR luminosity (L_{IR}/L_{tot}) was not found to be significantly correlated with the position of the ~10 μm silicate peak, indicating that the degree of silicate processing is not directly related to the amount of warm dust. The fact that the strength of the feature is correlated with the position of the peak, but the fractional IR luminosity is not, indicates that the former correlation is most likely due to a change in opacity of the dust, rather than a change in the number of grains. L_{IR}/L_* is found to be correlated to the strength of the emission feature (Figure 5.16), indicating that the amount of warm grains does effect the amount of silicates, if not the degree of dust processing.

5.9 Conclusions and future work

Spectra from 8–13 μm have been obtained for several low and intermediatemass YSOs. An evolutionary sequence from absorption in young, embedded sources, to emission in isolated stars and complete absence in older "debris" disks seen in ISO observations of high/intermediate mass YSOs (Meeus & Waelkens, 1999) was confirmed and extended here to $\sim$ solar mass stars. The shape of the silicate spectra of most T Tauri stars differed little from that toward the ISM, in contrast to the structured emission feature observed for most HAE stars. It is unclear whether crystalline silicates are truly absent in T Tauri stars, for colder or larger crystalline silicate grains would not emit in the 8–13 μm region, but may be visible through far-infrared lattice modes accessible from space born observations. The spectra obtained in this study were compared with other observations and it was found that variations in shape of the spectrum with time did not appear to be correlated with the evolutionary class of the star nor the shape of the silicate emission feature. For the objects with silicate in emission, the shape of the feature was evaluated using the quantitative method of Egan & Sloan (2001) and it was found to be consistent with optically thin disks of amorphous silicate (>80%) dust of geometries similar to those predicted by Dullemond (2002). We also find a correlation between the peak shape and feature strength for 4 TTs and 4 HAE in our sample, which is consistent with that found for 11 HAE stars by van Boekel et al. (2003), which they attribute to changes in grain size (from 0.1–2 μm). Two exceptions were the T Tauri star Hen 3-600A and the HAE star HD 179218, which both lie above the correlation and show strong emission at 11.3 μm, suggesting that the evolution of the silicate feature does not solely represent a change in grain size. Lastly, we found that the strength, but not the shape of the silicate emission feature was correlated with the fractional infrared luminosity (optical depth of the disk).

Due to sensitivity limitations, the ISO studies of silicates described above were confined to intermediate or high-mass stars. Silicate emission features in solar mass T-Tauri stars have only been observed from the ground, recently with the availability of 10m telescopes, in the 10 μm atmospheric window. SIRTF will greatly expand these studies. For example, a large sample of low mass stars, ranging from embedded protostars to optically thin disks, will be studied by the Evans ($\tau_{dust} > 1$) and Meyer ($\tau_{dust} < 1$) Legacy Science programs. In this manner, the study of the crystalline and amorphous silicates in disks, will be expanded to include disks around low mass, sun-like stars, creating a database analogous to ISO studies of high/intermediate-mass stars. These studies will include higher wavelength silicate bands, which depend intricately on the coordination of the silicon atoms and can provide more specific information about the minerals present, including the Mg/Fe ratio. The mineral content of the grains in each stage of evolution can thus be directly compared to that of meteorites, asteroids and comets.

Chapter 6

Concluding remarks and suggestions for future work

Abstract

Circumstellar disks similar to models of the solar nebula have now been detected around several stars with masses comparable to our sun (0.2–10 $M_\odot$) and, as I have discussed in this thesis, are a good environment in which to address the question of planet formation. As analogs to the solar nebula, circumstellar disks offer a unique opportunity to study the conditions during the star and planet formation process. The assessment of the chemical composition in these disks can provide valuable information (i.e., density, thermal history and composition) about the initial conditions in planet-forming zones, in the solar nebula and in exoplanetary systems, and help to determine the origin of primitive bodies such as comets. Wile disk structure is complex, when observed at sufficient spatial and spectral resolution molecular lines can be used to probe the effects of UV fields, temperature variations, ionization and grain-surface reactions on the composition of the gas. Studies of the grain composition and grain surface reactions are also very important, as current models of the chemistry in the outer regions of circumstellar disks (Aikawa et al., 2002; Willacy & Langer, 2000; Finocchi et al., 1997; Bauer et al., 1997) suggest that at large radii the chemistry is highly affected by adsorption onto and desorption from grains. Grains also play a large role in determining the temperature structure and geometry of disks, through reprocessing of stellar radiation. The interpretation of the observed molecular line emission and comparison with chemical models requires knowledge of molecular excitation and disk radiative transfer. Through the comparison of the chemical abundances in circumstellar disks with those of other YSOs, changes in the physical structure during the process of star and planet formation can be monitored. Here I summarize briefly what is known about the evolution of molecular complexity in star and planet formation before turning to an assessment of future observations and modeling of circumstellar disks.

6.1 Chemistry as a function of star formation

Interstellar dust, gas and ice are the building blocks of stars, planets and comets. Modification of this material during the star formation process is believed to result in complex chemical networks in the gas phase and in ices on grain surfaces. The desorption of these ices in turn enhances the complexity of gas-phase chemistry. Interstellar materials are precursors to that in circumstellar disks, similar to our own solar nebula, in which the planets and comets were formed. The material in the outer radii of these disks is relatively unprocessed and similar to its interstellar origin, while material near the star has been significantly modified by the star formation process. Thus, observations tracing the evolution of material in young stellar objects (YSOs) are essential for addressing issues such as the formation of comets and the origin of life.

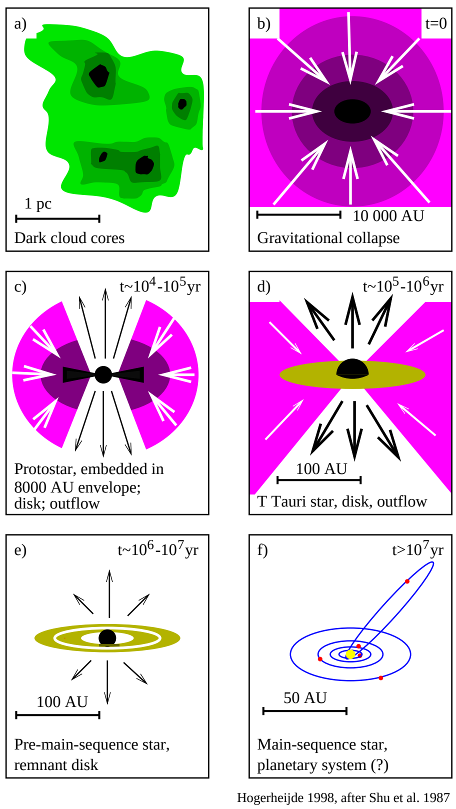

Figure 6.1 The star and planet formation process (Hogerheijde, private communication, 1998). Interstellar gas and dust condenses into dense cores, shielding the enclosed gas and dust from interstellar radiation and allowing the buildup of ices on dust surfaces. Collapse ensues and a star is born in the center of the core, heating and processing the material in the surrounding envelope. Dust and gas accretes onto the star through a circumstellar disk and a bipolar outflow sweeps out surrounding gas. The grain mantle ice may be processed by shocks in this outflow, but remains pristine in the outer, quiescent parts of the disk. The solar system produced will show evidence of the star formation process in the composition of its planets, meteorites and comets.

A diagram of the star formation process is presented in Figure 6.1. At the low temperatures of dense molecular cores (T = 10–40 K; n = 10^2–10^6 molecules/cm^3), gaseous species (atoms and molecules) rapidly accrete onto grain surfaces at roughly the collision rate forming ice mantles that are on the order of 1 μm thick. Laboratory experiments indicate that C, N, O atoms and H_2 can hop across grain surfaces and hydrogen and deuterium atoms tunnel through barriers, scanning the entire grain surface in $\sim 10^{-7}$s. Thus, hydrogenation is efficient on these cold grains and laboratory studies confirm that H_2, NH_3, CH_4 and H_2O are indeed produced in such environments. CO and

H_2, once formed, are self-shielding, and CO is the most abundant observable molecule by 3 orders of magnitude in these cores. This does not imply chemical simplicity, however, as long carbon-chain molecules have been observed toward even the youngest cores, i.e., TMC-1 (Kawaguchi et al., 1992; Takano et al., 1998). The carbon-chain molecules C_2S and HC_3N were found to be correlated with each other, but not with NH_3 nor N_2H^+ and the C_2S/N_2H^+ or C_2S/NH_3 ratios have been used as indicators of the amount of time since the gas was atomic-carbon rich (Bergin & Langer, 1997).

The star formation process continues with collapse of the dense core and the newborn star will heat the surrounding material, leading to desorption of grain-mantle ices and enrichment of the gas-phase chemistry. Systematic observations of molecules other than CO have been pursued only for a few low mass sources during the collapse (or Class 0) stage, the most notable of which is IRAS 16293-2422 (Table 6.1). For this source, large chemical gradients have been seen, with organics such as CH_3OH and CH_3CN in warm, inner parts of the envelope, while the edge of the envelope is dominated by optically thick HCO^+, N_2H^+ and HNC (van Dishoeck et al., 1995). Recent studies indicate that the chemical composition in the inner regions is quite similar to that seen in hot cores around high-mass stars (Schöier et al., 2002). Due to efficient desorption of grain mantles, fully hydrogenated molecules, such as H_2O, NH_3, H_2S and CH_3OH are very abundant in hot cores. Because sulfur is effectively locked up as H_2S on grain surfaces in cold clouds, the abundance of S-bearing molecules in general is much higher in hot cores (2–3 orders of magnitude higher than in earlier stages; see Table 6.1) as well, and the relative abundances of S-bearing molecules has been used as a "chemical clock" to monitor the thermal desorption process and the time elapsed since warming began. The chemistry of ices in this stage can also be enriched by energetic processing, such as ultraviolet irradiation and cosmic rays. Laboratory UV photolysis of "astronomical," methanol-containing ices produce a variety of complex molecules, including alcohols, nitriles and isonitriles, hexamethylenetetramine (HMT), polyoxymethylene (POM), amides and ketones on grain surfaces (Allamandola et al., 1999; Bernstein et al., 1995). Species such as alcohols and ethers, and molecules as complex as glycolaldehyde (Hollis et al., 2000) have been observed in hot cores, indicating that energetic processing of grains may provide a facile route to the development of prebiotic molecules.

As infall continues, a disk forms around the star and an outflow develops perpendicular to the plane of the disk. The outflow clears a cavity in the core and reveals warm dust close to the forming star. In such Class I objects, the high densities and velocities within the outflow in this phase lead to increased collisions between grains resulting in the continued evaporation of ices from grain mantles and additional sputtering of metals from grain cores. For this reason, the outflows of Class I YSOs are characterized by gas-phase emission from the species mentioned above as well as from molecules which require atoms located in grain cores, such as SiO. Gas-phase abundances for the well monitored class I object L1157 are presented in Table 6.1. In comparison with IRAS 16293-2422, L1157 possesses higher abundances of SiO, S-bearing molecules, and organics such as CH_3OH and

H_2CO as predicted for the above scenario.

As the outflow continues, the outer envelope begins to clear ($\sim 10^6$ yr) and the star becomes visible. The SED at this stage is characterized by emission from the star in the optical and UV and radiation from circumstellar dust at $\lambda > 1$ μm (Class II). The objects for which we obtained gas-phase abundances reside in this category (and are discussed thoroughly in this thesis and reviewed below). The observed abundances for the class II T Tauri star LkCa 15 are presented in Table 6.1[1]. The abundances are in general lower than those observed for L1157, which (as discussed below) is likely indicative of the quiescent nature of the disk, but higher than for IRAS 16293-2422, indicating that desorption from grain mantles is still important.

Comets are the most volatile-rich and pristine objects in the solar system. The composition of comets is expected to be similar to that of the early solar nebula (at R$\sim$30 AU). Observations of comets probe the comae during close approaches to the Sun and therefore the chemistry observed may be altered from the original abundances (or even core abundances). Models of gas-phase chemistry (Charnley et al., 2002) are usually used to infer parent molecule abundances in the nucleus, but there are several uncertainties associated with doing so. In accordance with this, the abundances measured in comets appear to be similar to, those observed in (the outer radii of) disks, with the exception of molecules formed on grain mantles, such as CH_3OH, H_2CO and the S-bearing molecules, which are likely larger in comets due to outgassing upon approach to the Sun.

6.2 Understanding the physical properties of disks through molecular line observations

As the second most abundant molecule, next to molecular hydrogen, CO is a useful tracer of the physical structure of circumstellar disks. Via comparison with models, or through examination of the data itself, CO emission is often used to constrain the disk size, inclination and rotation axis and velocity. Due to optical depth effects, however, recent studies (Qi et al., 2003) indicate that CO emission is not a good probe of the total disk mass, although this is a common practice (using a conversion of $[CO]/[H_2] = 10^{-4}$). Observations of multiple CO transitions can also provide information about the temperature structure in the disk (see Chapter 2; van Zadelhoff et al., 2001). In this study, we use a non-LTE Monte Carlo radiative transfer model (Hogerheijde & van der Tak, 2000) and a physical disk model based on D'Alessio et al. (2001) to simulate molecular line emission from the T Tauri star disk LkCa 15. After using the CO 2-1 transition to constrain the disk structure, these models were used to solve the radiative transfer and molecular excitation for the observed 1-0 transitions of ^{13}CO, $C^{18}O$, HCO^+, $H^{13}CO^+$ and N_2H^+. The results indicated that the assumption

[1]For reasons discussed in Chapter 2 and Qi et al. (2003), this refers to abundances in the warm surface layer at R$\sim$300 AU and not the total column.

Table 6.1. Fractional abundances in YSOs and comets (adapted from Schöier et al., 2002)

Species	Comets Hale-Bopp[a]	Disks LkCa 15[b]	Class I L1157[c]	Hot cores Orion[d]	Class 0 IRAS 16293-2422[e]
CO	1(-5)	1(-4)	1(-4)	1(-4)	4(-5)
H_2O	5(-5)	<9(-4)	...	>1(-5)	...
HCN	1(-7)	1(-7)	5(-7)	4(-7)	1(-9)
CN	...	6(-9)	5(-8)	...	8(-11)
HNC	2(-8)	<3(-10)	5(-8)	...	3(-8)
HCO^+	...	5(-10)	3(-8)	1(-9)	8(-9)
CH_3OH	1(-6)	5(-8)	2(-5)	2(-7)	3(-7)
H_2CO	5(-7)	(0.4-1)(-9)	3(-7)	1(-8)	6(-8)
CS	5(-8)	1(-9)	2(-7)	1(-7)	2.5(-9)
SO	1(-7)	<3(-9)	3(-7)	5(-8)	3.5(-9)
SO_2	1(-7)	<4(-9)	5(-7)	6(-8)	2(-10)
OCS	2(-7)	<42(-9)	2(-7)	5(-8)	<3(-9)
H_2S	7(-7)	<4(-8)	4(-7)	<1(-7)	...
SiO	...	<1(-10)	7(-8)	6(-8)	2.5(-11)

Note. — X(Y) = $X\times10^{Y}$ is the fractional abundance with respect to H_2

[a]From Bockelée-Morvan et al., 2000 for comet Hale-Bopp at 1 AU, assuming $H_2O/H_2=5\times10^{-5}$

[b]From Aikawa et al., 2003 (H_2CO), this thesis (HCN,H_2O), and Qi, 2001 (others)

[c]From Bachiller et al., 1997 at position B2 assuming $CO/H_2 = 10^{-4}$

[d]From van Dishoeck & Blake, 1998 (and references cited); otherwise from Sutton et al., 1995

[e]From Schöier et al. (2002) in the warm, dense inner part of the envelope ≤150 AU in radius around IRAS 16293-2422

that the emitting region is in LTE was not strictly valid and produces an error of a factor of ∼2 in the calculated column densities. These results were consistent with previous LVG calculations for LkCa 15 (van Zadelhoff et al., 2001) and support prior indications that the molecular line emission observed here arises from warm layers near the disk surface (Qi et al., 2003).

Although located a good distance from the star, these emission layers are kept relatively warm due to the flared disk geometry and direct stellar and scattered UV. This suggests that UV fields have a large impact on disk structure (and chemistry). In Chapter 3 CN, HCN and HCO^+ were used as tracers of the effective UV field in several circumstellar disks. Although CN and HCN are produced in a similar manner, through reactions of N with neutral and ionic hydrocarbons, CN is destroyed through neutral-neutral reactions, while HCN is destroyed by ion-molecule chemistry and UV photolysis (to form CN). An increase in the effective UV field results in increased photoionization and photodissociation, which in turn leads to increased production of CN, HCN and HCO^+. The increase in HCN production, however, is moderated by a coincident increase in HCN destruction, while the destruction rate of CN remains constant (or decreases). Observations of the CN/HCN ratio should therefore trace the strength of the effective UV field at disk surfaces, with increased CN/HCN corresponding to stronger UV fields. This has been found to be true in molecular clouds and photodissociation regions. Here, CN and HCO^+ were found to be (at least weakly) correlated with tracers of the effective UV field; abundances of both molecules increased with increases in the fractional IR luminosity and the dust settling parameter H/h. HCN, on the other hand, did not appear to be correlated with these or other disk parameters, likely due to the complexity of the reaction network for this molecule. Surprisingly, no molecular abundances appeared to be correlated with stellar parameters, such as L_*. This suggests that the interstellar radiation field may be more important than the stellar radiation field in the outer regions of disks (R > 70 AU) probed by these observations. HNC is produced and destroyed via ion-molecule reactions and thus is a very good probe of ion-molecule chemistry. Because it was only observed toward one source in our sample, a statistical analysis was not performed, but future studies may prove to be very valuable to the understanding of nitrogen chemistry in disks.

Deuterium fractionation has been observed to vary by 3 orders of magnitude between molecular clouds and the planets in our solar system. Thus, D/H ratios are a sensitive tracer of the conditions throughout the star formation process. Deuterium observations in the outer regions of disks are particularly interesting as a way to constrain the location and timescales of comet formation. In Chapter 4, we present the first detections of HDO and DCN toward circumstellar disks. The resulting deuterium fractionations in LkCa 15 and HD 163296 were found to be similar to those found toward the T Tauri star disk TW Hya and those observed in molecular clouds and hot cores.

The HDO emission presented in Chapter 4, as well as previous observations toward LkCa 15 (Qi et al., in prep), indicate large differences in the morphology of the emission in the integrated intensity maps (Figure 4.5). CO and HCO^+ emission peak at the source position while the HCN, CN and HDO emission peak approximately $2''$ away along the major axis of the disk. This is particularly interesting because the spectra for CO 2-1, HCO^+, HDO and HCN do not differ significantly. Lack of emission toward the star results in only small changes to the line wings, which are often indistinguishable due to the noise in the spectrum. Clearly, imaging is necessary to study this type of disk structure and there is a need for detailed models which can be used to reproduce and interpret these images. For these reasons, we used the model described in Chapter 2, to simulate our observed channel maps and images of protoplanetary disks, first for the case of the emission for a telescope with infinite resolution and complete (u, v) coverage and then for the observed (u, v) coverage and resolution. We find that even with $2''$ resolution, the detailed disk structure is largely washed out by current observations and image deconvolution techniques.

The chemical models of Aikawa & Herbst (2001) and Willacy & Langer (2001) suggest that the radial distribution of HCN and CN in disks is determined by the processes of photodissociation by interstellar and stellar UV combined with desorption from grain surfaces. The newest models (Aikawa et al. 2002) suggest that the competition between interstellar and stellar UV in particular determine the variation in the amount of HCN as a function of radius. We simulate the emission morphology discussed above by concentrating the HCN in a ring around the star with an outer radius determined from the CO 2-1 observations (~430 AU) and an inner radius which is varied to match the observed integrated intensity maps. These models can reproduce the structure of the HCN emission only with large depletion zones in the disk center ($R_i \sim 200$–300 AU). More realistic models will be used in the future to simulate the combined effects of desorption from grains and photodissociation of HCN from interstellar and stellar UV.

Although we have not yet modeled the HDO emission, the observed double peaked intensity map may also result from a ring-like distribution (or a steep outward gradient). Here models suggest that the annulus could be formed due to reduced production of HDO near the central star as H_2D^+, the primary precursor to HDO, is created less efficiently due to the increasing temperature gradient in the inner disk. This causes the HDO abundance to peak at R≈250 AU (Aikawa & Herbst 2001). As the previous HCN models show, this morphology is consistent with the observed emission.

6.3 Grain composition and grain-surface chemistry

Current models of the chemistry in the outer regions of circumstellar disks (Willacy & Langer, 2000; Aikawa & Herbst, 2001), suggest that at large radii adsorption onto and desorption from grains can have a large effect on the gas-phase chemistry by removing (adding) molecules to (from) the gas. Additionally, due to the high mobility of hydrogen (and moderate mobility of C, N, S, and O), a higher degree of chemical complexity can be achieved on grain surfaces than in the gas phase and grains-surface chemistry is believed to play a critical role in the formation of pre-biotic molecules. The grain composition directly affects the extent of grain-molecule interactions (e.g., freezout onto grain surfaces) and resulting chemistry through molecule-to-grain binding energies and sticking coefficients. Recent models also indicate that disks are heated by the reprocessing of stellar radiation by grains near disk surfaces. This heating results in a flared geometry of the disk, with a cool midplane and warmer surface layer, and radiative transfer models (c.f. Chapter 2) suggest that it is these warm surface layers which are probed by the studies discussed above.

CO is the most abundant carbon-bearing species in the gas phase of the interstellar medium. It is also deposited very quickly on grain surfaces at high densities. Therefore, if prebiotic molecules are to be formed, the process must begin with the destruction of CO. If hydrogen is abundant on the grain surface, it will likely react with CO, possibly resulting in the formation of formaldehyde and methanol (Tielens & Whittet 1997). In the absence of large amounts of hydrogen on grain surfaces, oxygen may react with CO to form CO_2, which can then be converted into formic acid. Formation of methanol and/or formic acid is necessary for the initialization of the formation of prebiotic molecules (Charnley et al., 1997). Thermal and energetic (UV/cosmic ray) processing of grains will likely determine the degree of chemical complexity in the grain-mantle ice. However, neither the exact dependence of the reactions above on these types of processing, nor the degree of processing of actual interstellar grains, have yet been determined.

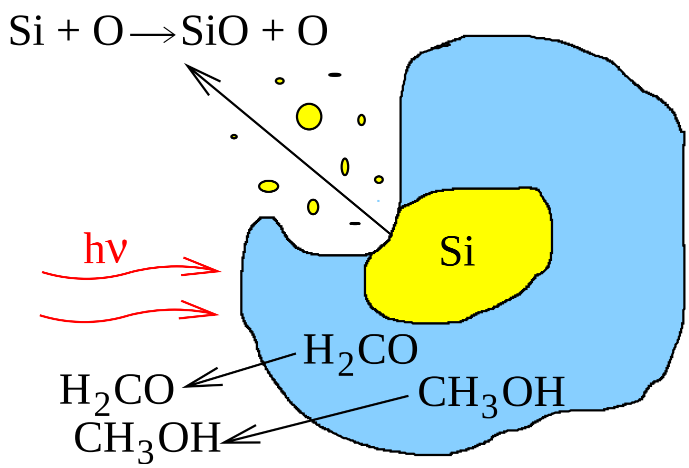

Figure 6.2 Dust processing. Exposure to high temperatures (>20 K for CO) or UV radiation leads to evaporation of the ices, and the influx of more complex molecules may stimulate gas-phase chemistry. In high-velocity environments (i.e., outflows), grain-grain collisions lead to sputtering, releasing grain core substituents into the gas phase, which leads to gas-phase production of molecules such as SiO.

The nature of grain mantle and coupled gas-grain chemistry has been extensively studied in the warm, dense hot cores around massive protostars (Charnley et al., 1997), but little is known about grain mantle processes in circumstellar disks. Accordingly, we have examined grain and grain surface chemistry through the observation of a few key species, namely, methanol, formaldehyde and silicon monoxide. These particular molecules have been widely observed in hot cores and their chemistry is fairly well understood. Both methanol and formaldehyde have been detected in the disks encircling the solar type stars LkCa 15 (Qi, 2001; Aikawa et al., 2003) and DM Tau (Dutrey et al., 1997) indicating the effectiveness of complex molecule formation on grains in disks (as well as hot cores) and a possible route to the in situ formation of pre-biotic molecules within the solar nebula through thermal and energetic (UV/cosmic ray) processing of grains. A summary of the LkCa 15 observations is shown in Figure 6.3. Because methanol and formaldehyde are formed on grain surfaces, they can desorb easily in warm environments and remain somewhat stable in the gas phase in the absence of ions (see Figure 6.2). In contrast, SiO is formed from grain interiors when silicon is released from grain cores through violent interactions of grains and is a tracer of more violent disk processing, such as occurs in shocks or outflows. SiO was searched for, but not detected toward LkCa 15; inferences on the turbidity of outer disks can be made from this result. The presence of methanol and formaldehyde in disks, indicates that the disk surrounding LkCa 15 is reasonably quiescent.

Sulfur chemistry is also used to trace the evolution of hot cores; atomic sulfur depletes onto grains surfaces (and can be converted into H_2S or OCS) due to low temperatures in the dense cloud core, evaporates in the hot core stage, and is rapidly converted to SO and SO_2, and more slowly into CS, in the gas phase. In this manner, the relative abundances of S-bearing molecules can be used as

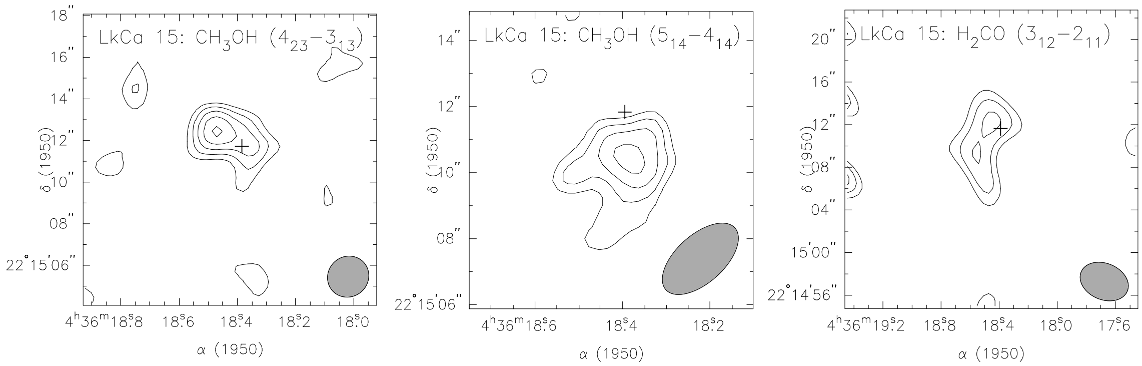

Figure 6.3 OVRO observations of formaldehyde and methanol toward T Tauri star LkCa 15 (Qi, 2001). The left and center panels show emission from CH_3OH and the right panel shows H_2CO emission. The H_2CO emission toward LkCa 15 is consistent with that observed at the Nobeyama Millimeter Array by Aikawa et al. (2003). Both molecules show emission which does not peak at the source position, similar to that observed for emission from other species in this disk.

a “chemical clock”, which measures the time since H_2S was released from grain surfaces (Hatchell et al., 1998). In the case of disks, the abundances of S-bearing molecules indicate the time since significant reprocessing of the grains has occurred. Toward LkCa 15 we observed large amounts of CS, including the isotope, $C^{34}S$ (= [CS]/20), but no SO, SO_2, H_2S or OCS were detected (see Figure 6.4). The upper limits are only low enough to limit the abundances of these molecules to $\sim$[CS]. According to the models of Hatchell et al. (1998), comparable abundances of sulfur species indicate that this region of the disk is reasonably quiescent, which is consistent with the discussion of grain chemistry above. The fact that there is a lack of freshly desorbed H_2S may also suggest that the outer regions of disks are stratified, where the timescale for mixing between the observable layer and the layers where thermal desorption is occurring is longer than the chemical timescale for conversion of H_2S to CS.

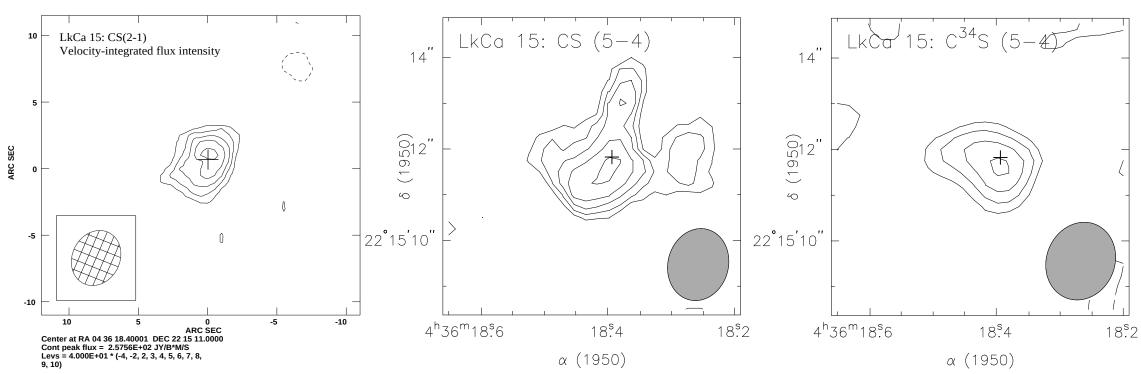

Figure 6.4 Observations of S-bearing molecules toward the protoplanetary disk around the T Tauri star LkCa 15 (Qi, 2001). From left to right, the panels show the CS 2-1, CS 5-4 and $C^{34}S$ 5-4 emission.

As mentioned above, the dust composition can have large effects on the gas-phase chemistry

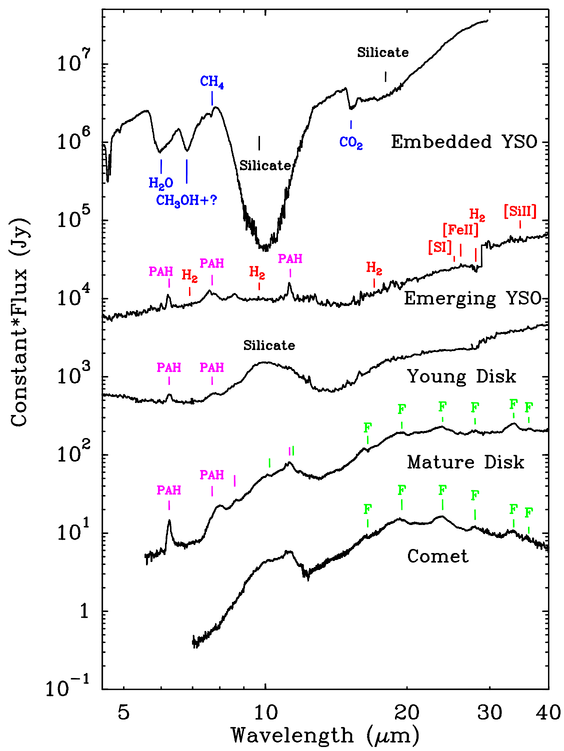

Figure 6.5 Evolution of IR spectra toward YSOs and comets (from Evans et al., 2003). The silicate feature changes from absorption of amorphous silicates in young, embedded protostars, to emission of amorphous and crystalline silicates in older disks and comets (F = forsterite).

and physical geometry of disks, and therefore knowledge of the dust composition is essential. Dust in early stages of star formation appears to be primarily amorphous silicates (Hanner et al., 1998). Observations of silicate emission in high-mass YSOs suggest an evolutionary sequence in which some of these amorphous silicates are crystallized during the star (and planet) formation process, resulting in the crystalline materials found in primitive solar system objects such as carbonaceous chondrites, comets and interplanetary dust particles (Figure 6.5). In Chapter 5, the 8–13 μm spectra were obtained for several low and intermediate mass YSOs. An evolutionary sequence from absorption in young, embedded sources, to emission in isolated stars and complete absence in older "debris" disks seen in ISO observations of high/intermediate-mass YSOs (Meeus & Waelkens, 1999) was confirmed and extended here to $\sim$ solar mass stars. In contrast to the structured emission feature observed for most HAE stars, the shape of the silicate spectra of most T Tauri stars in our sample was very similar to that of the ISM and source-to-source variations in this shape are consistent with growth in the average size of the dust grains from 0.1$\rightarrow$2 μm (van Boekel et al., 2003), with models of optically thin disks of amorphous silicate (>80%) dust whose geometries are similar to those predicted by

Dullemond (2002). The spectrum toward the T Tauri star Hen 3-600A *does* show emission typical of crystalline silicates (similar to the HAE star HD 179218 observed in our sample), indicating that under some conditions crystallization of silicates *can* occur in disks around *low mass* stars. The strength, but not the shape, of the emission features was found to be correlated with the fractional infrared luminosity (that is, the optical depth of the disk).

6.4 Future observations and models

As discussed in Chapter 5, the determination of the dust composition in disks around ∼solar mass has been limited by the sensitivity of current instrumentation; ISO studies of silicates were confined to intermediate or high-mass stars and ground based observations are restricted to the 10 μm observing window. With the successful August 2003 launch of the Space Infrared Telescope Facility (SIRTF), much expanded studies, including disks around low mass, sun-like stars, can be expected creating a database analogous to ISO studies of high/intermediate-mass stars. Early SIRTF observations will include a large sample of low mass YSOs, ranging from embedded protostars to optically thin disks, via the combination of the Evans ($\tau_{dust} > 1$) and Meyer ($\tau_{dust} < 1$) Legacy Science programs (Evans et al., 2003; http://feps.as.arizona.edu), whose data will become publically available upon collection and pipeline reduction. Additionally, these studies will include observations of silicate emission features in the 15–40 μm region, which are inaccessible from the ground and depend intricately on the coordination of the silicon atoms; thus providing more specific information about the minerals present, including the Mg/Fe ratio. The mineral content of the grains in each stage of evolution can thus be directly compared to that of meteorites, asteroids and comets. These studies will allow the crystallinity of the silicates in disks to be calculated, and the connections between disk temperatures and morphology (begun in Chapter 5), to be established through comparison of the amorphous/crystalline silicate ratios with indicators of disk flaring, such as the shape of the far IR excess (Chiang et al., 2001). In this manner, the ubiquity of cold crystalline silicates could be assessed and their formation mechanism can be explored through correlations with age or grain growth indicators.

Details of disk chemistry are most completely examined with high sensitivity, dynamic range and spatial resolution of interferometric studies of molecular species. CO emission and dust radiation has been observed for disks around many stars, but extensive chemical studies have been performed toward only a few T-Tauri star disks, including those presented in this thesis, LkCa 15, DM Tau, GG Tau and TW Hya (Qi, 2001; Dutrey et al., 1997; Kastner et al., 1997). Even for the brightest disks, millimeter arrays are not yet sensitive enough at high frequencies to reliably detect molecules with emission lines in the 1 mm region (i.e., H_2CO, CH_3OH, HDO) unless very long integration times are used. In the somewhat near future, a new generation of interferometers, including the Submillimeter

Array (SMA) and the Combined Array for Research in Millimeter-wave Astronomy (CARMA) will offer improved sensitivity ($\sim$5$\times$) over current arrays, enabling studies such as those discussed above to be more efficiently performed over larger samples. The improved sensitivity should also enable the detection of more weakly emitting species, such as prebiotic molecules, which have currently only been detected in hot cores. In the more distant future, the Atacama Large Millimeter Array (ALMA), will offer improvements in sensitivity by a factor of 20 over current arrays! Additionally, ALMA will be able to achieve a spatial resolution of $10^{-3\prime\prime}$, which corresponds to $\sim$0.1 AU for sources in nearby star-forming regions (at a distance of 140 pc). At this resolution, the planet-forming regions of disks can be probed and truly in situ measurements of the nebular chemistry will be possible for the first time.

Even before the advent of ALMA, molecular observations of circumstellar disks may be able to detect signatures of planet formation in progress, shedding light on the formation process. Although circumstellar disks have now been observed in the millimeter and infrared (as discussed above), and some of these disks are clearly old enough to possess large planetesimals or protoplanets, clear signatures of planet formation are difficult to observe. Accretion of a protoplanet of size greater than $\sim$10 M_E results in the formation of a gap in the disk, but models indicate the difficulty of detecting changes in the spectral energy distribution due to disk clearing (Wood et al., 2002, Steinacker & Henning, 2003) and direct imaging of gaps (Wolf et al., 2002) or rings of material disturbed by protoplanets (Ozernoy et al., 2000). To date, evidence for planet formation has only been observed in disks of reprocessed material around older stars. High-resolution IR imaging of the 20 Myr old, debris disk β Pictoris (Wahhaj 2003), shows evidence of four such rings, with orbits at 14, 29.1, 51 and 81 AU from the star. Structure seen in the emission from debris disks around ϵ Eridani and Vega have also been reproduced with models involving protoplanets, but the exact origin of the observed structure is unclear.

Observations of the chemistry in disks may be able to more selectively probe the planet formation process. After gap formation, material accretes onto the planet through narrow flows onto a circumplanetary disk with spiral density structure. The properties of the circumplanetary disk are very different from the circumstellar disk, resulting in a significant change in the chemistry. For example, NH_3 and CH_4 dominate in the circumplanetary disk, whereas N_2, HCN and CO dominate in the circumstellar disk. Additionally, NH_3 and CH_4 are the predominant species on grains and are released into the gas in the shocked regions, resulting in enhanced abundances of these species near the site of planet formation. The planet formation process may therefore be detectable through chemical tracers, such as CO/CH_4 and HCN/NH_3 ratios via infrared observations of CO/CH_4 and HCN/NH_3, using the line shape and the excitation of each transition to assign the observed density ratios with the circumplanetary disk. Such studies require high dynamic range, high spectral resolution observations to distinguish between emission from the circumstellar and circumplanetary disks, and should be attainable with new instruments such as NIRSPEC at the Keck telescope, VISIR at the VLT and the EXES spectrograph on SOFIA.

As discussed in Chapter 2, radiative transfer modeling is essential for the interpretation of spectral line shapes and maps of molecular distributions of circumstellar disks. The application of such models in this thesis is but a preliminary step, and merely indicate the usefulness of combining radiative transfer models with standard imaging techniques to more closely simulate observed molecular distributions, such as those of HCN and HDO in LkCa 15. In the near future, we will expand the current model to include radial gradients in the abundance of these molecules and establish the slope of the gradient required to reproduce the observed emission. Fits will also be carried out in the (u, v) plane where rigorous error propagation enables detailed least squares fits to the observational data (see, for example, Dartois et al., 2003). These complexity of these computations are currently limited by computer processor speed and memory. In the not-so-distant future, the combination of accurate radiative transfer calculations with detailed models of disk chemistry will be possible, enabling the direct comparison, and thus the eventual convergence, of the predicted and observed molecular distributions.

Bibliography

Adams, F. C., Lada, C. J., & Shu, F. H. 1987, ApJ, 312, 788

Aikawa, Y. & Herbst, E. 1999, ApJ, 526, 314

—. 2001, A&A, 371, 1107

Aikawa, Y., Momose, M., Thi, W., van Zadelhoff, G., Qi, C., Blake, G. A., & van Dishoeck, E. F. 2003, PASJ, 55, 11

Aikawa, Y., Umebayashi, T., Nakano, T., & Miyama, S. M. 1999, ApJ, 519, 705

Aikawa, Y., van Zadelhoff, G. J., van Dishoeck, E. F., & Herbst, E. 2002, A&A, 386, 622

Allamandola, L. J., Bernstein, M. P., Sanford, S. A., & Walker, R. L. 1999, Space Sci. Rev., 90, 219

Bachiller, R., Forveille, T., Huggins, P. J., & Cox, P. 1997, A&A, 324, 1123

Backman, D. E. & Paresce, F. 1993, in Protostars and Planets III, 1253–1304

Bauer, I., Finocchi, F., Duschl, W. J., Gail, H.-P., & Schloeder, J. P. 1997, A&A, 317, 273

Beckwith, S. V. W. & Sargent, A. I. 1993, ApJ, 402, 280

—. 1996, Nature, 383, 139

Beckwith, S. V. W., Sargent, A. I., Chini, R. S., & Guesten, R. 1990, AJ, 99, 924

Beichman, C. A., Neugebauer, G., Habing, H. J., Clegg, P. E., & Chester, T. J. 1988, NASA Reference Publication, 1190, 1

Bell, K. R., Cassen, P. M., Klahr, H. H., & Henning, T. 1997, ApJ, 486, 372

Bergin, E., Calvet, N., D'Alessio, P., & Herczeg, G. J. 2003, ApJ, 591, L159

Bergin, E. A. & Langer, W. D. 1997, ApJ, 486, 316

Bernstein, M. P., Sandford, S. A., Allamandola, L. J., & Chang, S. 1995, ApJ, 454, 327

Berrilli, F., Corciulo, G., Ingrosso, G., Lorenzetti, D., Nisini, B., & Strafella, F. 1992, ApJ, 398, 254

Bockelée-Morvan, D., Gautier, D., Lis, D. C., Young, K., Keene, J., Phillips, T., Owen, T., Crovisier, J., Goldsmith, P. F., Bergin, E. A., Despois, D., & Wooten, A. 1998, Icarus, 133, 147

Bockelée-Morvan, D., Lis, D. C., Wink, J. E., Despois, D., Crovisier, J., Bachiller, R., Benford, D. J., Biver, N., Colom, P., Davies, J. K., Gérard, E., Germain, B., Houde, M., Mehringer, D., Moreno, R., Paubert, G., Phillips, T. G., & Rauer, H. 2000, A&A, 353, 1101

Bouwman, J., de Koter, A., Dominik, C., & Waters, L. B. F. M. 2003, A&A, 401, 577

Bouwman, J., Meeus, G., de Koter, A., Hony, S., Dominik, C., & Waters, L. B. F. M. 2001, A&A, 375, 950

Brown, P. D., Charnley, S. B., & Millar, T. J. 1988, MNRAS, 231, 409

Brown, P. D. & Millar, T. J. 1989, MNRAS, 237, 661

Calvet, N., D'Alessio, P., Hartmann, L., Wilner, D., Walsh, A., & Sitko, M. 2002, ApJ, 586, 1008

Casanova, S., Montmerle, T., Feigelson, E. D., & Andre, P. 1995, ApJ, 439, 752

Charnley, S. B., Rodgers, S. D., Butner, H. M., & Ehrenfreund, P. 2002, Earth Moon and Planets, 90, 349

Charnley, S. B., Tielens, A. G. G. M., & Rodgers, S. D. 1997, ApJ, 482, 203

Chiang, E. I. & Goldreich, P. 1997, ApJ, 490, 368

Chiang, E. I., Joung, M. K., Creech-Eakman, M. J., Qi, C., Kessler, J. E., Blake, G. A., & van Dishoeck, E. F. 2001, ApJ, 547, 1077

Cohen, M., Emerson, J. P., & Beichman, C. A. 1989, ApJ, 339, 455

Cohen, M., Walker, R. G., & Witteborn, F. C. 1992, AJ, 104, 2030

Cohen, M. & Witteborn, F. C. 1985, ApJ, 294, 345

Cox, P., Omont, A., Huggins, P. J., Bachiller, R., & Forveille, T. 1992, A&A, 266, 420

Creech-Eakman, M. J., Chiang, E. I., Joung, R. M. K., Blake, G. A., & van Dishoeck, E. F. 2002, A&A, 385, 546

D'Alessio, P., Calvet, N., & Hartmann, L. 2001, ApJ, 553, 321

D'Alessio, P., Calvet, N., Hartmann, L., Lizano, S., & Cantó, J. 1999, ApJ, 527, 893

D'Alessio, P., Cantó, J., Calvet, N., & Lizano, S. 1998, ApJ, 500, 411

Damiani, F., Micela, G., Sciortino, S., & Harnden, F. R. 1995, ApJ, 446, 331

Dartois, E., Dutrey, A., & Guilloteau, S. 2003, A&A, 399, 773

de La Reza, R., Torres, C. A. O., Quast, G., Castilho, B. V., & Vieira, G. L. 1989, ApJ, 343, 61

Deloule, E., Doukhan, J.-P., & Robert, F. 1997, in Lunar and Planetary Institute Conference Abstracts, 291

Dorminey, B. 2002, Distant wanderers: the search for planets beyond the solar system (Copernicus Books, an imprint of Springer-Verlag, New York, 2002 ISBN 0387950745.)

Drouart, A., Dubrulle, B., Gautier, D., & Robert, F. 1999, Icarus, 140, 129

Duley, W. W. & Williams, D. A. 1984, Inorganic Chemistry

Dullemond, C. P. 2002, A&A, 395, 853

Duncan, M., Quinn, T., & Tremaine, S. 1988, ApJ, 328, 69

Duschl, W. J., Gail, H.-P., & Tscharnuter, W. M. 1996, A&A, 312, 624

Dutrey, A. 2003, in Proceedings of the IAU, Star Formation at High Angular Resolution, in press

Dutrey, A., Guilloteau, S., Duvert, G., Prato, L., Simon, M., Schuster, K., & Menard, F. 1996, A&A, 309, 493

Dutrey, A., Guilloteau, S., & Guelin, M. 1997, A&A, 317, L55

Duvert, G., Guilloteau, S., Ménard, F., Simon, M., & Dutrey, A. 2000, A&A, 355, 165

Eberhardt, P., Reber, M., Krankowsky, D., & Hodges, R. R. 1995, A&A, 302, 301

Egan, M. P. & Sloan, G. C. 2001, ApJ, 558, 165

Encrenaz, T. 2001, LNP, 577, 76

Evans, N. J., Allen, L. E., Blake, G. A., Boogert, A. C. A., Bourke, T., Harvey, P. M., Kessler, J. E., Koerner, D. W., Lee, C. W., Mundy, L. G., Myers, P. C., Padgett, D. L., Pontoppidan, K., Sargent, A. I., Stapelfeldt, K. R., van Dishoeck, E. F., Young, C. H., & Young, K. E. 2003, PASP, 115, 965

Fabian, D., Henning, T., Jäger, C., Mutschke, H., Dorschner, J., & Wehrhan, O. 2001, A&A, 378, 228

Fajardo-Acosta, S. B., Knacke, R. F., & Telesco, C. M. 1993, Bulletin of the American Astronomical Society, 25, 1340

Feigelson, E. D. & Montmerle, T. 1999, ARA&A, 37, 363

Fernandez, J. A. & Ip, W.-H. 1991, in ASSL Vol. 167: IAU Colloq. 116: Comets in the post-Halley era, 487–535

Festou, M. C., Rickman, H., & West, R. M. 1993, A&A Rev., 4, 363

Finocchi, F. & Gail, H.-P. 1997, A&A, 327, 825

Finocchi, F., Gail, H.-P., & Duschl, W. J. 1997, A&A, 325, 1264

Friedemann, C., Guertler, J., & Reimann, H.-G. 1995, A&A, 300, 269

Fuente, A., Martin-Pintado, J., Cernicharo, J., & Bachiller, R. 1993, A&A, 276, 473

Gail, H.-P. 1998, A&A, 332, 1099

Gautier, D. 1988, Royal Society of London Philosophical Transactions Series A, 325, 583

Gautier, D. & Morel, P. 1997, A&A, 323, L9

Geiss, J. & Reeves, H. 1981, A&A, 93, 189

Gensheimer, P. D., Mauersberger, R., & Wilson, T. L. 1996, A&A, 314, 281

Geoffray, H. & Monin, J. L. 2001, A&A, 369, 239

Gibb, E. L., Whittet, D. C. B., Schutte, W. A., Boogert, A. C. A., Chiar, J. E., Ehrenfreund, P., Gerakines, P. A., Keane, J. V., Tielens, A. G. G. M., van Dishoeck, E. F., & Kerkhof, O. 2000, ApJ, 536, 347

Glass, I. S. 1975, MNRAS, 171, 19P

Glassgold, A. E., Najita, J., & Igea, J. 1997, ApJ, 480, 344

Goldreich, P. & Sari, R. 2003, ApJ, 585, 1024

Goldsmith, P. F., Langer, W. D., & Velusamy, T. 1999, ApJ, 519, 173

Grossman, L. 1972, GeCoA, 38, 47

Guilloteau, S. & Dutrey, A. 1998, A&A, 339, 467

Habing, H. J., Dominik, C., Jourdain de Muizon, M., Laureijs, R. J., Kessler, M. F., Leech, K., Metcalfe, L., Salama, A., Siebenmorgen, R., Trams, N., & Bouchet, P. 2001, A&A, 365, 545

Hanner, M. S., Brooke, T. Y., & Tokunaga, A. T. 1995, ApJ, 438, 250

—. 1998, ApJ, 502, 871

Hanner, M. S., Lynch, D. K., & Russell, R. W. 1994, ApJ, 425, 274

Hatchell, J., Thompson, M. A., Millar, T. J., & MacDonald, G. H. 1998, A&A, 338, 713

Hawley, J. F. & Balbus, S. A. 1991, ApJ, 376, 223

Hayashi, C. 1981, Progress of Theoretical Physics Supplement, 70, 35

Helmich, F. P., van Dishoeck, E. F., & Jansen, D. J. 1996, A&A, 313, 657

Herbig, G. H. & Goodrich, R. W. 1986, ApJ, 309, 294

Herbst, E., Defrees, D. J., & McLean, A. D. 1987, ApJ, 321, 898

Hillenbrand, L. A., Strom, S. E., Vrba, F. J., & Keene, J. 1992, ApJ, 397, 613

Hogerheijde, M. R. & van der Tak, F. F. S. 2000, A&A, 362, 697

Hollis, J. M., Lovas, F. J., & Jewell, P. R. 2000, ApJ, 540, L107

Honda, M., Kataza, H., Okamoto, Y. K., Miyata, T., Yamashita, T., Sako, S., Takubo, S., & Onaka, T. 2003, ApJ, 585, L59

Horne, K. & Marsh, T. R. 1986, MNRAS, 218, 761

Igea, J. & Glassgold, A. E. 1999, ApJ, 518, 848

Imhoff, C. L. & Appenzeller, I. 1987, in ASSL Vol. 129: Exploring the Universe with the IUE Satellite, 295–319

Jacq, T., Walmsley, C. M., Henkel, C., Baudry, A., Mauersberger, R., & Jewell, P. R. 1990, A&A, 228, 447

Jansen, D. J., van Dishoeck, E. F., Black, J. H., Spaans, M., & Sosin, C. 1995, A&A, 302, 223

Jayawardhana, R., Fisher, R. S., Telesco, C. M., Piña, R. K., Barrado y Navascués, D., Hartmann, L. W., & Fazio, G. G. 2001, AJ, 122, 2047

Johansson, L. E. B., Andersson, C., Ellder, J., Friberg, P., Hjalmarson, A., Hoglund, B., Irvine, W. M., Olofsson, H., & Rydbeck, G. 1984, A&A, 130, 227

Johnstone, R. M. & Penston, M. V. 1986, MNRAS, 219, 927

Jura, M., Zuckerman, B., & Becklin, E. E.and Smith, R. C. 1993, ApJ, 418, 37

Kastner, J. H., Zuckerman, B., Weintraub, D. A., & Forveille, T. 1997, Science, 277, 67

Kawaguchi, K., Ohishi, M., Ishikawa, S., & Kaifu, N. 1992, ApJ, 386, L51

Kenyon, S. J., Calvet, N., & Hartmann, L. 1993, ApJ, 414, 676

Kenyon, S. J. & Hartmann, L. 1987, ApJ, 323, 714

—. 1995, ApJ, 101, 117

Knacke, R. F., Fajardo-Acosta, S. B., Telesco, C. M., Hackwell, J. A., Lynch, D. K., & Russell, R. W. 1993, ApJ, 418, 440

Koerner, D. W. & Sargent, A. I. 1995, AJ, 109, 2138

Koerner, D. W., Schneider, G., Smith, B. A., Becklin, E. E., Hines, D. C., Kirkpatrick, J. D., Lowrance, P. J., Meier, R., Reike, M., Terrile, R. J., Thompson, R. I., & NICMOS/IDT EONS Teams. 1998, in American Astronomical Society Meeting, Vol. 193, 7314

Kuiper, G. P. 1951, in Proceedings of a topical symposium, commemorating the 50th anniversary of the Yerkes Observatory and half a century of progress in astrophysics, New York: McGraw-Hill, 1951, edited by Hynek, J.A., 357

Langer, W. D. & Graedel, T. E. 1989, ApJS, 69, 241

Lawrence, G., Jones, T. J., & Gehrz, R. D. 1990, AJ, 99, 1232

Lay, O. P. 1997, A&AS, 122, 547

Linsky, J. L., Diplas, A., Wood, B. E., Brown, A., Ayres, T. R., & Savage, B. D. 1995, ApJ, 451, 335

Linsky, J. L. & Wood, B. E. 1996, ApJ, 463, 254

Malfait, K., Yamamura, I., Waters, L. B. F. M., Tielens, A. G. G. M., de Graauw, M. S., de Jong, T., de Koter, A., Malfait, K., van den Ancker, M. E., Van Winckel, H., Voors, R. H. M., & Waelkens, C. 1999, Nature, 401, 563

Mangum, J. G., Plambeck, R. L., & Wooten, A. 1991, ApJ, 369, 169

Mannings, V. & Sargent, A. I. 1997, ApJ, 490, 792

—. 2000a, ApJ, 529, 391

—. 2000b, ApJ, 529, 391

Meeus, G. & Waelkens, C. 1999, in ESA SP-427: The Universe as Seen by ISO, 373–+

Meeus, G., Waters, L. B. F. M., Bouwman, J., van den Ancker, M. E., Waelkens, C., & Malfait, K. 2001, A&A, 365, 476

Meier, R., Owen, T. C., Jewitt, D. C., Matthews, H. E., Senay, M., Biver, N., Bockelee-Morvan, D., Crovisier, J., & Gautier, D. 1998a, Science, 279, 1707

Meier, R., Owen, T. C., Matthews, H. E., Jewitt, D. C., Bockelee-Morvan, D., Biver, N., Crovisier, J., & Gautier, D. 1998b, Science, 279, 842

Men'shchikov, A. B. & Henning, T. 1997, A&A, 318, 879

Metchev, S. A., Hillenbrand, L. A., & Meyer, M. R. 2003, ArXiv Astrophysics e-prints

Millar, T. J., Bennett, A., & Herbst, E. 1989, ApJ, 340, 906

Millar, T. J., Bennett, A., Rawlings, J. M. C., Brown, P. D., & Charnley, S. B. 1991, A&AS, 87, 585

Millar, T. J., Farquhar, P. R. A., & Willacy, K. 1997, A&AS, 121, 139

Miroshnichenko, A. S., Mulliss, C. L., Bjorkman, K. S., Morrison, N. D., Kuratov, K. S., & Wisniewski, J. P. 1999, MNRAS, 302, 612

Molster, F. J., Yamamura, I., Waters, L. B. F. M.and Tielens, A. G. G. M., de Graauw, T., de Jong, T., de Koter, A., Malfait, K., van den Ancker, M. E., Van Winckel, H., Voors, R. H. M., & Waelkens, C. 1999, Nature, 401, 563

Montmerle, T. 1992, Memorie della Societa Astronomica Italiana, 63, 663

Mouillet, D., Larwood, J. D., Papaloizou, J. C. B., & Lagrange, A. M. 1997, MNRAS, 292, 896

Mumma, M. J., Dello Russo, N., DiSanti, M. A., Magee-Sauer, K., Novak, R. E., Brittain, S., Rettig, T., McLean, I. S., Reuter, D. C., & Xu, L. 2001, Science, 292, 1334

Myers, P. C., Fuller, G. A., Mathieu, R. D., Beichman, C. A., Benson, P. J., Schild, R. E., & Emerson, J. P. 1987, ApJ, 319, 340

Nakano, T. & Tademaru, E. 1972, ApJ, 173, 87

Natta, A., Grinin, V. P., Mannings, V., & Ungerechts, H. 1997, ApJ, 491, 885

Natta, A., Meyer, M. R., & Beckwith, S. V. W. 2000, ApJ, 534, 838

Natta, A., Prusti, T., Neri, R., Wooden, D., Grinin, V. P., & Mannings, V. 2001, A&A, 371, 186

Nee, J. B. & Lee, L. C. 1985, ApJ, 291, 202

Nesbitt, F., Marston, G., & Stief, L. 1990, J. Phys. Chem., 94, 4946

Neuhaeuser, R., Sterzik, M. F., Schmitt, J. H. M. M., Wichmann, R., & Krautter, J. 1995, A&A, 297, 391

Nuth, J. A. & Donn, B. 1982, ApJ, 257, L103

Nuth, J. A. & Glicker, S. 1982, Journal of Quantitative Spectroscopy and Radiative Transfer, 28, 223

Ozernoy, L. M., Gorkavyi, N. N., Mather, J. C., & Taidakova, T. A. 2000, ApJ, 537, L147

Pickett, H. M., Poynter, R. L., Cohen, E. A., Delitsky, M. L., Pearson, J. C., & Muller, H. S. P. 1998, Journal of Quantitative Spectroscopy and Radiative Transfer, 60, 883

Pineau des Forets, G., Roueff, E., & Flower, D. R. 1990, MNRAS, 244, 668

Piskunov, N., Wood, B. E., Linsky, J. L., Dempsey, R. C., & Ayres, T. R. 1997, ApJ, 474, 315

Pollack, J. B., Hubickyj, O., Bodenheimer, P., Lissauer, J. J., Podolak, M., & Greenzweig, Y. 1996, Icarus, 124, 62

Prasad, S. S. & Huntress, W. T. 1980, ApJS, 43, 1

Qi, C. 2001, PhD thesis, California Institute of Technology

Qi, C., Kessler, J. E., Koerner, D. W., Sargent, A. I., & Blake, G. A. 2003, ArXiv Astrophysics e-prints

Rice, W. K. M., Wood, K., Armitage, P. J., Whitney, B. A., & Bjorkman, J. E. 2003, MNRAS, 342, 79

Rodgers, S. D. & Charnley, S. B. 2002, Planet. Space Sci., 50, 1125

Sargent, A. I. & Beckwith, S. 1987, ApJ, 323, 294

Sault, R. J., Teuben, P. J., & Wright, M. C. H. 1995, in ASP Conf. Ser. 77: Astronomical Data Analysis Software and Systems IV, 433–+

Schöier, F. L., Jørgensen, J. K., van Dishoeck, E. F., & Blake, G. A. 2002, A&A, 390, 1001

Scoville, N. Z., Carlstrom, J. E., Chandler, C. J., Phillips, J. A., Scott, S. L., Tilanus, R. P. J., & Wang, Z. 1993, PASP, 105, 1482

Scoville, N. Z., Sargent, A. I., Sanders, D. B., Claussen, M. J., Masson, C. R., Lo, K. Y., & Phillips, T. G. 1986, ApJ, 303, 416

Simon, M., Dutrey, A., & Guilloteau, S. 2001, ApJ, 545, 1034

Sitko, M. L., Grady, C. A., Lynch, D. K., Russell, R. W., & Hanner, M. S. 1999, ApJ, 510, 408

Skinner, C. J., Barlow, M. J., & Justtanont, K. 1992, MNRAS, 255, 31P

Skinner, C. J., Sylvester, R. J., Graham, J. R., Barlow, M. J., Meixner, M., Keto, E., Arens, J. F., & Jernigan, J. G. 1995, ApJ, 444, 861

Sloan, G. C. & Price, S. D. 1995, ApJ, 451, 758

—. 1998, ApJS, 119, 141

Spaans, M. 1996, in IAU Symp. 178: Molecules in Astrophysics: Probes & Processes, 431

Steinacker, J. & Henning, T. 2003, ApJ, 583, L35

Sternberg, A. & Dalgarno, A. 1995, ApJS, 99, 565

Sutton, E. C., Peng, R., Danchi, W. C., Jaminet, P. A., Sandell, G., & Russell, A. P. G. 1995, ApJS, 97, 455

Sylvester, R. J., Skinner, C. J., Barlow, M. J., & Mannings, V. 1996, MNRAS, 279, 915

Takano, S., Masuda, A., Hirahara, Y., Suzuki, H., Ohishi, M., Ishikawa, S., Kaifu, N., Kasai, Y., Kawaguchi, K., & Wilson, T. L. 1998, A&A, 329, 1156

Thi, W. F., van Dishoeck, E. F., Blake, G. A., van Zadelhoff, G. J., Horn, J., Becklin, E. E., Mannings, V., Sargent, A. I., van den Ancker, M. E., Natta, A., & Kessler, J. 2001, ApJ, 561, 1074

Tielens, A. G. G. M. & Allamandola, L. J. 1987, in ASSL Vol. 134: Interstellar Processes, 397–469

Tielens, A. G. G. M. & Hollenbach, D. 1985, ApJ, 291, 747

Turner, B. E., Pirogov, L., & Minh, Y. C. 1997, ApJ, 483, 235

Umebayashi, T. & Nakano, T. 1981, PASJ, 33, 617

van Boekel, R., Waters, L. B. F. M., Dominik, C., Bouwman, J., de Koter, A., Dullemond, C. P., & Paresce, F. 2003, A&A, 400, L21

van den Ancker, M. E., Bouwman, J., Wesselius, P. R., Waters, L. B. F. M., Dougherty, S. M., & van Dishoeck, E. F. 2000, A&A, 357, 325

van den Ancker, M. E., de Winter, D., & Tjin A Djie, H. R. E. 1998, A&A, 330, 145

van Dishoeck, E. F. & Blake, G. A. 1998, ARA&A, 36, 317

van Dishoeck, E. F., Blake, G. A., Jansen, D. J., & Groesbeck, T. D. 1995, ApJ, 447, 760

van Dishoeck, E. F., Thi, W.-F., & van Zadelhoff, G.-J. 2003, A&A, 400, L1

van Zadelhoff, G.-J. 2002, PhD thesis, Leiden University, The Netherlands van Zadelhoff, G.-J., van Dishoeck, E. F., Thi, W.-F., & Blake, G. A. 2001, A&A, 377, 566

Walmsley, C. M., Hermsen, W., Henkel, C., Mauersberger, R., & Wilson, T. L. 1987, A&A, 172, 311

Weaver, H. A., Chin, G., Bockelée-Morvan, D., Crovisier, J., Brooke, T. Y., Cruikshank, D. P., Geballe, T. R., Kim, S. J., & Meier, R. 1999, Icarus, 142, 482

Weinberger, A. J., Becklin, E. E., & Zuckerman, B. 2003, ApJ, 584, L33

White, R. J. & Ghez, A. M. 2001, ApJ, 556, 265

Willacy, K., Klahr, H. H., Millar, T. J., & Henning, T. 1998, A&A, 338, 995

Willacy, K. & Langer, W. D. 2000, ApJ, 544, 903

Wilson, T. L. & Rood, R. 1994, ARA&A, 32, 191

Wiscombe, W. J. & Joseph, J. H. 1977, Icarus, 32, 362

Wolf, S., Gueth, F., Henning, T., & Kley, W. 2002, ApJ, 566, L97

Wood, K., Lada, C. J., Bjorkman, J. E., Kenyon, S. J., Whitney, B., & Wolff, M. J. 2002, ApJ, 567, 1183

Wooden, D. H. 2002, Earth Moon and Planets, 89, 247

Wootten, A. 1987, in IAU Symp. 120: Astrochemistry, Vol. 120, 311–318

Zinnecker, H. & Preibisch, T. 1994, A&A, 292, 152

Zuckerman, B., Forveille, T., & Kastner, J. H. 1995, Nature, 373, 494

Zuckerman, B., Song, I., Bessell, M. S., & Webb, R. A. 2001, ApJ, 562, L87